

N° d'ordre : 7294

LAL 03-51  
Septembre 2003

UNIVERSITÉ PARIS XI  
UFR SCIENTIFIQUE D'ORSAY

THÈSE

présentée

pour obtenir

Le GRADE de DOCTEUR EN SCIENCES  
DE L'UNIVERSITÉ PARIS XI – ORSAY

par

Ladislav VÁLA

Sujet : **Measurement of the  $2\nu\beta\beta$  decay of  $^{100}\text{Mo}$  to the excited  $0_1^+$  state in the NEMO3 experiment**

Soutenue le **24 septembre 2003** devant la Commission d'examen

MM. AUGÉ Etienne	Président
KOVALÍK Alojz	Rapporteur
LALANNE Dominique	
STOCCHI Achille	Rapporteur
ŠIMKOVIC Fedor	
ŠTEKL Ivan	



*To my parents*



# Preface

The work towards this thesis has been done within the framework of the Ph.D. study under double French-Czech supervision (“thèse en cotutelle franco-tchèque”) involving LAL Orsay and the Czech Technical University in Prague. The Ph.D. programme and the scientific research of L. Vála within the NEMO3 experiment have been supported by an 18-month scholarship from the French Government (1999-2002) and by two grants from the Czech Technical University in Prague No. CTU 300010304 (in 2000) and No. CTU 300111314 (in 2001) respectively. The project was also partially financed within the framework of the France-Czech Republic collaboration agreement No. 01-18.

## Acknowledgement

Firstly, I would like to thank Serge Jullian, the spokesman of the NEMO Collaboration, who officially admitted me to the NEMO Collaboration and introduced me into the NEMO group in LAL Orsay.

Next my thanks go to Ivan Štekl and Dominique Lalanne for having conducted and supervised my Ph.D. work, as well as for their valuable advice, help, and support through the last years.

I would like to express my gratitude also to my colleagues and friends from the NEMO Collaboration for their encouragement, help, and friendship, in particular to those with whom I worked on the NEMO3 experiment in LAL Orsay and in the LSM Modane: Cécile Jollet, Corinne Augier, Christine Marquet, Xavier Sarazin, Oleg Kochetov, Fabrice Piquemal, Laurent Simard, Yuriy Shitov, Georges Szklarz etc.

My thanks also go to Leo Jenner and Phil Adamson for their attentive reading and English correction of this thesis.

I also appreciate all the help of the administrative staff of LAL Orsay and of the technical staff of the LSM Modane.

Finally, the biggest thanks and my highest gratitude are dedicated to my parents and my sister for their full support, encouragement, and understanding through all the years of my graduate (1995-1998) and post-graduate (1998-2003) studies in France.

Thank you!



# Contents

<b>Introduction</b>	<b>1</b>
<b>1 The physics of the neutrino</b>	<b>3</b>
1.1 Introduction – history	3
1.2 Mass and nature of neutrinos	4
1.2.1 Majorana or Dirac neutrinos?	4
1.2.2 Neutrino mixing and oscillations	5
1.3 Measurements of neutrino masses	7
1.3.1 Direct techniques for neutrino mass measurements	8
1.3.2 Review of indirect techniques for neutrino mass measurements	10
<b>2 Double beta decay – theory and experiments</b>	<b>15</b>
2.1 Introduction	15
2.2 Double beta decay mechanisms	19
2.2.1 Two-neutrino double beta decay	21
2.2.2 Neutrinoless double beta decay	22
2.3 Experimental techniques	22
2.3.1 Indirect methods of $\beta\beta$ decay measurement	22
2.3.2 Direct methods of $\beta\beta$ decay measurement	22
2.3.3 Calorimetric experiments	23
2.3.4 Experiments using particle track reconstruction	24
2.3.5 Review of the main results for $2\nu\beta\beta$ and $0\nu\beta\beta$ decays	25
<b>3 <math>2\nu\beta\beta</math> decay of <math>^{100}\text{Mo}</math> to excited states</b>	<b>29</b>
3.1 Theoretical calculations	29
3.2 Previous experiments and their results	30
3.3 NEMO3 and the $2\nu\beta\beta$ decay to excited states	34
<b>4 The NEMO3 experiment</b>	<b>35</b>
4.1 Introduction	35
4.2 General description of the detector	36
4.3 Tracking wire chamber	39
4.3.1 Wire chamber geometry	39
4.3.2 Geiger cell working principle	40
4.4 Calorimeter	42
4.4.1 Energy and time calibration	43
4.5 Source foils	44
4.5.1 Installed sources	44

4.5.2	Source foil production . . . . .	44
4.5.3	Radiopurity of foils . . . . .	47
4.6	Reduction of external backgrounds . . . . .	47
4.6.1	Iron shield . . . . .	47
4.6.2	Neutron shielding . . . . .	47
4.6.3	Magnetic field . . . . .	48
4.7	Electronics . . . . .	49
4.7.1	Wire chamber electronics . . . . .	49
4.7.2	Calorimeter electronics . . . . .	50
4.7.3	Trigger . . . . .	52
4.7.4	Data acquisition system and detector monitoring . . . . .	52
4.8	Backgrounds in NEMO3 . . . . .	53
4.8.1	Internal background . . . . .	53
4.8.2	External background . . . . .	57
4.9	Radiopurity of the detector . . . . .	63
<b>5</b>	<b>Monte-Carlo studies</b>	<b>65</b>
5.1	Introduction . . . . .	65
5.2	Monte-Carlo simulations . . . . .	65
5.2.1	Simulation program . . . . .	65
5.2.2	Trigger for the Monte-Carlo simulations . . . . .	66
5.2.3	Types of simulated events . . . . .	66
5.3	Definition of particles for Monte-Carlo events . . . . .	67
5.3.1	Electrons and positrons . . . . .	67
5.3.2	Photons . . . . .	68
5.3.3	$\alpha$ -particles . . . . .	68
5.4	Response of the detector to the de-excitation photons . . . . .	68
5.5	eeN $\gamma$ channel . . . . .	70
5.6	Two-electron preselection . . . . .	76
5.7	Reduction of background from radon . . . . .	76
5.8	Kinematic and temporal cuts on the eeN $\gamma$ channel . . . . .	78
5.8.1	Time-of-flight test for electrons . . . . .	78
5.8.2	Energy cuts applied on two-electron events with photons . . . . .	84
5.8.3	$\gamma$ -clusters with low energy deposits . . . . .	86
5.8.4	Time-of-flight tests applied to photons . . . . .	86
5.9	Final set of cuts for the eeN $\gamma$ channel . . . . .	93
5.10	Effect of the cuts for the eeN $\gamma$ channel . . . . .	95
5.10.1	Internal background . . . . .	96
5.10.2	External background . . . . .	96
5.10.3	$\beta\beta$ events from molybdenum . . . . .	97
5.10.4	Radon contribution . . . . .	99
5.11	Number of expected events . . . . .	104
5.11.1	Calculation of number of expected events . . . . .	104
5.11.2	Expected contributions to the eeN $\gamma$ channel . . . . .	104
5.12	Conclusions . . . . .	105

<b>6</b>	<b>Data analysis</b>	<b>107</b>
6.1	Software tools for the data analysis . . . . .	107
6.2	Definition of particles in real events . . . . .	108
6.3	Selection of events for the eeN $\gamma$ channel . . . . .	108
6.4	Analysed runs . . . . .	109
6.4.1	Trigger used for data acquisition . . . . .	110
6.4.2	Betabeta runs . . . . .	110
6.4.3	Runs with sources of $^{208}\text{Tl}$ and $^{214}\text{Bi}$ . . . . .	112
6.5	Estimation of the real detection efficiency . . . . .	114
6.5.1	Calorimeter efficiency estimation . . . . .	114
6.5.2	Wire chamber efficiency estimation . . . . .	115
6.5.3	Global efficiency of the detector . . . . .	115
6.6	Results for the $\beta\beta$ runs in the eeN $\gamma$ channel . . . . .	115
6.6.1	Observation for Period I . . . . .	115
6.6.2	Observation for Period II . . . . .	117
6.6.3	Summary for both periods of runs . . . . .	122
6.7	The origin of systematic errors . . . . .	126
6.8	Conclusions . . . . .	128
	<b>Conclusion</b>	<b>129</b>
	<b>Bibliography</b>	<b>131</b>



# List of Figures

1.1	An example of a tritium beta decay spectrum and of a Kurie plot . . . . .	9
1.2	Spectrum of solar neutrinos according to the Standard Solar Model (SSM). . . . .	12
1.3	An overview of the reactor neutrino oscillation experiments showing the excluded regions at 90% C.L. in the the $\Delta m^2$ versus $\sin^2 2\theta$ plot. . . . .	13
2.1	A scheme of double beta decay with intermediate virtual $1^+$ states. . . . .	16
2.2	The Feynman diagram of the two-neutrino double beta decay. . . . .	16
2.3	The Feynman diagram of neutrinoless double beta decay involving only the left-handed currents ( $V - A$ couplings). . . . .	17
2.4	The Feynman diagram of neutrinoless double beta decay involving the right-handed current ( $V + A$ coupling) in addition to the left-handed one ( $V - A$ coupling). . . . .	18
2.5	The Feynman diagram of neutrinoless double beta decay with majoron emission. . . . .	18
2.6	Schematic electron sum-energy spectra of the three double beta decay modes. . . . .	20
3.1	A double beta decay scheme of $^{100}\text{Mo}$ to the ground and excited states of $^{100}\text{Ru}$ . . . . .	30
3.2	The $\gamma$ -ray energy spectrum in the region of interest measured in [124]. . . . .	32
3.3	Partial $\gamma$ -ray spectra in the energy windows corresponding to the decay of the first excited states of $^{100}\text{Ru}$ obtained in [125]. . . . .	33
3.4	The $\gamma$ -ray spectra in coincidence (a) with $540 \pm 2.5$ keV and (b) with $591 \pm 2.5$ keV obtained in [128]. . . . .	34
4.1	A schematic diagram of the NEMO2 detector without shielding. . . . .	36
4.2	A schematic diagram of the NEMO3 detector. . . . .	37
4.3	A view of a sector of the NEMO3 detector. . . . .	38
4.4	A diagram of an elementary drift Geiger cell. . . . .	40
4.5	The Geiger cell layout in a sector (top view). . . . .	41
4.6	The primary avalanche in the proximity of an anode wire triggered by a single electron. . . . .	42
4.7	Distribution by individual sectors of the NEMO3 sources (top view). . . . .	45
4.8	Diagram of the iron shielding. . . . .	48
4.9	A general view of magnetic coil. . . . .	49
4.10	An overview of different TDC times associated with the wire chamber acquisition electronics. . . . .	51
4.11	A simplified decay scheme of $^{208}\text{Tl}$ showing only the principal $\gamma$ and $\beta^-$ transitions with intensities per decay greater than 2%. . . . .	54
4.12	A simplified decay scheme of $^{214}\text{Bi}$ showing only the principal $\gamma$ and $\beta^-$ transitions with intensities per decay greater than 2%. . . . .	55

4.13	The main ways of creation of two-electron events inside a source foil imitating double beta decay events. . . . .	60
4.14	The main methods of creation of two-electron events due to the interaction of photons coming from outside the source foils. . . . .	61
4.15	The $^{238}\text{U}$ and $^{232}\text{Th}$ decay chains of natural radioactivity. . . . .	62
5.1	Energy spectra $E_\gamma$ (upper graph) and $E_{N\gamma}$ (lower graph) for 540 keV photons which were generated by the Monte-Carlo simulation program uniformly in the NEMO3 source foils. . . . .	69
5.2	Energy spectra $E_\gamma$ (upper graph) and $E_{N\gamma}$ (lower graph) for 590 keV photons which were generated by the Monte-Carlo simulation program uniformly in the NEMO3 source foils. . . . .	69
5.3	Number of fired $\gamma$ -clusters detected by the NEMO3 calorimeter after interaction of photons of 540 or 590 keV which were generated in source foils. . . . .	71
5.4	Distribution of the number of $\gamma$ -clusters triggered in the NEMO3 calorimeter for the Monte-Carlo simulation of the $2\nu\beta\beta$ decay of $^{100}\text{Mo}$ to the excited $0_1^+$ state. . . . .	71
5.5	An example of simulated $2\nu\beta\beta$ decay of $^{100}\text{Mo}$ to excited $0_1^+$ state. . . . .	72
5.6	Another example of a Monte-Carlo $2\nu\beta\beta(\text{g.s.} \rightarrow 0_1^+)$ event. . . . .	73
5.7	One more example of a $2\nu\beta\beta(\text{g.s.} \rightarrow 0_1^+)$ event generated by Monte-Carlo simulation program. . . . .	74
5.8	The transverse view of the event of Fig. 5.7. . . . .	75
5.9	An example of a $^{214}\text{Bi} - ^{214}\text{Po}$ ee $2\gamma\alpha$ event with bad track reconstruction. . . . .	77
5.10	An illustration of two different scenarios for the two-electron events. . . . .	78
5.11	$\Delta T_{\text{ee}}$ distributions for internal events from the $2\nu\beta\beta$ decay of $^{100}\text{Mo}$ , g.s. $\rightarrow 0_1^+$ and g.s. $\rightarrow$ g.s. transitions, for the external background from $^{208}\text{Tl}$ and $^{214}\text{Bi}$ and for $^{214}\text{Bi}$ present in the gas of the wire chamber. . . . .	80
5.12	Distributions of probability that two-electron events simulated for the g.s. $\rightarrow 0_1^+$ transition of the $2\nu\beta\beta$ decay of $^{100}\text{Mo}$ are of the internal type ( <i>Prob_int</i> ) or of the crossing particle type ( <i>Prob_cross</i> ). . . . .	82
5.13	Distributions of probability that two-electron events simulated for the external background from $^{208}\text{Tl}$ and $^{214}\text{Bi}$ are of the internal type ( <i>Prob_int</i> ) or of the crossing particle type ( <i>Prob_cross</i> ). . . . .	83
5.14	$E_{\text{ee}}$ spectra for simulated events of the $2\nu\beta\beta$ decay of $^{100}\text{Mo}$ , g.s. $\rightarrow 0_1^+$ and g.s. $\rightarrow$ g.s. transitions, for external background from $^{208}\text{Tl}$ (middle row, at left) and $^{214}\text{Bi}$ and for $^{214}\text{Bi}$ present in the gas of the wire chamber. . . . .	85
5.15	$E_{N\gamma}$ spectra for simulated events of the $2\nu\beta\beta$ decay of $^{100}\text{Mo}$ , g.s. $\rightarrow 0_1^+$ and g.s. $\rightarrow$ g.s. transitions, for external background from $^{208}\text{Tl}$ (middle row, at left) and $^{214}\text{Bi}$ and for $^{214}\text{Bi}$ present in the gas of the wire chamber. . . . .	87
5.16	Two-dimensional $E_{N\gamma}$ vs. $E_{\text{ee}}$ plots for simulated events of the $2\nu\beta\beta$ decay of $^{100}\text{Mo}$ , g.s. $\rightarrow 0_1^+$ and g.s. $\rightarrow$ g.s. transitions, for external background from $^{208}\text{Tl}$ (middle row, at left) and $^{214}\text{Bi}$ and for $^{214}\text{Bi}$ present in the gas of the wire chamber. . . . .	88
5.17	An external photon detected at the time $t_\gamma$ generating two electrons in the source foils at time $t_0$ . . . . .	90
5.18	An event of the internal type with all the four particles emitted from the source foils at the same time $t_0$ . . . . .	91

5.19	In this event only one of the two detected photons ( $\gamma_1$ ) comes from the vertex of the two electrons. The second photon, $\gamma_2$ , is in reality generated by reflection or re-emission of the first one. . . . .	92
5.20	Distributions of probability for photons from the $2\nu\beta\beta$ decay of $^{100}\text{Mo}$ to the excited state in the cases of the external hypothesis and in the case of the internal hypothesis. . . . .	94
5.21	The distribution of finally selected eeN $\gamma$ events for the $2\nu\beta\beta$ decay of $^{100}\text{Mo}$ to the excited $0_1^+$ state in the $E_{N\gamma}$ vs. $E_{ee}$ plot. . . . .	98
5.22	Distribution of the number of $\gamma$ -clusters generated in the $2\nu\beta\beta$ decay of $^{100}\text{Mo}$ to the ground state. . . . .	99
5.23	An example of a $^{214}\text{Bi} - ^{214}\text{Po}$ e $\alpha$ event in the wire chamber gas. . . . .	100
5.24	An example of a $^{214}\text{Bi} - ^{214}\text{Po}$ e $2\gamma\alpha$ event generated in the wire chamber gas. . .	101
5.25	A two-dimensional $E_{N\gamma}$ vs. $E_{ee}$ plot for the finally selected events from $^{214}\text{Bi}$ decay inside the wire chamber. . . . .	102
5.26	An example of a $^{214}\text{Bi} - ^{214}\text{Po}$ decay generated in the wire chamber gas producing a two-electron event accompanied by an $\alpha$ -particle. . . . .	102
5.27	Another example of a simulated $^{214}\text{Bi} - ^{214}\text{Po}$ decay in the gas of the wire chamber producing an ee $2\gamma\alpha$ event. . . . .	103
5.28	Top and transverse views of a $^{214}\text{Bi} - ^{214}\text{Po}$ decay generated by Monte-Carlo in the gas of the wire chamber giving an ee $2\gamma\alpha$ event. . . . .	103
6.1	A view of the only event from runs with sources of $^{208}\text{Tl}$ and $^{214}\text{Bi}$ that satisfied all the selection criteria for the eeN $\gamma$ channel. . . . .	113
6.2	$E_{N\gamma}$ vs. $E_{ee}$ plot of events without any $\alpha$ -particle which were selected in Mo foils and corresponding to the $\beta\beta$ runs of Period I. . . . .	118
6.3	$E_{N\gamma}$ vs. $E_{ee}$ plot of events containing $\alpha$ -particles selected either in molybdenum foils (plain blue boxes) or in non-molybdenum foils (empty red boxes) and corresponding to the $\beta\beta$ runs of Period I. . . . .	118
6.4	$E_{N\gamma}$ vs. $E_{ee}$ plot of events selected in non-molybdenum foils either without any $\alpha$ -particle (patterned black boxes) or with detected $\alpha$ -particle (empty red boxes) issued from the $\beta\beta$ runs of Period I. . . . .	119
6.5	$E_{N\gamma}$ vs. $E_{ee}$ plot of all the selected background events corresponding to the $\beta\beta$ runs of Period I. . . . .	119
6.6	$E_{N\gamma}$ vs. $E_{ee}$ plot of events without any $\alpha$ -particle which were selected in Mo foils and corresponding to the $\beta\beta$ runs of Period II. . . . .	123
6.7	$E_{N\gamma}$ vs. $E_{ee}$ plot of events containing $\alpha$ -particles selected either in molybdenum foils (plain blue boxes) or in non-molybdenum foils (empty red boxes) and corresponding to the $\beta\beta$ runs of Period II. . . . .	123
6.8	$E_{N\gamma}$ vs. $E_{ee}$ plot of events selected in non-molybdenum foils either without any $\alpha$ -particle (patterned black boxes) or with detected $\alpha$ -particle (empty red boxes) issued from the $\beta\beta$ runs of Period II. . . . .	124
6.9	$E_{N\gamma}$ vs. $E_{ee}$ plot of all the selected background events corresponding to the $\beta\beta$ runs of Period II. . . . .	124



# List of Tables

1.1	Limits on $\overline{M_{\nu_e}}$ from recent tritium beta decay experiments. . . . .	8
1.2	Current limits on neutrino masses from direct experiments. . . . .	10
2.1	A list of the $\beta^-\beta^-$ decay transitions for naturally occurring parent isotopes and the corresponding $Q_{\beta\beta}$ values in keV and the natural abundances of the parent isotopes. . . . .	26
2.2	A list of the $\beta^+\beta^+$ decay transitions for naturally occurring parent isotopes and the corresponding $Q_{\beta\beta}$ values in keV and the natural abundances of the parent isotopes. . . . .	27
2.3	Experimentally determined half-lives for the $2\nu\beta\beta$ decay mode in the principal double beta decay experiments. . . . .	27
2.4	Experimentally determined half-life limits for the $0\nu\beta\beta$ decay mode in the principal double beta decay experiments. . . . .	28
3.1	Calculated half-life values for $2\nu\beta\beta$ decay of $^{100}\text{Mo}$ to the two first excited states for different theoretical models. . . . .	31
3.2	Experimentally determined half-life values or limits for the $2\nu\beta\beta$ decay of $^{100}\text{Mo}$ to the excited $0_1^+$ state. . . . .	32
4.1	The half-life values for $2\nu\beta\beta$ decay determined with the NEMO2 detector. . . . .	35
4.2	The $Q_{\beta\beta}$ -values and abundance of isotopes studied with the NEMO3 detector. . . . .	39
4.3	Measured activities of the NEMO3 PMTs [133] compared with the allowed upper limits. . . . .	43
4.4	A list of sources installed in the NEMO3 detector with respective net masses of isotopes and their occupation of sectors [135]. . . . .	44
4.5	Foil types and enrichment rates of isotopes used in NEMO3 [135]. . . . .	46
4.6	Measured activities of the source foils installed in the NEMO3 detector . . . . .	47
4.7	A summary of $\gamma$ -rays from decay of $^{208}\text{Tl}$ sorted by their energy according to Ref. [131] where only transitions with intensity per decay higher than 1% are listed here. . . . .	56
4.8	A summary of $\gamma$ -rays from decay of $^{214}\text{Bi}$ sorted by their energy [131] where only transitions with intensity per decay higher than 1% are listed. . . . .	57
4.9	A list of electrons from decay of $^{208}\text{Tl}$ sorted by their energy according to Ref. [131]. Only $\beta^-$ transitions with intensity per decay higher than 0.1% are given. . . . .	58
4.10	A list of electrons from decay of $^{214}\text{Bi}$ sorted by their energy according to Ref. [131]. Only $\beta^-$ transitions with intensity per decay higher than 1% are given. . . . .	59
4.11	A list of $\alpha$ -particles and their relative intensities from direct decay of $^{214}\text{Bi}$ according to Ref. [131]. . . . .	60

4.12	Main activities in NEMO3 measured with HPGe detectors. . . . .	64
5.1	Types of simulated processes together with numbers of generated and recorded events after the Monte-Carlo trigger. . . . .	67
5.2	Monte-Carlo simulations of de-excitation photons in NEMO3. . . . .	70
5.3	Proportions of Monte-Carlo events, obtained from simulations of photons of 540 and 590 keV in source foils, generating 1, 2, 3, or more $\gamma$ -clusters in the NEMO3 detector. . . . .	70
5.4	Number of $\gamma$ -clusters for Monte-Carlo events of the $2\nu\beta\beta$ decay of $^{100}\text{Mo}$ to the excited $0_1^+$ state. . . . .	76
5.5	Proportions of events satisfying the $\Delta T_{ee} < x$ condition for different values of $x$ . . . . .	79
5.6	Proportions of events satisfying the $E_{ee} < X$ cut for different values of $X$ . . . . .	84
5.7	Proportions of events satisfying the $X < E_{N\gamma} < 1200$ keV cut for different values of $X$ . . . . .	86
5.8	Numbers of events and corresponding probabilities at different stages of event selection for internal background from $^{208}\text{Tl}$ . . . . .	96
5.9	Numbers of events and corresponding probabilities at different stages of event selection for the internal background from $^{214}\text{Bi}$ . . . . .	96
5.10	Numbers of events and corresponding probabilities at different stages of event selection for external background from $^{208}\text{Tl}$ . . . . .	97
5.11	Numbers of events and corresponding probabilities at different stages of event selection for external background from $^{214}\text{Bi}$ . . . . .	97
5.12	Numbers of events and corresponding probabilities at different stages of event selection for the $2\nu\beta\beta$ decay of $^{100}\text{Mo}$ to the excited $0_1^+$ state. . . . .	98
5.13	Numbers of events and corresponding probabilities at different stages of event selection for the $2\nu\beta\beta$ decay of $^{100}\text{Mo}$ to the ground state. . . . .	99
5.14	Numbers of $\gamma$ -clusters for the $2\nu\beta\beta$ decay of $^{100}\text{Mo}$ to the ground state. . . . .	100
5.15	Numbers of events and corresponding probabilities at different stages of event selection for $^{214}\text{Bi} - ^{214}\text{Po}$ events (background from radon). . . . .	101
5.16	Numbers of $^{214}\text{Bi} - ^{214}\text{Po}$ events with and without detected $\alpha$ -particle which satisfy all the cuts with two different $E_{ee}$ cut-offs. . . . .	104
5.17	Numbers of expected events issued from Monte-Carlo simulations for different studied processes after the application of the complete set of energy and TOF cuts for the eeN $\gamma$ channel. . . . .	105
6.1	Monthly totals of net acquisition time of the $\beta\beta$ runs of Period I used for data analysis. . . . .	111
6.2	Monthly totals of net acquisition time of the $\beta\beta$ runs of Period II used for data analysis. . . . .	111
6.3	Activities of $^{208}\text{Tl}$ and $^{214}\text{Bi}$ sources, net running times, and corresponding equivalent times for acquisition without sources. . . . .	112
6.4	Parameters of the only event from runs with source of $^{214}\text{Bi}$ that satisfied all the selection criteria for the eeN $\gamma$ channel. . . . .	113
6.5	Efficiency of the calorimeter, $\eta_{PMT}$ , regarding the eeN $\gamma$ channel for different running periods used for the current analysis. . . . .	114
6.6	The global detection efficiency, $\eta$ , for the eeN $\gamma$ channel for two different periods of runs and the efficient time $T_{eff}$ for these periods. . . . .	116

6.7	Parameters of events selected in Mo foils and without any $\alpha$ -particle corresponding to $\beta\beta$ runs of Period I that satisfied all the selection criteria for the eeN $\gamma$ channel.	120
6.8	Parameters of events selected in non-molybdenum foils and without any $\alpha$ -particle corresponding to $\beta\beta$ runs of Period I that satisfied all the selection criteria for the eeN $\gamma$ channel. . . . .	121
6.9	Parameters of events selected in the eeN $\gamma$ channel in both molybdenum and non-molybdenum foils and containing $\alpha$ -particles which correspond to $\beta\beta$ runs of Period I. . . . .	121
6.10	Parameters of events selected in Mo foils and without any $\alpha$ -particle corresponding to $\beta\beta$ runs of Period II that satisfied all the selection criteria for the eeN $\gamma$ channel.	122
6.11	Parameters of events selected in non-molybdenum foils and without any $\alpha$ -particle corresponding to $\beta\beta$ runs of Period II that satisfied all the selection criteria for the eeN $\gamma$ channel. . . . .	122
6.12	Parameters of events selected in the eeN $\gamma$ channel in both molybdenum and non-molybdenum foils and containing $\alpha$ -particles which correspond to $\beta\beta$ runs of Period II. . . . .	125
6.13	A summary of numbers of finally selected events in the eeN $\gamma$ channel for both considered periods of runs. . . . .	125



# Introduction

Observation of neutrinoless double beta decay ( $0\nu\beta\beta$ ) is the most promising test of the Majorana nature of the neutrino that exists today. Contrary to two-neutrino double beta decay ( $2\nu\beta\beta$ ), this process violates lepton number conservation by two units and also requires a helicity flip which can be produced only by the neutrino being massive or by the existence of right-handed lepton charged currents. So, the  $0\nu\beta\beta$  decay opens the gates of new physics beyond the Standard Model and is a very attractive topic in particle physics today for both theoretical and experimental physicists.

One of the currently running experiments searching for neutrinoless double beta decay is NEMO. The main goal of the NEMO Collaboration was to construct a detector with sensitivity to the effective neutrino mass  $\langle m_\nu \rangle$  at the level of (0.3 – 0.1) eV. Since the beginning of the experiment in 1988, two technological prototypes, NEMO1 and NEMO2, have proven the feasibility of such a project and contributed to the background studies; NEMO2 has already measured half-lives of the  $2\nu\beta\beta$  decay of  $^{100}\text{Mo}$ ,  $^{82}\text{Se}$ ,  $^{116}\text{Cd}$ , and  $^{96}\text{Zr}$ . The NEMO3 detector combines two techniques: particle identification provided by a tracking wire chamber and a calorimeter for energy and time measurements of particles. The apparatus which is installed in the Modane Underground Laboratory accomodates around 10 kg of different double beta decay isotopes, including  $^{100}\text{Mo}$ ,  $^{82}\text{Se}$ ,  $^{116}\text{Cd}$ ,  $^{130}\text{Te}$ ,  $^{150}\text{Nd}$ ,  $^{96}\text{Zr}$ , and  $^{48}\text{Ca}$ . Due to its size and its ability to efficiently suppress backgrounds, NEMO3 reaches the original sensitivity requirements of the NEMO Collaboration. The detector has been taking experimental data for the study of various double beta decay modes since May 2002. At present, these data already gives very encouraging results for the ordinary  $2\nu\beta\beta$  decay of all installed isotopes, as well as for the  $2\nu\beta\beta$  decay of  $^{100}\text{Mo}$  to the excited  $0_1^+$  state in  $^{100}\text{Ru}$ .

The present document starts with a concise review of basic facts about the neutrino and its physical properties. Chapter 1 continues with an overview of different experiments (historical, present, and future projects) allowing either direct (tritium decay) or indirect (double beta decay, neutrino oscillations) measurement of neutrino mass.

Chapter 2 describes in detail various modes of double beta decay. After that, a description of the different techniques used in the quest for double beta decay, as well as a review of the main projects, either historically important, current, or promising in the future, are given. A summary of experimentally determined half-lives for the  $2\nu\beta\beta$  mode and a summary of limits on half-lives for the  $0\nu\beta\beta$  mode, issued from the principal experiments, are also given.

The next chapter deals with the  $2\nu\beta\beta$  decay of  $^{100}\text{Mo}$  to excited states of  $^{100}\text{Ru}$ . The first part of Chapter 3 explains the motivation for the study of this process. Then recently published results of theoretical calculations are given and they are followed by an overview of the experimental results.

Chapter 4 gives a detailed description of the NEMO3 experiment. To begin, the goal of

the experiment, its history, and the general description of the experimental setup are described. The following part deals with the conception and performances of the tracking wire chamber and the calorimeter, the sources installed in NEMO3, including their production, purification, and radiopurity measurements; measures taken against different kinds of external backgrounds, and the electronics used for data acquisition. In the last part of the chapter, the different types of backgrounds that have to be managed in the NEMO3 experiment are discussed.

Chapter 5 is devoted to Monte-Carlo simulations. The NEMO3 simulation program, and parameters applied to generate Monte-Carlo events, as well as all the different processes that were simulated (effect and backgrounds) are mentioned at the beginning. They are followed by the definitions of the particles identified in the detector (electrons, positrons, photons, and  $\alpha$ -particles) by means of unambiguous signatures. The goal of the subsequent part is to construct a set of appropriate selection conditions allowing the observation of the  $2\nu\beta\beta$  decay of  $^{100}\text{Mo}$  to the excited  $0_1^+$  state whilst efficiently discriminating against the backgrounds. The construction of such conditions starts by the examination of the detector's response to de-excitation photons generated with the simulation program. Then, the optimal kinematic cuts and temporal criteria applied to electrons and photons are defined step by step; their effect is tested each time on the simulated signal and background events. Attention is paid also to the reduction of background events coming from radon that penetrate the detector. After the review of the final set of selection conditions for the  $eeN\gamma$  channel, the effect of the principal stages of the selection is studied on simulated data for the  $2\nu\beta\beta$  decay to the ground and excited  $0_1^+$  states, internal and external backgrounds from  $^{208}\text{Tl}$  and  $^{214}\text{Bi}$ , and for the background from radon. At the end of the chapter, the expected contributions to the  $eeN\gamma$  channel from each process after the application of the complete set of selection criteria are given.

The last chapter of the thesis, Chapter 6, deals with the analysis of experimental data that were available from May 2002 to May 2003. At the beginning of the chapter, a brief description of the software tools that were used is given. Afterwards particle definitions, the complete set of selection criteria, as well as details of the analysed  $\beta\beta$  runs and special runs with sources of  $^{208}\text{Tl}$  and  $^{214}\text{Bi}$  follow. The next part of the chapter explains how to determine the real detection efficiency of the detector and gives the calculated estimations of the global efficiency of NEMO3 for the  $eeN\gamma$  channel during two different running periods. The last part gives results of the analysis of the experimental data from these two periods in the form of numbers of observed signal and background events. Finally, intervals at 95% confidence level for the half-life of the  $2\nu\beta\beta$  decay of  $^{100}\text{Mo}$  to the excited  $0_1^+$  state are determined and compared with previously published experimental results.

One of the main goals of the present Ph.D. thesis is the explanation of the study of the Monte-Carlo data which has been simulated for the  $2\nu\beta\beta$  decay of  $^{100}\text{Mo}$  to the excited  $0_1^+$  state and for all the possible backgrounds, for example the  $2\nu\beta\beta$  decay of  $^{100}\text{Mo}$  to the ground state, the internal and external backgrounds coming from  $^{208}\text{Tl}$  and  $^{214}\text{Bi}$ , and the background from radon that penetrated inside the detector. These simulations were essentially used to provide the definitions of the appropriate selection criteria for the  $eeN\gamma$  channel designed for the study of the  $2\nu\beta\beta$  decay to the excited  $0_1^+$  state. Another principal goal of this work is to describe the analysis applied on the available experimental data from May 2002 to May 2003 and to give the result obtained for the  $2\nu\beta\beta$  decay of  $^{100}\text{Mo}$  to the excited  $0_1^+$  state of  $^{100}\text{Ru}$ . The final aim of this document is to give a detailed description of the experimental apparatus, since this is the first Ph.D. thesis ever written in English on NEMO3 which will be available to all members of the multinational NEMO Collaboration.

# Chapter 1

## The physics of the neutrino

### 1.1 Introduction – history

The concept of **neutrinos** was derived from experiments held in the late 1920s and early 1930s that demonstrated continuous beta decay spectra, in contrast to alpha and gamma ray spectra. The “missing energy” in the beta decay spectrum could either be explained by the existence of a new particle, or, as Niels Bohr postulated, by the principle of conservation of energy being valid only statistically. The concept of a new particle was introduced by Wolfgang Pauli in December 1930: he assumed it to be a light, neutral, spin-1/2 particle, that he at first called the “neutron” [1]. The name of “neutrino”, meaning “little neutral one”, was given to this mysterious, and at that time only hypothetical, particle by Enrico Fermi in 1931.

In 1934, Fermi formally developed his theory of beta decay [2] in the framework of the quantum electrodynamics developed by Dirac, Heisenberg and Pauli. Although the remarkable success of the Fermi theory left few in doubt of the neutrino’s existence, none had ever been observed interacting. Neutrino detection seemed impossible since the predicted strength of the weak interaction would allow a neutrino to pass through 50 billion miles of water without interaction. However, in the early 1950’s Reines and Cowan [3] decided to search for evidence of inverse beta decay  $\bar{\nu}_e + p \rightarrow n + e^+$ . This reaction would yield a prompt light flash in the scintillator owing to the positron’s annihilation with electron, producing two 511 keV  $\gamma$ -rays, followed several microseconds later by another flash due to neutron capture. In June 1956, Reines and Cowan observed at the Savannah River reactor  $3.0 \pm 0.2$  events per hour, signal much greater than the backgrounds from cosmic rays or accidental coincidences [4].

At present three neutrino species are known to exist: the electron neutrino  $\nu_e$ , the  $\nu_\mu$  associated with the muon, and the  $\nu_\tau$  associated with the  $\tau$  lepton. The  $\nu_\mu$  was first observed by Schwartz and collaborators in Brookhaven in 1961 [5], whilst the evidence for the  $\nu_\tau$  came from the DONUT experiment in 2000 [6]. Altogether, there are now six leptons in nature: three charged ( $e^-$ ,  $\mu^-$ ,  $\tau^-$ ) and three neutral ( $\nu_e$ ,  $\nu_\mu$ ,  $\nu_\tau$ ), as well as the six corresponding antileptons.

Despite of all the progress of neutrino physics, a great number of questions remain. For a long time, it was considered that the neutrino has zero mass; in fact it was also one of the assumptions of the Standard Model (SM). Due to recent results from several neutrino oscillation experiments like SuperKamiokande [7], SNO [8, 9], and KamLAND [10], we now believe neutrinos are massive, but we still have no measurement of an absolute neutrino mass, and we do not know the particle-antiparticle conjugation properties of neutrinos: both the Dirac and the Majorana

possibilities are open. An associated possibility is the existence of non-zero electromagnetic moments [11, 12]. Finally, there are many questions about the role of neutrinos in astrophysics and cosmology.

## 1.2 Mass and nature of neutrinos

There are three main topics in neutrino physics today. The first one is the key question of the nature of the neutrino, i.e. whether it is a Majorana or Dirac type particle. In the first case a neutrino is its own antiparticle ( $\nu \equiv \bar{\nu}$ ), in the second case it is not ( $\nu \neq \bar{\nu}$ ). In the Dirac mass scenario, one can define a lepton number symmetry under which the theory is invariant. Such a question does not arise for other fermions because of the fact that they are electrically charged, unlike the neutrino. Naturally, mass is not the only property that can determine whether a neutrino is its own antiparticle. Interactions can also give the answer to this question, if they violate lepton number symmetry.

According to the results of several experiments we know that the mass of neutrino is rather small but we are not sure how large the masses of the three individual neutrino types are because of the difficulty in their detection. This is a crucial fact because neutrinos are by far the most numerous particle in the Universe (other than massless photons) and so even a tiny mass for the neutrinos can enable them to have an effect on the evolution of the Universe through their gravitational effects.

A second topic of great interest is neutrino mixing and the oscillations that occur during the time evolution of neutrinos. This is another way to distinguish between massive and massless neutrinos. In reality, the evidence for massive neutrinos at present comes only from oscillation experiments.

Finally, the third topic of interest and another distinguishing feature of massive neutrinos is that a member of one species could decay to another one.

### 1.2.1 Majorana or Dirac neutrinos?

Unlike other fermions, the neutrinos are only sensitive to weak interactions. In the Glashow-Salam-Weinberg (GSW) standard model [13, 14], the following two assumptions on the neutrinos are explicitly made:

1. their masses are identically zero,
2. only their left-handed components  $\psi_L = \frac{1}{2}(1 - \gamma_5)\psi$  are operative in physical processes.

The right-handed components of neutrinos  $\psi_R = \frac{1}{2}(1 + \gamma_5)\psi$ , even if they exist, do not interact with other particles and are thus absent from the Standard Model Lagrangian.

A neutral fermion may exist either as a Dirac particle (fermion  $\neq$  antifermion) or as a Majorana particle (fermion  $\equiv$  antifermion). For a Dirac fermion, the mass term has the following form:

$$-m\bar{\psi}\psi = -m(\bar{\psi}_R + \bar{\psi}_L)(\psi_R + \psi_L) = -m(\bar{\psi}_R\psi_L + \psi_R\bar{\psi}_L), \quad (1.1)$$

where terms  $\bar{\psi}_R\psi_R$  and  $\bar{\psi}_L\psi_L$  vanished. The mass term always connects the opposite chiral components of the same field. The absence of either,  $\psi_R$  or  $\psi_L$ , automatically leads to  $m = 0$ .

If neutrinos are of the Majorana type, even in the absence of right-handed components, a mass term can be built by using the antiparticle which is identical to its conjugate, only

with opposite chirality. Contrary to charged fermions, the neutrino and the antineutrino, being chargeless, can be self-conjugated  $\nu_M \equiv \nu_M^c$  and are hence called Majorana neutrinos  $\nu_M$ . The principal consequences of the Majorana nature of the neutrino are the following:

- there is no lepton number conservation for Majorana neutrinos,
- the neutrino's charge radius and magnetic moment are zero,
- the electric dipole moment of the neutrino vanishes,
- a Majorana neutrino can oscillate and/or contribute towards dark matter.

In general terms, a free neutrino described by a wave function  $\psi$  satisfies the following Dirac equation:

$$i\gamma^\lambda \partial_\lambda \psi - m\psi = 0. \quad (1.2)$$

This equation is issued from the free Lagrangian and is written as:

$$\mathcal{L} = i\bar{\psi}\gamma^\lambda \partial_\lambda \psi - m\bar{\psi}\psi. \quad (1.3)$$

A spin-half particle is said to be a Majorana particle if the spinor field  $\psi$  satisfies the condition of being self-charge-conjugate, i.e.

$$\psi = \psi^c \equiv C\bar{\psi}^T, \quad (1.4)$$

where  $C$  is the charge conjugation operator.

For the charged leptons, we have a mass term expressed in the following way:

$$\mathcal{L}_{m_\ell} = -\bar{\ell}_R \mathcal{M}_\ell \ell_L + \text{h.c.}, \quad (1.5)$$

where  $\ell_R$  is the right-handed counterpart of the spinor  $\ell_L$ , and  $\mathcal{M}_\ell$  is the charged-lepton mass matrix. For the neutrinos, there can be both Dirac and Majorana masses. Thus, the most general neutrino mass term is as follows:

$$\mathcal{L}_{M_\nu} = -\frac{1}{2}(\bar{\nu}_L^c, \bar{\nu}_R) \mathcal{M}_\nu \begin{pmatrix} \nu_L \\ \nu_R^c \end{pmatrix} + \text{h.c.}, \quad (1.6)$$

where  $\nu_R$  is the right-handed counterpart of the spinor  $\nu_L$ , and  $\mathcal{M}_\nu$  is the neutrino mass matrix. The matrix  $\mathcal{M}_\nu$  may be decomposed in the following way:

$$\mathcal{M}_\nu = \begin{pmatrix} M_L & M_D^T \\ M_D & M_R \end{pmatrix}, \quad (1.7)$$

where submatrices  $M_L$  and  $M_R$  contain left-handed and right-handed Majorana mass terms, while  $M_D$  contains Dirac mass terms.

### 1.2.2 Neutrino mixing and oscillations

In any case, whether neutrinos are Dirac or Majorana particles in nature, massless neutrinos of different families do not mix. If the neutrinos are massless, i.e. degenerate in mass, their lepton flavours can not be mixed. All states with degenerate masses are physically equivalent and are eigenstates of their common mass operator. This implies the absence of nondiagonal charged currents like  $\bar{\nu}_e \gamma_\lambda (1 - \gamma_5) \mu$ . There remain only three diagonal currents  $\bar{\nu}_e \gamma_\lambda (1 - \gamma_5) e$ ,

$\bar{\nu}_\mu \gamma_\lambda (1 - \gamma_5) \mu$ , and  $\bar{\nu}_\tau \gamma_\lambda (1 - \gamma_5) \tau$  that separately conserve their respective lepton numbers  $L_e$ ,  $L_\mu$ ,  $L_\tau$ . Consequently, all lepton flavour-changing interactions are forbidden.

In the Standard Model, e.g. [13, 14], neutrinos are assumed to be massless. If the neutrinos turn out to be massive, then like the three quark families, the three lepton families can mix, and the presumably small neutrino mass could be indirectly revealed by the neutrino oscillation experiments. The mixing of massive neutrinos may follow one of two different scenarios. The first, identical to that for quarks, involves Dirac neutrinos which acquire mass through the usual Higgs mechanism. The second involves Majorana neutrinos whose masses are only generated beyond the Standard Model.

Following the analogy with the quark mixing, the lepton mixing can be realised by a  $3 \times 3$  unitary matrix  $V_{\text{lep}}$ . Thus, we can express the weakly interacting neutrino eigenstates  $\nu_e$ ,  $\nu_\mu$ ,  $\nu_\tau$  as a linear combination of  $\nu_1$ ,  $\nu_2$ ,  $\nu_3$ , the neutrino mass eigenstates  $m_1$ ,  $m_2$ ,  $m_3$ :

$$\begin{pmatrix} \nu_e \\ \nu_\mu \\ \nu_\tau \end{pmatrix} = V_{\text{lep}} \begin{pmatrix} \nu_1 \\ \nu_2 \\ \nu_3 \end{pmatrix} = \begin{pmatrix} U_{e1} & U_{e2} & U_{e3} \\ U_{\mu1} & U_{\mu2} & U_{\mu3} \\ U_{\tau1} & U_{\tau2} & U_{\tau3} \end{pmatrix} \begin{pmatrix} \nu_1 \\ \nu_2 \\ \nu_3 \end{pmatrix}. \quad (1.8)$$

The idea of neutrino oscillations was put forward for the first time by Pontecorvo in 1957 [15], and the mixing was suggested by Maki, Nakagawa, and Sakata [16]. In honour of their work,  $V_{\text{lep}}$  is often called the ‘‘Pontecorvo–Maki–Nakagawa–Sakata matrix’’. In the Standard Model the parameters in the  $V_{\text{lep}}$  matrix are free and can only be determined by experiment. In the present state of our knowledge, the Standard Model does not predict either the masses of the fermions, or their mixings.

Marking the weak eigenstates by the symbols  $\alpha$ ,  $\beta$  (or simply by  $e, \mu, \tau$ ) and the mass eigenstates by  $i, j, k$ , the survival probability of a particular weak eigenstate  $\alpha$  is given by the following formula:

$$P_{\alpha\alpha} = 1 - 4 \sum_{i < j} |U_{\alpha i}|^2 |U_{\alpha j}|^2 \sin^2 \Delta_{ij}, \quad (1.9)$$

where  $\Delta_{ij} = (m_i^2 - m_j^2)L/4E$  with  $L$  being the distance travelled by the neutrino and  $E$  its energy. The transition probability from one weak eigenstate to another is given by:

$$P_{\alpha\beta} = 4 \sum_{i < j} U_{\alpha i} U_{\beta i}^* U_{\alpha j}^* U_{\beta j} \sin^2 \Delta_{ij}. \quad (1.10)$$

For two-neutrino oscillation, the probability of a given neutrino flavour  $\nu_\alpha$  oscillating into  $\nu_\beta$  after travelling a distance  $L$  through a vacuum is:

$$P_{\alpha\beta} = \sin^2 2\theta \sin^2 \left( 1.27 \frac{\Delta m^2 (\text{eV}^2) L (\text{km})}{E (\text{GeV})} \right), \quad (1.11)$$

where  $E$  is the neutrino energy in GeV,  $\theta$  is the mixing angle between the flavour and the mass eigenstates, and  $\Delta m^2$  is the mass squared difference of the two mass eigenstates in  $\text{eV}^2$ .

Until now, we have considered only the case of vacuum oscillations. However, neutrino oscillations can be enhanced by matter interactions. This phenomenon is called the **Mikheyev-Smirnov-Wolfenstein (MSW) effect** [17, 18]. In a medium the neutrino oscillation parameters are different from the vacuum parameters  $\theta$  (mixing angle) and  $l_\nu$  (oscillation length). First of all, the difference between the interactions of neutrinos with the medium implies that  $\nu_1 \leftrightarrow \nu_2$

transitions occur, that is, that the eigenstates in the matter  $\nu_1^m$  and  $\nu_2^m$  are different from the vacuum eigenstates  $\nu_1$  and  $\nu_2$ . Secondly, in the medium the refractive index is not equal to 1 and is different for  $\nu_1^m$  and  $\nu_2^m$  waves. This leads to both a change of the oscillation length and a change of the mixing angle  $\theta_m$ . As  $\theta_m$  is now defined in terms of  $\nu_1^m$  and  $\nu_2^m$ , it implies that  $\theta_m$  is different from the vacuum mixing angle  $\theta$ . Hence, the corresponding relations for a medium with constant density are the following:

$$\sin^2 2\theta_m = \frac{\sin^2 2\theta}{1 - 2(l_\nu/l_0) \cos 2\theta + (l_\nu^2/l_0^2)}, \quad (1.12)$$

$$l_m = \frac{l_\nu}{\sqrt{1 - 2(l_\nu/l_0) \cos 2\theta + (l_\nu^2/l_0^2)}}. \quad (1.13)$$

The vacuum oscillation length  $l_\nu$  is given by:

$$l_\nu = 4\pi E/\Delta m^2$$

and

$$l_0 = 2\pi \left( \frac{\Delta f_0}{k} \rho \frac{Y_e}{m_N} \right)^{-1}$$

is a quantity characteristic of the medium, which can be considered as the proper oscillation length in matter where,  $\rho$  is the matter density,  $m_N$  is the nucleon mass,  $Y_e$  is the number of electrons per nucleon, and  $\Delta f(0) = f_\alpha(0) - f_\beta(0)$  is the difference of the amplitudes for the forward scattering of  $\nu_\alpha$  and  $\nu_\beta$  on the electrons and nucleons of the medium [18].

According to the model developed by Wolfenstein (see, for example, Ref. [17]) and Mikheyev with Smirnov (see Ref. [18]), two different manifestations of the resonant enhancement of the oscillations can be distinguished. The first occurs when a beam of neutrinos with a continuous energy spectrum passes through a medium of constant density. In this case the enhancement of the neutrino oscillations will occur in the portion of spectrum near  $E_{\text{res}}$  given by:

$$E_{\text{res}} = a \frac{\Delta m^2 \cos 2\theta}{\rho}, \quad (1.14)$$

where  $a = (m_N/Y_e)(k/2\Delta f(0))$ . The second occurs when a monoenergetic beam of neutrinos passes through a medium of varying density. Then a significant enhancement of the oscillations occurs in the layer with density given by:

$$\rho \sim \rho_{\text{res}} = a \frac{\Delta m^2 \cos 2\theta}{E}. \quad (1.15)$$

### 1.3 Measurements of neutrino masses

Experimental techniques that probe the question of neutrino mass are classified into two categories: direct and indirect techniques [19]. The direct measurements are accomplished either through precise observations of decay kinematics in nuclear or particle decay processes, or by the utilisation of time-of-flight measurements in the detection of supernova neutrinos incident on terrestrial neutrino detectors. Typical examples of decay measurements are studies of  $\beta$ -decay spectra, measurements of muon momentum in pion decay, and invariant mass studies of multiparticle semi-leptonic decays of the  $\tau$  lepton. Limits on neutrino masses have also been

derived from observations of neutrinos from Supernova 1987A. A strength of direct techniques is that they make few theoretical assumptions about neutrino properties, since the measurements are based on purely kinematic observables. On the contrary, indirect methods, such as measurements of neutrinoless double beta decay and searches for neutrino oscillations, require both violation of lepton number conservation and non-zero neutrino mass.

### 1.3.1 Direct techniques for neutrino mass measurements

The measurements of the shape of the  $\beta$ -decay energy spectrum can provide a sensitive test of the mass of  $\bar{\nu}_e$ . In 1948 Curran, Angus and Cockroft [20] made the first such measurement and set a limit  $\overline{M}_{\nu_e} < 1$  keV [21]. They used a weighted average mass that is defined as:

$$\overline{M}_{\nu_\alpha} = \sqrt{\sum_{i=1}^k |U_{\alpha i}|^2 m_{\nu_i}^2}, \quad (1.16)$$

where  $\alpha = (e, \mu, \tau)$ ,  $U_{\alpha i}$  are the amplitudes in the lepton mixing matrix, and the sum over  $k$  includes all mass eigenstates that are kinematically allowed for a particular measurement.

During the following decades this limit was reduced by enhancing the sensitivity of **tritium beta decay experiments** and this limit was pushed down to the level of a few eV. A summary of recent measurements is given in Tab. 1.1. At the present time, there is an international project to begin a new generation of  $\beta$ -spectrometers called KATRIN<sup>1</sup> which is expected to determine the electron neutrino mass (or to set its upper limit) down to the level of  $\sim 0.3$  eV [22].

Experiment	$\overline{M}_{\nu_e}^2$ (eV <sup>2</sup> )	Mass limit (95% C.L.)	Year	Ref.
Mainz University	-1.6 $\pm$ 2.5 $\pm$ 2.1	< 2.2	2000	[23]
INR Troitsk	-1.9 $\pm$ 3.4 $\pm$ 2.3	< 2.5	1999	[24]
Zürich	-24 $\pm$ 48 $\pm$ 6	< 11.7	1992	[25]
Los Alamos	-147 $\pm$ 68 $\pm$ 41	< 9.3	1991	[26]
INS Tokyo	-65 $\pm$ 85 $\pm$ 65	< 13.1	1991	[27]
ITEP Moscow	+676 $\pm$ 235	26 <sup>+6</sup> <sub>-5</sub>	1987	[28]

Table 1.1: Limits on  $\overline{M}_{\nu_e}$  from recent tritium beta decay experiments.

The technique for measuring neutrino mass by means of  $\beta$ -decay is based on a distortion in shape of the beta spectrum in the endpoint energy region. The spectrum can be described using the Fermi form for the probability of emitting an electron with total energy  $E$  in  $\beta$ -decay:

$$dN(E) = K|M|^2 \mathcal{F}(Z, R, E) p_e E (E_0 - E) \sqrt{(E_0 - E)^2 - \overline{M}_{\nu_e}^2} c^4 dE, \quad (1.17)$$

where

$$K = G_F^2 \frac{m^5 c^4}{2\pi^3 \hbar^7} \cos^2 \theta_c, \quad (1.18)$$

$G_F$  is the weak coupling constant,  $M$  is the nuclear matrix element for the transition,  $p_e$  is the electron momentum,  $E_0$  is the endpoint energy (i.e. the maximum electron energy for zero

<sup>1</sup>KATRIN = KARlsruhe TRItium Neutrino experiment

neutrino mass),  $m$  is the mass of the electron, and  $\overline{M}_{\nu_e}$  is the mass of  $\bar{\nu}_e$ . The Fermi function,  $\mathcal{F}(Z, R, E)$ , is a Coulomb correction term that results from the influence of the nuclear charge on the wave function of the emitted electron. The spectrum can be linearised by plotting the Kurie amplitude:

$$K(E) = \sqrt{\frac{dN(E)/dE}{p_e E \mathcal{F}(Z, R, E)}} \sim \left( (E_0 - E) \sqrt{(E_0 - E)^2 - \overline{M}_{\nu_e}^2} \right)^{1/2}. \quad (1.19)$$

The plot of this function is called the Kurie plot and is a very useful quantity for seeing the effect of the neutrino mass as it is illustrated in Fig. 1.1. For  $m_\nu = 0$ , the Kurie plot becomes a straight line  $\sim E_0 - E$ , intercepting the energy axis at  $E = E_0$ . On the contrary, if  $m_\nu \neq 0$ , the spectrum shape near the endpoint  $E = E_0$  will be modified as shown in Fig. 1.1.

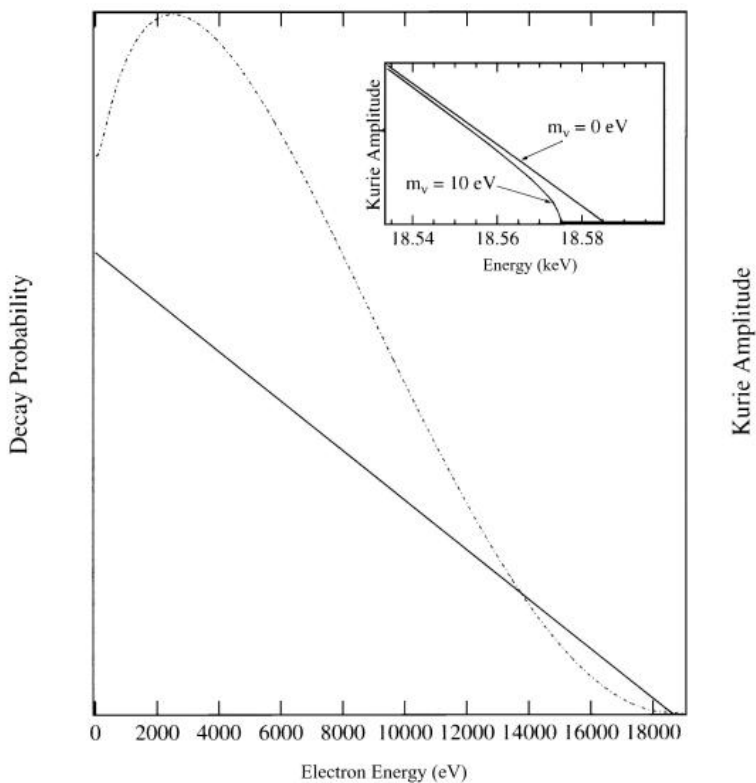


Figure 1.1: An example of a tritium beta decay spectrum (dot and dash line) and of a Kurie plot (solid line). The inset shows the shape of the Kurie amplitude in the region of interest (around the spectrum endpoint) assuming  $m_\nu = 0$  eV and  $m_\nu = 10$  eV.

The difficulty of this experimental method is that there are very few decays in the region of interest. That means that backgrounds must be carefully eliminated or minimised. The other problem is related to the shape distortion caused by effects such as instrumental resolution. Thus, precise determination of a value or limit for  $\overline{M}_{\nu_e}$  requires complete and accurate understanding of all systematic effects that can alter the shape of the spectrum.

The direct limits on the  $\nu_\mu$  and  $\nu_\tau$  masses are based on kinematic **particle decay measurements**. The muon neutrino mass measurements use the pion decay  $\pi^+ \rightarrow \mu^+ + \nu_\mu$ . Such an experiment was realised for the first time by Barkas and collaborators in 1956 [29]. The simple two-body decay is still the most sensitive method of setting limits on  $\overline{M}_{\nu_\mu}$  from the following kinematic formula:

$$\overline{M}_{\nu_\mu}^{-2} = m_\pi^2 + m_\mu^2 - 2m_\pi \sqrt{p_\mu^2 + m_\mu^2}. \quad (1.20)$$

Limits on the  $\nu_\tau$  mass have been derived by looking at rare multi-particle semi-leptonic decays of the  $\tau$  lepton, with only one neutrino in the final state and where the effective mass of the detected particles is close to  $m_\tau$ . The experiments ALEPH, ARGUS, CLEO, DELPHI, and OPAL have all examined a variety of decay modes. The current limits on neutrino masses derived from direct mass measurements are summarised in Tab. 1.2.

$\nu$ type	Mass limit	Experiment	Ref.
$\overline{M}_{\nu_e}$	< 2.2 eV (95% C.L.)	Mainz 2000	[23]
$\overline{M}_{\nu_\mu}$	< 170 keV (90% C.L.)	PSI 1996	[30]
$\overline{M}_{\nu_\tau}$	< 18.2 MeV (95% C.L.)	ALEPH 1998	[31]

Table 1.2: Current limits on neutrino masses from direct experiments.

### 1.3.2 Review of indirect techniques for neutrino mass measurements

The typical process that provides experimental evidence for the Majorana nature of  $\nu_e$  is **neutrinoless double beta decay**:  $(A, Z) \rightarrow (A, Z + 2) + 2e^-$ . The process itself, as well as a review of double beta decay experiments are both treated in details in Chapter 2. However, these experiments cannot determine the absolute neutrino mass, only the effective mass of  $\nu_e$ :

$$\langle m_\nu \rangle_e = \left| \sum_i U_{ei}^2 m_i \right|, \quad (1.21)$$

where the sum over  $i$  covers the mass eigenstates. In the general, for a particular weak eigenstate  $\alpha$  ( $\alpha = e, \mu, \tau$ ), the effective mass is given by:

$$\langle m_\nu \rangle_\alpha = \left| \sum_i U_{\alpha i}^2 m_i \right|. \quad (1.22)$$

**Neutrino oscillation measurements** offer the most sensitive method of probing neutrino mass, but they measure only the square of the mass difference  $\Delta m_{ij}^2 = m_i^2 - m_j^2$ . Thus, although they are able to tell us that neutrinos have mass, they can say nothing about the actual mass eigenvalues  $m_1, m_2, m_3$ .

There is now clear evidence from three experiments and strong indications from other experiments of neutrino oscillations. The evidence comes from the atmospheric neutrino data in the SuperKamiokande experiment [7], from the SNO (Sudbury Neutrino Observatory) solar neutrino data [8, 9], and recently also from the KamLAND reactor neutrino data [10]. Indications of atmospheric neutrino oscillations were also revealed by the Kamiokande, IMB, Soudan II, and MACRO experiments. The two main conclusions from the existing data are:

1. the data cannot be fitted assuming  $\nu_e \leftrightarrow \nu_\mu$  oscillation;

2. two possible cases that fit the data are  $\nu_\mu \leftrightarrow \nu_\tau$  and  $\nu_\mu \leftrightarrow \nu_s$  (where  $\nu_s$  is a “sterile neutrino”) oscillations.

### Atmospheric neutrinos

The atmospheric neutrinos are produced in decays of pions, muons and other mesons resulting from collisions of cosmic rays with nuclei in the Earth’s upper atmosphere. Production of  $\nu_e$ ’s and  $\nu_\mu$ ’s is dominated by the process  $\pi^+ \rightarrow \mu^+ + \nu_\mu$  followed by  $\mu^+ \rightarrow e^+ + \bar{\nu}_\mu + \nu_e$  (and their charge conjugates) giving an expected ratio of the flux of  $\nu_\mu + \bar{\nu}_\mu$  to the flux  $\nu_e + \bar{\nu}_e$  of about 2. The  $\nu_e/\nu_\mu$  flux ratio is measured by observing final state leptons produced via charged-current interactions of neutrinos on nuclei. The flavour of the final state lepton is used to identify the flavour of the incoming neutrino. The measurements use the double ratio of observed to expected neutrino fluxes  $R$  defined in the following way:

$$R \equiv \frac{(N_{(\nu_\mu + \bar{\nu}_\mu)}/N_{(\nu_e + \bar{\nu}_e)})_{\text{data}}}{(N_{(\nu_\mu + \bar{\nu}_\mu)}/N_{(\nu_e + \bar{\nu}_e)})_{\text{M.C.}}} . \quad (1.23)$$

The deficit of  $\nu_\mu$ ’s was first observed in 1983 in the IMB experiment [32], using a large underground water Čerenkov detector. This was soon confirmed by the second large water Čerenkov detector, the Kamioka experiment [33]. However, two European experiments, the NUSEX and Fréjus [34] detectors, did not observe any anomaly. Later the  $\nu_\mu$  deficit was confirmed in the Soudan II and the MACRO experiments and the evidence for oscillation was given by the SuperKamiokande experiment in 1998 [7]. The data of the later experiment exhibited a deficit of muon neutrinos dependent on zenith angle which was inconsistent with expectations based on calculations of the atmospheric neutrino flux. Their data are consistent with  $\nu_\mu \leftrightarrow \nu_\tau$  oscillations with  $\sin^2 2\theta > 0.82$  and  $5 \times 10^{-4} < \Delta m^2 < 6 \times 10^{-3} \text{ eV}^2$  at 90% confidence level [16].

### Solar neutrinos

Other evidence for neutrino oscillations comes from the solar neutrino experiments that have observed a deficit in the flux of  $\nu_e$ ’s compared with the predictions of the Standard Solar Model (SSM). The first solar neutrino experiment was realised by R. Davis Jr. and his Brookhaven collaborators in the Homestake Gold Mine (South Dakota) in 1968 [35]. Solar neutrinos were captured by the reaction  $^{37}\text{Cl}(\nu, e^-)^{37}\text{Ar}$ . Similar radiochemical experiments, started in the early 1990s, were SAGE and GALLEX using  $^{71}\text{Ga}$ . Other solar neutrino experiments are based on different detection techniques. While Kamiokande II/III, SuperKamiokande, and SNO<sup>2</sup> exploit water Čerenkov detectors to view solar neutrinos event by event, Borexino [36, 37] is a detector consisting of 300 tons of liquid scintillator, and the HELLAZ experiment is based on a gaseous helium TPC detector.

The experiment of R. Davis found evidence for only one third of the expected number of neutrino events. One half of the expected events for the part of solar neutrino spectrum for which light water Čerenkov detectors are sensitive was observed at Kamiokande in 1986. The gallium detectors SAGE [38] and GALLEX [39], which have lower energy thresholds, found about 60–70% of the expected rate. The Sudbury Neutrino Observatory (SNO) is able, through the elastic scattering, charge and neutral current reactions, to determine the electron and non-electron (i.e.  $\mu$  plus  $\tau$ ) active neutrino components of the  $^8\text{B}$  solar neutrino flux with  $E_\nu > 5 \text{ MeV}$ . It was reported in 2002 [8, 9] that the measured total neutrino flux is consistent with solar

---

<sup>2</sup>The SNO experiment uses very pure (99.92%) heavy water, surrounded by a shield of ordinary water.

models. Furthermore, the observed  $\nu_e$  and the non- $\nu_e$  fluxes provide a strong evidence for solar  $\nu_e$  transformation.

The observed electron neutrino deficit appears to depend on the energy of the neutrino. The Sun produces neutrinos with a range of energies (see Fig. 1.2), and the different detectors are sensitive to different energy ranges. One could argue that all the experiments are simply wrong, but this is highly unlikely, especially after the announcement of the SNO results. The different experiments use diverse detection techniques, overseen by large collaborations, and have been calibrated with a variety of sources. At present, it is believed that no SSM change can completely remove the discrepancy with experiment. The suggested solutions of the solar neutrino problem favour neutrino oscillations enhanced by matter interactions called the Mikheyev-Smirnov-Wolfenstein (MSW) effect (see Sec. 1.2.2, p. 6). The MSW mechanism, providing a natural explanation for the pattern of observed solar neutrino fluxes, requires profound new neutrino physics including both massive neutrinos and neutrino mixing.

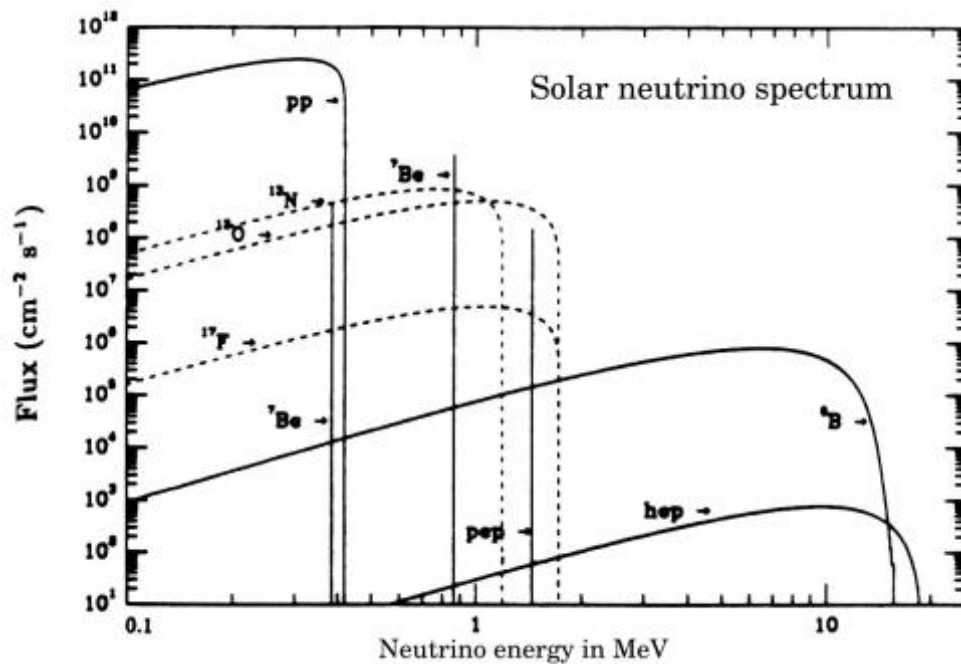


Figure 1.2: Spectrum of solar neutrinos according to the Standard Solar Model (SSM).

### Neutrinos at nuclear reactors

As was the case for the first neutrino experiments, reactor (anti-)neutrinos are used also in neutrino oscillation experiments. Most reactor neutrino detectors are based on the interaction with the proton  $\bar{\nu}_e + p \rightarrow e^+ + n$ , with a threshold of 1.8 MeV. This inverse neutron decay has the largest cross-section among neutrino-nuclear reactions. The simultaneous detection of  $e^+$  (two gamma rays from its annihilation) and the neutron (gamma ray from the neutron capture) is a clear signature of the reaction and provides a powerful way to separate the signal from backgrounds. In these experiments one searches for the “disappearance” of  $\bar{\nu}_e$ 's (i.e. the reduction of the  $\bar{\nu}_e$  flux) according to the Eq. 1.11.

The first such reactor neutrino experiment searching for neutrino oscillations was realised in 1977 at the research reactor of the Institute Laue-Langevin (ILL) [40]. At that time there was no evidence for neutrino oscillations. Then a certain number of reactor neutrino experiments followed. We can cite for example Gosgen, Bugey [41], Rovno, Krasnoyarsk, Palo Verde [42], CHOOZ [43, 44] and KamLAND<sup>3</sup> [45]. The results of these experiments, can be shown as excluded regions in a  $\Delta m^2$  versus  $\sin^2 2\theta$  plot, and are summarised in Fig. 1.3. Except KamLAND [10], none of these experiments have shown any evidence for the neutrino disappearance mode  $\bar{\nu}_e \rightarrow \bar{\nu}_x$ . Particularly from the results of the Palo Verde and CHOOZ experiments, it can be concluded that the  $\nu_\mu$  deficiency in the atmospheric neutrino oscillation experiments cannot be attributed to  $\bar{\nu}_e \leftrightarrow \bar{\nu}_\mu$  oscillations.

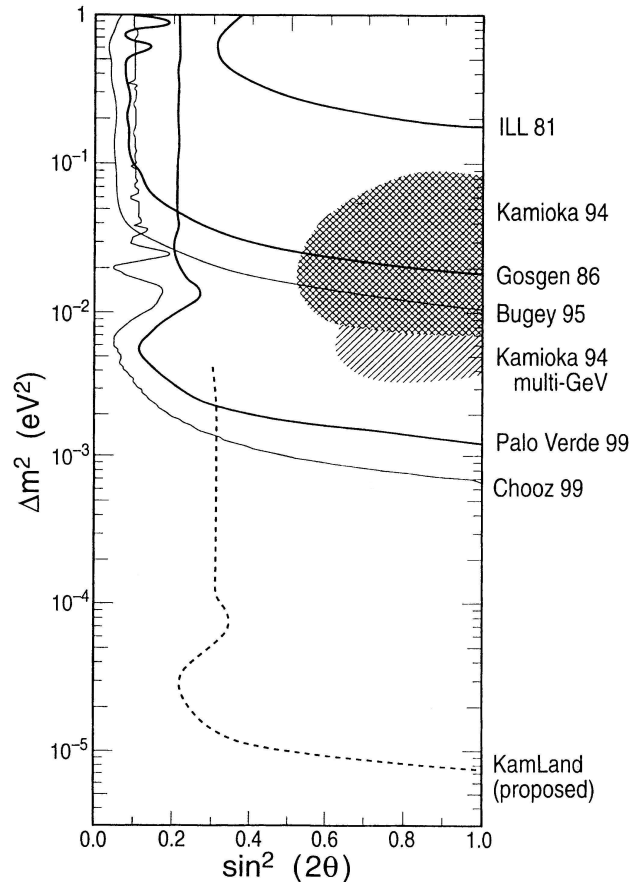


Figure 1.3: An overview of the reactor neutrino oscillation experiments showing the excluded regions at 90% C.L. in the  $\Delta m^2$  versus  $\sin^2 2\theta$  plot.

### Neutrinos at particle accelerators

Another source of terrestrial neutrinos (and antineutrinos) exploited in oscillation experiments are particle accelerators. The high intensity neutrino beams at accelerators are produced by protons on fixed targets, generating pions and kaons which dominantly give neutrinos of the

<sup>3</sup>KamLAND stands for Kamioka Liquid scintillator Anti-Neutrino Detector.

$\mu$  flavour.  $\nu_\mu$  or  $\bar{\nu}_\mu$  beams are used primarily for appearance experiments. The detection mechanism is via charged-current weak interactions,  $\nu_\alpha + N \rightarrow \alpha + X$ , where  $\alpha = e, \mu, \tau$ .

Experiments worthy of mention are CERN's NOMAD and CHORUS, LSND and KARMEN<sup>4</sup>. Both CHORUS and NOMAD searched for appearance of  $\nu_\tau$  by identifying the  $\tau$  lepton decay. The LSND [46] and KARMEN [47, 49] experiments searched for the  $\bar{\nu}_\mu \leftrightarrow \bar{\nu}_e$  oscillations which would be detected via the reaction  $\bar{\nu}_e + p \rightarrow e^+ + n$ . The only evidence for neutrino oscillations from accelerators comes from the LSND experiment, for which the  $\Delta m^2$  of  $\nu_\mu \rightarrow \nu_e$  oscillation is in the range from about 0.2 to about 10 eV<sup>2</sup> [48]. As regards the future neutrino beam experiments, the MiniBooNE experiment is expected to either confirm or refute the LSND result. The long-baseline experiments are expected to confirm the  $\nu_\mu \rightarrow \nu_e$  disappearance oscillations at the  $\Delta m_{\text{atm}}^2$  scale. The recently proposed long-baseline neutrino oscillation projects are K2K (KEK to SuperKamiokande,  $L \simeq 250$  km) [50], MINOS (Fermilab to Soudan,  $L \simeq 730$  km) [51, 52], and OPERA (CERN to Gran Sasso,  $L \simeq 730$  km) [53].

---

<sup>4</sup>NOMAD stands for Neutrino Oscillation MAgnetic Detector, CHORUS means Cern Hybrid Oscillation Research apparatus, LSND is an abbreviation for Liquid Scintillator Neutrino Detector, and KARMEN stands for Karlsruhe-Rutherford Medium Energy Neutrino.

## Chapter 2

# Double beta decay – theory and experiments

### 2.1 Introduction

The most promising test of the Majorana versus Dirac nature of the neutrino is neutrinoless double beta decay. Such a process is expected to occur if there are Majorana neutrinos which couple to the electron. Then, these neutrinos can be exchanged in the intermediate state. In the case of Dirac neutrinos the process cannot take place because it would violate lepton number conservation and imply the existence of right-handed currents as well.

Double beta decay [54, 55, 56] is a rare spontaneous transition between two nuclei with the same mass number  $A$  in which the charge  $Z$  changes by two units. Such a decay takes place when the normal first-order beta decay is energetically forbidden (or strongly suppressed by a high spin difference as for  $^{48}\text{Ca}$ ), but a double beta decay is energetically allowed, as it is schematically illustrated in Fig. 2.1. If the proton and neutron number,  $Z$  and  $N$ , of the parent nucleus are both even, the daughter nucleus in normal beta decay would be an odd-odd nucleus. Such nuclei are not usually strongly bound and are highly unstable. The “grand-daughter” nucleus ( $Z + 2, N - 2$ ) is again an even-even nucleus and therefore strongly bound. In many cases it is more strongly bound than the parent nucleus.

This type of nuclear transition can proceed in two ways, either as a double beta decay with emission of two  $\bar{\nu}_e$ 's, or as a neutrinoless double beta decay (i.e. without emission of neutrinos).

The first mode, originally discussed by Maria Goeppert-Mayer in 1935 [57], is **double beta decay with emission of two electron antineutrinos** ( $2\nu\beta\beta$ ) [58]:

$$(A, Z) \rightarrow (A, Z + 2) + e_1^- + e_2^- + \bar{\nu}_{e1} + \bar{\nu}_{e2} .$$

This decay mode, illustrated in Fig. 2.2, conserves the lepton number and is therefore allowed by the Standard Model of electro-weak interactions. Because of the five-body final state, the two electron energy-sum spectrum,  $E_{ee} = E_{e1} + E_{e2}$ , is continuous.

The two-neutrino double beta decay,  $2\nu\beta\beta$ , can be understood as a normal effect of second-order perturbation theory, where the accessible  $1^+$  states of the daughter ( $Z + 1, N - 1$ ) nucleus serve as intermediate states:

$$\begin{array}{ccc} 0_{(Z,N)}^+ & \longrightarrow & 1_{(Z+1,N-1)}^+ + e^- + \bar{\nu}_e \\ & & \downarrow \\ & & 0_{(Z+2,N-2)}^+ + e^- + \bar{\nu}_e \end{array}$$

15

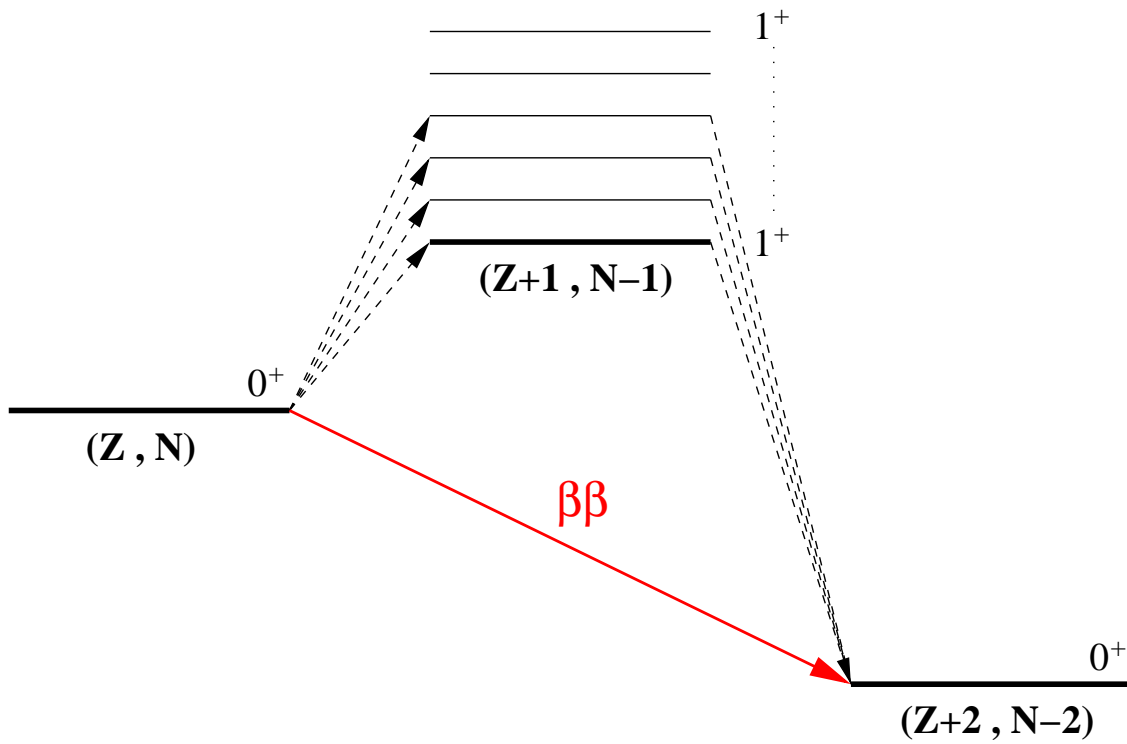


Figure 2.1: A scheme of double beta decay with intermediate virtual  $1^+$  states.

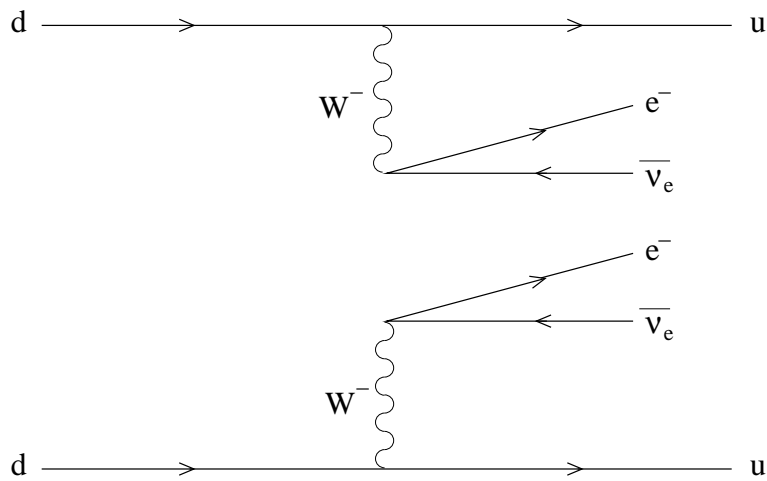


Figure 2.2: The Feynman diagram of the two-neutrino double beta decay.

In such decay each step corresponds to an allowed Gamow–Teller transition. The calculation is complicated by the necessity of summing over all  $1^+$  states of the daughter  $(Z + 1, N - 1)$  nucleus, most of which are not known experimentally.

The second possible transition, the **neutrinoless double beta decay** ( $0\nu\beta\beta$ ) [59]:

$$(A, Z) \rightarrow (A, Z + 2) + e_1^- + e_2^-$$

violates lepton number conservation and is therefore forbidden in the Standard Model. This process was suggested by W.H. Furry in 1939 [60] after the development of Majorana’s theory [62]. The  $0\nu\beta\beta$  process is kinematically more favoured because there are only three final states instead of five in  $2\nu\beta\beta$  decay. In this case, the  $E_{ee}$  spectrum is a sharp peak with a width given by detector resolution and, for experiments using  $\beta\beta$  decay sources in the form of foils, also by energy losses of electrons inside source foils (thus the peak’s width is also a function of foil thickness). Neutrinoless processes are possible only when the lepton number is violated by two units and  $\bar{\nu}_e$  can turn into  $\nu_e$ . The helicity flip necessary for this  $\bar{\nu}_e \rightarrow \nu_e$  conversion can be achieved by the massiveness of the Majorana neutrino or by the presence of right-handed charged lepton currents. The Feynman diagrams for the  $0\nu\beta\beta$  decay with respectively the  $V - A$  and  $V + A$  couplings are showed in Figs. 2.3 and 2.4.

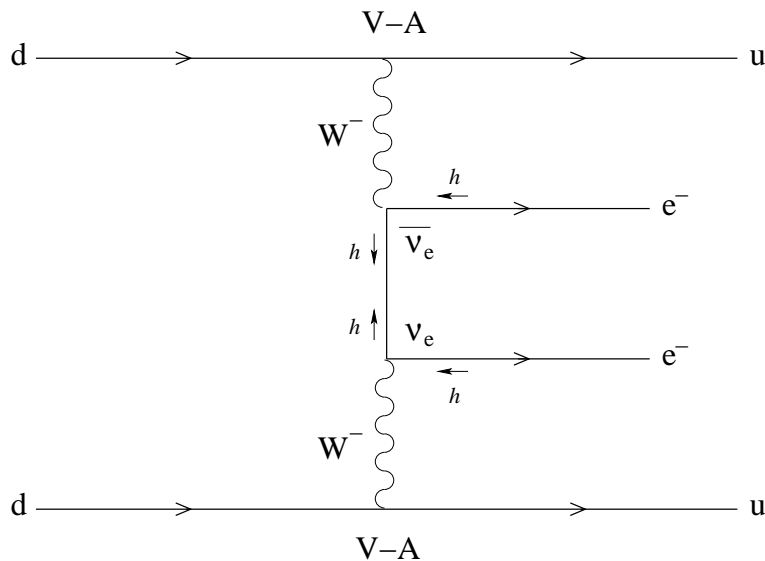


Figure 2.3: The Feynman diagram of neutrinoless double beta decay involving only the left-handed currents ( $V - A$  couplings). In this case, the helicity flip occurs.

Another possible mode of neutrinoless decay is **double beta decay with majoron emission** ( $0\nu\chi\beta\beta$ ) [61]:

$$(A, Z) \rightarrow (A, Z + 2) + e_1^- + e_2^- + \chi .$$

This decay mode, illustrated in Fig. 2.5, belongs to the category of lepton-number-violating decays, even though the lepton number is formally conserved when  $\chi$  is assigned the lepton number  $-2$ . The hypothetical scalar particle  $\chi$ , which must be light enough to be emitted in the  $\beta\beta$  decay, is usually associated with spontaneous breaking of the  $B - L$  symmetry.

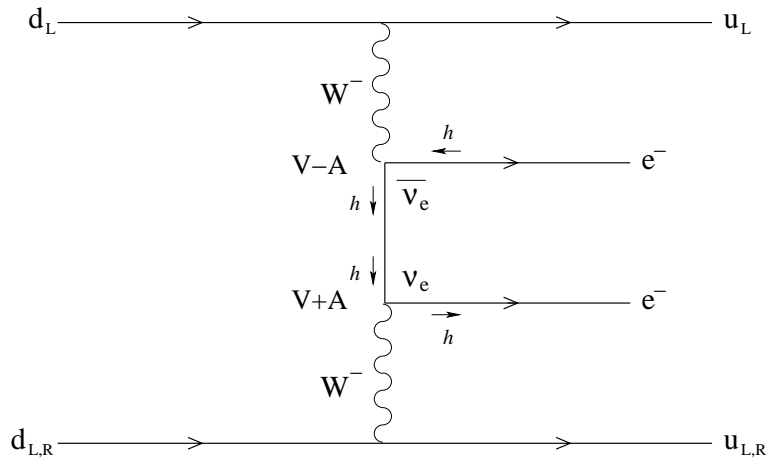


Figure 2.4: The Feynman diagram of neutrinoless double beta decay involving the right-handed current ( $V + A$  coupling) in addition to the left-handed one ( $V - A$  coupling).

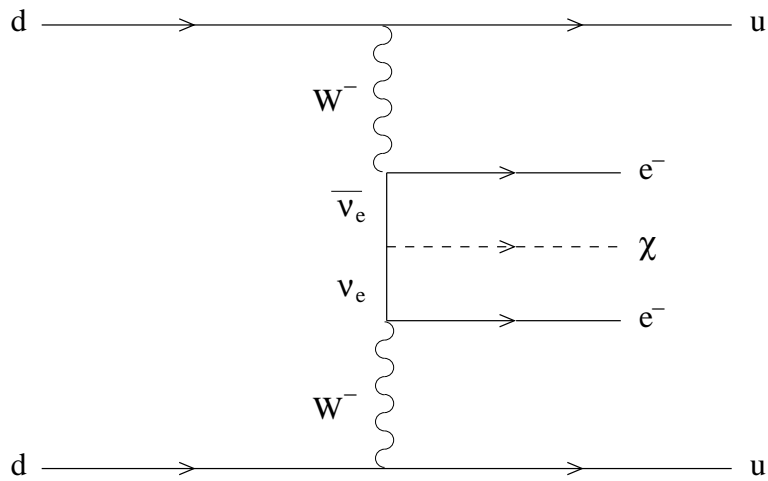


Figure 2.5: The Feynman diagram of neutrinoless double beta decay with majoron emission.

In the previous paragraphs, only the  $\beta^-\beta^-$  processes were mentioned. Nevertheless, there also exist other possible modes of double beta decay [63]:

1. two-neutrino double positron decay ( $2\nu\beta^+\beta^+$ ):

$$(A, Z) \rightarrow (A, Z - 2) + e_1^+ + e_2^+ + \nu_{e_1} + \nu_{e_2} ,$$

2. neutrinoless double positron decay ( $0\nu\beta^+\beta^+$ ):

$$(A, Z) \rightarrow (A, Z - 2) + e_1^+ + e_2^+ ,$$

3. positron-emitting two-neutrino electron capture ( $2\nu\beta^+/EC$ ):

$$(A, Z) + e^- \rightarrow (A, Z - 2) + e^+ + \nu_{e_1} + \nu_{e_2} ,$$

4. positron-emitting neutrinoless electron capture ( $0\nu\beta^+/EC$ ):

$$(A, Z) + e^- \rightarrow (A, Z - 2) + e^+ ,$$

5. two-neutrino double electron capture ( $2\nu EC/EC$ ):

$$(A, Z) + e_1^- + e_2^- \rightarrow (A, Z - 2) + \nu_{e_1} + \nu_{e_2} .$$

If  $\beta^+\beta^+$  decay takes place, it should always be accompanied by  $\beta^+/EC$  and  $EC/EC$  decays. In reality, the capture processes are more favourable than the  $\beta^+\beta^+$  decay because their available energy is larger and the suppression by the nuclear Coulomb repulsion on the positron is avoided. The most interesting nuclei are therefore  $^{78}\text{Kr}$ ,  $^{96}\text{Ru}$ ,  $^{106}\text{Cd}$ , and  $^{124}\text{Xe}$  because of the large values of available kinetic energy.

There are some thirty five naturally occurring isotopes, listed with their  $Q_{\beta\beta}$  values and natural abundances in Tab. 2.1, that disintegrate by the  $\beta^-\beta^-$  process and only six other isotopes, listed in Tab. 2.2, decaying by the  $\beta^+\beta^+$  process.

## 2.2 Double beta decay mechanisms

If we measure the energy of the two emitted electrons, we can easily distinguish between the three modes of  $\beta\beta$  decay. The electron sum-energy spectra are determined by the phase space of the outgoing leptons and they characterise the decay mode as illustrated in Fig. 2.6. The two-electron energy sum of the  $0\nu\beta\beta$  decay is theoretically equal to the  $Q$ -value of the reaction,  $E_0$ . In reality, one obtains a narrow peak around the  $E_0$  value because of the non zero resolution of a real detector. For the two other modes, the electron sum-energy spectra are continuous because a fraction of the available kinetic energy of the decay is carried away by the two  $\bar{\nu}_e$  for  $2\nu\beta\beta$  or by the Majoron for  $0\nu\chi\beta\beta$ .

Allowing the existence of right-handed currents and the Majorana mass for neutrinos, the most general effective weak-interaction Hamiltonian density is given by the following formula [65]:

$$h_W = \left( G_F \cos \theta_c / \sqrt{2} \right) \left( j_{L\mu} J_L^{\mu\dagger} + \kappa j_{L\mu} J_R^{\mu\dagger} + \eta j_{R\mu} J_L^{\mu\dagger} + \lambda j_{R\mu} J_R^{\mu\dagger} \right) + \text{h.c.} , \quad (2.1)$$

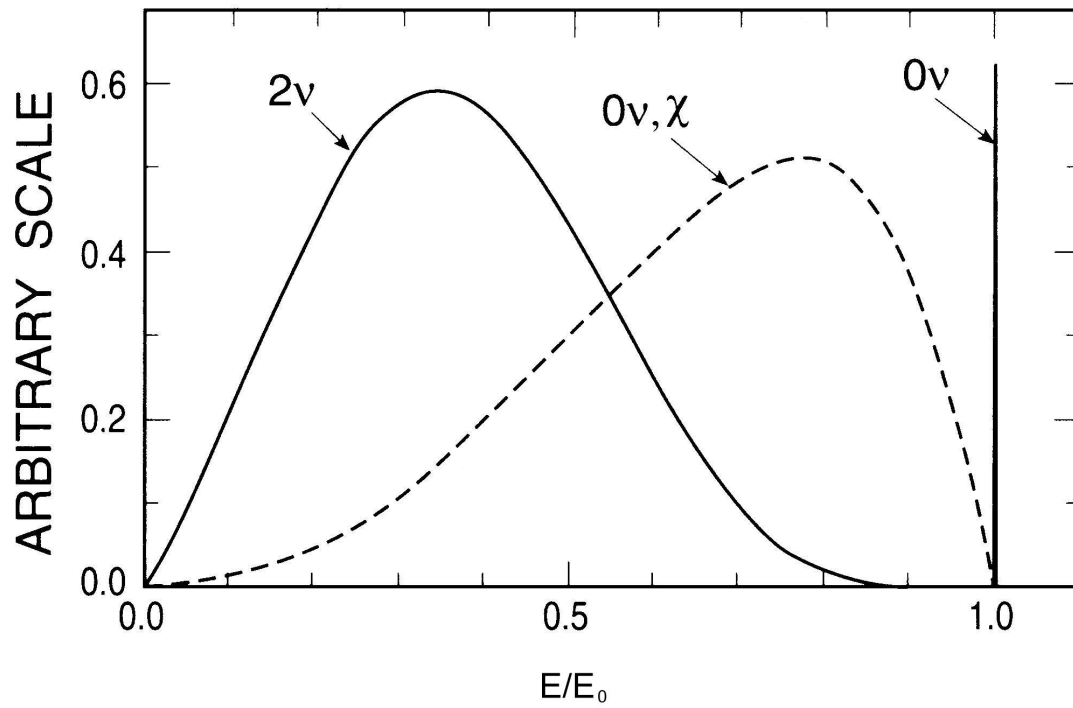


Figure 2.6: Schematic electron sum-energy spectra of the three double beta decay modes. Each distribution is arbitrarily normalised. The ratio  $E/E_0$ , i.e. two electron energy sum  $E$  divided by the maximum kinetic energy of the decay  $E_0$ , is represented on the abscissa.

where  $G_F$  is the Fermi coupling constant ( $G_F = 1.16637 \times 10^{-5} \text{ GeV}^{-2}$ ) and  $\theta_c$  is the mixing angle of the Cabibbo–Kobayashi–Maskawa mechanism for quark flavour mixing. The left- and right-handed leptonic currents have in the  $\beta^-\beta^-$  decay case the following familiar form:

$$\begin{aligned} j_{L\mu} &= \bar{e}\gamma_\mu(1 - \gamma_5)\nu_{e,L} \\ j_{R\mu} &= \bar{e}\gamma_\mu(1 + \gamma_5)\nu_{e,R} . \end{aligned} \quad (2.2)$$

The hadronic currents are given in terms of the u and d quarks as follows:

$$\begin{aligned} J_L^{\mu\dagger} &= \bar{u}\gamma^\mu(1 - \gamma_5)d \\ J_R^{\mu\dagger} &= \bar{u}\gamma^\mu(1 + \gamma_5)d . \end{aligned} \quad (2.3)$$

Finally,  $\kappa$ ,  $\eta$ , and  $\lambda$  are the current-current coupling coefficients.

### 2.2.1 Two-neutrino double beta decay

The **ground-state-to-ground-state transition** rate for  $2\nu\beta\beta$  decay is given by the half-life  $T_{1/2}^{2\nu}$  [65] as follows:

$$\left(T_{1/2}^{2\nu}\right)^{-1} = G^{2\nu}|M_{\text{GT}}^{2\nu}|^2 , \quad (2.4)$$

where  $G^{2\nu}$  is the phase-space factor and  $M_{\text{GT}}^{2\nu}$  is the double Gamow–Teller nuclear matrix element between the initial ( $0_{\text{g.s.}}^i$ ) and final ( $0_{\text{g.s.}}^f$ ) ground states, which is given by the following expression [65]:

$$M_{\text{GT}}^{2\nu} = \sum_m \frac{\langle 0_{\text{g.s.}}^f \| \sum_i \sigma(i)\tau^\pm(i) \| 1_m^+ \rangle \langle 1_m^+ \| \sum_i \sigma(i)\tau^\pm(i) \| 0_{\text{g.s.}}^i \rangle}{[\frac{1}{2}Q_{\beta\beta}(0_{\text{g.s.}}^f) + E(1_m^+) - M_i]/m_e + 1} , \quad (2.5)$$

where  $m_e$  is the electron rest mass,  $Q_{\beta\beta}(0_{\text{g.s.}}^f)$  is the  $Q$ -value of the double beta decay into the final  $0_{\text{g.s.}}^f$  ground state,  $E(1_m^+) - M_i$  is the energy difference between the  $m^{\text{th}}$  intermediate  $1^+$  state and the initial ground state,  $\sigma$  is the Pauli operator and  $\tau^-$  ( $\tau^+$ ) corresponds to the  $\beta^-$  ( $\beta^+$ /EC) decay operator; the sum  $\sum_i$  then runs over all the protons (neutrons) of the decaying nucleus. Because of the smallness of the contribution coming from Fermi-type virtual transitions, only Gamow–Teller-type transitions were considered in Eq. 2.4.

In the case of **transitions to excited states  $J_f$**  ( $J_f = 0^+, 2^+$ ), the  $2\nu\beta\beta$  decay rate is the following [65, 66, 67, 68]:

$$\left(T_{1/2}^{2\nu}(J_f)\right)^{-1} = G^{2\nu}(J_f)|M_{\text{GT}}^{2\nu}(J_f)|^2 , \quad (2.6)$$

where the nuclear matrix element is given by:

$$M_{\text{GT}}^{2\nu}(J_f) = \frac{1}{\sqrt{s}} \sum_m \frac{\langle J_f^+ \| \sum_i \sigma(i)\tau^\pm(i) \| 1_m^+ \rangle \langle 1_m^+ \| \sum_i \sigma(i)\tau^\pm(i) \| 0_{\text{g.s.}}^i \rangle}{([\frac{1}{2}Q_{\beta\beta}(J_f) + E(1_m^+) - M_i]/m_e + 1)^s} , \quad (2.7)$$

with  $s = 1 + 2\delta_{J_f 2}$ . These transitions are disfavoured by smaller phase space factors  $G^{2\nu}(J_f)$  due to a smaller available energy release for these processes.

### 2.2.2 Neutrinoless double beta decay

The half-life for the transitions to the  $0^+$  final states for  $0\nu\beta\beta$  decay can be written in the following form [65, 69, 70, 71]:

$$\begin{aligned} \left(T_{1/2}^{0\nu}\right)^{-1} &= G^{0\nu} |M^{0\nu}|^2 \langle m_\nu \rangle^2 \\ &= C_{mm}^{(0)} \left(\frac{\langle m_\nu \rangle}{m_e}\right)^2 + C_{m\lambda}^{(0)} \langle \lambda \rangle \left(\frac{\langle m_\nu \rangle}{m_e}\right) + C_{m\eta}^{(0)} \langle \eta \rangle \left(\frac{\langle m_\nu \rangle}{m_e}\right) \\ &\quad + C_{\lambda\lambda}^{(0)} \langle \lambda \rangle^2 + C_{\eta\eta}^{(0)} \langle \eta \rangle^2 + C_{\lambda\eta}^{(0)} \langle \lambda \rangle \langle \eta \rangle, \end{aligned} \quad (2.8)$$

where  $\langle m_\nu \rangle$  is the Majorana-neutrino mass term,  $\langle \lambda \rangle$  and  $\langle \eta \rangle$  are the right-handed coupling terms, and  $C_{ij}$  ( $i, j = m, \lambda, \eta$ ) are the nuclear response coefficients (their explicit form is given, for example, in [65, 69, 70]).

In the case of  $0\nu\chi\beta\beta$  decay mode with the emission of a Majoron, the transition rate is given by [72]:

$$\left(T_{1/2}^{0\nu\chi}\right)^{-1} = G^{0\nu\chi} |M^{0\nu\chi}|^2 \langle g_{\nu\chi} \rangle^2, \quad (2.9)$$

where  $G^{0\nu\chi}$  and  $M^{0\nu\chi}$  are the phase-space factor and the nuclear matrix element, and  $\langle g_{\nu\chi} \rangle$  is the Majoron-neutrino coupling term.

## 2.3 Experimental techniques

### 2.3.1 Indirect methods of $\beta\beta$ decay measurement

Historically, the existence of double beta decay was established for the first time by the **geochemical method**. Taking advantage of geological integration times (of the order of billions of years), geochemical methods are based on the search for daughter products accumulated in ancient minerals that are rich in the parent isotope. The quantity of daughter isotopes is then determined by chemical analysis or by mass spectroscopy. Since the energy information is missing, the mode of  $\beta\beta$  decay cannot be directly determined which is the weakness of such a method. Instead, the total decay rate is determined and then also an upper limit on each decay mode. The first measurement of double beta decay using this technique was made by T. Kirsten and his coworkers in late 1960s [73]. A 17 g sample of natural tellurium ore was used for the mass spectroscopy and chemical analysis measurements in order to detect the  $\beta\beta$  decay of  $^{130}\text{Te}$  into  $^{130}\text{Xe}$  by searching for an excess of  $^{130}\text{Xe}$ . From the measured excess of  $^{130}\text{Xe}$ , the tellurium concentration, and the gas-retention age of the mineral, the half-life of  $T_{1/2}^{\beta\beta}(^{130}\text{Te}) = 10^{21.34 \pm 0.12} \text{ yr} \simeq 2.19 \times 10^{21} \text{ yr}$  was calculated [73]. Similar experiments studying  $^{128}\text{Te}$  [74, 75] and  $^{82}\text{Se}$  [76, 77] soon followed.

Similar to the above method is the **radiochemical method** where the energy of  $\alpha$ -particles emitted by daughter nuclei of some  $\beta\beta$  decay isotopes is measured. Typically, this is used for  $^{238}\text{U}$ ,  $^{232}\text{Th}$ , and  $^{244}\text{Pu}$ .

### 2.3.2 Direct methods of $\beta\beta$ decay measurement

The decay mode can be directly distinguished only by measuring the energies of the electrons released in the  $\beta\beta$  decay. Thus, the observation of  $\beta\beta$  decay requires either an extremely efficient background suppression or additional information, such as could be obtained from tracking

capability. The direct techniques for double beta decay measurements can use either active sources which are at the same time the detecting device (source  $\equiv$  detector), e.g. germanium detectors, bolometers, xenon TPC; or passive sources (often in the form of thin foils) where particles emitted are detected by surrounding counters providing particle tracking and energy measurement (source  $\neq$  detector). Generally, experimental double beta decay setups can be classified into two categories: calorimeters or tracking detectors; the latter can be also combined with a calorimeter.

### 2.3.3 Calorimetric experiments

In this category, we class **germanium detector experiments** which provide a very good detection efficiency, as well as an excellent energy resolution making them very suitable for the  $0\nu\beta\beta$  decay search. At present, there are two international experiments using enriched, ultra pure  $^{76}\text{Ge}$  detectors: IGEX<sup>1</sup> and Heidelberg–Moscow. The IGEX experiment [78, 79] is installed at two sites, in the Baksan and Canfranc underground laboratories and contains about 8 kg of Ge, enriched to 86% in  $^{76}\text{Ge}$ .

The Heidelberg–Moscow experiment [80, 81, 82] searches for the  $0\nu\beta\beta$  decay of  $^{76}\text{Ge}$ . It is a second generation double beta decay experiment which uses a large quantity of highly enriched isotopes as double beta emitter. Five p-type HPGe detectors enriched to 86% in  $^{76}\text{Ge}$  and of active mass 10.96 kg were installed in the Gran Sasso underground laboratory (3500 m.w.e.). For the future, the construction of a similar kind of a detector, GENIUS (GERmanium in liquid NITrogen Underground Setup), has been proposed, consisting of an array of 400 large germanium diodes enriched in  $^{76}\text{Ge}$  with a total mass of around 1 ton and shielded by a very large tank of liquid nitrogen purified at a very high level [83]. Because of the cost and time necessary for the enrichment of such a large mass of germanium, a test experiment of reduced size called GENINO is considered, which would consist of 100 kg of natural germanium and 2 kg of  $^{76}\text{Ge}$  diodes in liquid nitrogen tank.

Another of the future experiments using the germanium detector technique is the Majorana project [84, 85]. It plans to operate with 500 kg of  $^{76}\text{Ge}$  (86% enrichment). The apparatus will consist of 210 segmented germanium crystals placed in ten large cryostats. The setup will be located in the US underground facility in Carlsbad, New Mexico.

Although also using germanium detectors, the TGV (Telescope Germanium Vertical) experiment [86] is based on a different principle. In contrast to the previously mentioned germanium experiments where the double beta decay source was also the calorimeter, this experiment is one of those where the double beta decay source is distinct from the particle detecting device. The TGV facility is a low-background and high sensitivity **Ge multi-detector spectrometer** composed of 16 HPGe planar type detectors mounted vertically one over another in the same cryostat. The TGV I experiment, which was situated in the Modane underground laboratory (known also as the Fréjus underground laboratory or the LSM laboratory), studied the double beta decay of  $^{48}\text{Ca}$  (1 g). These sources were placed into the cryostat between neighbouring detectors [87]. Using the experience with the TGV I spectrometer, the TGV II detector is being developed at present. It is made of 32 HPGe planar detectors, of larger size than in TGV I, and besides the improvement of the  $\beta\beta$  decay measurement of  $^{48}\text{Ca}$ , it will be the first experiment to study the  $2\nu EC/EC$  decay of  $^{106}\text{Cd}$  [88, 89]. The detection of the  $2\nu EC/EC$  decay events will be done via observation of two characteristic X-rays from the de-excitation of the orbital electrons.

---

<sup>1</sup>IGEX stands for International Germanium EXperiment

The use of **cryogenic (bolometer) detectors** to search for double beta decay was suggested in 1984 [90]. These detectors are based on the fact that the heat capacity at low temperatures of a diamagnetic and dielectric crystal is proportional to the cube of the ratio between the operating and Debye temperatures. Even the tiny energy released by a single particle in form of heat can be revealed by the increase of temperature of absorber [91]. As an example, we can cite the MIBETA experiment which was built by Milano group and installed in Gran Sasso underground laboratory. The detector was a segmented device consisting of 20 elements of natural  $\text{TeO}_2$ , each of 340 g, thus having active mass of 6.8 kg [92, 93, 94]. On the same principle as MIBETA, a new detector called CUORE, the Cryogenic Underground Observatory for Rare Events, will be built in the Gran Sasso laboratory [95]. This future thermal detector will be composed of an array of 1020 tellurium crystals with an active mass of 775 kg; the mass of each crystal will be about 760 g. However, CUORE will be preceded by a research and development project called CUORICINO. The CUORICINO detector will be made of an array of 56 crystals of the same size and weight as those intended for CUORE; the active mass of  $\text{TeO}_2$  crystals will be about 42 kg [92, 94].

### 2.3.4 Experiments using particle track reconstruction

Double beta decay experiments exploiting passive sources are not only capable of measuring the energy of particles emitted from the sources placed inside the detector, but they provide also track reconstruction which allows good particle identification and, in consequence, an efficient background rejection. The sources must be in the form of thin foils to limit the energy loss of electrons created inside the sample. The main advantage of these experiments is that they allow the study of a great variety of double beta decay isotopes, while the semiconductor experiments with active sources (germanium and bolometer detectors) are restricted to just a few isotopes.

The first such experiment was constructed by the group of M.K. Moe from the University of California in Irvine. The group used a 38 g sample of selenium enriched to 97% in  $^{82}\text{Se}$  placed inside a **cloud chamber** providing particle tracking [96]. Later the Irvine group lead by M.K. Moe employed a **time projection chamber (TPC)** [97, 98], filled with helium gas and with an applied magnetic field for electron-positron recognition. As the source, mylar strips with a thin film of selenium enriched to 97% in  $^{82}\text{Se}$  (14 g of the isotope) deposited on them were used. To begin with, the double beta decay isotope under study was  $^{82}\text{Se}$ , but later they moved to other sources: 16.7 g of metallic molybdenum enriched to 97.4% in  $^{100}\text{Mo}$  and 15.5 g of  $\text{Nd}_2\text{O}_3$  enriched to 91% in  $^{150}\text{Nd}$  [99].

The group from ITEP Moscow also used a TPC in magnetic field to search for neutrinoless double beta decay. After having studied double beta decay of  $^{136}\text{Xe}$ , two sources with samples of  $^{150}\text{Nd}$  (92% enrichment, 40.8 g of  $^{150}\text{Nd}$ ) and  $^{nat}\text{Nd}$  (5.6% natural isotopic abundance of  $^{150}\text{Nd}$ , 2.5 g of  $^{150}\text{Nd}$ ) deposited on mylar film were measured [100].

The Gotthard  $\beta\beta$  decay experiment, built by Caltech–Neuchâtel–PSI<sup>2</sup> [101] in the Gotthard underground laboratory (3700 m.w.e), was based on completely different technique. This experiment searched for the double beta decay of  $^{136}\text{Xe}$  by means of a **gas time projection chamber**. The xenon gas was enriched to 62.5% in  $^{136}\text{Xe}$  (3.3 kg) and was at the same time the source and the detection medium. The advantage of a TPC consists of its tracking capability, allowing event recognition and good background reduction. Compared to germanium detectors, the energy resolution is lower; it reaches 6.6% at the  $\beta\beta$  decay  $Q$ -value of  $^{136}\text{Xe}$  (2481 keV).

One of the proposed xenon experiments for studying the double beta decay of  $^{136}\text{Xe}$  with a

---

<sup>2</sup>PSI = Paul-Scherrer Institute

sensitivity on the effective neutrino mass of the order of 0.01 eV is EXO, the Enriched Xenon  $\beta\beta$  decay Observatory. The setup would consist of a xenon TPC with background suppression based on tagging the  $^{136}\text{Ba}^{++}$  ions produced by double beta decay with a laser [102].

The NEMO detector (see Chapter 4) is made of a **wire chamber** providing three dimensional tracking **combined with a calorimeter** measuring the energy of electrons, positrons, and photons. Although the experiment was originally focused on double beta decay of  $^{100}\text{Mo}$ , the NEMO2 detector also allowed the measurement of  $2\nu\beta\beta$  decays of  $^{82}\text{Se}$ ,  $^{116}\text{Cd}$ , and  $^{96}\text{Zr}$ . At present, the running NEMO3 detector houses up to 10 kg of several double beta decay isotopes simultaneously:  $^{100}\text{Mo}$ ,  $^{82}\text{Se}$ ,  $^{116}\text{Cd}$ ,  $^{130}\text{Te}$ ,  $^{150}\text{Nd}$ ,  $^{96}\text{Zr}$ , and  $^{48}\text{Ca}$ . The NEMO3 experiment as well as the detector are described in details in Chapter 4.

The Japanese experiment ELEGANTS V<sup>3</sup>, situated in the Oto Cosmo Observatory (1200 m.w.e), is using a  $\beta$ - $\gamma$  spectrometer which consists of three drift chambers for particle tracking and of a calorimeter. Two  $^{100}\text{Mo}$  sources (94.5% enrichment) in the form of a thin film and of total mass 171 g are set inside the detector [103, 72, 104]. Another Japanese project which is currently in the research and development phase is DCBA, the Drift Chamber Beta Analyzer [105].

Among the recently proposed projects, we can cite for instance MOON, the MOlybdenum Observatory Of Neutrinos, which aims to study both double beta decay and solar neutrinos [106]. The detector would consist of foils of natural molybdenum interleaved with plastic scintillator modules. The project proposes to use 1950 modules and 40 tons of natural molybdenum, corresponding to 3.3 tons of  $^{100}\text{Mo}$ . The expected sensitivity on the average neutrino mass is of  $\sim 0.03$  eV.

### 2.3.5 Review of the main results for $2\nu\beta\beta$ and $0\nu\beta\beta$ decays

The principal results in term of half-lives for  $2\nu\beta\beta$  decay and half-life limits for  $0\nu\beta\beta$  decay of the experiments mentioned in Secs. 2.3.3 and 2.3.4 are listed in Tabs. 2.3 and 2.4. However, this overview is not meant to be an exhaustive list of all the double beta decay experiments but rather a review of some historically important measurements and the main experimental results obtained up to now. For both double beta decay modes, only the half-life values for the ground state to ground state transitions are mentioned. A more complete list of the present positive  $2\nu\beta\beta$  decay results can be found, for instance, in Ref. [107]. The  $2\nu\beta\beta$  half-lives and corresponding nuclear matrix elements, as well as the half-life and corresponding  $\langle m_\nu \rangle$  limits for the  $0\nu\beta\beta$  and  $0\nu\chi\beta\beta$  modes are summarised, for instance, in Refs. [56] and [108].

---

<sup>3</sup>ELEGANTS = ELEctron GAMMA-ray NeuTrino Spectrometer

Transition	$Q_{\beta\beta}$ (keV) <sup>a</sup>	Abundance (%) <sup>b</sup>
$^{46}\text{Ca} \rightarrow ^{46}\text{Ti}$	987(4)	0.004(3)
$^{48}\text{Ca} \rightarrow ^{48}\text{Ti} \star$	4271(4)	0.187(4)
$^{70}\text{Zn} \rightarrow ^{70}\text{Ge}$	1001(3)	0.6(1)
$^{76}\text{Ge} \rightarrow ^{76}\text{Se} \star$	2039.6(9)	7.44(2)
$^{80}\text{Se} \rightarrow ^{80}\text{Kr}$	130(9)	49.61(10)
$^{82}\text{Se} \rightarrow ^{82}\text{Kr} \star$	2995(6)	8.73(6)
$^{86}\text{Kr} \rightarrow ^{86}\text{Sr}$	1256(5)	17.3(2)
$^{94}\text{Zr} \rightarrow ^{94}\text{Mo}$	1145.3(25)	17.38(4)
$^{96}\text{Zr} \rightarrow ^{96}\text{Mo} \star$	3350(3)	2.80(2)
$^{98}\text{Mo} \rightarrow ^{98}\text{Ru}$	112(7)	24.13(7)
$^{100}\text{Mo} \rightarrow ^{100}\text{Ru} \star$	3034(6)	9.63(3)
$^{104}\text{Ru} \rightarrow ^{104}\text{Pd}$	1299(4)	18.7(2)
$^{110}\text{Pd} \rightarrow ^{110}\text{Cd}$	2013(19)	11.72(9)
$^{114}\text{Cd} \rightarrow ^{114}\text{Sn}$	534(4)	28.73(28)
$^{116}\text{Cd} \rightarrow ^{116}\text{Sn} \star$	2802(4)	7.49(12)
$^{122}\text{Sn} \rightarrow ^{122}\text{Te}$	364(4)	4.63(3)
$^{124}\text{Sn} \rightarrow ^{124}\text{Te}$	2288.1(16)	5.79(5)
$^{128}\text{Te} \rightarrow ^{128}\text{Xe}$	868(4)	31.69(1)
$^{130}\text{Te} \rightarrow ^{130}\text{Xe} \star$	2533(4)	33.80(1)
$^{134}\text{Xe} \rightarrow ^{134}\text{Ba}$	847(4)	10.4(2)
$^{136}\text{Xe} \rightarrow ^{136}\text{Ba} \star$	2479(10)	8.9(1)
$^{142}\text{Ce} \rightarrow ^{142}\text{Nd}$	1417(25)	11.08(10)
$^{146}\text{Nd} \rightarrow ^{146}\text{Sm}$	56(5)	17.19(9)
$^{148}\text{Nd} \rightarrow ^{148}\text{Sm}$	1928.3(19)	5.76(3)
$^{150}\text{Nd} \rightarrow ^{150}\text{Sm} \star$	3367.1(22)	5.64(3)
$^{154}\text{Sm} \rightarrow ^{154}\text{Gd}$	1251.9(15)	22.7(2)
$^{160}\text{Gd} \rightarrow ^{160}\text{Dy}$	1729.5(14)	21.86(4)
$^{170}\text{Er} \rightarrow ^{170}\text{Yb}$	653.9(16)	14.9(2)
$^{176}\text{Yb} \rightarrow ^{176}\text{Hf}$	1078.8(27)	12.7(2)
$^{186}\text{W} \rightarrow ^{186}\text{Os}$	490.3(22)	28.6(2)
$^{192}\text{Os} \rightarrow ^{192}\text{Pt}$	417(4)	41.0(8)
$^{198}\text{Pt} \rightarrow ^{198}\text{Hg}$	1048(4)	7.2(2)
$^{204}\text{Hg} \rightarrow ^{204}\text{Pb}$	416.5(19)	6.87(4)
$^{232}\text{Th} \rightarrow ^{232}\text{U}$	858(6)	100
$^{238}\text{U} \rightarrow ^{238}\text{Pu}$	1145.8(17)	99.2745(60)

<sup>a</sup>The  $Q_{\beta\beta}$  values are taken from Ref. [54].<sup>b</sup>The values of natural abundances of the parent isotopes are taken from Ref. [64].

Table 2.1: A list of the  $\beta^-\beta^-$  decay transitions for naturally occurring parent isotopes, the corresponding  $Q_{\beta\beta}$  values in keV and the natural abundances of the parent isotopes. The isotopes marked with  $\star$  are used in current  $\beta\beta$  decay experiments.

Transition	$Q_{\beta\beta}$ (keV) <sup>a</sup>	Abundance (%) <sup>b</sup>
$^{78}\text{Kr} \rightarrow ^{78}\text{Se}$	833.1(80)	0.35(2)
$^{96}\text{Ru} \rightarrow ^{96}\text{Mo}$	677.1(80)	5.52(6)
$^{106}\text{Cd} \rightarrow ^{106}\text{Pd}$	734.0(78)	1.25(4)
$^{124}\text{Xe} \rightarrow ^{124}\text{Te}$	821.0(27)	0.10(1)
$^{130}\text{Ba} \rightarrow ^{130}\text{Xe}$	538.1(80)	0.106(2)
$^{136}\text{Ce} \rightarrow ^{136}\text{Ba}$	366.0(500)	0.19(1)

<sup>a</sup>The  $Q_{\beta\beta}$  values are taken from Ref. [54].

<sup>b</sup>The values of natural abundances of the parent isotopes are taken from Ref. [64].

Table 2.2: A list of the  $\beta^+\beta^+$  decay transitions for naturally occurring parent isotopes and the corresponding  $Q_{\beta\beta}$  values in keV and the natural abundances of the parent isotopes.

Experiment	Isotope	$T_{1/2}^{2\nu\beta\beta}$ (yr)	Year	Ref.
Kirsten <i>et al.</i>	$^{130}\text{Te}$	$10^{21.34 \pm 0.12} \simeq 2.19 \times 10^{21}$	1968	[73]
Irvine group $\star$	$^{82}\text{Se}$	$1.1^{+0.8}_{-0.3} \times 10^{20}$	1987	[97]
Irvine group	$^{100}\text{Mo}$	$6.82^{+0.38}_{-0.53}(\text{stat}) \pm 0.68(\text{syst}) \times 10^{18}$	1997	[99]
Irvine group	$^{150}\text{Nd}$	$6.75^{+0.37}_{-0.42}(\text{stat}) \pm 0.68(\text{syst}) \times 10^{18}$	1997	[99]
ITEP (TPC)	$^{150}\text{Nd}$	$1.88^{+0.66}_{-0.39}(\text{stat}) \pm 0.19(\text{syst}) \times 10^{19}$	1995	[100]
Heidelberg–M. $\star$	$^{76}\text{Ge}$	$1.77^{+0.01}_{-0.01}(\text{stat})^{+0.13}_{-0.11}(\text{syst}) \times 10^{21}$	1997	[82]
ELEGANTS V $\star$	$^{100}\text{Mo}$	$1.15^{+0.3}_{-0.2} \times 10^{19}$	1996	[103, 104]
NEMO2	$^{100}\text{Mo}$	$9.5 \pm 0.4(\text{stat}) \pm 0.9(\text{syst}) \times 10^{18}$	1995	[110, 111]
NEMO2	$^{82}\text{Se}$	$0.83 \pm 0.10(\text{stat}) \pm 0.07(\text{syst}) \times 10^{20}$	1998	[112]
NEMO2	$^{116}\text{Cd}$	$3.75 \pm 0.35(\text{stat}) \pm 0.21(\text{syst}) \times 10^{19}$	1996	[113]
NEMO2	$^{96}\text{Zr}$	$2.1^{+0.8}_{-0.4}(\text{stat}) \pm 0.2(\text{syst}) \times 10^{19}$	1999	[114]
Gotthard	$^{136}\text{Xe}$	$> 3.6 \times 10^{20}$	1998	[101]
TGV I	$^{48}\text{Ca}$	$4.2^{+3.3}_{-1.3} \times 10^{19}$	2000	[87]

Table 2.3: Experimentally determined half-lives for the  $2\nu\beta\beta$  decay mode in the principal double beta decay experiments. All the results are given at 90% C.L. except the geochemical experiment of Kirsten and co-workers and experiments marked with  $\star$  where the half-lives were determined at 68% C.L.

Experiment	Isotope	$T_{1/2}^{0\nu\beta\beta}$ (yr)	Year	Ref.
Irvine group	$^{100}\text{Mo}$	$> 1.23 \times 10^{21}$	1997	[99]
Irvine group	$^{150}\text{Nd}$	$> 1.22 \times 10^{21}$	1997	[99]
LBL-MHC-UNM-INEL *	$^{100}\text{Mo}$	$> 0.44 \times 10^{23}$	1993	[109]
Heidelberg–Moscow	$^{76}\text{Ge}$	$> 1.1 \times 10^{25}$	1997	[81]
ELEGANTS V *	$^{100}\text{Mo}$	$> 5.2 \times 10^{22}$	1996	[103]
NEMO2	$^{100}\text{Mo}$	$> 6.4 \times 10^{21}$	1995	[110, 111]
NEMO2	$^{82}\text{Se}$	$> 9.5 \times 10^{21}$	1998	[112]
NEMO2	$^{116}\text{Cd}$	$> 5.0 \times 10^{21}$	1996	[113]
NEMO2	$^{96}\text{Zr}$	$> 1.0 \times 10^{21}$	1999	[114]
Gotthard	$^{136}\text{Xe}$	$> 4.4 \times 10^{23}$	1998	[101]
IGEX	$^{76}\text{Ge}$	$> 1.57 \times 10^{25}$	2000	[79, 115]
TGV I	$^{48}\text{Ca}$	$> 1.5 \times 10^{21}$	2000	[87]

Table 2.4: Experimentally determined half-life limits for the  $0\nu\beta\beta$  decay mode in the principal double beta decay experiments. All the results are given at 90% C.L. except those marked with \* where the half-life limits were determined at 68% C.L.

## Chapter 3

# $2\nu\beta\beta$ decay of $^{100}\text{Mo}$ to excited states

Neutrinoless double beta decays, which violate the lepton number conservation law, provide one with very sensitive tests for the neutrino mass  $\langle m_\nu \rangle$  and for the possible right-handed weak currents. The  $0\nu\beta\beta$  decay to the  $0^+$  ground state involves both the massive Majorana neutrinos and the right-handed currents, while the  $0\nu\beta\beta$  decay to the  $2^+$  excited state involves only the right-handed currents [117, 118]. Two-neutrino double beta decays provide one with the important information on the spin-isospin interactions, which are relevant to the  $0\nu\beta\beta$  nuclear matrix elements [119]. Since the energy released in  $\beta\beta$  decay to the excited state is less than that for the ground state transition, the probability of the decay is consequently also less. In the first approximation, the decay probability for the  $2\nu$  mode is proportional to the 11<sup>th</sup> power of the available energy while for the  $0\nu$  mode it is proportional to the 5<sup>th</sup> or 7<sup>th</sup> power of the energy [120].

It is very important to note that in the framework of QRPA models, which are the most commonly used for theoretical calculations, the dependence of nuclear matrix elements on the particle–particle strength parameter  $g_{pp}$  is completely different for transitions to the ground and excited states [65]. This is why the decay to excited states probes different aspects of these calculations.

The  $2\nu\beta\beta$  decay through the  $0^+ \rightarrow 2^+$  transition is unfavourable because of the cancellation in the phase-space integral. In addition, theoretical calculations show that the nuclear matrix element  $M_{\text{GT}}^{2\nu}(2^+)$  is much smaller than that for the  $0^+ \rightarrow 0^+$  transition. Thus the resulting half-lives for  $2\nu\beta\beta(0^+ \rightarrow 2^+)$  decays are a few orders of magnitude longer than those for the  $2\nu\beta\beta(0^+ \rightarrow 0^+)$  transitions [54].

Fig. 3.1 illustrates the double beta decay scheme of  $^{100}\text{Mo}$  to the ground and the first excited states of  $^{100}\text{Ru}$ . The first excited level at 540 keV is the  $2_1^+$  state, the next one is the  $0_1^+$  state at 1130 keV, then the  $4_1^+$  and  $2_2^+$  states at 1227 and 1362 keV respectively follow.

### 3.1 Theoretical calculations

Half-life values of the  $2\nu\beta\beta$  decay to excited states of the daughter nucleus calculated by theoreticians for various theoretical models are inconsistent one with other; the difference is often a few orders of magnitude. Recently published results of theoretical calculations for different models expressed in term of half-lives of the  $2\nu\beta\beta$  decay of  $^{100}\text{Mo}$  to the first two excited states ( $2_1^+$  and  $0_1^+$ ) of  $^{100}\text{Ru}$  are given in Tab. 3.1. More about theoretical calculations for various  $\beta\beta$

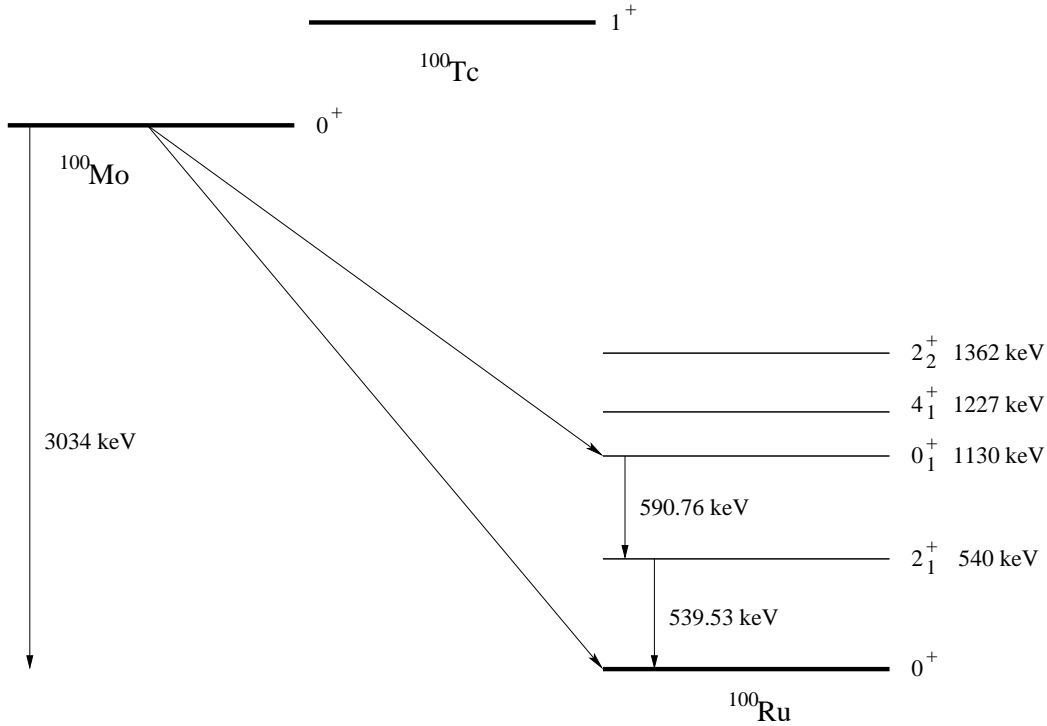


Figure 3.1: A double beta decay scheme of  $^{100}\text{Mo}$  to the ground and excited states of  $^{100}\text{Ru}$ .

decaying isotopes can be found in Ref. [65].

## 3.2 Previous experiments and their results

Double beta decay is becoming a valuable tool of nuclear spectroscopy. The observation of the  $2\nu\beta\beta$  decay of  $^{100}\text{Mo}$  to the excited  $0_1^+$  state (at 1130 keV) of  $^{100}\text{Ru}$  has been reported in 1995 by Barabash, Avignone and collaborators [124]. Their experiment studied a 956 g sample of molybdenum powder enriched to 98.5% in  $^{100}\text{Mo}$  and used the technique based on the observation of the subsequent  $\gamma$  decays which can be applied to other nuclei as well. An ultra-low background germanium detector in a Marinelli geometry which was placed in the Soudan mine at a depth of 2090 m.w.e. was used for the detection of de-excitation  $\gamma$ -rays of 539.53 and 590.76 keV from the  $0_1^+ \rightarrow 2_1^+ \rightarrow 0_1^+$  cascade. The  $\gamma$ -ray energy spectrum in the region of interest which was obtained in 415.43 d of counting is shown in Fig. 3.2. The resulting half-life value for the  $2\nu\beta\beta$  decay of  $^{100}\text{Mo}$  to the  $0_1^+$  excited state of  $^{100}\text{Ru}$  at 68% confidence level (C.L.) is then the following [124]:

$$T_{1/2}^{2\nu\beta\beta}(^{100}\text{Mo}, 0_1^+) = (6.1_{-1.1}^{+1.8}) \times 10^{20} \text{ yr} .$$

At approximately the same time, the NEMO collaboration measured a 994 g sample of metallic molybdenum powder enriched to 99.5% in  $^{100}\text{Mo}$  with a HPGe detector in the Modane Underground Laboratory. The powder was arranged in the Marinelli geometry in order to optimise the detector efficiency and to avoid any free space between the detector and the copper part of the shielding. The latter measure avoided a possible radon contamination. After 2298 hours

Theoretical model	Calculated $T_{1/2}$ (yr)		Ref.
	$0_1^+$	$2_1^+$	
single particle basis (s.p.)	$1.6 \times 10^{22}$	$2.3 \times 10^{23}$	[65]
sQRPA <sup>a</sup>	$5.5 \times 10^{21}$	$3.9 \times 10^{24}$	[65]
SU(3) basis	$4.2 \times 10^{20}$	$2.5 \times 10^{25}$	[65]
Wood-Saxon basis (WS)	$1.8 \times 10^{20}$	$2.1 \times 10^{21}$	[70]
gap WS basis (GWS)	$1.7 \times 10^{20}$	$2.1 \times 10^{21}$	[70]
pseudo-SU(3) basis <sup>b</sup>	$1.6 \times 10^{21}$	$5.5 - 24 \times 10^{25}$	[121, 108]
sQRPA	$2.1 \times 10^{21}$	$3.4 \times 10^{22}$	[122]
SSD <sup>c</sup>	$4.45 \times 10^{20}$	$1.73 \times 10^{23}$	[123]

<sup>a</sup>second-QRPA = second-quasiparticle random-phase approximation

<sup>b</sup>pseudo-SU(3) model for deformed nuclei

<sup>c</sup>SSD = single state dominance hypothesis

Table 3.1: Calculated half-life values for  $2\nu\beta\beta$  decay of  $^{100}\text{Mo}$  to the two first excited states for different theoretical models.

of running time, no peaks were seen in the  $\gamma$ -ray spectrum at the de-excitation energies of  $^{100}\text{Ru}$ . Thus the following limit on the half-life was deduced [125]:

$$T_{1/2}^{2\nu\beta\beta}({}^{100}\text{Mo}, 0_1^+) \geq 1.2 \times 10^{21} \text{ yr} \quad (90\% \text{ C.L.}) .$$

Fig. 3.3 shows the measured  $\gamma$ -ray spectra restricted to the energy ranges corresponding to the decay of the first excited states of  $^{100}\text{Ru}$ , respectively the  $2_1^+ \rightarrow 0_{\text{g.s.}}^+$ ,  $0_1^+ \rightarrow 2_1^+$ ,  $2_2^+ \rightarrow 2_1^+$ , and  $2_2^+ \rightarrow 0_{\text{g.s.}}^+$  transitions.

The ELEGANTS V spectrometer also measured the  $\beta\beta$  decays of  $^{100}\text{Mo}$  to the low-lying excited states of  $^{100}\text{Ru}$ . The 94.5% enriched  $^{100}\text{Mo}$  and natural Mo sources, both chemically purified, were used for comparison. The measurements of the  $2\nu$  and  $0\nu$  double beta decay modes to the  $2_1^+$ ,  $0_1^+$ ,  $4_1^+$ , and  $2_2^+$  excited states were carried out for 1275.54 hours and produced only half-life limits (see Ref. [119]). The limit determined for the  $0_{\text{g.s.}}^+ \rightarrow 0_1^+$  transition is:

$$T_{1/2}^{2\nu\beta\beta}({}^{100}\text{Mo}, 0_1^+) > 0.8 \times 10^{20} \text{ yr} \quad (68\% \text{ C.L.}) .$$

A new positive result for the  $2\nu\beta\beta$  decay of  $^{100}\text{Mo}$  to the excited  $0_1^+$  state was announced again by Barabash and coworkers in 1999 [126]. This experiment was performed in the Modane Underground Laboratory. A set of enriched  $^{100}\text{Mo}$  metallic powder samples destined for the NEMO3 experiment was measured with a low-background HPGe detector. Data from 17 measurements were analysed and the following half-life was deduced from the summed  $\gamma$ -ray spectrum:

$$T_{1/2}^{2\nu\beta\beta}({}^{100}\text{Mo}, 0_1^+) = (9.3_{-1.7}^{+2.8}) \times 10^{20} \text{ yr} \quad (90\% \text{ C.L.}) .$$

Later, another positive result for the  $2\nu\beta\beta$  ( $0_{\text{g.s.}}^+ \rightarrow 0_1^+$ ) decay of  $^{100}\text{Mo}$  was published by the TUNL-ITEP<sup>1</sup> collaboration. Compared with previous experiments focused on very low background detection systems, this experiment used a  $\gamma$ - $\gamma$  coincidence technique which provided better background rejection. By this coincidence method, two separate HPGe detectors

<sup>1</sup>TUNL = Triangle Universities Nuclear Laboratory, Durham, North Carolina, USA; ITEP = Institute of Theoretical and Experimental Physics, Moscow, Russia

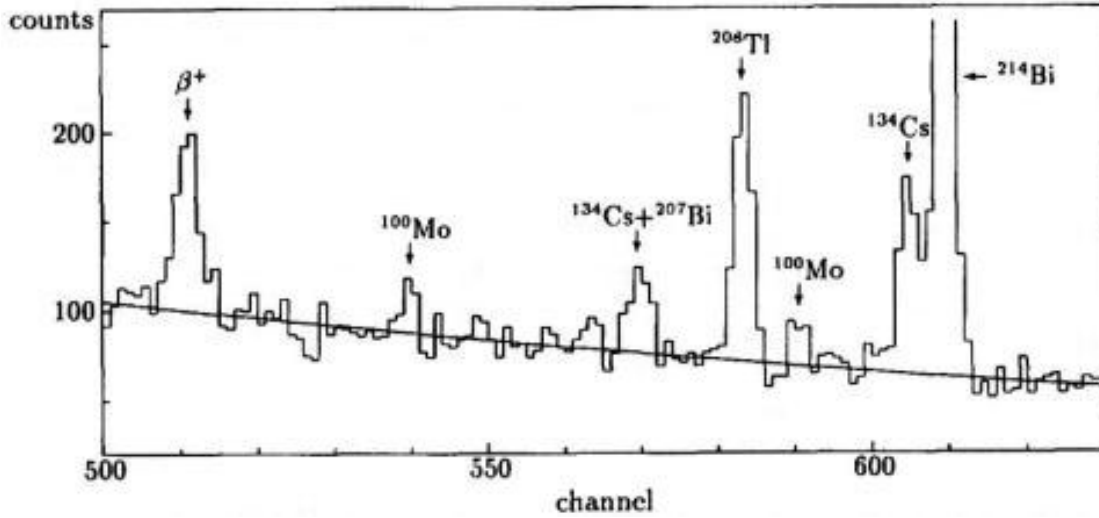


Figure 3.2: The  $\gamma$ -ray energy spectrum in the region of interest measured in 415.43 d by Barabash, Avignone and coworkers [124].

simultaneously detect the two emitted  $\gamma$ -rays from the  $2\nu\beta\beta$  ( $0_{g.s.}^+ \rightarrow 0_1^+$ ) decay of  $^{100}\text{Mo}$  with  $E_{\gamma_1} = 590.76$  keV and  $E_{\gamma_2} = 539.53$  keV (see Fig. 3.4). Finally, the result obtained in term of half-life is the following:

$$T_{1/2}^{2\nu\beta\beta}(^{100}\text{Mo}, 0_1^+) = (5.9_{-1.1}^{+1.7}(\text{stat}) \pm 0.6(\text{syst})) \times 10^{20} \text{ yr}$$

at 68% confidence limit [127, 128].

If the weighted average value is produced from the previously cited positive results as is done in Ref. [107], the following average value and the corresponding error are obtained:

$$T_{1/2}^{2\nu\beta\beta}(^{100}\text{Mo}, 0_1^+) = (6.8 \pm 1.2) \times 10^{20} \text{ yr} .$$

All the previously cited results are summarised in Tab. 3.2.

$T_{1/2}$ (yr)	Year	Ref.
$(6.1_{-1.1}^{+1.8}) \times 10^{20}$	1995	[124]
$\geq 1.2 \times 10^{21}$	1992	[125]
$> 0.8 \times 10^{20}$	1992	[119]
$(9.3_{-1.7}^{+2.8}(\text{stat}) \pm 1.4(\text{syst})) \times 10^{20}$	1999	[126]
$(5.9_{-1.1}^{+1.7}(\text{stat}) \pm 0.6(\text{syst})) \times 10^{20}$	2001	[127, 128]
<b>Average value from positive results</b>		
$(6.8 \pm 1.2) \times 10^{20}$	2001	[107]

Table 3.2: Experimentally determined half-life values or limits for the  $2\nu\beta\beta$  decay of  $^{100}\text{Mo}$  to the excited  $0_1^+$  state.

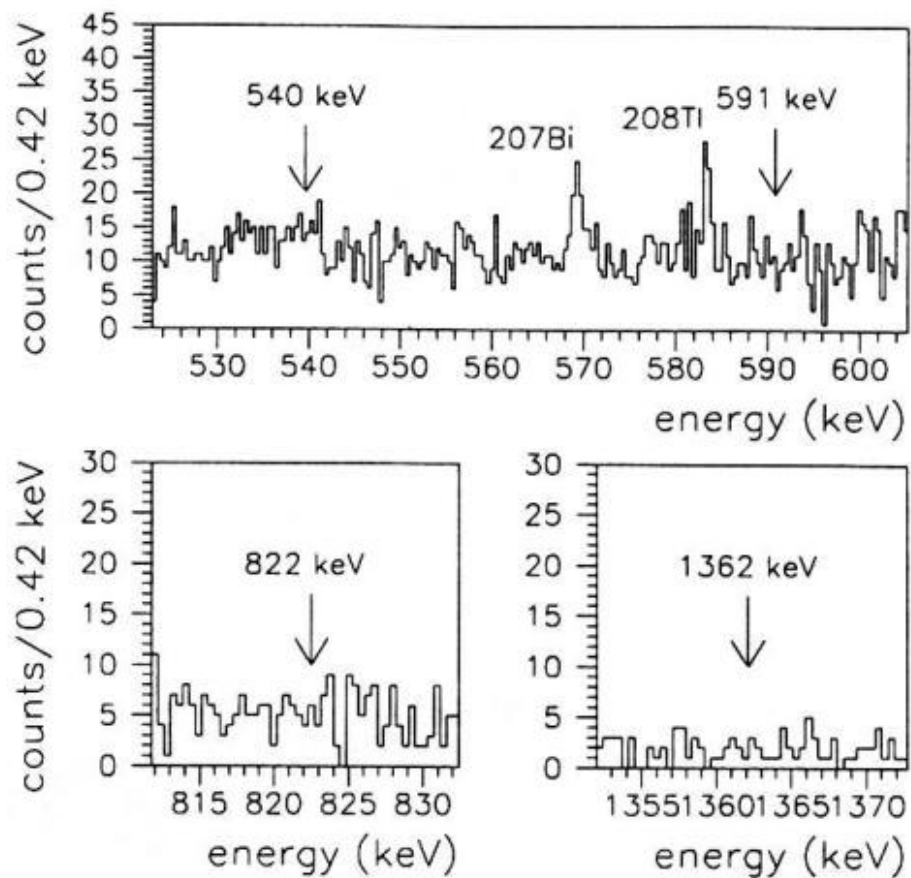


Figure 3.3: Partial  $\gamma$ -ray spectra in the energy windows corresponding to the decay of the first excited states of  $^{100}\text{Ru}$ . The expected positions of the 540, 591, 822, and 1362 keV  $\gamma$ -ray lines which corresponds respectively to the  $2_1^+ \rightarrow 0_{\text{g.s.}}^+$ ,  $0_1^+ \rightarrow 2_1^+$ ,  $2_2^+ \rightarrow 2_1^+$ , and  $2_2^+ \rightarrow 0_{\text{g.s.}}^+$  transitions in  $^{100}\text{Ru}$  are indicated by arrows [125].

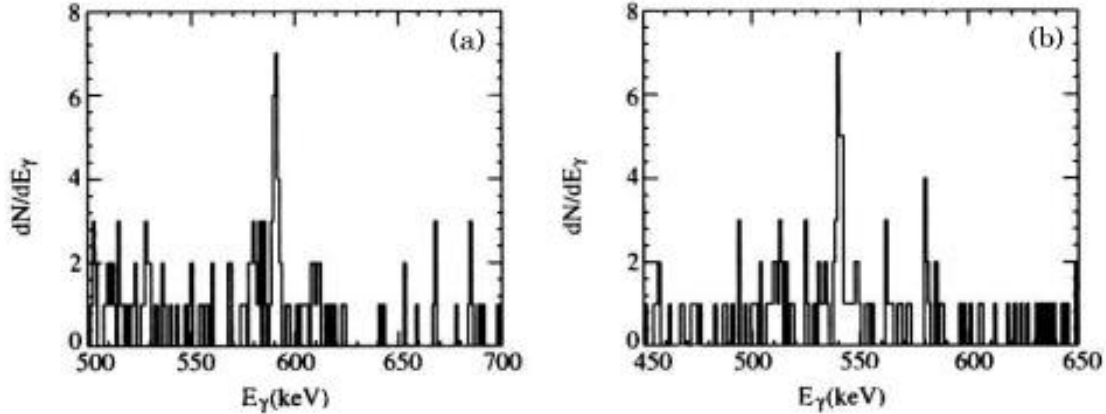


Figure 3.4: The  $\gamma$ -ray spectra in coincidence (a) with  $540 \pm 2.5$  keV and (b) with  $591 \pm 2.5$  keV obtained in [128].

### 3.3 NEMO3 and the $2\nu\beta\beta$ decay to excited states

Compared to spectroscopic experiments which generally use HPGe detectors and detect only  $\gamma$ -rays, the NEMO3 detector<sup>2</sup> is able to detect both photons and electrons due to its original design combining a calorimeter with a tracking detector. The wire chamber of NEMO3 provides three dimensional tracking of charged particles which, in consequence, allows the correct identification of electrons from  $\beta\beta$  decay. The calorimeter detects these electrons and the de-excitation photons and provides a measurement of their energy and time of their detection. Although the energy resolution of the NEMO3 calorimeter, which is made of plastic scintillators coupled to photomultiplier tubes (PMTs), does not reach the same level as HPGe detectors do, the advantage of the adopted solution consists of the simultaneous detection of the two electrons and the de-excitation photons from the  $2\nu\beta\beta$  decay to the excited states. As the NEMO3 calorimeter also measures the detection time of particles, the use of an appropriate time-of-flight criterion, in addition to energy cuts, can very efficiently reduce all the kinds of external and internal backgrounds (see Chapters 5 and 6). Moreover, after the accumulation of a sufficiently high number of observed events from the  $2\nu\beta\beta$  decay to excited states, the NEMO3 experiment can produce the two electron energy sum spectrum, as well as the single electron energy spectrum, which is impossible to measure with HPGe detectors. So, NEMO3 will be the first  $\beta\beta$  decay experiment to obtain such spectra.

<sup>2</sup>Detailed description of the NEMO3 detector is given in Chapter 4.

# Chapter 4

## The NEMO3 experiment

### 4.1 Introduction

The main goal of the NEMO3 experiment is to study neutrinoless double beta decay to a half-life limit of  $10^{25}$  years. This value corresponds to a sensitivity for the effective neutrino mass  $\langle m_\nu \rangle$  of the order of  $(0.3 - 0.1)$  eV. Besides the  $0\nu\beta\beta$  decay, it allows the thorough study of the  $2\nu\beta\beta$  decay of several nuclei. Moreover, due to the large amount of  $^{100}\text{Mo}$  in the NEMO3 detector (7 kg), the  $2\nu\beta\beta$  decay to the  $0_1^+$  and  $2_1^+$  excited states can be also measured. Another interesting feature of NEMO3 is the possibility of measuring the ultra-low intrinsic contamination in  $^{208}\text{Tl}$  and  $^{214}\text{Bi}$  of the source foils. Such result can be achieved only thanks to an efficient background suppression and specially developed detection techniques, both of which are described later in this chapter.

In 1988 the NEMO collaboration started a research and development programme in order to construct a detector with the performance mentioned above. Two technological prototypes, NEMO1 [129] and NEMO2 [130], have proven the feasibility of such a project and have also contributed to the background studies for the NEMO3 detector. Additionally, the NEMO2 detector (Fig. 4.1) has measured the half-lives of the two-neutrino double beta decay of  $^{100}\text{Mo}$ ,  $^{116}\text{Cd}$ ,  $^{82}\text{Se}$ , and  $^{96}\text{Zr}$  (see Tab. 4.1).

Isotope	$T_{1/2}^{2\nu\beta\beta}$ (yr)	Ref.
$^{100}\text{Mo}$	$0.95 \pm 0.04(stat) \pm 0.09(syst) \times 10^{19}$	[110, 111]
$^{116}\text{Cd}$	$3.75 \pm 0.35(stat) \pm 0.21(syst) \times 10^{19}$	[113]
$^{82}\text{Se}$	$0.83 \pm 0.10(stat) \pm 0.07(syst) \times 10^{20}$	[112]
$^{96}\text{Zr}$	$2.1_{-0.4}^{+0.8}(stat) \pm 0.2(syst) \times 10^{19}$	[114]

Table 4.1: The half-life values for  $2\nu\beta\beta$  decay determined with the NEMO2 detector.

The NEMO3 experiment is realised by a large international collaboration involving today the following laboratories and institutions: CENBG Bordeaux, LPC Caen, CFR Gif-sur-Yvette, LAL Orsay, IReS Strasbourg (all France), JINR Dubna, ITEP Moscow (both Russia), Czech Technical University in Prague, Charles University of Prague (both the Czech Republic), IN-EEL Idaho Falls, MHC South Hadley (both the U.S.A.), Jyväskylä University (Finland), Saga University (Japan), and University College London (the U.K.).

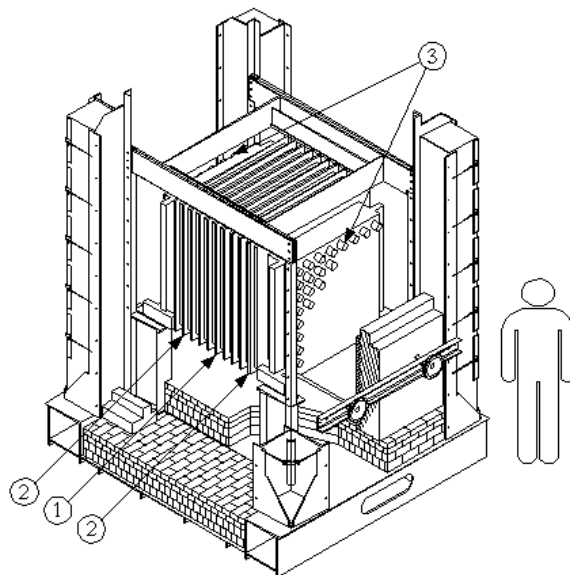


Figure 4.1: A schematic diagram of the NEMO2 detector without shielding: (1) central frame holding source foils; (2) tracking volume composed of ten frames, each consisting of two perpendicular planes of 32 Geiger cells; (3) calorimeter made of two scintillator arrays of  $8 \times 8$  counters each at the beginning and of  $5 \times 5$  counters each later.

## 4.2 General description of the detector

The NEMO3 detector (Fig. 4.2) has cylindrical shape, with height of about 3 m and diameter about 5 m. Both values correspond to the dimensions of the bare detector without any additional shielding. The detector is composed of twenty equal sectors (Fig. 4.3) with a frame made of pure copper (the external and the internal walls) and low-radioactivity stainless steel (top and bottom “petals”).

The NEMO3 detector is similar in function to the earlier prototype NEMO2 and is based on the direct detection (track reconstruction and energy measurement) of the two electrons produced by double beta decay. This is done with a tracking wire chamber allowing us to determine tracks of charged particles; energy of electrons, positrons, and photons is then measured with a calorimeter which surrounds the tracking volume. The detector operates with almost 10 kg in total of several double beta decay isotopes ( $^{100}\text{Mo}$ ,  $^{82}\text{Se}$ ,  $^{116}\text{Cd}$ ,  $^{130}\text{Te}$ ,  $^{150}\text{Nd}$ ,  $^{96}\text{Zr}$ ,  $^{48}\text{Ca}$ ) which are in the form of thin foils. To minimise radioactive backgrounds related to double beta decay events, interest is placed in isotopes with high  $Q$ -values for  $\beta\beta$  decay, such as  $^{100}\text{Mo}$ ,  $^{82}\text{Se}$ ,  $^{130}\text{Te}$ , and  $^{116}\text{Cd}$  (see Tab. 4.2). A great effort was also focused on the procedure of purification of the  $\beta\beta$  decay sources and on the stringent selection of low activity materials for all the detector components. Both the source foils and the detector components have to be ultra free from  $^{214}\text{Bi}$ ,  $^{208}\text{Tl}$ , and  $^{40}\text{K}$ . To minimise external backgrounds, NEMO3 is made of thoroughly selected low-radioactivity materials. Moreover, it is surrounded with iron and neutron shielding which screen the detector from photons and neutrons coming from the laboratory. The NEMO3 detector was installed and is now running in the Modane Underground Laboratory (Laboratoire

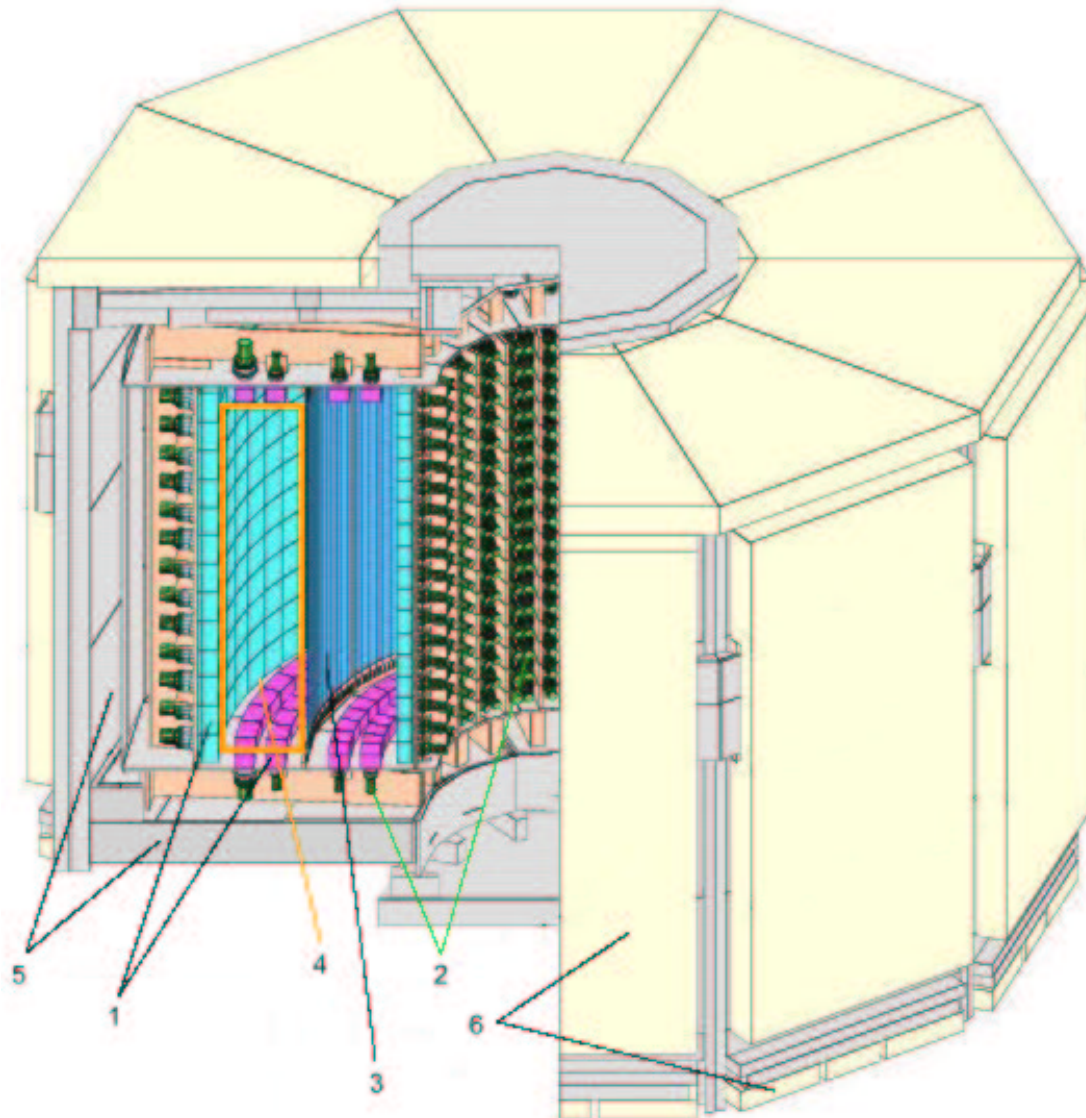


Figure 4.2: A schematic diagram of the NEMO3 detector: (1) plastic scintillators, (2) PMTs, (3) source foils, (4) tracking volume (wire chamber), (5) iron shielding, (6) neutron shielding.

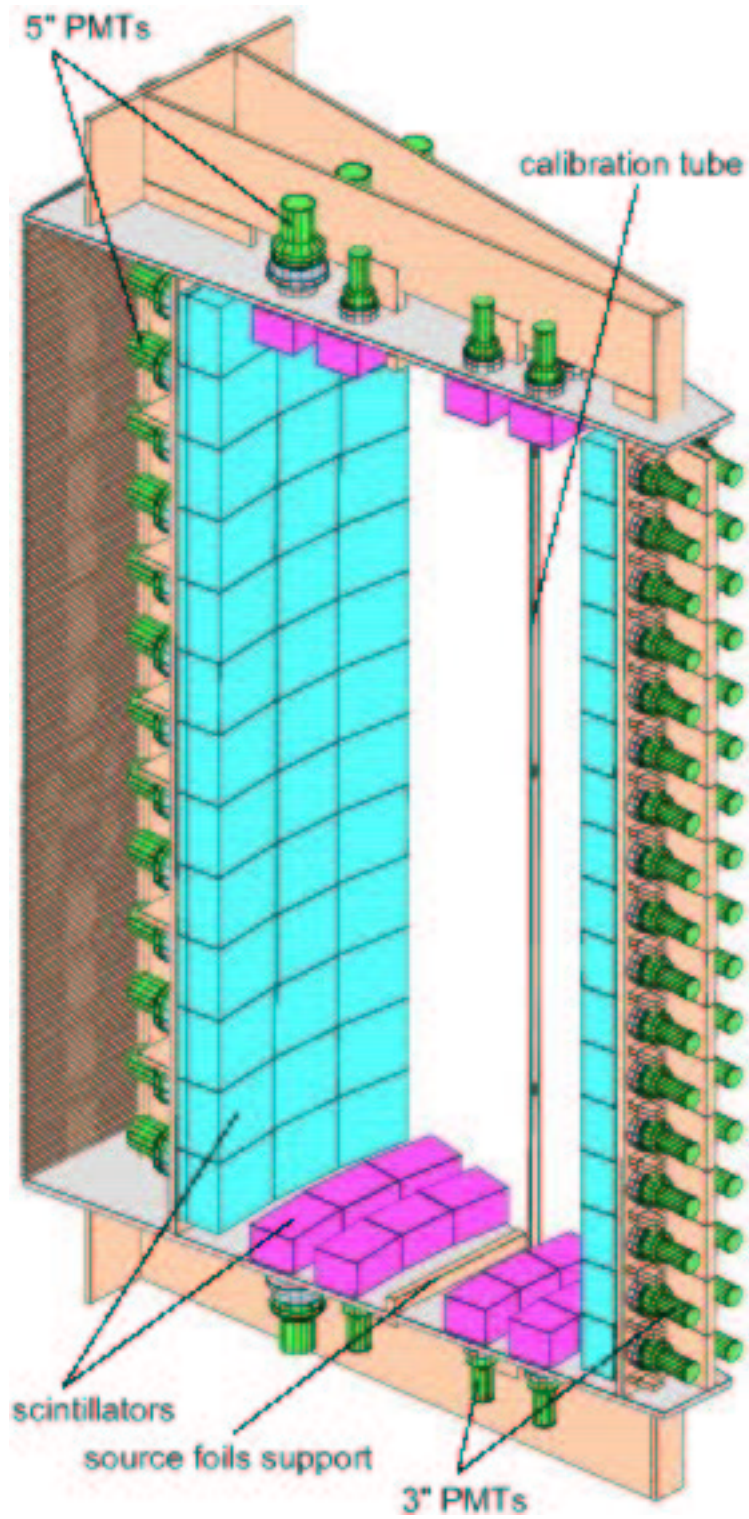


Figure 4.3: A view of a sector of the NEMO3 detector.

Souterrain de Modane, LSM<sup>1</sup>) in France. The placement of the detector in the underground laboratory considerably reduces the cosmic-ray background contribution which then becomes negligible. The LSM laboratory provides an efficient shield of 1780 m of rock that corresponds to 4850 m water-equivalent (m.w.e).

Isotope	Abundance (%)	$Q_{\beta\beta}$ (keV) <sup>a</sup>
<sup>100</sup> Mo	9.63	3034
<sup>82</sup> Se	8.73	2995
<sup>116</sup> Cd	7.49	2805
<sup>130</sup> Te	33.80	2529
<sup>96</sup> Zr	2.80	3350
<sup>150</sup> Nd	5.64	3367
<sup>48</sup> Ca	0.19	4272

<sup>a</sup>The values of natural abundances and of  $Q_{\beta\beta}$  are taken from Refs. [131, 132]

Table 4.2: The  $Q_{\beta\beta}$ -values and abundance of isotopes studied with the NEMO3 detector.

### 4.3 Tracking wire chamber

The tracking part of the NEMO3 detector consists of a wire chamber providing three dimensional tracking of charged particles. The chamber is made of 6180 open octagonal drift cells (309 cells per sector) (Fig. 4.4) which operate in Geiger mode and so are called Geiger cells. The cells, 270 cm long and with a diameter of 3 cm, are stretched between top and bottom petals of sectors. They are composed of one anodic and nine or ten cathodic wires (depending on their position in the detector), all made of stainless steel and with a diameter of 50  $\mu\text{m}$ . Each Geiger cell shares two or three cathodic wires with the neighbouring cells. All the cathodic wires are maintained at the same voltage which has been set to ground (0 V). There are two copper rings, 3 cm long and with a diameter of 2.3 cm, at both extremities of the cells. Their role is to detect the arrival of Geiger plasma at the top and the bottom of a cell. The adopted design of the NEMO3 wire chamber endeavours to achieve maximum transparency of the tracking volume to charged particles, in particular to electrons from double beta decay.

#### 4.3.1 Wire chamber geometry

Each sector has 18 rows of cells in the following configuration: four rows on each side of the source foils, then two between PMTs and finally another three rows on the most interior and the most exterior side of a sector (Fig. 4.5). This “4-2-3” configuration in each half-sector allows a precise reconstruction of the event vertex in the source foils. It also guarantees good track reconstruction of charged particles throughout the internal volume of the detector. The number of Geiger cells in a row varies with the radius of the row. So, the three most external rows have each 23 cells per sector, the next two rows behind the 5” PMTs have 20 cells, the four rows on the exterior side of the source foils have 18 cells, the four rows on the interior side of the foils have 16 cells, the next two rows between the 3” PMTs have 14 cells, and finally the most internal three rows have 12 cells.

<sup>1</sup>The LSM laboratory is referred also as the Fréjus Underground Laboratory.

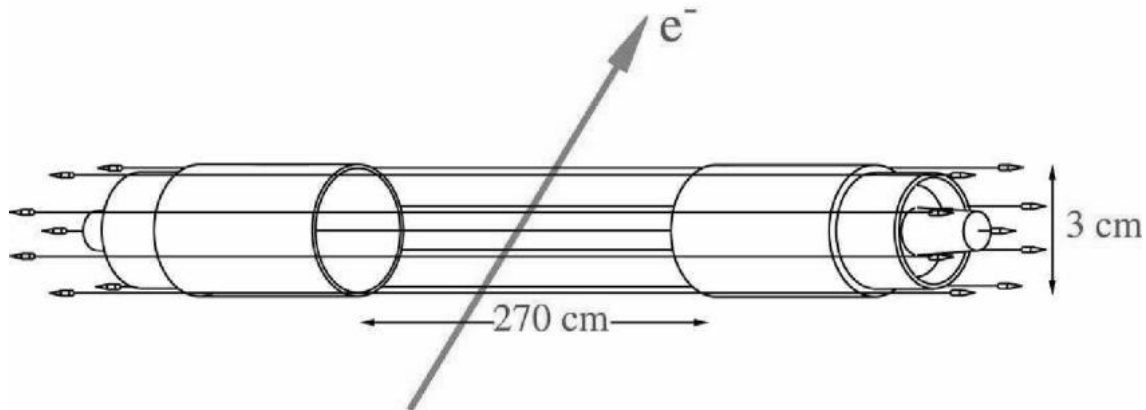


Figure 4.4: A diagram of an elementary drift Geiger cell.

### 4.3.2 Geiger cell working principle

The wire chamber provides three dimensional tracking of charged particles. The transverse position of a crossing particle is determined from the drift time of ionisation electrons for each fired cell. The longitudinal position is calculated from the two measurements of the time taken for the avalanche to propagate along the anode wire to the top and the bottom of the Geiger cell.

A charged particle going through the detector ionises the gas in the wire chamber. Electrons created this way drift in the electric field of the chamber to the closest anodic wire. The average drift velocity is about  $1 \text{ cm}/\mu\text{s}$  which means that electrons travel the distance corresponding to the radius of a Geiger cell ( $1.5 \text{ cm}$ ) within  $1.5 \mu\text{s}$ . When their distance from the anodic wire becomes of the order of  $100 \mu\text{m}$ , the electrons attain enough kinetic energy to ionise the gas. Thus, an avalanche of ionization is born in proximity to the anodic wire (Fig. 4.6) and it propagates along the wire to its extremities. This is actually the Geiger mode of classic gas detectors and, in consequence, the elementary cells of such tracking detector are called Geiger cells. The ions of the avalanche create a plasma, called a Geiger plasma, which propagates at a speed of about  $6 \text{ cm}/\mu\text{s}$ . That means that the plasma will travel the length of the anodic wire of  $2.7 \text{ m}$  within approximately  $45 \mu\text{s}$ .

To minimise the effect of multiple scattering of particles, the detector is filled with a mixture of 95% of helium gas, 4% of ethyl-alcohol, and 1% of argon; the latter two additives are used as quenchers. The quantities of quenchers (4% of ethanol and 1% of argon) are considered to be optimal for the correct working of the NEMO3 wire chamber and were determined after series of tests conducted in LAL Orsay with a prototype of the wire chamber and in the LSM Modane with the detector in the real experimental conditions. For concentrations higher than 4%, ethyl-alcohol quenches too much and the plasma avalanche does not manage to propagate along the anodic wire as far as to the extremities of a Geiger cell. On the contrary, for lower concentrations, ethyl-alcohol does not quench enough and the plasma avalanche lasts for too long time causing a long dead-time of the counter. The pressure inside the detector is maintained at about 7 mbar above the local atmospheric pressure of the LSM laboratory.

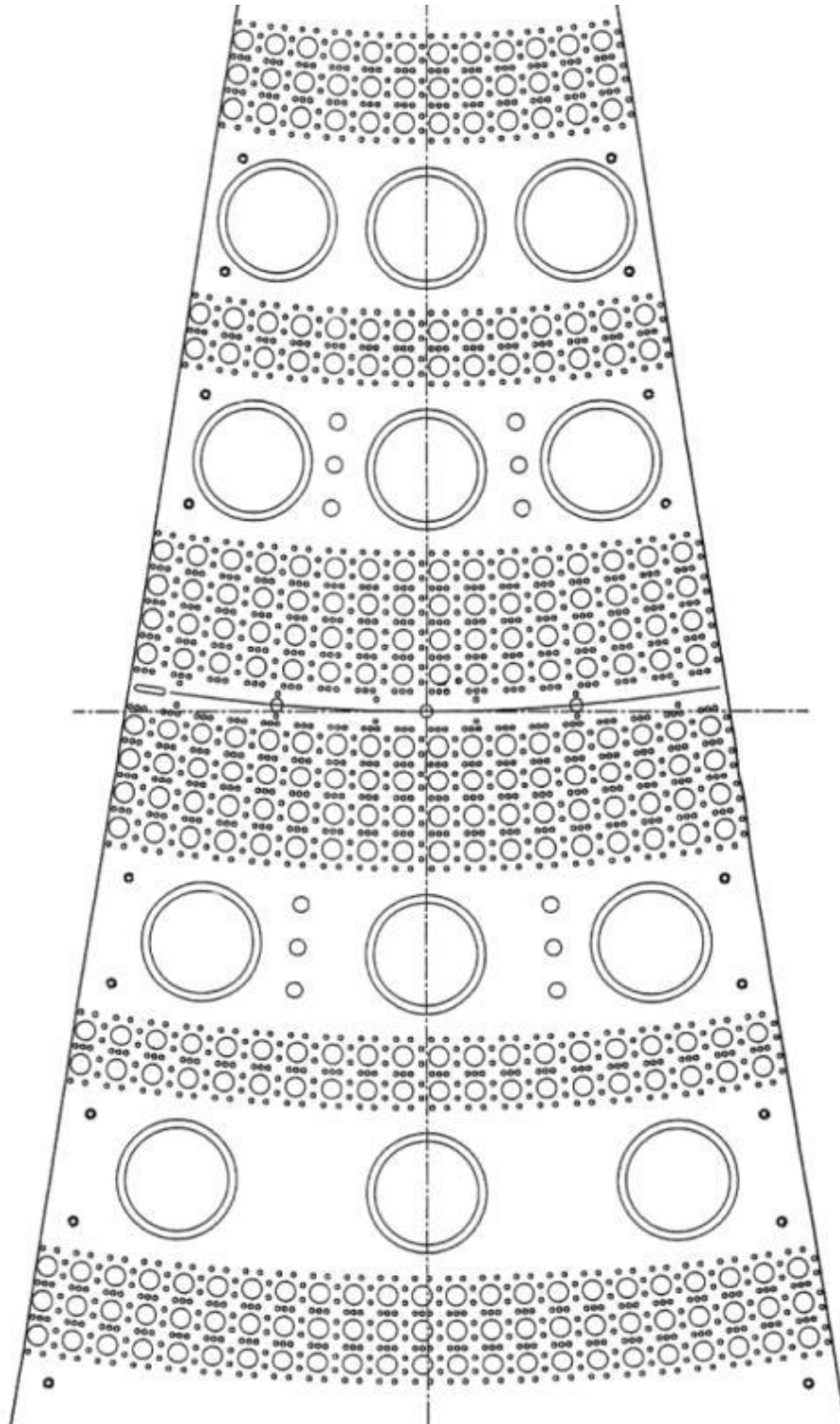


Figure 4.5: The Geiger cell layout in a sector (top view).

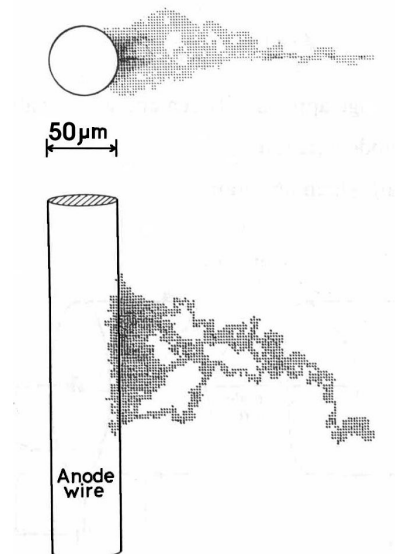


Figure 4.6: The primary avalanche in the proximity of an anode wire triggered by a single electron.

## 4.4 Calorimeter

The main role of the calorimeter in NEMO3 is to measure the energy of electrons (or positrons) in the energy range from 150 keV to 12 MeV and of photons in the energy range from 80 keV to 12 MeV. It also provides the time-of-flight measurement which is important for efficient recognition and hence rejection of external backgrounds.

The NEMO3 calorimeter is composed of 1940 blocks of plastic scintillators. Each sector is equipped with 97 blocks as follows: 34 on the internal wall (two columns of 17 counters), 39 on the external wall (three columns of 13 counters), 12 on the upper petal (four rows of 3 counters) and another 12 on the bottom petal. The scintillator blocks are different in size according to their position inside the detector ( $20 \times 20 \times 10 \text{ cm}^3$  for external walls and  $15 \times 15 \times 10 \text{ cm}^3$  for internal walls) but their thickness (10 cm) is common to all the counters and has been chosen in order to obtain a good efficiency for the  $\gamma$ -ray detection (50% at 500 keV). The NEMO3 scintillators are made of polystyrene which is produced by the standard method of styrene polymerization. The scintillating agent, p-Terphenyl (PTP), and the wavelength shifter (POPOP) are dissolved in the styrene. The composition of the NEMO3 scintillator, resulting from several years long research and development programmes in JINR Dubna and INR Kharkov, is 98.49% of polystyrene, 1.5% of PTP, and 0.01% of POPOP for the wall scintillators; and 98.75% of polystyrene, 1.2% of PTP, and 0.05% of POPOP for the petal scintillators. In order to protect them mechanically, they are wrapped in aluminised mylar foil (6  $\mu\text{m}$  thickness, 0.3 nm layer of Al). Moreover, the lateral faces of each scintillator block are covered with five layers of a teflon band (each 70  $\mu\text{m}$  thick) which reflects light back inside the scintillators and thus increases the efficiency of light collection. Hence scintillations inside a scintillator block which are not emitted into the solid angle seen by the photo-multiplier tube are partially reflected back by teflon and hence a part of the energy, which would be otherwise lost, is recuperated.

These scintillator blocks are coupled to very low radioactivity Hamamatsu photomultiplier tubes (PMTs). The 5" PMTs (type R6594) are installed on the external wall and on the most external row of scintillator blocks on the petals, while the 3" PMTs (type R6091) are placed on the internal wall and the petals. These PMTs are special because their activities in  $^{214}\text{Bi}$ ,  $^{208}\text{Tl}$ , and  $^{40}\text{K}$  are three orders of magnitude below standard PMTs. This is a very important fact ensuring a low external background of the experiment. Measured activities in  $^{214}\text{Bi}$  and  $^{208}\text{Tl}$  of the NEMO3 PMTs as well as the imposed upper limits are summarised in Tab. 4.3. We note that the main contribution comes from the PMT glass.

PMT type	Activity in $^{214}\text{Bi}$ (Bq/kg)		Activity in $^{208}\text{Tl}$ (Bq/kg)	
	measured	upper limit	measured	upper limit
5"	$0.37 \pm 0.03$	1.6	$0.037 \pm 0.005$	0.4
3"	$0.27 \pm 0.03$	1.3	$0.029 \pm 0.004$	0.3

Table 4.3: Measured activities of the NEMO3 PMTs [133] compared with the allowed upper limits.

The PMTs are enclosed in black plastic boxes to protect them from the ambient light. All the PMTs are also screened from the magnetic field generated by a coil (see Sec. 4.6.3) with cylindrical  $\mu$ -metal shields.

The energy resolution  $\sigma_E/E$  of the NEMO3 calorimeter is 6 – 7% at 1 MeV. The time resolution at 1 MeV is about 250 ps. The fact that the calorimeter allows measurements of time is especially important for the NEMO3 trigger and data analysis of events. The time-of-flight information is indispensable for the efficient rejection of external background events during the data analysis.

#### 4.4.1 Energy and time calibration

A daily survey of the absolute time and energy calibration is provided by a laser-based system which is incorporated into the NEMO3 calorimeter. This daily calibration is important because certain parameters like the PMT gain can vary over time. In this system, a small bulbous scintillator converts the laser pulse into a properly shaped and wavelength-shifted (420 nm) signal which simulates a one-electron event in the scintillator. This light is then delivered by optical fibers to each of the photomultipliers in the calorimeter and to six reference PMTs. An accuracy of 1% for the energy calibration survey is assured via a comparison of the laser light stability with the six reference PMTs that are continuously exposed to  $^{207}\text{Bi}$  sources [134].

Each sector has a so called calibration tube which is placed in the central vertical plane (the plane of source foils). This flattened, rectangular profile, copper tube has three kapton windows on each side: at the bottom, the central, and the top level. Inside the tube, a plastic carrier with three calibration sources corresponding to the tube window positions can be inserted from the upper part of a sector. This system was designed for the energy and time calibration of the calorimeter. Moreover, it is also used for the PMT time and gain alignments, various tests of the trigger and data acquisition systems, and for measurements of the track reconstruction performance of the wire chamber. Sources of  $^{207}\text{Bi}$ ,  $^{90}\text{Sr}$ , and  $^{106}\text{Ru}$  are used especially for the energy calibration of the calorimeter and for the tests of the tracking wire chamber; sources of  $^{60}\text{Co}$ , which emit two photons of 1333 keV and 1173 keV in coincidence, are used for the time alignment.

## 4.5 Source foils

### 4.5.1 Installed sources

The NEMO3 detector is equipped with different double beta decay isotopes, as well as with foils devoted to measurements of the external background. The whole detector contains 140 source strips (seven strips per sector), each with dimensions as follows: width of 7 cm, length of 270 cm and thickness of about 55  $\mu\text{m}$ . The strips are fixed by a special rail support attached to the petals in the central plane of each sector.

Although the NEMO experiment was originally focused on the study of the double beta decay of  $^{100}\text{Mo}$ , techniques of isotopic enrichment and purification developed in recent years have enabled the use of other double beta decay isotopes in the experiment. Today the NEMO3 detector accomodates several isotopes:  $^{100}\text{Mo}$ ,  $^{82}\text{Se}$ ,  $^{116}\text{Cd}$ ,  $^{130}\text{Te}$  (in the form of oxide) in large quantities (kilogrammes) and also  $^{150}\text{Nd}$ ,  $^{96}\text{Zr}$  and  $^{48}\text{Ca}$  (grammes). In order to study the background, foils of Cu and  $^{nat}\text{TeO}_2$  are also used. A list of foil materials and respective quantities are summarised in Tab. 4.4. Tab. 4.5 shows enrichment and foil type for the  $\beta\beta$  decaying isotopes used in NEMO3. One can note the high enrichment rates of  $^{100}\text{Mo}$  and  $^{82}\text{Se}$  achieving 95 to 99%. This shows the very good efficiency of the enrichment procedures developed for the NEMO experiment. The final source distribution by sectors in the detector is represented in Fig. 4.7.

Isotope	Studied process	Net mass of isotope (g)	Occupation of sectors
$^{100}\text{Mo}$	$0\nu\beta\beta$ , $2\nu\beta\beta$	6914	12
$^{82}\text{Se}$	$0\nu\beta\beta$ , $2\nu\beta\beta$	932	2.3
$^{116}\text{Cd}$	$0\nu\beta\beta$ , $2\nu\beta\beta$	405	1
$^{130}\text{Te}$	$0\nu\beta\beta$ , $2\nu\beta\beta$	454	1.8
$^{150}\text{Nd}$	$0\nu\beta\beta$ , $2\nu\beta\beta$	36.6	0.14
$^{96}\text{Zr}$	$2\nu\beta\beta$	9.4	0.03
$^{48}\text{Ca}$	$2\nu\beta\beta$	7.0	0.03
Cu	background	621	1
$^{nat}\text{Te}$	background	207	1.7

Table 4.4: A list of sources installed in the NEMO3 detector with respective net masses of isotopes and their occupation of sectors [135].

### 4.5.2 Source foil production

The upper limits on the source foil radiopurity were fixed in order to minimise the contribution to the  $0\nu\beta\beta$  signal from  $^{208}\text{Tl}$  and  $^{214}\text{Bi}$ . All the  $^{100}\text{Mo}$  source foils must have activities lower than 20  $\mu\text{Bq/kg}$  in  $^{208}\text{Tl}$  and 300  $\mu\text{Bq/kg}$  in  $^{214}\text{Bi}$ . Because the enrichment process failed to satisfy these purity requirements, two different purification and production methods for molybdenum have been investigated in parallel: a physical and a chemical process.

The first purification technique, which was developed at ITEP (Moscow, Russia), is based on the melting of molybdenum by an electron beam, then a crystal of pure material is drawn from the liquid portion into a long narrow cylinder. The impurities are left behind in the molten part. Subsequently the crystal cylinders are cut to a fiducial length and rolled in vacuum between very

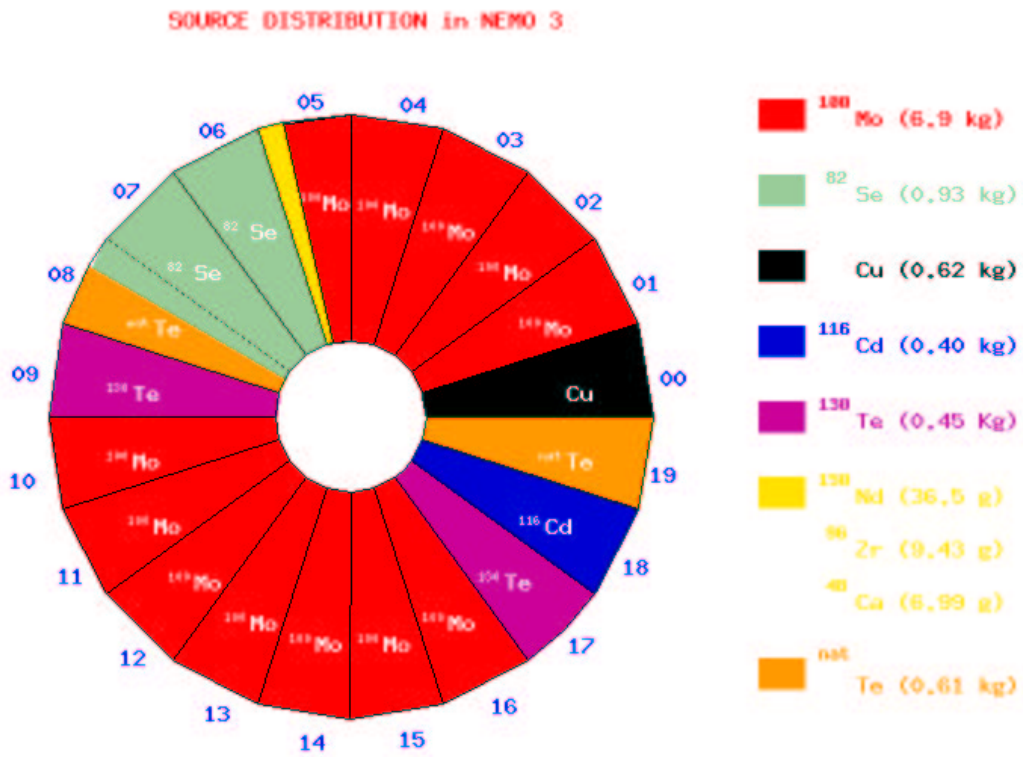


Figure 4.7: Distribution by individual sectors of the NEMO3 sources (top view).

Source	Foil type	Enrichment
$^{100}\text{Mo}$	metallic	95.1 - 98.9%
$^{100}\text{Mo}$	composite	95.1 - 98.9%
$^{82}\text{Se}$	composite	96.8 - 97.0%
$^{116}\text{Cd}$	metallic	93.3%
$^{130}\text{TeO}_2$	composite	89.4%
$^{nat}\text{TeO}_2$	composite	—
$^{150}\text{Nd}_2\text{O}_3$	composite	91.0%
$^{96}\text{ZrO}_2$	composite	57.3%
$^{48}\text{CaF}_2$	sealed powder	73.0%
$^{nat}\text{Cu}$	metallic	—

Table 4.5: Foil types and enrichment rates of isotopes used in NEMO3 [135].

pure steel rollers to form thin metallic foils. The edges of the foils are then trimmed and lengths patched together to form the foils which hang in the detector. The remaining molybdenum from cutting the foils is recycled and used again at the beginning of the next purification and foil production cycle when it is melted with molybdenum powder. This process has yielded 2.479 kg of  $^{100}\text{Mo}$  for the experiment.

The second technique of purification is a chemical method developed and processed at INEEL (Idaho, USA). The method, described in details in Ref. [136], is based on the chemical extraction of the daughters of the  $^{238}\text{U}$  and  $^{232}\text{Th}$  decay chains. In order to reduce the level of  $^{214}\text{Bi}$  and  $^{208}\text{Tl}$  efficiently, one has to remove isotopes preceding them in the decay chains (see Fig. 4.15) which have high disintegration periods. For the  $^{238}\text{U}$  decay chain this is  $^{226}\text{Ra}$  with  $T_{1/2} = 1600$  yr; for the  $^{232}\text{Th}$  chain one removes  $^{228}\text{Th}$  ( $T_{1/2} = 1.913$  yr) and  $^{228}\text{Ra}$  ( $T_{1/2} = 5.75$  yr).

First, the molybdenum metal powder is dissolved in 4M  $\text{HNO}_3$  solution, containing 2 mg of very pure  $\text{Ba}(\text{NO}_3)_2$ , a salt nearly free in Ra with only 0.08 mBq/g of  $^{226}\text{Ra}$ . The barium salt is added to block the sites on the  $\text{MoO}_3$  that precipitates, which would otherwise carry Ra. Then the solution is heated, which increases the acid strength. The nitric acid solution is evaporated until there is a thick slurry of  $\text{MoO}_3$  in  $\text{HNO}_3$ . Once the slurry is cool, it is filtered through plastic filter units, which separate the molybdenum from impurity radioisotopes, as most of the impurities are soluble in acid. After the filtered material is rinsed with ultra-pure  $\text{H}_2\text{O}$ , it is loaded into quartz boats that are inserted into a quartz-lined tube furnace. The  $\text{MoO}_3$  is further dried in an inert He atmosphere at  $200^\circ\text{C}$ . The  $\text{MoO}_3$  is then reduced to metal powder by passing  $\text{H}_2$  through the quartz tube at successively higher temperatures until it is ultimately heated for five hours at  $850^\circ\text{C}$ . At the end of the process, the molybdenum powder typically contains less than 1% of  $\text{O}_2$  and is slightly hygroscopic. The purified molybdenum powder is used for fabrication of composite foils with a binding paste (rhodovial) and mylar strips. The mylar strips had been previously irradiated with an ion beam and then etched by a chemical process to assure good adhesion of the molybdenum powder containing paste to the mylar strips.

The expected purification factor is greater than 100 times, as indicated by a study made with a sample of natural molybdenum. Originally, this sample had an activity of 28 mBq/kg before the chemical purification and less than 0.3 mBq/kg after the process. The enriched molybdenum for NEMO3 had a typical activity of 1.3 mBq/kg before purification. One can then expect an activity at the level of 0.013 mBq/kg or better for the final powder. This level of contamination will be easily measured with the NEMO3 detector through the  $e\gamma\gamma$  and  $e\gamma\gamma\gamma$  channels [137].

### 4.5.3 Radiopurity of foils

The radiopurity of the foil samples was measured with several ultra-low background HPGe detectors in the LSM laboratory to check whether they achieved the NEMO3 stringent radiopurity specifications. The ultra-low background Ge spectrometers were developed by the French company Eurisys Mesures. As is common practice, the abundance of selected isotopes in the  $^{238}\text{U}$  and  $^{232}\text{Tl}$  decay chains was determined by the strength of their gamma lines. Tab. 4.6 shows that with the exception of the  $^{82}\text{Se}$  foils only upper limits in  $^{208}\text{Tl}$  and  $^{214}\text{Bi}$  activities were established for all the foils installed inside the NEMO3 detector. In the case of the  $^{82}\text{Se}$  foils however, no special purification method was used to reduce their activity. These sources were previously used in the NEMO2 experiment and it was proved that the activity comes from a few hot spots which can be well located. Then these tiny zones are not considered in the  $\beta\beta$  decay analysis.

NEMO3 foils		Activities (mBq/kg)	
Isotope	Type	$^{208}\text{Tl}$	$^{214}\text{Bi}$
$^{100}\text{Mo}$	metallic	< 0.104	< 0.300
$^{100}\text{Mo}$	composite	< 0.140	< 0.090
$^{82}\text{Se}$	composite	$0.4 \pm 0.1$	$1.2 \pm 0.5$
$^{116}\text{Cd}$	metallic	< 0.5	< 1.5
$^{130}\text{Te}$	composite	< 0.51	< 0.68
$^{150}\text{Nd}$	composite	$10 \pm 2$	< 3.3
$^{96}\text{Zr}$	composite	< 10	< 17
$^{48}\text{Ca}$	sealed powder	< 2	< 4
Cu	metallic	< 0.033	< 0.117
$^{nat}\text{Te}$	composite	< 0.333	< 0.167

Table 4.6: Measured activities of the source foils installed in the NEMO3 detector

## 4.6 Reduction of external backgrounds

### 4.6.1 Iron shield

In order to achieve the very low background character of the experiment, the NEMO3 detector is covered with an external shield made of low radioactivity iron. It is produced in the form of 20 cm thick plates which are attached to the external mechanical frame (Fig. 4.8). Its role is especially to reduce  $\gamma$ -ray and thermal neutron external backgrounds coming from the LSM laboratory hall. Previous Monte-Carlo simulations and results obtained with NEMO2 [139, 140] showed that an iron shield attenuates  $\gamma$ -rays very well, and completely absorbs thermal neutrons. Nevertheless, it does not entirely stop fast and epithermal neutrons and thus extra neutron shielding is necessary.

### 4.6.2 Neutron shielding

Fast and epithermal neutrons from the walls of the laboratory cave can pass through the iron shield. After having been slowed down, they can be captured by copper nuclei of the NEMO3 frame and, in consequence, high energy photons can be generated. To thermalise these neutrons

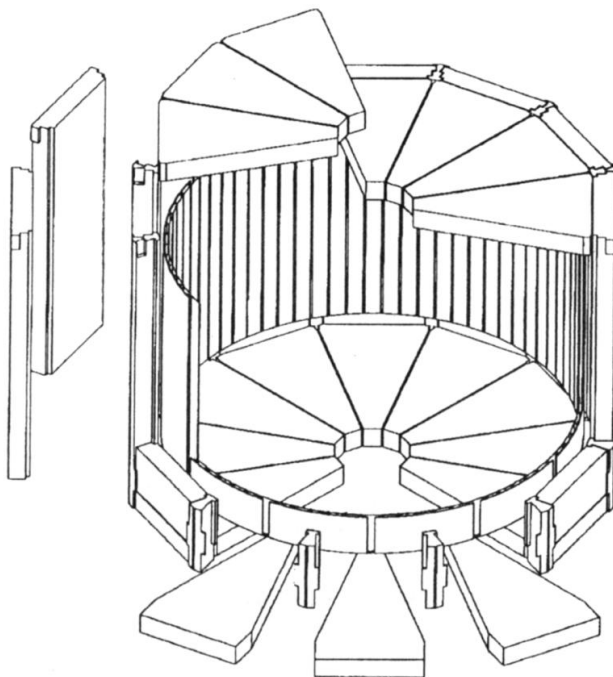


Figure 4.8: Diagram of the iron shielding.

before reaching the iron shield which will stop them completely, additional outer shielding was planned. It is composed of 10 water tanks, leakproof and made from stainless steel 304L, which are fixed to the external mechanical frame of the detector. These tanks are 430 cm high, have an inner and outer width of 165 cm and 185 cm respectively and have an internal capacity of 2.5 m<sup>3</sup> provided by a 34 cm layer of water. To cover the top and the bottom of the detector where the use of shielding based on water is risky, wooden blocks of 28 cm thickness are currently used; but in the future, polyethylene plates providing about a 20 cm layer will be used instead of wood since they have a better moderation efficiency for neutrons [138].

### 4.6.3 Magnetic field

A high energy photon interacting with the NEMO3 source foils can produce an electron-positron pair inside the detector. This will have the same signature as the two-electron events from double beta decay in the foils. Consequently, the ( $e^+e^-$ ) pair production is a dangerous kind of background for neutrinoless double beta decay. The recognition of a positron from an electron inside the detector is however possible due to the opposite curvatures of their tracks in a magnetic field. For this reason NEMO3 uses a vertical magnetic field in order to discriminate against this type of background in data analysis.

The previous studies of the impact of fast neutrons on NEMO3 [139] showed that their background contribution to the  $0\nu\beta\beta$  signal arises mainly from high energy photons from neutron capture which are able to produce principally ( $e^+e^-$ ) pairs. A 20 to 30 Gauss magnetic field, which provides the particle charge determination based on the track curvature, allows the rejection of 95% of the ( $e^+e^-$ ) pair events.

A vertical magnetic field is generated by a coil (Fig. 4.9) surrounding the detector which is

placed between the external wall of the detector and the iron shield. The coil is made of copper rods and is divided into ten segments (one segment covers two sectors) which are interconnected to form compact solenoid spirals. In consequence, to avoid an influence on the PMT performance due to their immersion in the magnetic field, all the PMTs are screened with  $\mu$ -metal shields of cylindrical shape.

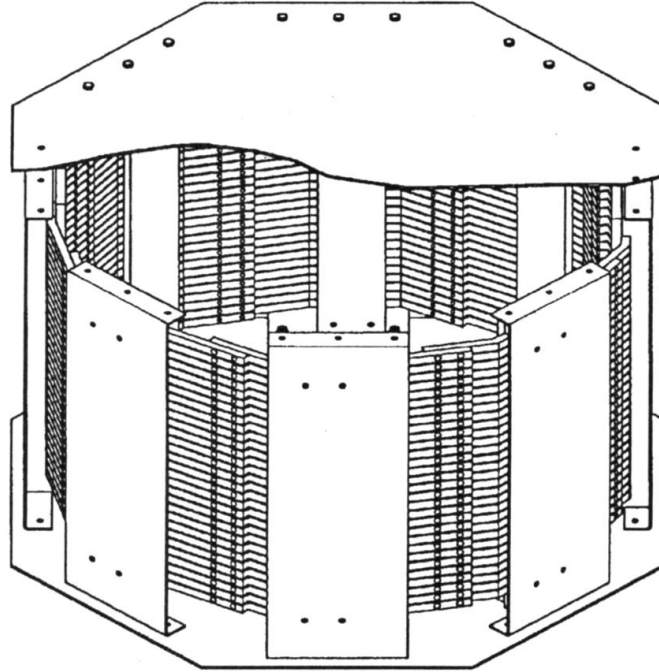


Figure 4.9: A general view of magnetic coil.

## 4.7 Electronics

### 4.7.1 Wire chamber electronics

The wire chamber electronics can be divided into two parts: analogue and digital. The first part is composed of 160 repartition boards (eight boards per sector) and the second is of the same number of VME acquisition cards. The role of the repartition boards is to distribute high voltage (HV) to all the Geiger cells, as well as to receive all the analogue signals from anodes and from the top and bottom cathodes.

High voltage is sent to these cards from two HV boards (see also Sec. 4.7.2) plugged into high voltage crates which also accommodate HV boards for the PMTs. To supply the inner Geiger cell layers (i.e. layers between the source foils and the internal wall of scintillator blocks) we use nine HV channels. In the case of the outer layers (the layers between the source foils and the external wall of scintillators), the high voltage is delivered by 18 HV channels. Because of the high number of cells in the outer layers, each one is supplied by two channels, the first one corresponding to sectors 00 to 09 and the second one to sectors 10 to 19. In total, we thus have 27 HV channels for the whole wire chamber.

The analogue signals arriving from anodes and cathodes are sent from repartition boards

to the VME acquisition cards which at first amplify and discriminate them, then convert them with ADCs and TDCs into digital form. The anodic signal starts the counting of one anodic and two cathodic TDCs. The cathodic TDCs are stopped when corresponding cathodic signals arrive, while the anodic one is stopped with a STOP signal sent by the acquisition trigger. The acquisition of an event begins after a START signal launched by the trigger when any scintillator detector is fired and is stopped at the end of a  $4 \mu\text{s}$  wide acquisition window. This is illustrated by diagrams in Fig. 4.10.

The cathodic times  $t_1$  and  $t_2$ , which correspond to the real longitudinal propagation times of the Geiger plasma since the birth of the primary ionization avalanche to the plasma arrival to the top and bottom cathode rings respectively, are proportional to the TDC contents and are calculated as follows:

$$\begin{aligned} t_1 &= \left( (TDC_{\text{top cath.}} \times 20) - 17.5 \right) \text{ ns} \\ t_2 &= \left( TDC_{\text{bot. cath.}} \times 20 \right) \text{ ns} . \end{aligned}$$

Because of the difference in length of signal cables between the top cathodes (9.5 m) and bottom cathodes (6 m), the correction of 17.5 ns for  $t_1$  (the top cathode time) is necessary. The anodic time  $t_a$  corresponding to the drift time of electrons in the transversal  $x$ - $y$  plane of the detector can be expressed as:

$$t_a = \left( (TDC_{\text{max}} - TDC_{\text{anode}}) \times 20 \right) \text{ ns} ,$$

where  $TDC_{\text{max}} = 307$ . This value corresponds to  $6.14 \mu\text{s}$  and is the result of anodic TDC spectrum measurements.

The wire chamber is also able to detect delayed  $\alpha$ -particles. For this purpose, a so called slow TDC (called also ALPHA TDC) is used. It allows the registration of delayed Geiger cells fired with  $\alpha$ -particles till  $640 \mu\text{s}$  after the anode STOP signal (see also Fig. 4.10).

#### 4.7.2 Calorimeter electronics

The high voltage (HV) supply of all the PMTs (1940 PMTs on the detector itself and 6 reference PMTs) is provided by three high voltage crates containing, in total, 28 HV boards. One crate has ten HV boards for PMT channels, while the two others have nine PMT HV boards and one HV board for Geiger cell channels each. The high voltage from these boards goes to so called repartition boards. One high voltage channel on the output of the HV board supplies a group of three PMTs. In order to send appropriate values of HV for each PMT in this group, the HV channel is divided in three on the repartition board and HV values are then adapted by two resistors  $R_1$  and  $R_2$  for each PMT channel. The value of the common high voltage for this group, as well as values of  $R_1$  and  $R_2$  for the three PMTs are determined during calorimeter gain alignment runs in order to have approximately the same gain from all the three PMTs.

The analogue signal from the PMTs, which corresponds to energy deposited in the scintillator, goes directly to the data acquisition cards. We have two acquisition cards for each sector, one for the inner half of a sector with 51 PMTs and the other for the outer half with 46 PMTs.

For data acquisition, we have two types of thresholds called **low** and **high thresholds**. The low threshold is used for PMT signal integration and for time measurement. When a signal exceeds this threshold, charge integration is begun and the TDC counting is started. The latter is then stopped by a STOP signal sent from the trigger. When the high threshold is passed, a signal that this scintillation counter was fired is sent to the trigger. In general, we have three types of information from the PMT acquisition cards:

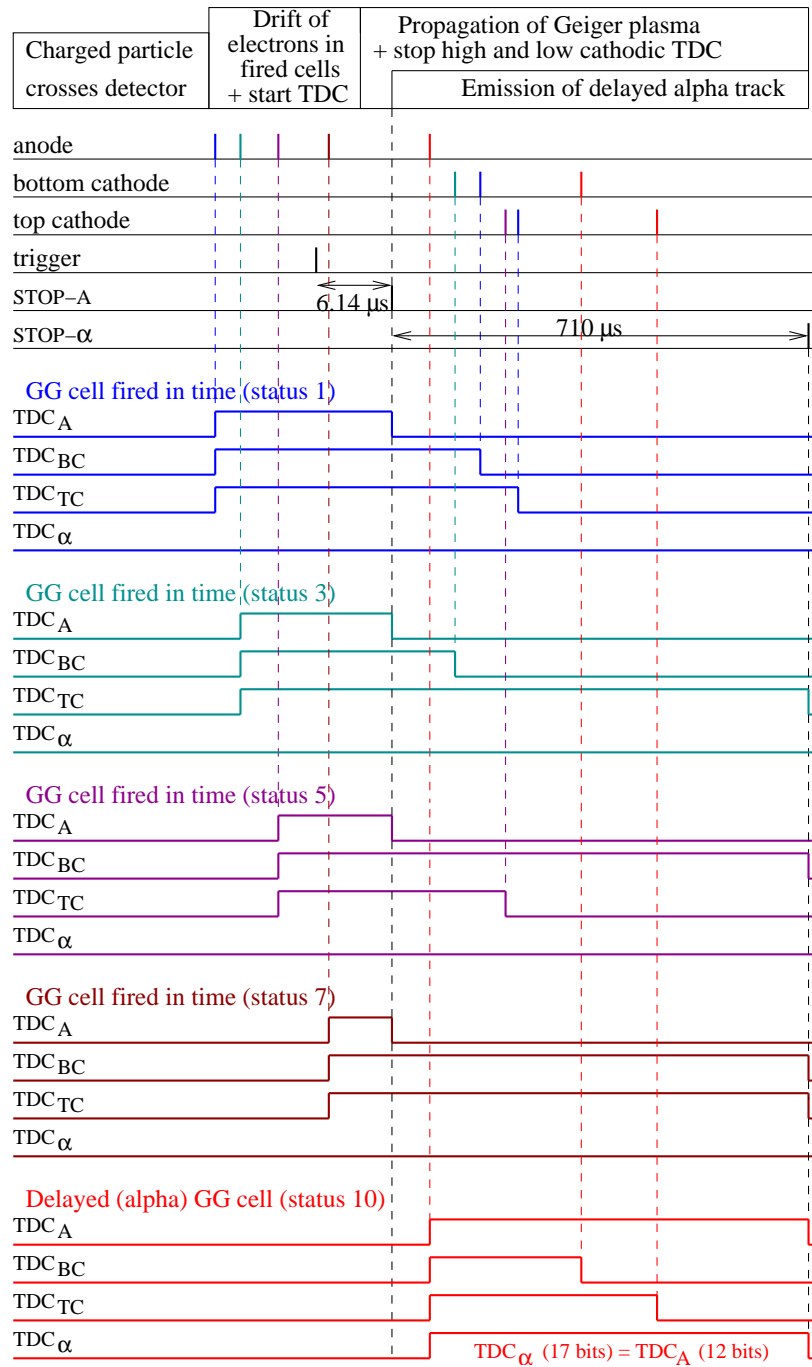


Figure 4.10: An overview of different TDC times associated with the wire chamber acquisition electronics.

1. collected charge in PMTs, equivalent to the energy deposited by a particle in a scintillation counter,
2. time when a counter was fired,
3. signal for the trigger.

In the case of the charge information, the size of one bin is 0.35 pC, as for the time information, the bin size is 50 ps. Because both kinds of data are saved in 12 bits, the time measurement can go as far as 200 ns and the charge measurement as far as 1400 pC which corresponds to energy of 12 MeV.

### 4.7.3 Trigger

The NEMO3 trigger does not need the complete information from the tracking wire chamber and calorimeter for each event candidate. Instead of information from all the hit Geiger cells, it deals with the Geiger cell rows in each sector (there are 360 such rows in the whole detector), and it is limited to the horizontal  $x$ - $y$  plane of the detector completely ignoring the vertical direction, i.e. the  $z$ -coordinate of a Geiger cell hit. Finally, the trigger uses information about the scintillator walls (2 walls  $\times$  20 sectors = 40 walls) involved in an event and the total multiplicity of involved scintillator/PMT counters instead of the information from each fired scintillator. Nevertheless, the trigger has to select a good physical event among  $2^{360+40}$  possibilities. The strategy is to process first a rough track recognition, based mainly on the information from Geiger cell rows, and then to refine the selection by searching for a geometric correlation between these Geiger cell rows and the scintillator walls involved in the event candidate [141].

The trigger system is designed with three levels T1, T2, and T3. The first one (T1) is based only on the PMT multiplicity. The second level (T2) consists of the track recognition in the tracking wire chamber and is performed on a per half-sector basis. However, it is quite probable that an electron crosses more than one half-sector, thus, in the second step, the system looks for tracks going through two adjacent half-sectors. At the end, the third level (T3) consists of the check for a possible coincidence between pre-tracks from the T2 level and hit scintillator walls.

### 4.7.4 Data acquisition system and detector monitoring

The control and readout of the calorimeter and tracking detector crates are provided via the inter-crate VICbus by a CES RIO 8062 computer. The data acquisition system is based on Cascade, a toolkit under Lynx OS which was developed at CERN for the construction of real time data acquisition systems [142]. It uses two boards, one for the calorimeter data processing (Corbo PMT) and the other for the tracking detector data processing (Corbo GG). If the trigger criteria are satisfied, then both these processors record into their registers the calorimeter and tracking detector data. After that, the trigger system synchronises both parts and gets ready for the next event acquisition. Afterwards the data from the two Corbo processors are sent to the Event-builder board and saved in an  $n$ -tuple file. Because the two Corbo processors are independent one of the other, the acquisition system allows one to run the data acquisition only with the calorimeter without the tracking detector and *vice versa*. The data acquisition rate can vary from a few Hz for normal  $\beta\beta$  decay runs to several kHz for calibration runs with radioactive sources introduced inside the detector.

The detector monitoring is provided by two PCs installed in the LSM laboratory. Their role is to read different data and parameters and allow the operators to check, via the graphic

LabView interface, the status and values of electric boxes, crates, high voltage boards for both the calorimeter and the wire chamber; gas pressure and temperature from the detector gas supplying system (gasworks); voltage and current supplying the magnetic coil and so on. Another very important feature of this survey system is that the graphic interface allows one to turn the calorimeter and tracking Geiger counters either on or off, as well as to change their high voltage values.

Both the data acquisition and detector monitoring can be performed, of course, from local (inside the LSM laboratory) or remote computers.

## 4.8 Backgrounds in NEMO3

Backgrounds to the  $0\nu\beta\beta$  signal in the NEMO3 experiment, which are expected to occur in the 2.8 to 3.2 MeV window of interest for the two-electron energy sum spectrum, have three main origins:

1. the natural radioactivity of materials used for the detector construction and radioactive impurities in source foils, particularly the contaminations in  $^{214}\text{Bi}$  and  $^{208}\text{Tl}$ ,
2. the interaction of external photons with source foils,
3. the tail of the  $2\nu\beta\beta$  decay distribution.

We will classify backgrounds into two categories according to the background origin: whether it comes from the source foils or from the outside. The first type of background, when photons, electrons, positrons, or  $\alpha$ -particles come from decays inside the foils, will be called **internal background**. The second type, referred as **external background**, giving electrons and photons which interact with foils is due to the natural radioactivity of the detector components and of the LSM laboratory, where NEMO3 is installed. In this category we also find  $\alpha$ -particles from decay of radon and thoron which could be present in the gas of the tracking volume.

During the whole construction of the NEMO3 experiment a great effort has been made to minimise internal and external backgrounds by the purification of enriched isotope samples and by careful selection of materials for all the detector components.

### 4.8.1 Internal background

#### Intrinsic impurities in the source foils

Although the isotopes studied in the NEMO3 experiment have high  $Q$ -values for double beta decay, there are two isotopes from the uranium and thorium decay chains that must be particularly taken into account. These isotopes are  $^{214}\text{Bi}$  with  $Q_\beta = 3.27$  MeV and  $^{208}\text{Tl}$  with  $Q_\beta = 4.99$  MeV which both represent very dangerous backgrounds for the  $0\nu\beta\beta$  signal in the 3 MeV region. Simplified decay schemes of these two isotopes which only show principal transitions are represented in Figs. 4.11 and 4.12. Tabs. 4.7 and 4.8 list the main  $\gamma$ -rays, for  $^{208}\text{Tl}$  and  $^{214}\text{Bi}$  respectively, whose intensity per decay is greater than 2%. Similar lists for the main  $\beta^-$  transitions are given in Tabs. 4.9 and 4.10. Finally, the intensities of  $\alpha$ -transitions in  $^{214}\text{Bi}$  are summarised in Tab. 4.11.

Despite the fact that the source purification procedure is very effective and despite the great care taken to achieve ultra-low activity during the fabrication and mounting of source foils, traces of natural radioactivity are still present. Such impurities can produce two-electron events which

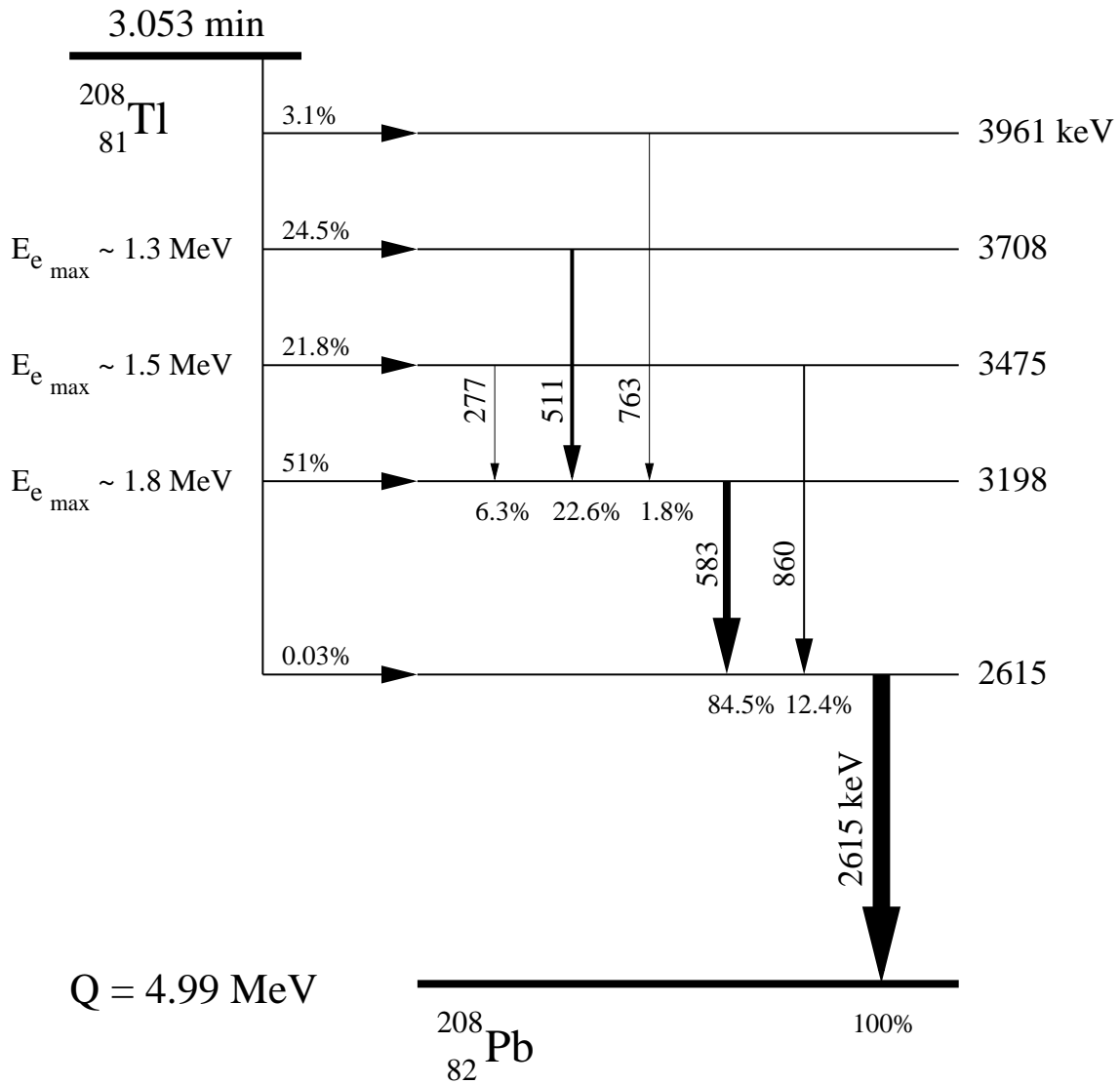


Figure 4.11: A simplified decay scheme of  $^{208}\text{Tl}$  showing only the principal  $\gamma$  and  $\beta^-$  transitions with intensities per decay greater than 2%.

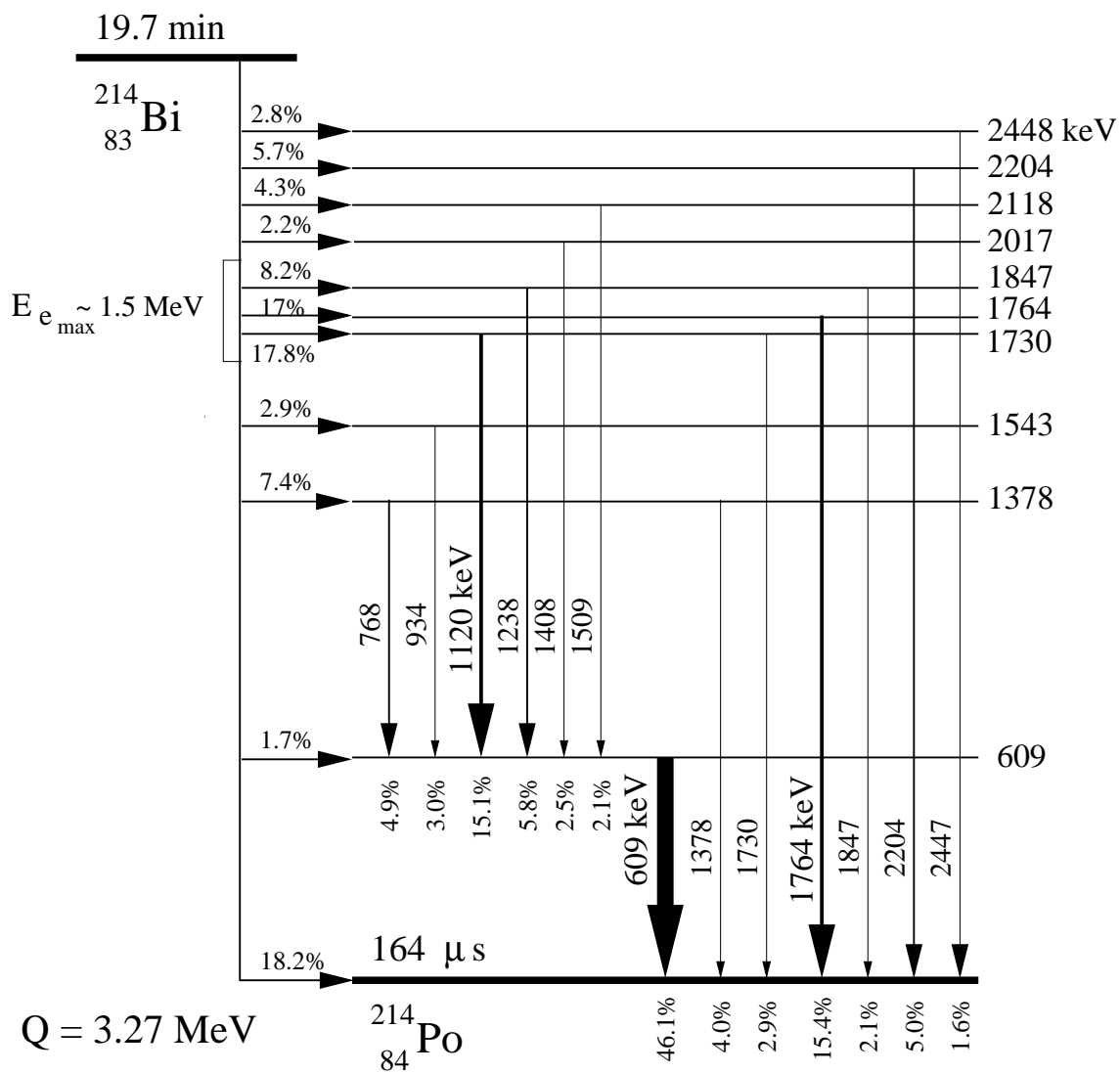


Figure 4.12: A simplified decay scheme of  $^{214}\text{Bi}$  showing only the principal  $\gamma$  and  $\beta^-$  transitions with intensities per decay greater than 2%.

Energy $E_\gamma$ (keV)	Level in $^{208}\text{Pb}$ (keV)	Intensity $I_\gamma$ (%)
277.351(10)	3475.113(14)	6.31(9)
510.77(10)	3708.44(7)	22.6(3)
583.191(2)	3197.743(14)	84.5(7)
763.13(8)	3960.96(7)	1.81(5)
860.564(5)	3475.113(14)	12.42(10)
2614.533(13)	2614.551(13)	99

Table 4.7: A summary of  $\gamma$ -rays from decay of  $^{208}\text{Tl}$  sorted by their energy according to Ref. [131] where only transitions with intensity per decay higher than 1% are listed here.

imitate double beta decay. In particular,  $\beta$ -decaying nuclei can generate a second electron by internal conversion from the excited daughter nucleus or by the Möller effect. Fig. 4.13 illustrates the three main ways that two-electron events can be generated inside the source foils. The three modes are the following:

- a) Internal conversion. A nucleus emits a  $\beta$ -particle and its daughter nucleus gets into the excited state. The excitation energy is then transferred to an orbital electron which is subsequently ejected from the nucleus. This is the most common process of the two-electron event production.
- b) Möller scattering. An emitted  $\beta$ -particle scatters in the source foil and ejects another, second electron.
- c) Compton effect. An electron from beta decay is followed by an de-excitation photon. This photon undergoes the Compton effect in the foil and generates the second electron.

Unfortunately, these internal background events cannot be rejected during data analysis by any time-of-flight criteria and can be eliminated only partially with energy cuts. That is the reason why so much attention has to be focused on the radiopurity of the sources and of the mylar foil in the case of composite foils. Thorough measurements of the powder samples, metallic source foils, binding paste, and mylar foils used as support for composite sources have been done with HPGe detectors in the LSM laboratory.

### **$2\nu\beta\beta$ decay as background of the $0\nu\beta\beta$ signal**

The two-electron energy-sum ( $E_{ee}$ ) spectrum of the  $2\nu\beta\beta$  decay stretches as far as the  $Q_{\beta\beta}$  value where the neutrinoless double beta decay signal is expected. That means that events from the  $2\nu\beta\beta$  decay will appear also in the 2.8 to 3.2 MeV energy window of interest. Obviously, the higher the half-life for  $2\nu\beta\beta$  decay of an isotope, the smaller its contribution to the background of the  $0\nu\beta\beta$  decay. Unlike the isotopic contamination and the external background, the contribution from the  $2\nu\beta\beta$  decay cannot be completely avoided. Therefore, a good knowledge of the  $2\nu\beta\beta$  decay half-life and of the  $E_{ee}$  spectrum shape are very important for the study of neutrinoless double beta decay as they allow us to predict the expected number of  $2\nu\beta\beta$  events in the energy window of interest.

Energy $E_\gamma$ (keV)	Level in $^{214}\text{Po}$ (keV)	Intensity $I_\gamma$ (%)
609.312(7)	609.316(7)	46.1(5)
665.453(22)	1274.761(22)	1.46(3)
768.356(10)	1377.675(12)	4.94(6)
806.174(18)	1415.489(19)	1.22(2)
934.061(12)	1543.375(14)	3.03(4)
1120.287(10)	1729.611(13)	15.1(2)
1155.19(2)	1764.498(14)	1.63(2)
1238.110(12)	1847.431(14)	5.79(8)
1280.96(2)	1890.287(21)	1.43(2)
1377.669(12)	1377.675(12)	4.00(6)
1401.50(4)	2010.81(4)	1.27(2)
1407.98(4)	2017.30(5)	2.15(5)
1509.228(15)	2118.552(17)	2.11(4)
1661.28(6)	1661.28(3)	1.15(3)
1729.595(15)	1729.611(13)	2.92(4)
1764.494(14)	1764.498(14)	15.4(2)
1847.420(25)	1847.431(14)	2.11(3)
2118.55(3)	2118.552(17)	1.14(3)
2204.21(4)	2204.13(9)	5.08(4)
2447.86(10)	2447.70(6)	1.57(2)

Table 4.8: A summary of  $\gamma$ -rays from decay of  $^{214}\text{Bi}$  sorted by their energy [131] where only transitions with intensity per decay higher than 1% are listed.

Using the half-life values for the  $2\nu\beta\beta$  decay of  $^{100}\text{Mo}$  [110] and of  $^{82}\text{Se}$  [112] determined with NEMO2, i.e.

$$T_{1/2}^{2\nu\beta\beta}(^{100}\text{Mo}) = 0.95 \pm 0.04(\text{stat.}) \pm 0.09(\text{syst.}) \times 10^{19} \text{ y}$$

$$T_{1/2}^{2\nu\beta\beta}(^{82}\text{Se}) = 0.83 \pm 0.10(\text{stat.}) \pm 0.07(\text{syst.}) \times 10^{20} \text{ y},$$

one can expect 1.1 events in the 2.8 to 3.2 MeV energy window from the  $2\nu\beta\beta$  decay of  $^{100}\text{Mo}$  (7 kg) and 0.1 events from  $2\nu\beta\beta$  decay of  $^{82}\text{Se}$  (1 kg) per year [133, 143].

#### 4.8.2 External background

The external background in NEMO3 has the following origins:

1. the natural radioactivity of the detector components,
2. radon ( $^{222}\text{Rn}$ ) and thoron ( $^{220}\text{Rn}$ ),
3. neutrons from the laboratory,
4. photons from the laboratory and the cosmic rays.

Energy $E_\beta$ (keV)	Level in $^{208}\text{Pb}$ (keV)	Intensity $I_\beta$ (%)
820.59	4180.41(17)	0.227(12)
875.69	4125.31(17)	0.168(11)
1040.04	3960.96(7)	3.09(17)
1081.2	3919.80(10)	0.63(6)
1292.56	3708.44(7)	24.5(6)
1525.89	3475.113(14)	21.8(4)
1803.26	3197.743(14)	48.7(12)

Table 4.9: A list of electrons from decay of  $^{208}\text{Tl}$  sorted by their energy according to Ref. [131]. Only  $\beta^-$  transitions with intensity per decay higher than 0.1% are given.

As regards the external background events that mimic  $\beta\beta$  decay, which are characterised by two electron tracks with a common vertex in the source foils<sup>2</sup>, we can distinguish two different cases. The first is the case of an electron generated in the plastic scintillator which crosses the wire chamber, interacts with the source foils and is then detected by another scintillation counter. If the first part of the track (scintillator  $\rightarrow$  foils) is rather straight, its curvature<sup>3</sup> can be evaluated by the track reconstruction program with the opposite sign to that which it had in reality. Then such events would be evaluated as two-electron events and could be confused with the  $\beta\beta$  decay. Fortunately, they can be rejected thanks to the time-of-flight (TOF) analysis which is explained in Sec. 5.8.1.

The second case corresponds to the situation where an incoming photon interacting with the source foils generates two electrons by different methods; these leave the source foil, cross the wire chamber and finally are detected by the scintillator counters. From the point of view of the TOF analysis the two electrons are, of course, in time and so such events may easily be confused with  $\beta\beta$  decay. Fig. 4.14 shows the five main ways in which such two-electron events can be produced. The five ways are the following:

- a) pair creation after the interaction of a high energy photon with the foil ( $E_\gamma > 1.022$  MeV). Without a good charge analysis the positron may be confused with an electron and such event would be considered as a two electron event.
- b) Compton effect followed by Möller scattering of an electron generated in the foil,
- c) double Compton effect in the foil,
- d) photoelectric effect followed by Möller scattering,
- e) Compton effect followed by the photoelectric effect.

### Radioactive isotopes in detector materials

Traces of natural radioactivity in the detector components are a source of the external background that cannot be avoided. Like the internal background, the most dangerous isotopes for

<sup>2</sup>See also Sec. 5.3.1

<sup>3</sup>In the analysis program the curvature of a track is always determined with reference to the source foils.

Energy $E_\beta$ (keV)	Level in $^{214}\text{Po}$ (keV)	Intensity $I_\beta$ (%)
789.54	2482.46(4)	1.33(7)
824.3	2447.70(6)	2.81(11)
1067.87	2204.13(9)	5.72(7)
1153.45	2118.552(17)	4.26(8)
1254.7	2017.30(5)	2.20(5)
1261.19	2010.81(4)	1.37(3)
1277.37	1994.63(3)	1.14(4)
1381.71	1890.287(21)	1.59(5)
1424.57	1847.431(14)	8.18(9)
1507.5	1764.498(14)	17.02(22)
1542.39	1729.611(13)	17.8(3)
1728.63	1543.375(14)	2.95(8)
1894.32	1377.669(12)	7.43(11)
2662.68	609.312(7)	1.7(6)
3272	0	18.2(6)

Table 4.10: A list of electrons from decay of  $^{214}\text{Bi}$  sorted by their energy according to Ref. [131]. Only  $\beta^-$  transitions with intensity per decay higher than 1% are given.

a  $\beta\beta$  decay experiment are  $^{214}\text{Bi}$  and  $^{208}\text{Tl}$ . One of the main goals during the research and development phase of the experiment was the choice of appropriate low activity materials for all the detector components. A great number of the thorough measurements with HPGe detectors has been performed for this purpose in the LSM laboratory. Their main results are summarised in Sec. 4.9.

### Radon and thoron

Radon is a rare radioactive gas which is created by the decay of uranium and thorium (see Fig. 4.15) present in rocks. As a gas, it can easily penetrate through rock and concrete coated walls of the laboratory and get into the air. The vigorous air ventilation system in the laboratory reduces radon levels to 10 – 20 Bq/m<sup>3</sup>. The radon gas can enter the inside of the detector by diffusion in places where the airtightness of the detector is not perfect. Even if it decays before intruding into the detector, a danger still exists because of its daughter isotopes. They can be transported by dust and deposited on the detector. Radon can also enter the detector through the gas supply system (gasworks). This can happen if bottles of helium gas already contain some quantity of radon, or if the pipes and joints of the gas system are not airtight enough.

Radon has three isotopes corresponding to the three decay chains: radon  $^{222}\text{Rn}$ , thoron  $^{220}\text{Rn}$ , and actinon  $^{219}\text{Rn}$ . Actinon, from the uranium  $^{235}\text{U}$  decay chain, is not dangerous for the experiment because its daughters do not have enough available energy to generate background events that could be confused with  $\beta\beta$  decay. The main danger then comes from radon ( $T_{1/2} = 3.8$  d) and thoron ( $T_{1/2} = 54.5$  s) which decay respectively to  $^{214}\text{Bi}$  and  $^{208}\text{Tl}$  as it is illustrated in Fig. 4.15.

Energy $E_\alpha$ (keV)	Intensity $I_\alpha$ (%)
4941	0.25(5)
5023	0.21(4)
5184	0.61(6)
5273(9)	5.8(1)
5452(3)	53.9(3)
5516(3)	39.2(3)

Table 4.11: A list of  $\alpha$ -particles and their relative intensities from direct decay of  $^{214}\text{Bi}$  according to Ref. [131].

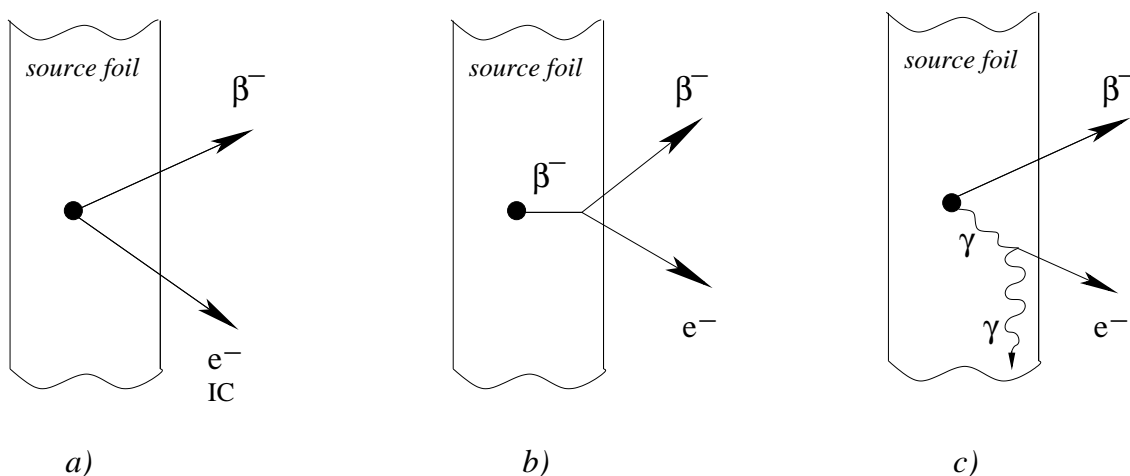


Figure 4.13: The main ways of creation of two-electron events inside a source foil imitating double beta decay events: a) beta decay accompanied by an internal conversion electron, b) beta decay followed by Möller scattering, c) beta decay accompanied by a Compton electron.

## Neutrons

Generally, neutrons are produced in the matter (rocks, detector components etc.) by spontaneous fission or the  $(\alpha, n)$  reaction of radioactive isotopes of the uranium and thorium decay chains. That means that neutrons, which are always present inside the laboratory cave where the detector is located, are also a source of background that we must take into account, especially for the search of the  $0\nu\beta\beta$  signal. Thermalised neutrons can be captured by nuclei in the detector frame, which is mainly made of steel and copper. The  $(n, \alpha)$  and  $(n, p)$  reactions can only produce  $\gamma$ -rays with energy lower than 3 MeV and so do not represent a big danger for the measurement of the neutrinoless double beta decay in the 3 MeV region. In contrast, the  $(n, \gamma)$  capture by iron or copper nuclei can produce photons with energy of the order of 3 MeV and even higher (up to 8 MeV). In consequence, it is of interest to use efficient neutron shielding (see Sec. 4.6.2) in order to eliminate this background contribution. The usual way to suppress neutrons consists of their moderation followed by their capture.

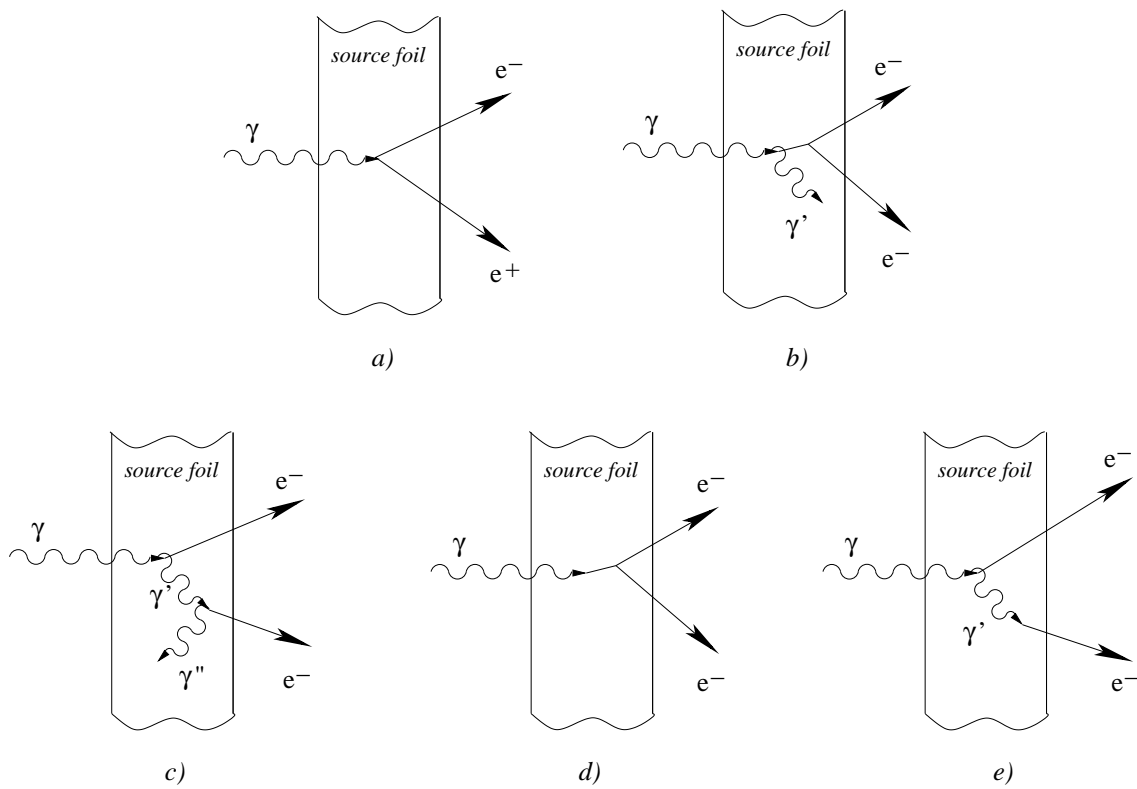


Figure 4.14: The main methods of creation of two-electron events due to the interaction of photons coming from outside the source foils: a) pair creation, b) Compton effect followed by Möller scattering, c) double Compton effect, d) photoelectric effect followed by Möller scattering, e) Compton effect followed by the photoelectric effect.

	$^{238}\text{U}$						$^{232}\text{Th}$						
U	U-238 4.47 $10^9$ yr		U-234 2.45 $10^5$ yr										
Pa	↓	↗ Pa-234 1.17 m	↓										
Th	Th-234 24.1 d		Th-230 75400 yr		α ↓				Th-232 14 $10^9$ yr		Th-228 1.913 yr		
Ac			↓						↓	↗ Ac-228 6.15 h	↓		
Ra			Ra-226 1600 yr						Ra-228 5.75 yr		Ra-224 3.66 d		
Fr			↓								↓		
Rn			Rn-222 3.824 d								Rn-220 55.6 s		
At			↓								↓		
Po			Po-218 3.10 m		Po-214 164 μs		Po-210 138.4 d				Po-216 145 ms		Po-212 300 ns
Bi			↓	↗ Bi-214 19.9 m	↓	Bi-210 5 d					↓	↗ Bi-212 60.5 m	↓
Pb			Pb-214 26.8 m	↘ 0.021%	Pb-210 22.3 yr		Pb-206 stable				Pb-212 10.6 h	↘ 36%	Pb-208 stable
Tl				↗ Tl-210 1.3 m		Tl-206 4.19 m						↗ Tl-208 3.1 m	

Figure 4.15: The  $^{238}\text{U}$  and  $^{232}\text{Th}$  decay chains of natural radioactivity. Note the decays of radon  $^{222}\text{Rn}$  to  $^{214}\text{Bi}$  and of thoron  $^{220}\text{Rn}$  to  $^{208}\text{Tl}$  (shaded cells).

### Photons from the laboratory and cosmic rays

Depending on the energy range, the  $\gamma$ -rays come from the natural radioactivity in the surrounding rock, from radiative neutron capture, and from muon bremsstrahlung. The  $\gamma$ -ray flux in the LSM laboratory has been studied with a low-background NaI detector [144]. In the region below 4 MeV, the energy spectrum obtained is dominated by  $\gamma$ -rays from natural radioactivity in the surrounding material and rocks. The natural radioactivity mostly contributes up to 2.6 MeV which corresponds to one of the  $\gamma$ -transitions in the  $^{208}\text{Tl}$  decay. In the 4 to 6 MeV energy region the measured spectrum was dominated by the residual internal activities from the uranium and thorium decay series which are present inside the NaI crystal. No contribution from the external natural radioactivity can be found above 6 MeV. Between 6 and 10 MeV, the  $\gamma$ -ray flux is strongly correlated to the neutron flux and is due to the radiative capture of neutrons in Cu, Fe, Pb etc. Above 10 MeV, the counting rate drops drastically and is due to the bremsstrahlung from the remaining but very small muon flux inside the laboratory. The muon flux in the LSM laboratory of  $4.9 \times 10^{-5} \text{ s}^{-1}\text{m}^{-2}$  (4.2 per  $\text{m}^2$  and per day) was previously deduced from the proton decay experiment [145]. This flux is lower by a factor of  $2 \times 10^6$  than the flux at the sea level [146].

## 4.9 Radiopurity of the detector

In  $\beta\beta$  decay experiments the activity of all the materials and components used for detector construction has to be as low as possible in order to significantly reduce the level of intrinsic background. Thus activity measurements, based on  $\gamma$ -spectroscopy, are essential for a  $\beta\beta$  decay experiment, especially during the research and development phase when the best construction materials from the point of view of radioactivity are to be selected.

As regards the NEMO3 experiment, activity measurements of a great number of samples (construction materials, electronics components, cables, glues and so on) have been carried out over a few years in the LSM laboratory. They were performed with low background HPGe detectors. One of them is located in the CENBG<sup>4</sup> (Ge crystal of  $100 \text{ cm}^3$ ), the others (one of  $100 \text{ cm}^3$  and two of  $400 \text{ cm}^3$ ) are in the LSM laboratory in order to avoid the contribution of cosmic rays.

The abundance of radioactive isotopes in a sample is determined from the strength of  $\gamma$ -lines in the spectrum obtained with a  $\gamma$ -ray spectrometer. For the source foils, activities after the purification process (see Sec. 4.5.2) are very low; only the upper limits can be determined. The activity limit  $A_{lim}$  at 90% C.L. for each  $\gamma$ -line is given by:

$$A_{lim} = 1.6 \sqrt{\frac{N_{bgd}}{T}} \frac{1}{\varepsilon RM}, \quad (4.1)$$

where  $N_{bgd}$  is the number of registered background events in the energy window of interest,  $T$  is the time of measurement,  $\varepsilon$  is the detection efficiency,  $R$  is the branching ratio for a given  $\gamma$ -line, and  $M$  is the sample mass. The radiopurity of the source foils has been discussed in Sec. 4.5.3 and the summary of the activity measurements of the foils is given in Tab. 4.6. The most important activities in NEMO3 are showed in Tab. 4.12. More complete results of the activity measurements can be found in Refs. [133, 147].

---

<sup>4</sup>Centre d'Études Nucléaires Bordeaux – Gradignan

Main parts of NEMO3	Total weight (kg)	Total activities (Bq)			
		$^{40}\text{K}$	$^{214}\text{Bi}$	$^{208}\text{Tl}$	$^{60}\text{Co}$
PMTs	600	830	300	18	—
Scintillators	5000	< 100	< 0.7	< 0.3	$1.8 \pm 0.4$
Copper frame	25000	< 125	< 25	< 10	< 6
Steel frame	10000	< 50	< 6	< 8	$17 \pm 4$
$\mu$ -metal	2000	< 17	< 2	$2.0 \pm 0.7$	$4.3 \pm 0.7$
Wires	1.7	$< 8 \times 10^{-3}$	$< 10^{-3}$	$< 6 \times 10^{-4}$	$10^{-2}$
Iron shield	180000	< 3000	< 300	< 300	$300 \pm 100$

Table 4.12: Main activities in NEMO3 measured with HPGe detectors.

# Chapter 5

## Monte-Carlo studies

### 5.1 Introduction

In this chapter, studies of signal and different kinds of background events generated with a Monte-Carlo simulation program, undertaken with the goal of defining optimal selection criteria are described. These criteria should ensure an unambiguous selection of the signal from the  $2\nu\beta\beta$  decay of  $^{100}\text{Mo}$  to the excited  $0_1^+$  state of  $^{100}\text{Ru}$  and, at the same time, an efficient suppression of relevant backgrounds.

First of all, a brief description of the simulation tools, triggers applied in simulations of events, and types of simulated processes followed by definitions of signatures for different particles are given. The next part deals with the step-by-step construction of conditions for the selection of the  $2\nu\beta\beta$  decay of  $^{100}\text{Mo}$  to the excited  $0_1^+$  state which would simultaneously efficiently discriminate against all the relevant internal and external backgrounds. This part is followed by a summary of the final set of selection conditions. Then, effects of the main stages of the selection on both the signal and different kinds of background events are discussed. The chapter closes with an estimation of individual contributions from each of the processes studied.

### 5.2 Monte-Carlo simulations

#### 5.2.1 Simulation program

All the Monte-Carlo events were generated with a special NEMO3 simulation tool called **nemos** [135] developed in IReS Strasbourg which is, in reality, a set of simulation, geometry describing, and particle tracking codes. This set of programs can be used on different computer platforms: PCs or Workstations which work either under the Linux, or Unix (e.g. OSF1, AIX, HP-UX) operating systems.

The **nemos** package requires the CERN libraries **cernlib** [148] including in particular the **GEANT 3.21** [149], **PAW** [150], and **PATCHY** [151] programs. The package also include files necessary for the NEMO3 simulation and tracking programs which provide the NEMO3 specific modifications to GEANT. These files describe to GEANT the full detector geometry (with a description of 20 sectors, 40 materials and 16 tracking media) and allow the correct compilation of the simulation and tracking codes. In summary, the NEMO3 simulation program consists of:

- the NEMO3 geometry description,
- the generation of the initial kinematics of events,

- the transport of generated particles in the detector,
- the recording of fired counters (Geiger cells and scintillators) and of their response to the generated particles,
- the graphical visualisation of events in the detector.

The event generator of the simulation program is very versatile. On the one hand, it is capable of the generation of various double beta decay modes (e.g. neutrinoless, two-neutrino, or with emission of Majorons) to the ground or different excited states for numerous nuclei, and on the other hand, it allows the simulation of a large variety of possible backgrounds generated anywhere inside or outside the experimental setup. The simulation program can reproduce either the natural radioactivity from different isotopes, or various independent particles (e.g. neutrons, photons, muon, protons, electron etc.) with user defined energy ranges, emission angles and so on, as well as different physical processes (e.g. Möller scattering of electrons, Compton scattering of photons etc.).

### 5.2.2 Trigger for the Monte-Carlo simulations

The simulation program also generates events that are useless for further data processing: for instance events without any hit counters or tracks, or events with only low deposited energy. These events would be rejected later by event selection criteria. In order not to save such idle data in the output file, one would like to use an appropriate trigger during the generation of events.

The trigger that is usually applied during simulations of various modes of  $\beta\beta$  decays and of corresponding backgrounds is defined in the following way:

- at least four Geiger cell layers closest to the source foils have to be hit,
- at least one scintillator counter has to be fired,
- if only one scintillator is fired, then the deposited energy has to be greater than 1300 keV,
- if more than one scintillator counter is fired, then the deposited energy in one of them has to be greater than 200 keV.

This trigger is not universal and can be modified by a user for Monte-Carlo simulations of other kinds of events for which the trigger described above will not be suited. The simulation of photons generated in the source foils for the study of their response inside the detector, as well as the simulation of  $^{214}\text{Bi}$  inside the gas of the wire chamber for the study of the radon contribution can be given as examples. In both these cases, an event generated by Monte-Carlo is saved if at least one scintillator counter is fired.

### 5.2.3 Types of simulated events

In order to study the  $2\nu\beta\beta$  decay of  $^{100}\text{Mo}$  to the excited  $0_1^+$  state and to define afterward the optimal selection conditions, the aforementioned decay, as well as all the significant backgrounds which have to be taken into account have been simulated. The following types of backgrounds were examined:

- the  $2\nu\beta\beta$  decay of  $^{100}\text{Mo}$  to the ground state,

- the internal background from  $^{208}\text{Tl}$  and  $^{214}\text{Bi}$  due to impurities of the source foils,
- the external background caused by  $^{208}\text{Tl}$  and  $^{214}\text{Bi}$  activity in the PMT glass, which are the dominant contributions to the external background in NEMO3,
- radon contamination of the He gas in the wire chamber.

A list of simulated processes with numbers of generated and triggered events, as well as the rate between recorded and generated events is given in Tab. 5.1.

Isotope	Type of events	Number of gener. events	Number of rec. events	Rate rec./gener.
$^{100}\text{Mo}$	$2\nu\beta\beta$ g.s. $\rightarrow 0_1^+$	$1 \times 10^6$	426 736	0.427
$^{100}\text{Mo}$	$2\nu\beta\beta$ g.s. $\rightarrow$ g.s.	$2 \times 10^6$	495 077	0.248
$^{208}\text{Tl}$	internal bgd (foils)	$0.5 \times 10^6$	229 570	0.459
$^{214}\text{Bi}$	internal bgd (foils)	$0.5 \times 10^6$	165 034	0.330
$^{208}\text{Tl}$	external bgd (PMTs)	$100 \times 10^6$	167 149	$1.671 \times 10^{-3}$
$^{214}\text{Bi}$	external bgd (PMTs)	$400 \times 10^6$	150 903	$0.377 \times 10^{-3}$
$^{214}\text{Bi}$	$^{222}\text{Rn}$ inside He gas	$15 \times 10^6$	11 930 827	0.795

Table 5.1: Types of simulated processes together with numbers of generated and recorded events after the Monte-Carlo trigger.

### 5.3 Definition of particles for Monte-Carlo events

For the study of simulated and real events, first of all one has to define in an unambiguous way the signatures of different particles. As both Monte-Carlo and real experimental data have exactly the same structure for the n-tuple data, the signatures of particles are common for both of them. The definitions of an electron (a positron), of a photon, and of an  $\alpha$ -particle, which all can be detected by the NEMO3 detector, are given in the following sections.

#### 5.3.1 Electrons and positrons

In the most general way, an **electron** (a **positron**) emitted from source foils is defined as a track reconstructed from fired Geiger cells which starts from the source foils, passes through the wire chamber and has negative (positive) curvature. In the NEMO3 data analysis, the curvature of tracks is always measured with reference to the source foils. That means that the track of an electron coming from foils is signed with negative curvature, while the track of an electron travelling in the opposite direction, from scintillators to source foils, is signed with positive curvature. In order to measure the energy of electrons (positrons) and to be able to use time criteria for data analysis, we usually ask that each track has an associated scintillator counter. To be sure that an electron (a positron) was emitted from source foils and thus to avoid case of a positron (an electron) coming from a scintillator towards the foils, one has to check in addition to the track curvature the chronology of the event. For instance, in the case of a two-electron event with a common vertex in foils, this is the time-of-flight test, checking the hypothesis that both electrons were emitted at the same time from the same vertex.

### 5.3.2 Photons

Once electrons and positrons are identified, the fired scintillator counters without any associated track can be therefore considered as  $\gamma$ -scintillators. While processing events, clusterisation of these  $\gamma$ -scintillators is applied because one photon can sometimes trigger two or even three neighbouring scintillators. Then, a real **photon** detected in the calorimeter is represented by a  $\gamma$ -cluster. Nevertheless, this description of a photon is not perfect. Using the current definitions of photons and of electrons (see Sec. 5.3.1), it can still happen that an electron back-scattered on one scintillator is subsequently detected by another one and is then erroneously taken for a photon. However, a back-scattered electron is revealed by the presence of fired Geiger cells in the proximity of the scintillator that the electron interacted with. Another case of a false photon is when an electron strikes the edge or close to the edge of two scintillators and fires both of them. Then one of them would be recognised like an electron (because of a track associated to this counter) while the other one would be confused with a photon. This false photon could also be revealed by the presence of fired Geiger cells, which belong to the track of the electron, close to the (false)  $\gamma$ -scintillator. Moreover, in this case both scintillators will have similar triggering times and the track impact point will be close to the other scintillator. These extra conditions have to be taken into account for the correct definition of a photon.

### 5.3.3 $\alpha$ -particles

In addition to electrons and positrons, the tracking wire chamber of NEMO3 also allows the detection of  $\alpha$ -particles coming, for example, from  $^{222}\text{Rn}$  decay. They are characterised by Geiger cell hits which are delayed in time compared to the cells fired by electrons. Their time is measured by slow TDC modules (see Sec. 4.7.1) and is recorded in the data in the ISLOTDC variable. Nevertheless, in the case of real experimental data a refired Geiger cell is often also evaluated like a delayed Geiger cell. However, its delay time is less than  $20 \mu\text{s}$  for an isolated cell and less than  $40 \mu\text{s}$  when an electron passes close to it. The latter value is then taken as a criterion for distinguishing between refired Geiger cells and cells fired with  $\alpha$ -particles. Although refired Geiger cells appear only in the real experimental data and not in the Monte-Carlo one's, the above mentioned condition on the delay time has to be included in selection criteria when Monte-Carlo events are treated in order to ensure coherence between simulated and real data.

## 5.4 Response of the detector to the de-excitation photons

In the  $2\nu\beta\beta$  decay through the g.s.  $\rightarrow 0_1^+$  transition, one expects to detect the two de-excitation photons. In the case of  $^{100}\text{Mo}$ , their energies are 540 and 590 keV respectively. To study the detector response to these photons generated in the source foils, it was necessary to modify the Monte-Carlo simulation trigger to accept all events where at least one scintillator counter had been fired. From Tab. 5.2, which summarises the results of these simulations, it can be seen that the NEMO3 detection efficiency for photons emitted uniformly from source foils is about 50%.

Considering the NEMO3 calorimeter design, particularly the use of plastic scintillators, we will not obtain sharp  $\gamma$ -lines for these photons but rather Compton-effect-shaped spectra showed in Figs. 5.1 and 5.2. They represent at the same time the deposited energy in the first fired  $\gamma$ -cluster,  $E_\gamma$  (upper spectrum), and the total energy of all the  $\gamma$ -clusters,  $E_{N\gamma}$  (lower spectrum).

However, the two de-excitation photons are often scattered inside the detector which explains the clear difference between the  $E_\gamma$  and  $E_{N\gamma}$  distributions. This is illustrated by Fig. 5.3 and

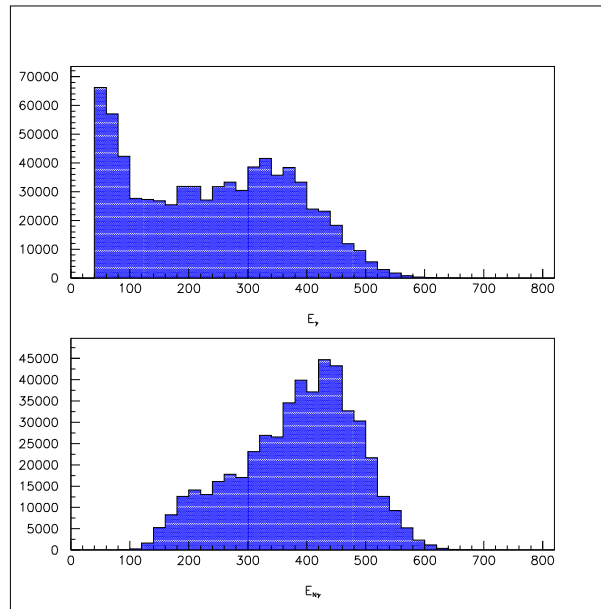


Figure 5.1: Energy spectra  $E_\gamma$  (upper graph) and  $E_{N\gamma}$  (lower graph) for 540 keV photons which were generated by the Monte-Carlo simulation program uniformly in the NEMO3 source foils.

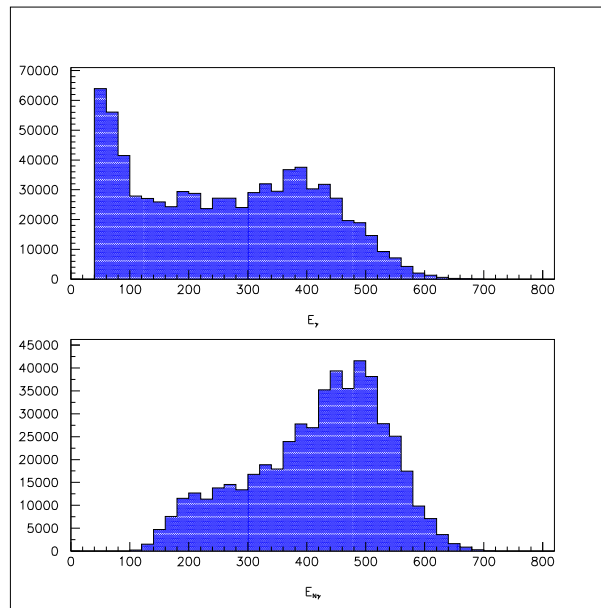


Figure 5.2: Energy spectra  $E_\gamma$  (upper graph) and  $E_{N\gamma}$  (lower graph) for 590 keV photons which were generated by the Monte-Carlo simulation program uniformly in the NEMO3 source foils.

$\gamma$ -ray	Number of gener. events	Number of rec. events	Detection efficiency
590 keV	1 000 000	507 449	50.7%
540 keV	1 000 000	498 205	49.8%

Table 5.2: Monte-Carlo simulations of de-excitation photons in NEMO3: numbers of generated and recorded events and corresponding detection efficiency for photons of 540 and 590 keV.

Tab. 5.3 which show the respective proportions of the number of events with one, two, three, and more fired  $\gamma$ -clusters after the interaction of one photon of 540 or 590 keV in the NEMO3 calorimeter. One can clearly see that in 50% of cases the photon is detected in only one  $\gamma$ -cluster and that in the other 50% of cases the photon is scattered after its first interaction with a plastic scintillator and subsequently registered in another counter.

# $\gamma$ -clusters	1	2	3	$\geq 4$
Proportion (%)	50.3	36.3	11.4	2.0

Table 5.3: Proportions of Monte-Carlo events, obtained from simulations of photons of 540 and 590 keV in source foils, generating 1, 2, 3, or more  $\gamma$ -clusters in the NEMO3 detector.

## 5.5 eeN $\gamma$ channel

As has been mentioned in Sec. 5.4, the de-excitation photons from the  $2\nu\beta\beta$  (g.s.  $\rightarrow 0_1^+$ ) decay of  $^{100}\text{Mo}$  are often scattered in the detector. Considering in addition to this the possibility of bremsstrahlung radiation from the two electrons, it is not rare to observe several  $\gamma$ -clusters for the  $2\nu\beta\beta$  (g.s.  $\rightarrow 0_1^+$ ) transition. This fact leads us to be interested not only in two-electron events with two photons of well defined energy but also in events with only one detected photon (the second one has escaped), as well as in those with three, four or even more  $\gamma$ -clusters (multiscattering of photons). Tab. 5.4 and Fig. 5.4 show the distribution of the number of fired  $\gamma$ -clusters for the  $2\nu\beta\beta$  decay events from the g.s.  $\rightarrow 0_1^+$  transition. Note that in about 10% of cases neither of the two photons is detected which means that events from the excited  $0_1^+$  state contribute also to the two-electron channel of the  $2\nu\beta\beta$  decay to the ground state. Because of the significant difference in the half-lives of these two transitions, this contribution is negligible (approximately 0.04%). In order to study the  $2\nu\beta\beta$  decay to the excited  $0_1^+$  state, we will therefore be interested in the eeN $\gamma$  channel, where  $N$  is the number of detected photons (i.e. the number of  $\gamma$ -clusters) in an event and is then  $N = 1, 2, 3, 4, \dots$ . Some examples of rather complicated tracks of photons in the NEMO3 detector, which often bounce off scintillators, as they were generated by Monte-Carlo simulation program, are illustrated by Figs. 5.5, 5.6, 5.7, and 5.8. All these examples of events are generated by Monte-Carlo simulations of the  $2\nu\beta\beta$  decay of  $^{100}\text{Mo}$  to the excited  $0_1^+$  state of  $^{100}\text{Ru}$ .

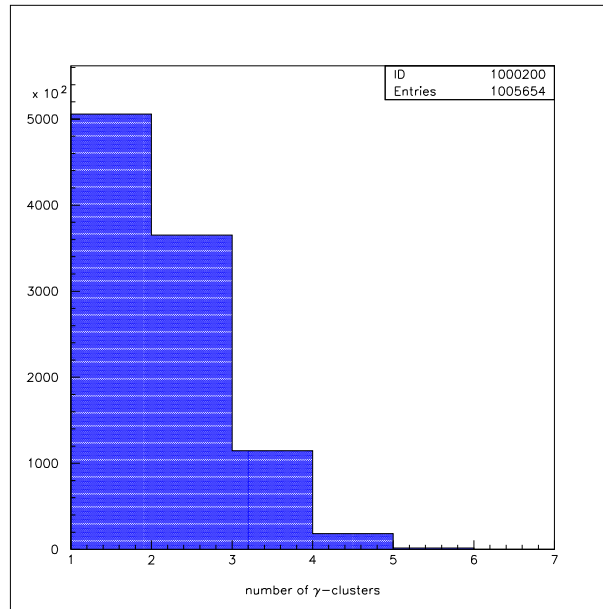


Figure 5.3: Number of fired  $\gamma$ -clusters detected by the NEMO3 calorimeter after interaction of photons of 540 or 590 keV which were generated in source foils.

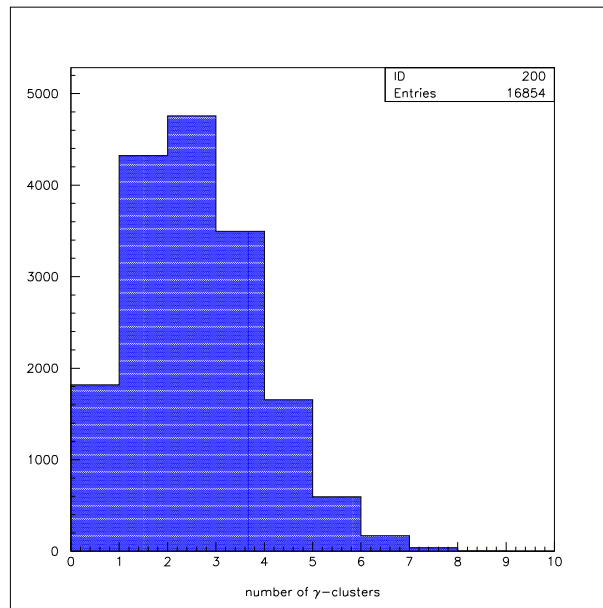


Figure 5.4: Distribution of the number of  $\gamma$ -clusters triggered in the NEMO3 calorimeter for the Monte-Carlo simulation of the  $2\nu\beta\beta$  decay of  $^{100}\text{Mo}$  to the excited  $0_1^+$  state.

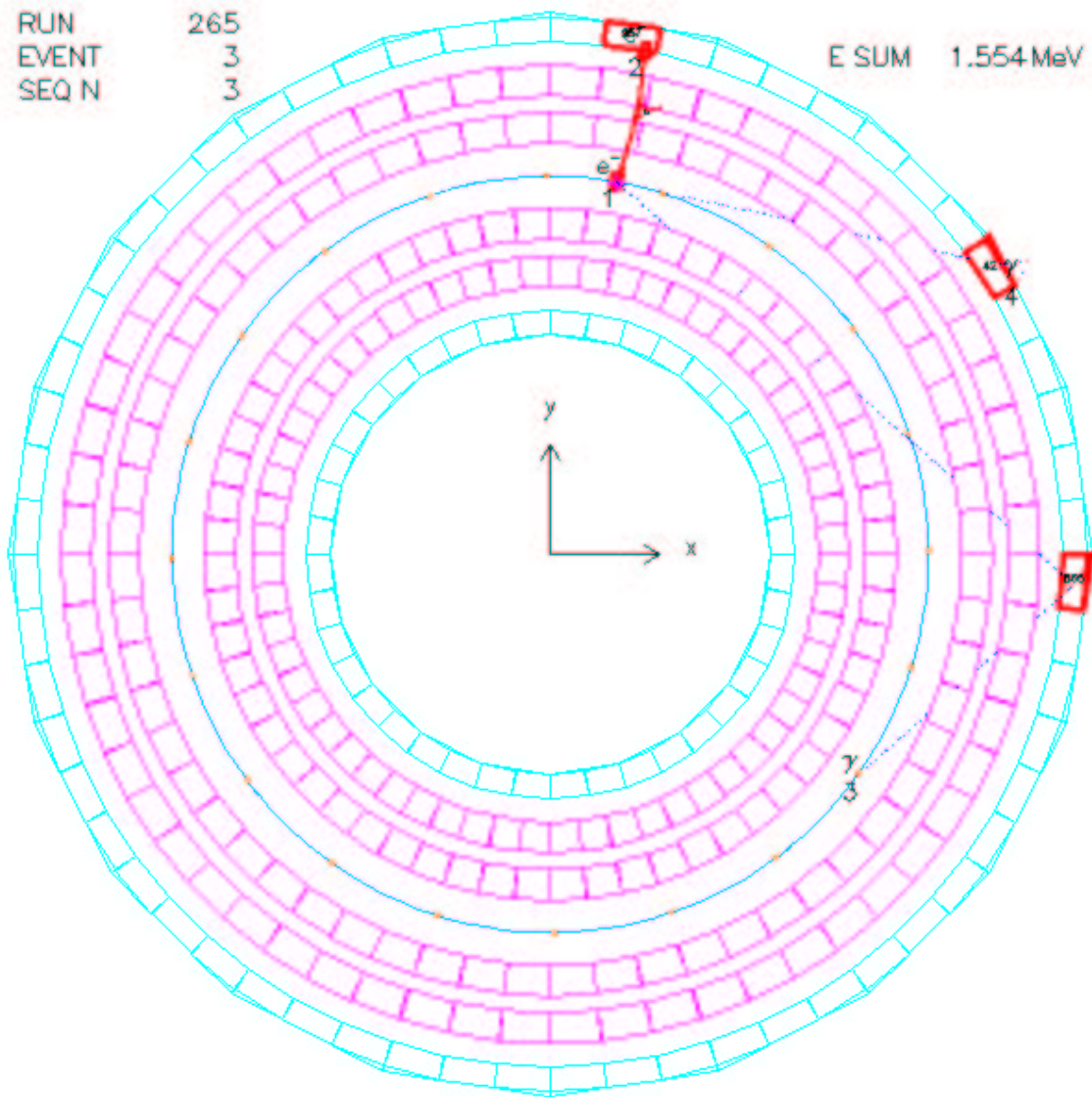


Figure 5.5: An example of simulated  $2\nu\beta\beta$  decay of  $^{100}\text{Mo}$  to excited  $0_1^+$  state. Dotted lines and particle numbers 3 and 4 are used for tracks of photons in the detector while red solid lines describe tracks of generated electrons which are labelled 1 and 2. Light-blue boxes correspond to the internal and external wall scintillators while purple ones correspond to the petal scintillators. Fired scintillators are indicated with thick red boxes. Here one electron (e1) did not leave the source foil, and one of the photons ( $\gamma_3$ ) was scattered on a scintillator, where it deposited a part of its energy, and then went on flying in the detector to finally escape.

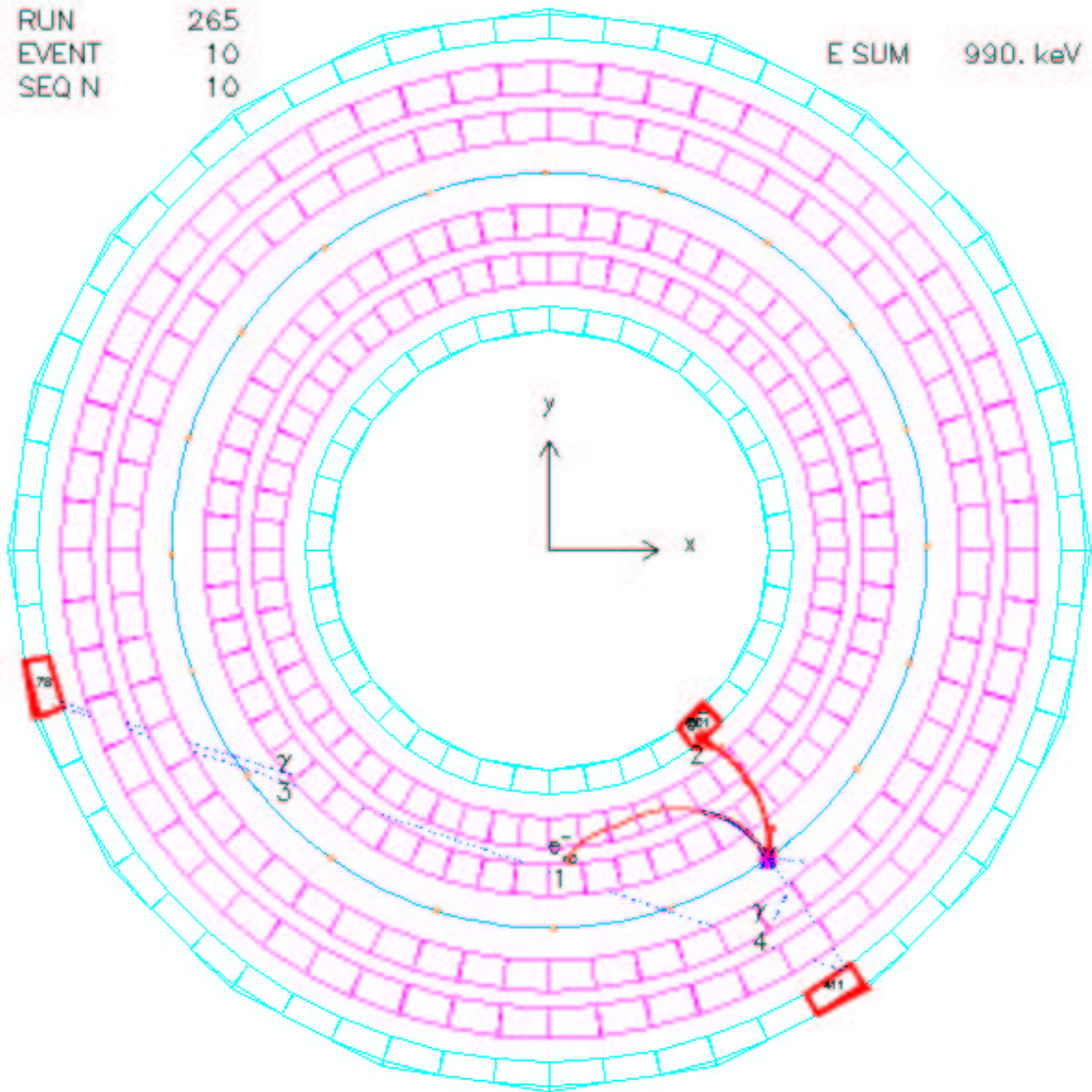


Figure 5.6: Another example of a Monte-Carlo  $2\nu\beta\beta(g.s. \rightarrow 0_1^+)$  event. Note reflections of both photons ( $\gamma_3$  and  $\gamma_4$ ) and their particularly complicated paths.

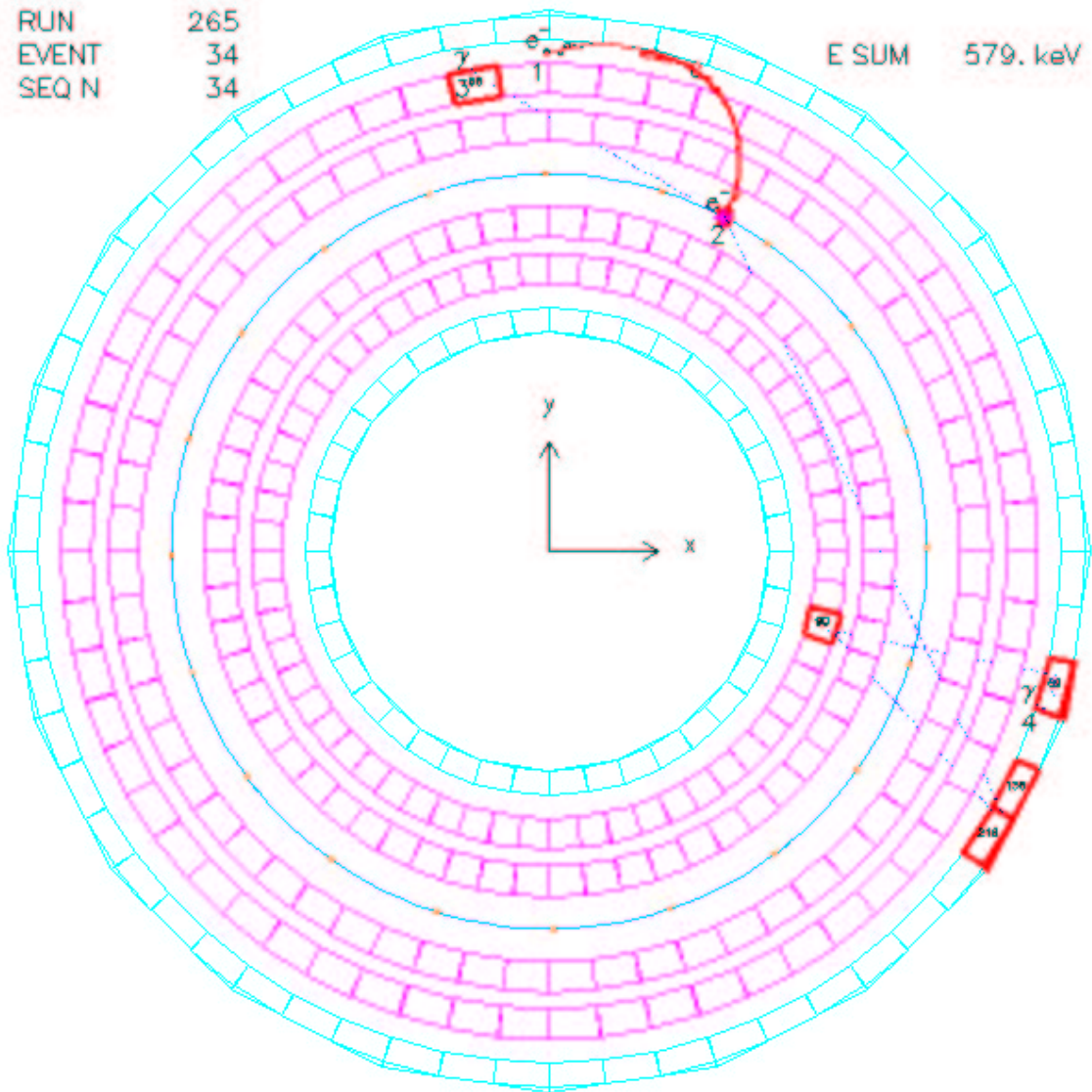


Figure 5.7: One more example of a  $2\nu\beta\beta(g.s. \rightarrow 0_1^+)$  event generated by Monte-Carlo simulation program. Note the especially complicated flight of a photon marked  $\gamma_4$ . Here the second electron (e2) did not leave the source foils.

RUN	265	E SUM	579. keV
EVENT	34		
SEQ N	34		

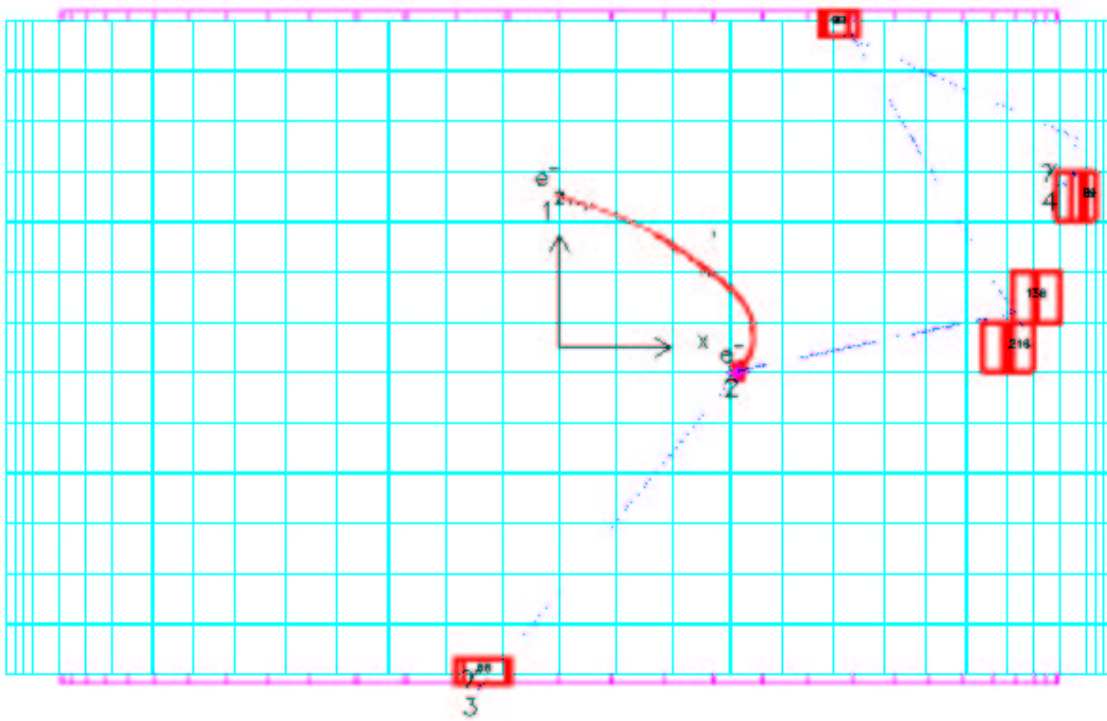


Figure 5.8: The transverse view of the event of Fig. 5.7.

# $\gamma$ -clusters	0	1	2	3	4	$\geq 5$
Proportion (%)	10.8	25.7	28.2	20.7	9.8	4.8

Table 5.4: Number of  $\gamma$ -clusters for Monte-Carlo events of the  $2\nu\beta\beta$  decay of  $^{100}\text{Mo}$  to the excited  $0_1^+$  state.

## 5.6 Two-electron preselection

First of all, a two-electron preselection is applied to Monte-Carlo events. That means that the only events containing two reconstructed tracks ( $N_{\text{TRA}} = 2$ ) with negative curvatures, which represent electrons emitted from source foils, having a common vertex in source foils are accepted. To decide whether the two tracks have or have not a common vertex, the relative distances in the horizontal plane  $x$ - $y$  ( $\Delta r$ ) and in the vertical direction  $z$  ( $\Delta z$ ) between vertices reconstructed for each track in source foils are calculated. If the conditions that  $\Delta r \leq 4$  cm and  $\Delta z \leq 4$  cm are simultaneously satisfied, then the event is accepted. The limit of 4 cm in both the horizontal plane and the vertical direction was chosen with regards to the position resolution of the tracking wire chamber [137, 152].

In order to make use of the information about the energy and the time of detection of each electron, we ask that each of the tracks has an associated scintillator counter. Events which, by chance, have both tracks connected with the same scintillator cannot be used for the further analysis and are therefore rejected. As we are interested in events with two electrons and  $N$  photons, we retain only events with more than two fired scintillators ( $N_{\text{SCIN}} \geq 2$ ).

As a result of the conditions described previously, we obtain events containing two electrons with a common vertex in the foils and with at least one “rough” photon; at this stage it can still be a false photon. Although it seems that such criteria should be sufficient, further conditions are imposed for the correct two-electron preselection. Events containing tracks connected with petal scintillators in the row of PMTs which follow just after the four Geiger cell layers closest to the source foils from both the internal and external sides (cf. Fig. 4.5) are not accepted. Such tracks are often very short, especially their projection in the horizontal  $x$ - $y$  plane, which can produce wrong reconstruction of the track curvature. Thus, an electron coming from the scintillator and then going through the foils could be erroneously considered as a good event. Not even the time-of-flight test<sup>1</sup> would help in such a case because of the shortness of the track since this also implies a short flight time for electrons from the scintillator to the foil or in the opposite direction.

Generally, we ask that the energy deposited by each of the electrons is greater than 200 keV. Above this value, we are sure that the energy and time calibrations, as well as the time-energy corrections are linear and well determined [133]. Moreover, the portion of real  $\beta\beta$  decay events with such low energy of electrons is small, and thus they are not very important for data analysis and we may omit them.

## 5.7 Reduction of background from radon

The most dangerous daughter isotope of  $^{222}\text{Rn}$  from the point of view of different two-electron channels is  $^{214}\text{Bi}$  decaying to  $^{214}\text{Po}$  which disintegrates after 164  $\mu\text{s}$  to  $^{210}\text{Pb}$  (see Figs. 4.12

---

<sup>1</sup>The time-of-flight test applied to electrons is explained in Sec. 5.8.1

and 4.15). In the case of the  $eeN\gamma$  channel, a possible way to identify and then to reduce the background contribution from radon, which has penetrated into the detector through gas leaks or the porosity of some of the construction materials, is to look for  $^{214}\text{Bi} - ^{214}\text{Po}$  events producing two-electron events accompanied by an  $\alpha$ -particle which is itself revealed by the presence of delayed Geiger cell hits. We search for the delayed Geiger cells in a circular volume surrounding the reconstructed vertex in the source foils which is common to the two electron tracks. However, if the decay of  $^{214}\text{Bi}$  comes about somewhere in the gas but rather far from the reconstructed vertex in foils, then such an event is rejected by the time-of-flight test for electrons (see Sec. 5.8.1). Although the reconstructed vertex of the two tracks is found in the foils, the real vertex of such a decay is in the gas. As the range of  $\alpha$ -particles from the  $^{214}\text{Bi}$  decay in the He gas of the NEMO3 wire chamber is of about 30 – 40 cm, the relative distance between the reconstructed vertex and the delayed Geiger cell(s) corresponding to an  $\alpha$ -particle where the latter is searched for, is set to  $\Delta z \leq 30 \text{ cm} + \text{erzg}$  in the vertical  $z$  direction, where  $\text{erzg}$  is the error (in cm) of the vertical position reconstruction for the Geiger cell concerned, and to  $\Delta r \leq 30 \text{ cm}$  in the horizontal  $x$ - $y$  plane. However,  $\alpha$ -particles in the gap between Geiger cell layers separated with scintillator blocks may not be detected. Fortunately, some of these events can be revealed and then rejected due to those Geiger cells which were obviously fired by electrons but which are not used for the reconstruction of either of the two tracks because they are incompatible with a track fit. An example of such event is given in Fig. 5.9.

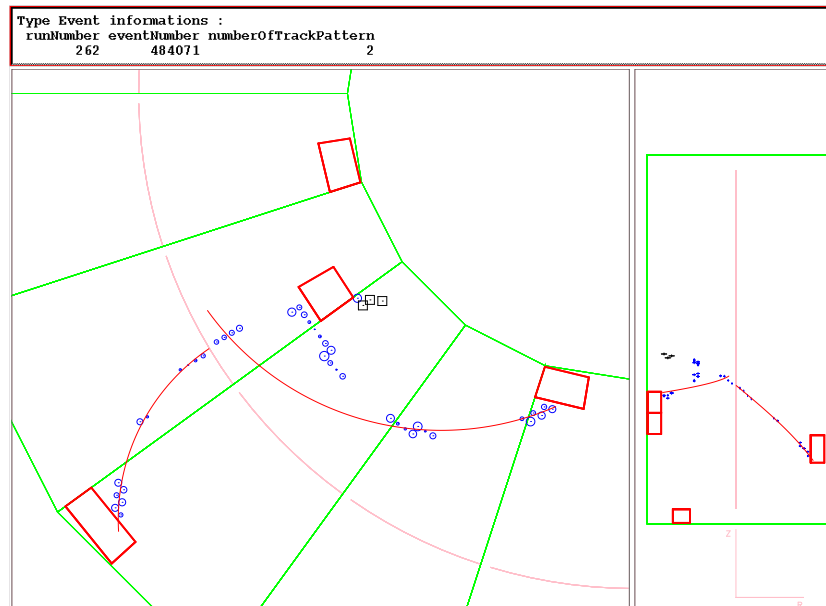


Figure 5.9: An example of a  $^{214}\text{Bi} - ^{214}\text{Po}$   $ee2\gamma\alpha$  event with bad track reconstruction: transverse (left) and longitudinal (right) views. Geiger cell hits are represented with blue circles, delayed Geiger cells with black squares, red lines correspond to reconstructed tracks, red boxes indicate fired scintillators, and the rose line in the middle of each sector represents the source foils. This event will be rejected because the electrons do not satisfy the time-of-flight test of the internal hypothesis. Moreover, it would also be rejected because of the presence of fired Geiger cells that were unused in the track reconstruction.

## 5.8 Kinematic and temporal cuts on the $eeN\gamma$ channel

### 5.8.1 Time-of-flight test for electrons

We will consider two hypotheses of the origin of the two reconstructed tracks, illustrated in Fig. 5.10. The first hypothesis will be of the **internal** origin of the two electrons, meaning that they were both generated at the same time  $t_0$  at a common point inside source foils, then they went through the wire chamber and were detected with two distinct scintillators. The second one will be the hypothesis of a **crossing** particle which entered the tracking volume of the detector by one scintillator, crossed through source foils and was finally detected by another scintillator. To decide as to which scenario an event belongs, the most powerful method is a  $\chi^2$ -based time-of-flight test. In the following part, definitions of  $\chi^2$  variables for both hypotheses of the event origin will be given. Nevertheless, we will first describe a rather simple test based only on the comparison of times of emission for the two electrons under the internal hypothesis. It is useful especially for preliminary, rough data analysis when one does not yet need strict criteria for the selection of good two-electron events. Anyway, a  $\chi^2$ -based time-of-flight test is by far the most efficient way allowing the classification of events according to their chronology.

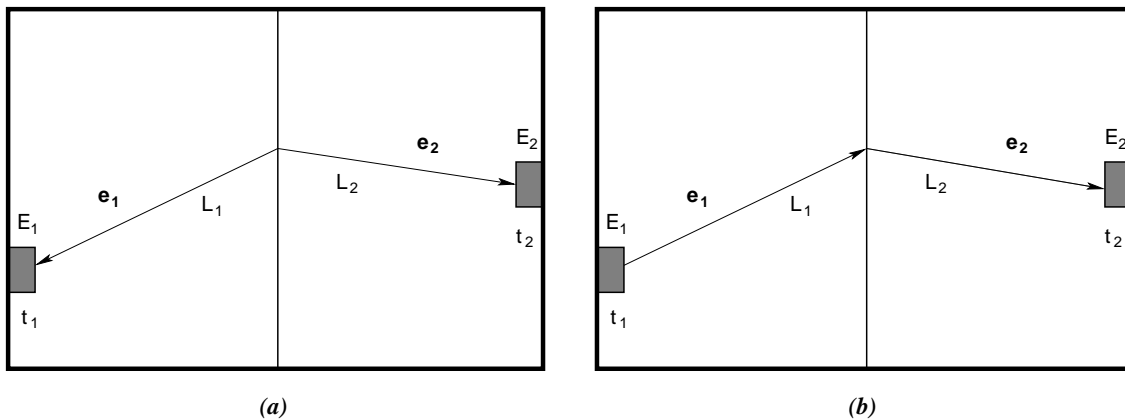


Figure 5.10: An illustration of two different scenarios for the two-electron events: (a) the case of internal origin of the electrons (both generated in the source foils) and (b) the case of external origin of the event (a crossing electron).

#### Simple test of the internal hypothesis

The following simple time-of-flight test is relatively powerful but less precise compared with the tests using the  $\chi^2$ -method for distinguishing between internal and external two-electron events. We study the  $\Delta T_{ee} = |T_0(e_1) - T_0(e_2)|$  variable, which represents the difference between emission times<sup>2</sup> of the two electrons ( $T_0(e_j)$ ,  $j = 1, 2$ ) supposing the internal hypothesis. The  $T_0(e_j)$  times are derived from the length of each track, from the energy deposited by the electrons, and from the times of their detection in the scintillator counters. The calculation is detailed next and is given by Eqs. 5.2, 5.3, and 5.4 with a difference in notation of the emission time ( $T_0(e_j) \equiv t_j^{int}$ ). Fig. 5.11 and Tab. 5.5 show that a rather good separation of internal events from external ones,

<sup>2</sup>Here the emission from source foils is assumed.

can be achieved by simply imposing the following condition on  $\Delta T_{ee}$ :

$$\Delta T_{ee} < 2 \text{ ns} . \quad (5.1)$$

Isotope	Type of events	Events satisfying $\Delta T_{ee} < x$			
		< 1 ns	< 1.5 ns	< 2 ns	< 3 ns
$^{100}\text{Mo}$	$2\nu\beta\beta \text{ g.s.} \rightarrow 0_1^+$	70.5%	87.1%	94.5%	98.7%
$^{100}\text{Mo}$	$2\nu\beta\beta \text{ g.s.} \rightarrow \text{g.s.}$	69.7%	85.4%	92.9%	98.0%
$^{208}\text{Tl}$	external bgd	5.9%	7.1%	7.9%	9.9%
$^{214}\text{Bi}$	external bgd	6.2%	7.8%	8.6%	9.9%
$^{214}\text{Bi}$	radon	31.3%	42.0%	51.2%	64.7%

Table 5.5: Proportions of events satisfying the  $\Delta T_{ee} < x$  condition for different values of  $x$  when applied on Monte-Carlo data for internal events ( $\beta\beta$  decay of  $^{100}\text{Mo}$ ) and external backgrounds ( $^{208}\text{Tl}$  and  $^{214}\text{Bi}$  in PMTs).

### Internal two-electron hypothesis – definition of $\chi_{int}^2$

Each of the two tracks is characterised by its length  $L_j$ , by the triggering time  $t_j$  of the associated scintillator, and by the deposited energy  $E_j$  in the scintillator. The time-of-flight of each particle ( $j = 1, 2$ ) from the source foils to its fired scintillator is given by:

$$\Delta t_j = \frac{L_j}{\beta_j c} , \quad (5.2)$$

where  $c$  is the speed of light in a vacuum and  $\beta_j$  takes the following form:

$$\beta_j = \frac{\sqrt{E_j(E_j + 2m_e c^2)}}{E_j + m_e c^2} . \quad (5.3)$$

So, the time of the emission of each particle,  $t_j^{int}$ , under the internal hypothesis is:

$$t_j^{int} = t_j - \Delta t_j = t_j - \frac{L_j}{\beta_j c} . \quad (5.4)$$

Then the  $\chi_{int}^2$  variable can be expressed in the following way:

$$\chi_{int}^2 = \frac{\left( \left( t_2 - \frac{L_2}{\beta_2 c} \right) - \left( t_1 - \frac{L_1}{\beta_1 c} \right) \right)^2}{\sigma_{tot}^2} , \quad (5.5)$$

where  $\sigma_{tot}^2$  is the total of all the errors related to the proper measurement of time and to the calculation of  $\Delta t_j$ , i.e. the errors on the time measurements  $\sigma_{(t)j}$ , energy  $\sigma_{(E)j}$  and distance  $\sigma_{(\ell)j}$ . The expression of  $\sigma_{tot}^2$ , which in our particular case can be rewritten like:

$$\sigma_{tot}^2 = \sigma_{tot,1}^2 + \sigma_{tot,2}^2 = \sigma_{tot(t)}^2 + \sigma_{tot(E)}^2 + \sigma_{tot(\ell)}^2 ,$$

finally has the following explicit form:

$$\sigma_{tot}^2 = \sum_{j=1}^2 \sigma_{(t)j}^2 + \sum_{j=1}^2 \left( \frac{t_j^{int} m_e c^2}{E_j(E_j + m_e c^2)(E_j + 2m_e c^2)} \right)^2 \sigma_{(E)j}^2 + \sum_{j=1}^2 \left( \frac{1}{\beta_j c} \right)^2 \sigma_{(\ell)j}^2 . \quad (5.6)$$

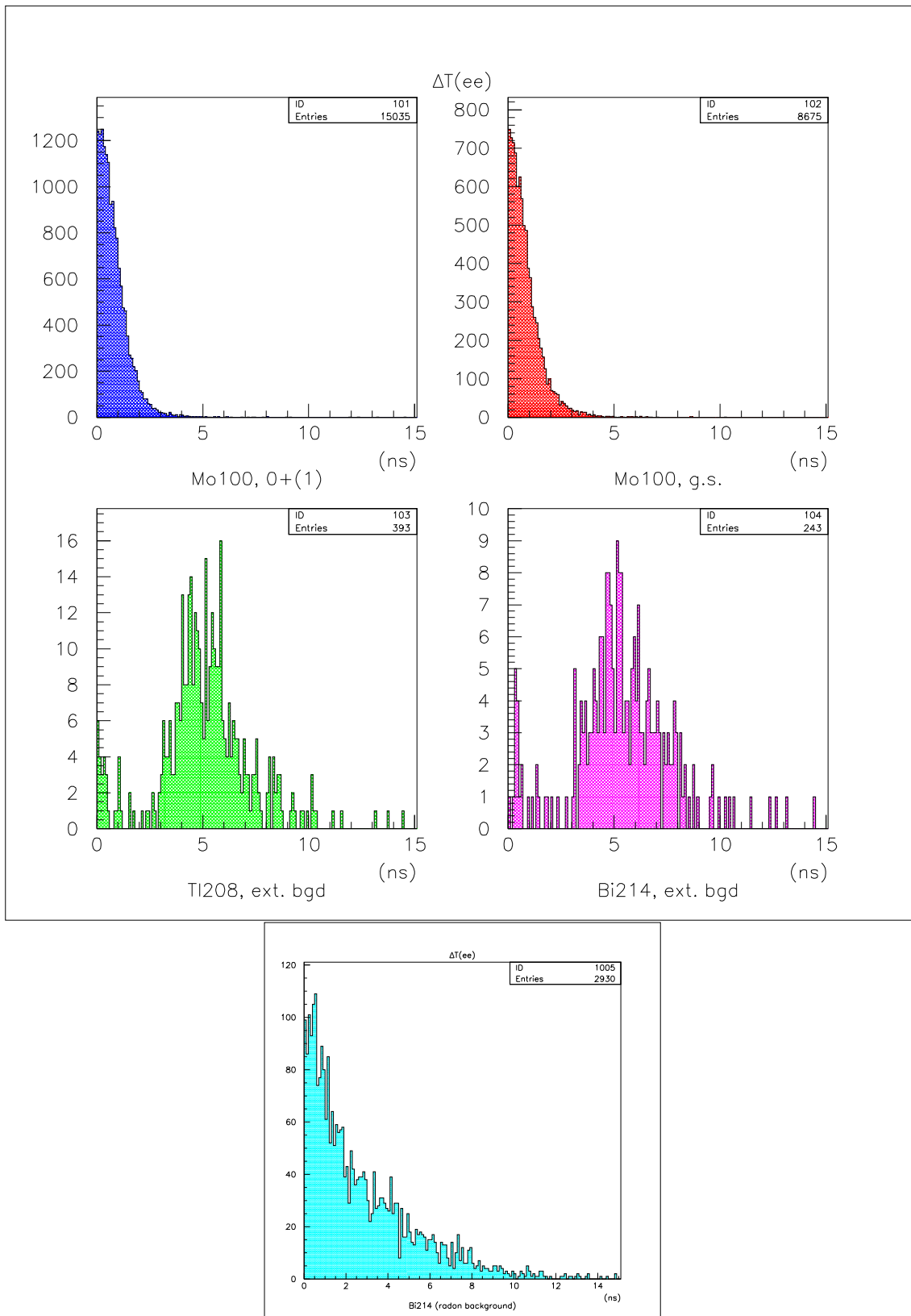


Figure 5.11:  $\Delta T_{ee}$  distributions for internal events from the  $2\nu\beta\beta$  decay of  $^{100}\text{Mo}$ ,  $g.s. \rightarrow 0_1^+$  and  $g.s. \rightarrow g.s.$  transitions (upper row), for the external background from  $^{208}\text{Tl}$  and  $^{214}\text{Bi}$  (middle row) and for  $^{214}\text{Bi}$  present in the gas of the wire chamber (lower row).

### Crossing electron hypothesis – definition of $\chi_{cross}^2$

We can check two possible external hypotheses supposing that the incoming particle is either electron marked like  $e_1$  as it is case in Fig. 5.10 or, in contrast, electron  $e_2$ . For the following mathematical description we will consider only the former situation; the latter can be simply obtained by index permutation.

The time-of-flight of a particle crossing through the detector as illustrated by Fig. 5.10 is given by:

$$t^{cross} = \frac{L_2}{\beta_2 c} + \frac{L_1}{\beta'_2 c}, \quad (5.7)$$

where  $\beta_2$  and  $\beta'_2$  have the same form as in Eq. 5.3. The only difference between  $\beta_2$  and  $\beta'_2$  comes from the fact that  $\beta'_2$  includes corrections of  $E_2$  due to the energy loss of the particle in the gas between the second fired scintillator and the source foil, as well as the energy loss while it comes through the foil. The  $\chi_{cross}^2$  variable can be then written in the following way:

$$\chi_{cross}^2 = \frac{((t_2 - t_1) - t^{cross})^2}{\sigma_{tot}^2}, \quad (5.8)$$

where  $\sigma_{tot}^2$  is given by:

$$\sigma_{tot}^2 = \sum_{j=1}^2 \sigma_{(t)j}^2 + \left( \frac{t^{cross} m_e c^2}{E_2(E_2 + m_e c^2)(E_2 + 2m_e c^2)} \right)^2 \sigma_{(E)2}^2 + \left( \frac{1}{\beta_2 c} \right)^2 (\sigma_{(\ell)1}^2 + \sigma_{(\ell)2}^2). \quad (5.9)$$

To get the contribution to  $\sigma_{tot}$  which is related to the uncertainty on the track length, the calculation was slightly simplified by replacing  $\beta'_2$  with  $\beta_2$ . In reality, the energy difference due to the combined losses in the gas and in the foils is about 100 keV [137]. The omission of this energy correction for the  $\sigma_{tot}$  calculation does not significantly change the result.

### Selection condition for good internal events

Now we can calculate for each two-electron event the values of  $\chi_{int}^2$  and  $\chi_{cross}^2$  and deduce from them probabilities of the two examined hypotheses, i.e. whether the event is either of the internal origin type, or of the crossing particle type. A criterion for the selection of good internal events is constructed on the basis of Monte-Carlo simulations of internal and external events. The good internal two-electron events have to satisfy the following two conditions to be accepted:

$$\begin{aligned} -\log(Prob_{int}) &< 2 \\ -\log(Prob_{cross}) &> 3, \end{aligned} \quad (5.10)$$

where  $Prob_{int} = Prob(\chi_{int}^2)$  and  $Prob_{cross} = Prob(\chi_{cross}^2)$  are probabilities that the event is of the internal type or of the crossing type respectively. This choice is justified with the probability distributions obtained for the internal events, the g.s.  $\rightarrow 0_1^+$  transition of the  $2\nu\beta\beta$  decay of  $^{100}\text{Mo}$  (Fig. 5.12), and for the external background from  $^{208}\text{Tl}$  and  $^{214}\text{Bi}$  (Fig. 5.13). Note that if the probability  $Prob_{xxx}$  is smaller than  $10^{-19}$ , then we set the value of  $-\log(Prob_{xxx})$  to 19 in these plots which explains the accumulation of events at this value in the form of a sharp line.

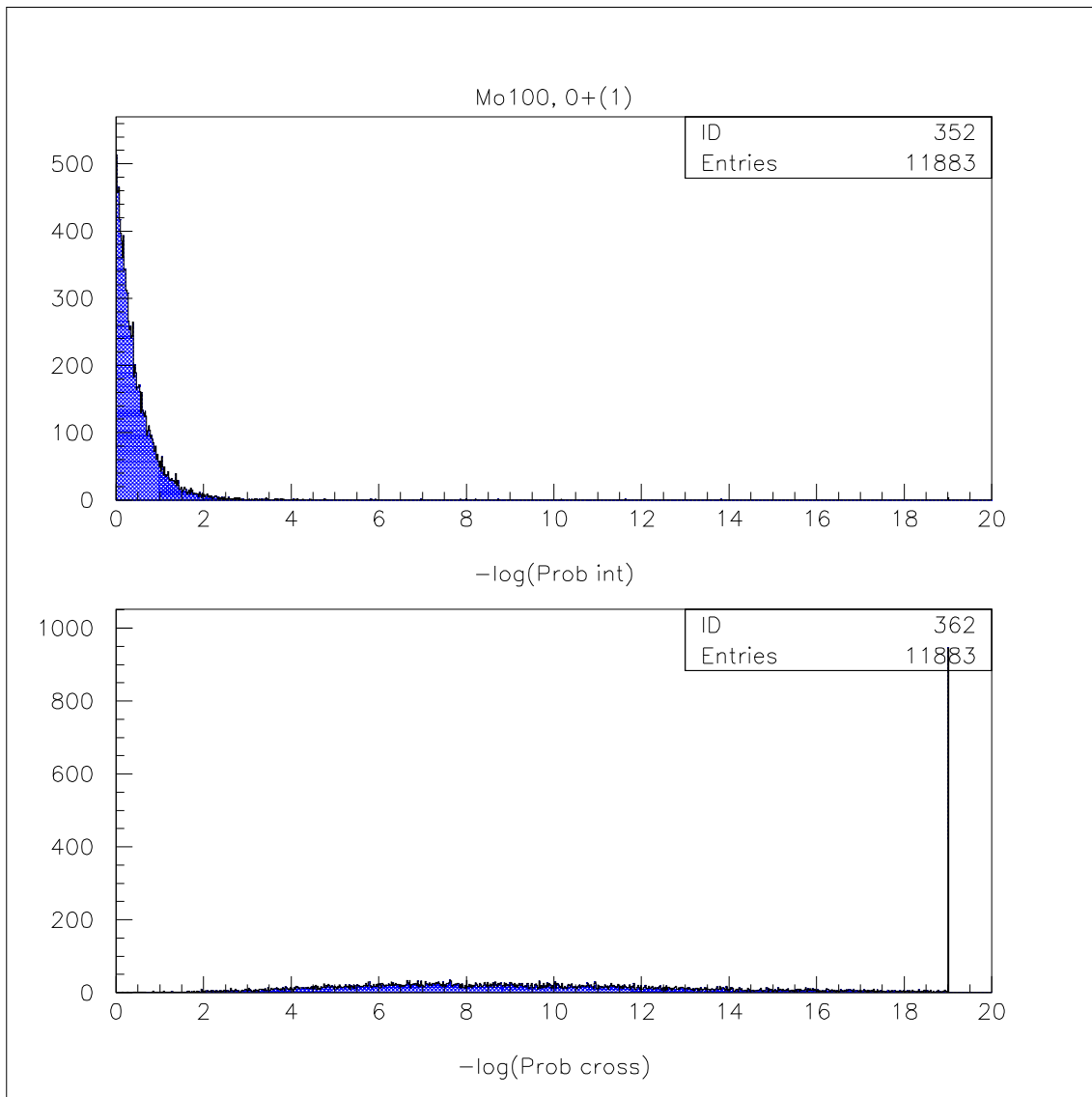


Figure 5.12: Distributions of probability that two-electron events simulated for the g.s.  $\rightarrow 0_1^+$  transition of the  $2\nu\beta\beta$  decay of  $^{100}\text{Mo}$  are of the internal type ( $\text{Prob}_{int}$ ) or of the crossing particle type ( $\text{Prob}_{cross}$ ). Note that events with  $-\log(\text{Prob}_{cross}) > 19$  are accumulated at 19 forming then a sharp line at this value.

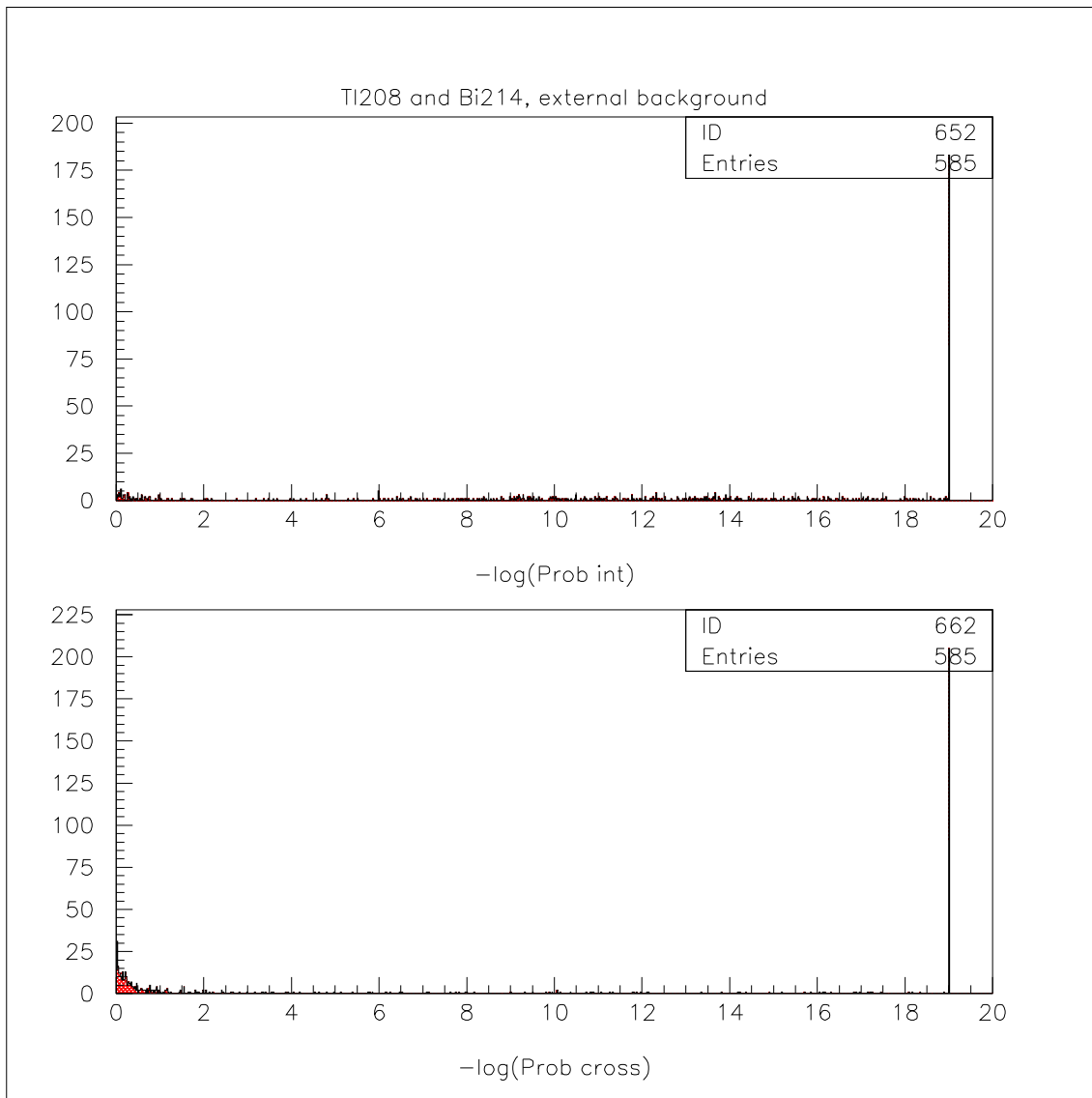


Figure 5.13: Distributions of probability that two-electron events simulated for the external background from  $^{208}\text{Tl}$  and  $^{214}\text{Bi}$  are of the internal type ( $\text{Prob}_{int}$ ) or of the crossing particle type ( $\text{Prob}_{cross}$ ). Note that events with  $-\log(\text{Prob}_{int}) > 19$  and  $-\log(\text{Prob}_{cross}) > 19$  respectively are accumulated at 19 forming then sharp lines at this value.

### 5.8.2 Energy cuts applied on two-electron events with photons

Although the  $Q$ -value of the  $\beta\beta$  decay of  $^{100}\text{Mo}$  is 3034 keV, a total of 1130 keV is taken away by the two de-excitation photons. Thus, the two electrons can carry away at most 1900 keV of the available energy. So, we may well suppose that events with the energy sum of the two electrons,  $E_{ee} = E_{e_1} + E_{e_2}$ , exceeding 2000 keV are due to background and cannot originate from the  $2\nu\beta\beta$  decay to the excited  $0_1^+$  state. As Fig. 5.14, which represents the  $E_{ee}$  spectra for internal and external events, and Tab. 5.6 show, we can even restrict more this condition and impose:

$$E_{ee} \leq 1200 \text{ keV} \quad (5.11)$$

because above 1200 keV we lose only 5% of two-electron events from the excited state while we eliminate about 50% or even more of other kinds of studied background processes. The condition given by Eq. 5.11 is also rather efficient against the background from radon as one can see from Fig. 5.14 and Tab. 5.6.

Studied process	$E_{ee} < X$			
	1200 keV	1500 keV	1800 keV	2000 keV
$^{100}\text{Mo}$ , g.s. $\rightarrow$ $0_1^+$	94.9%	99.7%	100%	100%
$^{100}\text{Mo}$ , g.s. $\rightarrow$ g.s.	45.9%	72.5%	90.4%	96.4%
$^{208}\text{Tl}$ , external bgd	19.1%	32.5%	49.2%	65.4%
$^{214}\text{Bi}$ , external bgd	55.3%	81.5%	92.3%	98.1%
$^{214}\text{Bi}$ , radon	50.1%	68.0%	82.1%	89.6%

Table 5.6: Proportions of events satisfying the  $E_{ee} < X$  cut for different values of  $X$ . The mentioned cut was applied on two-electron events before application of any further energy or time-of-flight cuts.

Next, the  $\gamma$ -scintillators are clusterised, which means that neighbouring  $\gamma$ -scintillators are regrouped into a  $\gamma$ -cluster. Such a cluster can be composed of one, two, three, or sometimes even more counters. In reality, the number of  $\gamma$ -clusters in an event,  $N$ , is significant to the number of detected photons. As we look for  $\gamma$ -rays of 540 and 590 keV, it is natural to ask that the energy deposited in each  $\gamma$ -cluster does not exceed 600 keV, which give us another condition for rejection of background events:

$$E_\gamma < 600 \text{ keV} . \quad (5.12)$$

As the total energy of de-excitation photons is 1130 keV, we can restrict the energy sum of the  $N$   $\gamma$ -clusters,  $E_{N\gamma} = \sum_{i=1}^N E_{\gamma_i}$ , imposing the following condition:

$$E_{N\gamma} < 1200 \text{ keV} . \quad (5.13)$$

In order to reduce the background contribution intrinsic to the experimental setup, i.e. in particular bremsstrahlung of electrons from the  $2\nu\beta\beta$  decay of  $^{100}\text{Mo}$  to the ground state and external backgrounds due to  $^{208}\text{Tl}$  and  $^{214}\text{Bi}$  contained inside the PMTs, which were not eliminated by the TOF test for the electrons, it is useful to also set a lower limit for  $E_{N\gamma}$ . Fig. 5.15 and 5.16 show respectively the  $E_{N\gamma}$  spectra and the  $E_{N\gamma}$  vs.  $E_{ee}$  plots for Monte-Carlo events simulated for  $^{100}\text{Mo}$  (both g.s.  $\rightarrow$  g.s. and g.s.  $\rightarrow$   $0_1^+$  transitions) and external backgrounds from  $^{208}\text{Tl}$  and  $^{214}\text{Bi}$ . Note that these spectra were drawn for the two-electron

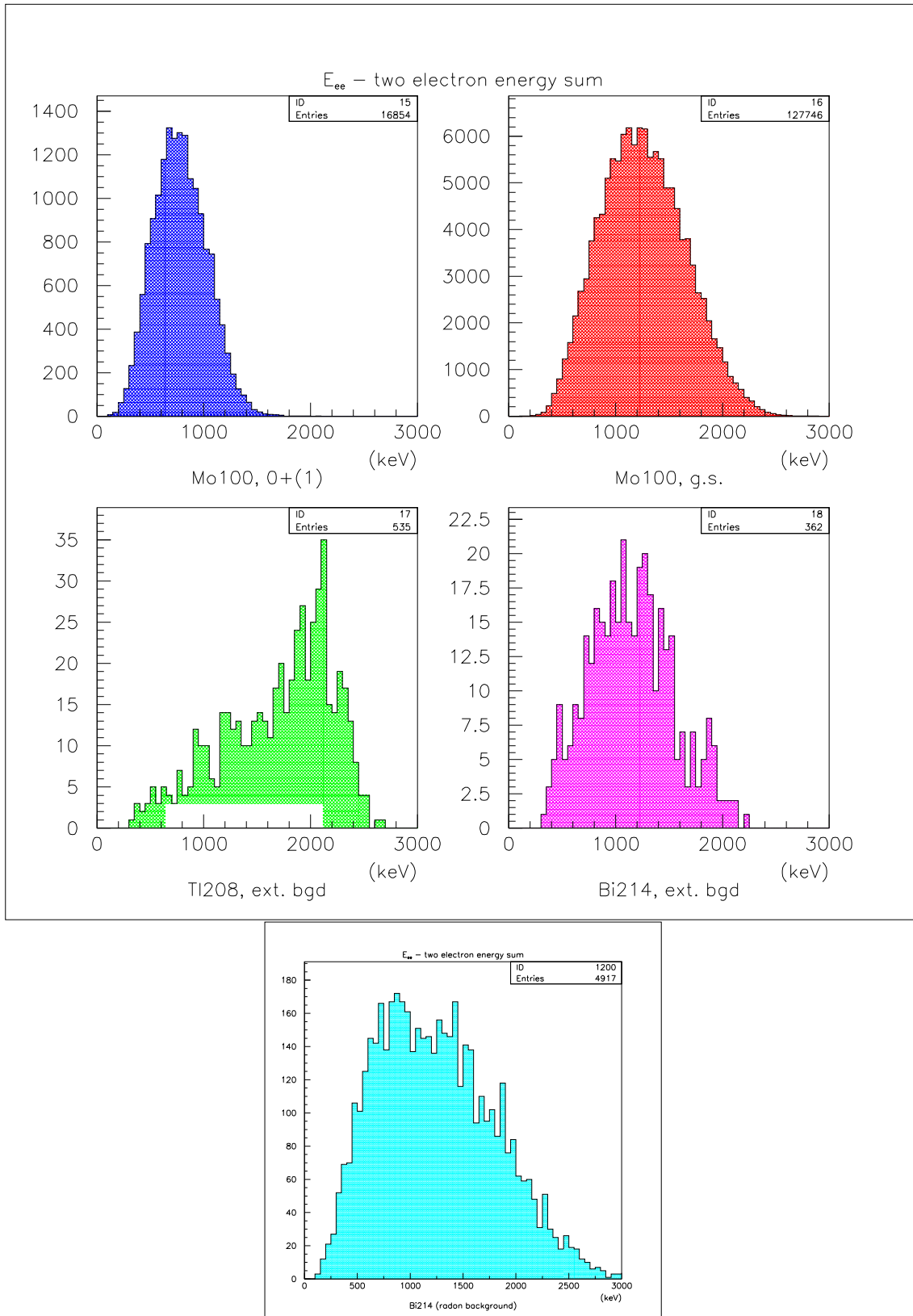


Figure 5.14:  $E_{ee}$  spectra for simulated events of the  $2\nu\beta\beta$  decay of  $^{100}\text{Mo}$ ,  $\text{g.s.} \rightarrow 0_1^+$  and  $\text{g.s.} \rightarrow \text{g.s.}$  transitions (upper row), for external background from  $^{208}\text{Tl}$  (middle row, at left) and  $^{214}\text{Bi}$  (middle row, at right) and for  $^{214}\text{Bi}$  present in the gas of the wire chamber (lower row). To plot these spectra, two-electron events were used before any further energy cuts or TOF conditions were applied on them.

events without any further energy and TOF cuts so that we may have enough events from  $^{208}\text{Tl}$  and  $^{214}\text{Bi}$  for these plots. The condition of Eq. 5.13 can be then generalised as follows:

$$X < E_{N\gamma} < 1200 \text{ keV} , \quad (5.14)$$

where  $X$  is the lower limit of  $E_{N\gamma}$ . The value of  $X$  has to be optimised in order to reach a good signal/background ratio whilst at the same time maintaining a reasonable number of events from the experimental data currently available. That means that the choice of  $X$  is not only a question of Monte-Carlo simulations but is strongly dependent on the available amount of the experimental data. Especially because of the latter reason, we will favour a relatively low value of  $X$ . According to the shapes of the  $E_{N\gamma}$  spectra (Fig. 5.15) or, eventually, according to the two-dimensional scatter plots of  $E_{N\gamma}$  vs.  $E_{ee}$  (Fig. 5.16), we can, for instance, decrease the value of  $X$  down to 200 keV conserving about 88% of the excited state events (see also Tab. 5.7).

Studied process	$X < E_{N\gamma} < 1200 \text{ keV}$					
	200 keV	300 keV	400 keV	500 keV	600 keV	700 keV
$^{100}\text{Mo}$ , g.s $\rightarrow 0_1^+$	87.7%	79.5%	66.0%	46.3%	31.6%	23.1%
$^{100}\text{Mo}$ , g.s $\rightarrow$ g.s.	54.8%	37.3%	25.7%	17.0%	11.2%	6.8%
$^{208}\text{Tl}$ , external bgd	81.3%	66.5%	56.0%	42.1%	32.1%	21.5%
$^{214}\text{Bi}$ , external bgd	80.2%	60.4%	43.6%	30.7%	20.1%	15.8%
$^{214}\text{Bi}$ , radon	64.4%	56.3%	48.5%	38.5%	27.6%	21.6%

Table 5.7: Proportions of events satisfying the  $X < E_{N\gamma} < 1200 \text{ keV}$  cut for different values of  $X$ . The cut was applied on two-electron events before application of any further energy or time-of-flight cuts.

### 5.8.3 $\gamma$ -clusters with low energy deposits

The time when a scintillator counter was fired by a particle is determined from the TDC content of the counter. The time-energy corrections<sup>3</sup> have to be taken into account because leading edge type TDCs are used for acquisition. However, good time-energy corrections can only be obtained for energies down to 75 keV [153]. That means that scintillator counters with low energy deposits can only be used for energy measurements but must be avoided for any temporal studies such as time-of-flight tests or time distributions. So that we may use the time-of-flight cuts designed for photons, we are obliged to demand that at least two  $\gamma$ -clusters used in the time-of-flight tests have  $\gamma$ -scintillators with deposited energy greater than 100 keV.

### 5.8.4 Time-of-flight tests applied to photons

Although all the previous conditions are efficient for rejection of a large part of the external background events, we cannot, however, completely exclude background events triggered by a photon coming from the outside which interacts with the source foils and produces by the subsequent Compton and Möller effects two electrons. As events from the  $2\nu\beta\beta$  decay to the excited  $0_1^+$  state have the two electrons and the two photons emitted from the same vertex, the photons which are directly detected, i.e. after their first interaction in the calorimeter and

---

<sup>3</sup>In fact, it is more exactly a time-charge correction.

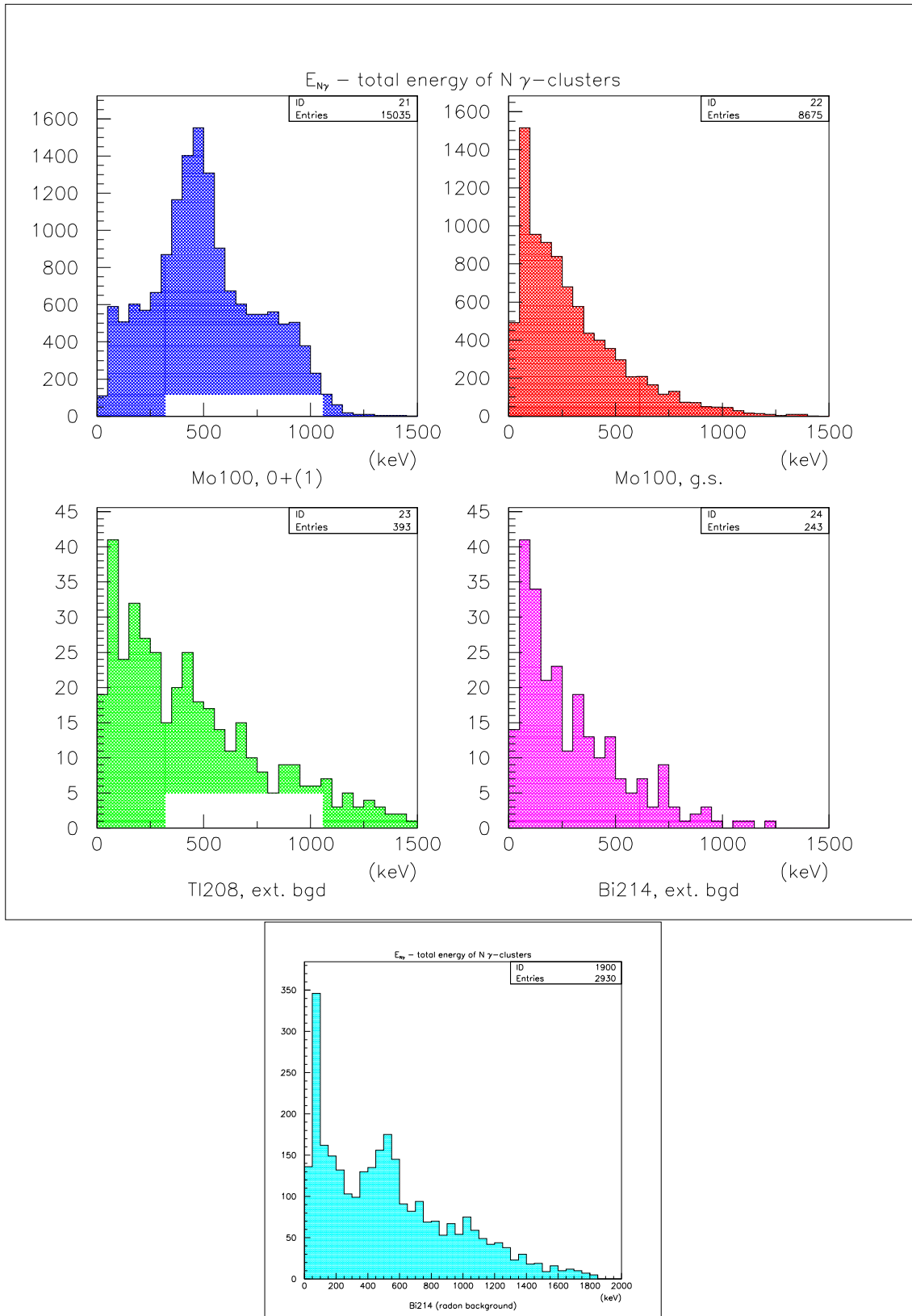


Figure 5.15:  $E_{N\gamma}$  spectra for simulated events of the  $2\nu\beta\beta$  decay of  $^{100}\text{Mo}$ ,  $g.s. \rightarrow 0_1^+$  and  $g.s. \rightarrow g.s.$  transitions (upper row), for external background from  $^{208}\text{Tl}$  (middle row, at left) and  $^{214}\text{Bi}$  (middle row, at right) and for  $^{214}\text{Bi}$  present in the gas of the wire chamber (lower row). To plot these spectra, two-electron events were used before any further energy cuts or TOF conditions were applied on them.

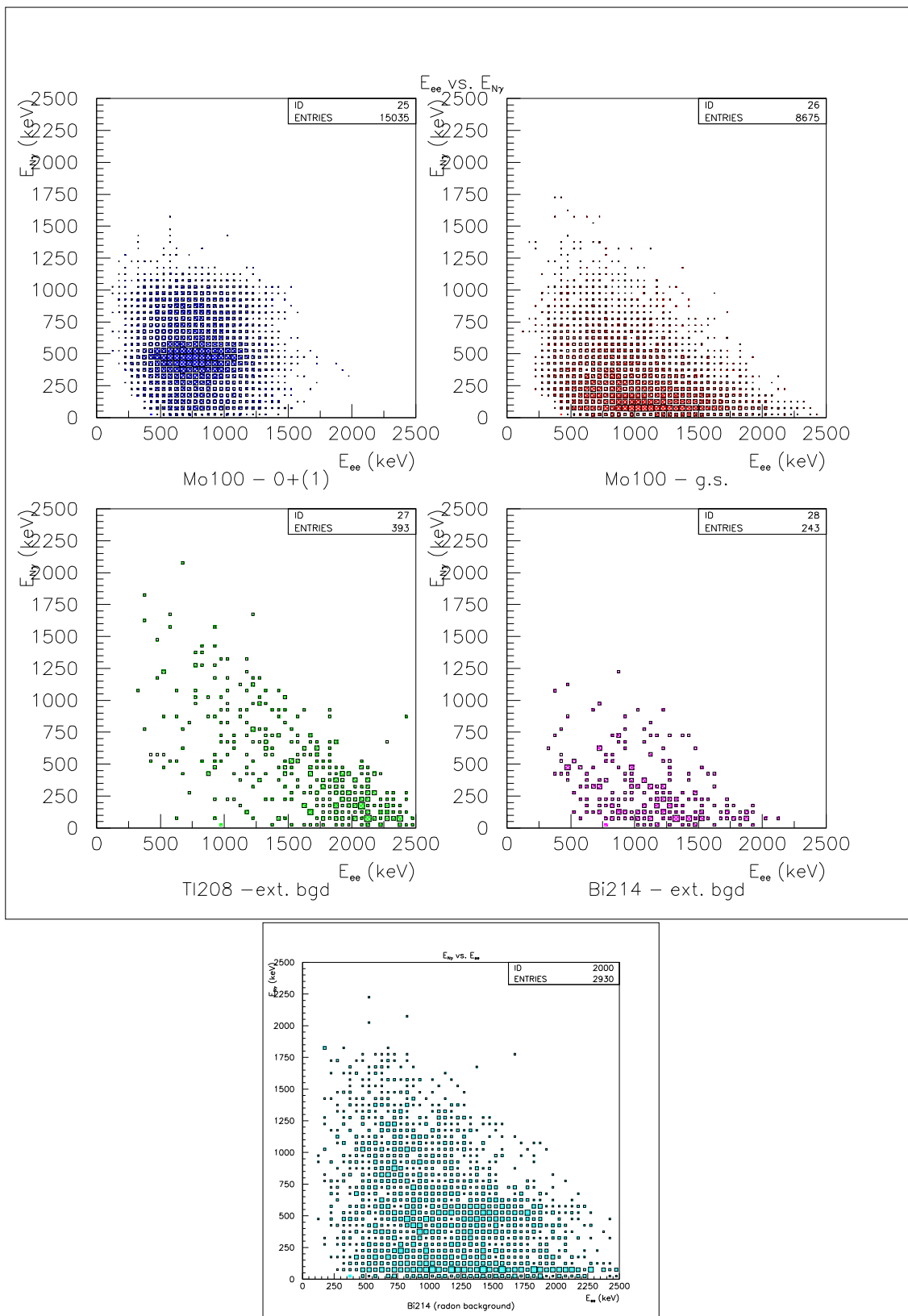


Figure 5.16: Two-dimensional  $E_{N\gamma}$  vs.  $E_{ee}$  plots for simulated events of the  $2\nu\beta\beta$  decay of  $^{100}\text{Mo}$ ,  $\text{g.s.} \rightarrow 0_1^+$  and  $\text{g.s.} \rightarrow \text{g.s.}$  transitions (upper row), for external background from  $^{208}\text{Tl}$  (middle row, at left) and  $^{214}\text{Bi}$  (middle row, at right) and for  $^{214}\text{Bi}$  present in the gas of the wire chamber (lower row). To plot these spectra, two-electron events were used before any further energy cuts or TOF conditions were applied to them.

not the reflected ones, have to be perfectly in time with the electrons. In order to decrease the number of background events further, we will apply time-of-flight tests regarding different hypotheses of the photons' origin.

First of all the  $t_0$  time and the related error  $\sigma_{t_0}$  corresponding to the common emission time of the two electrons from the source foils will be determined. Then the proper tests of the origin of photons will be made. First, the hypothesis of the external origin of the two-electron event triggered by a photon coming from the exterior (see Sec. 4.8.2 and Fig. 4.14), called here just **external hypothesis**, will be tested in order to reject more of the external background events. After that we may examine the so called **internal hypothesis about photons**, which is intended to verify whether a given event contains two photons perfectly in time with the two electrons, i.e. emitted at the same time as the electrons from the vertex common to all the four particles. Such an event would then be an obvious candidate for the  $2\nu\beta\beta$  decay to the excited  $0_1^+$  state. The alternative hypothesis, called the **reflection hypothesis** and meaning just that the second fastest photon is produced by reflection of the first one after its interaction with a scintillator counter will be introduced.

### Emission time $t_0$ of the two electrons and its error $\sigma_{t_0}$

Using the formalism and notation of Sec. 5.8.1, we can deduce for both electrons the emission times  $t_{0,1}$  and  $t_{0,2}$  as follows:

$$t_{0,j} = t_j - \Delta t_j = t_j - \frac{L_j}{\beta_j c}. \quad (5.15)$$

Then we can produce the weighted average value of  $t_0$ :

$$t_0 = \frac{\frac{t_{0,1}}{\sigma_{t_{0,1}}^2} + \frac{t_{0,2}}{\sigma_{t_{0,2}}^2}}{\frac{1}{\sigma_{t_{0,1}}^2} + \frac{1}{\sigma_{t_{0,2}}^2}},$$

which can be rewritten as:

$$t_0 = \left( \frac{t_{0,1}}{\sigma_{t_{0,1}}^2} + \frac{t_{0,2}}{\sigma_{t_{0,2}}^2} \right) \frac{\sigma_{t_{0,1}}^2 \sigma_{t_{0,2}}^2}{\sigma_{t_{0,1}}^2 + \sigma_{t_{0,2}}^2}. \quad (5.16)$$

As for the corresponding error  $\sigma_{t_0}$ , its expression is the following:

$$\sigma_{t_0} = \sqrt{\frac{1}{\frac{1}{\sigma_{t_{0,1}}^2} + \frac{1}{\sigma_{t_{0,2}}^2}}} = \sqrt{\frac{\sigma_{t_{0,1}}^2 \sigma_{t_{0,2}}^2}{\sigma_{t_{0,1}}^2 + \sigma_{t_{0,2}}^2}}, \quad (5.17)$$

where  $\sigma_{t_{0,1}}$  and  $\sigma_{t_{0,2}}$  are defined in the same way as in Sec. 5.8.1.

### Definition of $\chi_{\gamma ext}^2$ for the external hypothesis

If we consider the situation of a photon coming from the exterior and generating a two-electron event in the source foils, as illustrated in Fig. 5.17, then the corresponding  $\chi_{\gamma ext}^2$  variable is defined as follows:

$$\chi_{\gamma ext}^2 = \frac{\left( t_0 - \left( t_\gamma + \frac{L_\gamma}{c} \right) \right)^2}{\sigma_{tot,\gamma}^2}, \quad (5.18)$$

where  $\sigma_{tot,\gamma}^2$  is the total error related to the proper measurement of time and to the calculation of  $\Delta t_\gamma = L_\gamma/c$ , i.e. errors on proper measurement of time by calorimeter  $\sigma_{(t)\gamma}$ , and on determination of distances and of the  $t_0$  time expressed respectively by  $\sigma_{(\ell)\gamma}$  and  $\sigma_{t_0}$  (see Eq. 5.17). The expression of  $\sigma_{tot,\gamma}^2$  in such a case can be rewritten as:

$$\sigma_{tot,\gamma}^2 = \sigma_{(t)\gamma}^2 + \sigma_{t_0}^2 + \sigma_{(\ell)\gamma}^2. \quad (5.19)$$

The error  $\sigma_{(\ell)\gamma}$  on the determination of the distance travelled by the photon between the vertex in the source foils and the fired scintillator is given by:

$$\sigma_{(\ell)\gamma}^2 = \left(\frac{1}{cL_\gamma}\right)^2 \left( (x^{(f)} - x_\gamma^{(i)})^2 (\sigma_{x^{(f)}}^2 + \sigma_{x_\gamma^{(i)}}^2) + (y^{(f)} - y_\gamma^{(i)})^2 (\sigma_{y^{(f)}}^2 + \sigma_{y_\gamma^{(i)}}^2) + (z^{(f)} - z_\gamma^{(i)})^2 (\sigma_{z^{(f)}}^2 + \sigma_{z_\gamma^{(i)}}^2) \right), \quad (5.20)$$

where  $x^{(i)}, y^{(i)}, z^{(i)}$  are coordinates of the initial point of the track and  $x^{(f)}, y^{(f)}, z^{(f)}$  are coordinates of the final point of the track, and  $\sigma_{x^{(i)}}, \sigma_{y^{(i)}}, \sigma_{z^{(i)}}, \sigma_{x^{(f)}}, \sigma_{y^{(f)}}, \sigma_{z^{(f)}}$  are the corresponding errors.

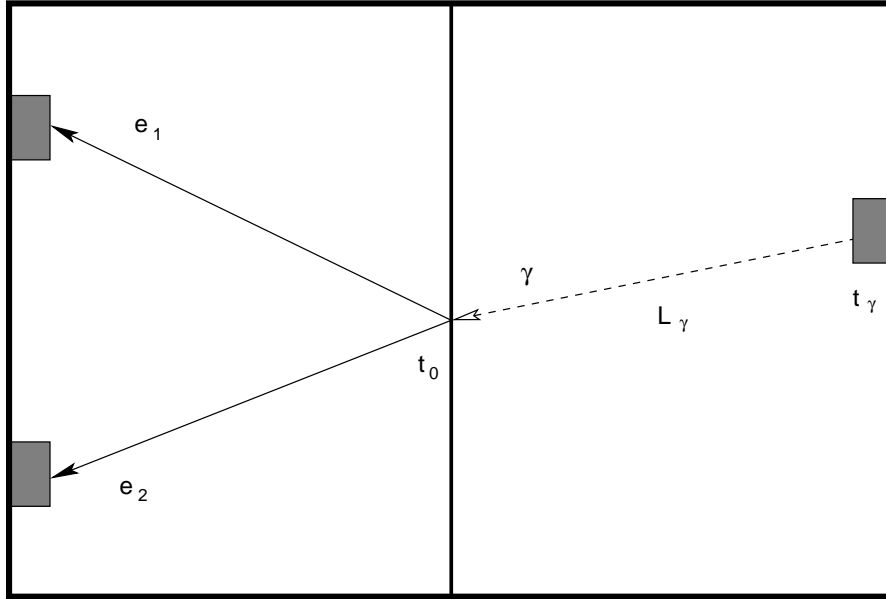


Figure 5.17: An external photon detected at the time  $t_\gamma$  generating two electrons in the source foils at time  $t_0$ .

### Definition of $\chi_{\gamma\gamma int}^2$ for the internal hypothesis for the photons

The  $\chi_{\gamma\gamma int}^2$  variable corresponding to the situation of two photons being both in time with the two electrons (see Fig. 5.18) can be expressed by the following formula:

$$\chi_{\gamma\gamma int}^2 = \frac{\left(t_1 - \left(t_0 + \frac{L_1}{c}\right)\right)^2}{\sigma_{tot,1}^2} + \frac{\left(t_2 - \left(t_0 + \frac{L_2}{c}\right)\right)^2}{\sigma_{tot,2}^2}, \quad (5.21)$$

where  $\sigma_{tot}^2$  is the total error related to the proper measurement of time and to the calculation of  $\Delta t_j = L_j/c$ , i.e. errors on measurements of time  $\sigma_{(t)j}$ , and distance  $\sigma_{(\ell)j}$ , and can be written for the discussed case as:

$$\sigma_{tot,j}^2 = \sigma_{(t)j}^2 + \sigma_{t_0}^2 + \sigma_{(\ell)j}^2.$$

The errors  $\sigma_{(\ell)j}$  on the determination of the distance travelled by photons are given by:

$$\sigma_{(\ell)j}^2 = \left( \frac{1}{cL_j} \right)^2 \left( (x_j^{(f)} - x^{(i)})^2 (\sigma_{x_j^{(f)}}^2 + \sigma_{x^{(i)}}^2) + (y_j^{(f)} - y^{(i)})^2 (\sigma_{y_j^{(f)}}^2 + \sigma_{y^{(i)}}^2) + (z_j^{(f)} - z^{(i)})^2 (\sigma_{z_j^{(f)}}^2 + \sigma_{z^{(i)}}^2) \right), \quad (5.22)$$

where  $x^{(i)}$ ,  $y^{(i)}$ ,  $z^{(i)}$  are the initial coordinates of the tracks, that means that of the common vertex of the two electrons and of both photons,  $x_j^{(f)}$ ,  $y_j^{(f)}$ ,  $z_j^{(f)}$  are coordinates of the track-ends, and  $\sigma_{x^{(i)}}$ ,  $\sigma_{y^{(i)}}$ ,  $\sigma_{z^{(i)}}$ ,  $\sigma_{x_j^{(f)}}$ ,  $\sigma_{y_j^{(f)}}$ ,  $\sigma_{z_j^{(f)}}$  are the corresponding errors.

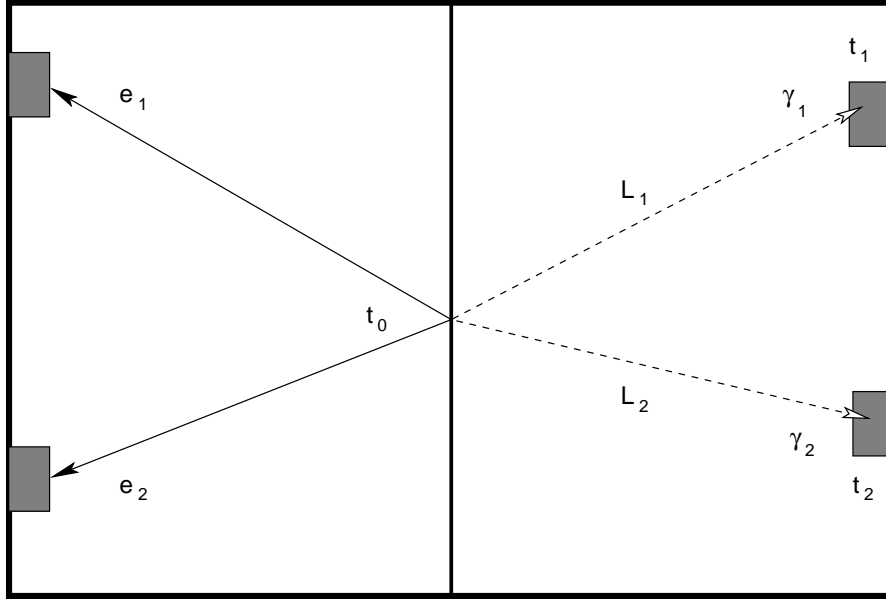


Figure 5.18: An event of the internal type with all the four particles emitted from the source foils at the same time  $t_0$ . Both photons  $\gamma_1$  and  $\gamma_2$ , detected respectively at times  $t_1$  and  $t_2$  after having travelled distances  $L_1$  and  $L_2$ , are thus perfectly in time with the electrons.

### Definition of $\chi_{\gamma\gamma ref}^2$ for the reflection hypothesis

Let us now consider the case of Fig. 5.19 when only one of the two detected photons ( $\gamma$ -clusters) is in time with the two electrons because it was emitted simultaneously with them and then it was reflected and re-detected by another counter. For this situation the  $\chi_{\gamma\gamma ref}^2$  variable takes the following form:

$$\chi_{\gamma\gamma ref}^2 = \frac{\left( t_1 - \left( t_0 + \frac{L_1}{c} \right) \right)^2}{\sigma_{tot,1}^2} + \frac{\left( t_2 - \left( t_0 + \frac{L_{12}}{c} \right) \right)^2}{\sigma_{tot,2}^2}, \quad (5.23)$$

where  $\sigma_{tot,j}^2$  is the total error related to the proper measurement of times  $t_j$  and to the calculation of  $t_0$ , as well as to the distances  $L_1$  between the vertex and the first  $\gamma$ -cluster, and  $L_{12}$  between the first and the second  $\gamma$ -cluster. Then the expressions of  $\sigma_{tot,j}^2$  under the reflection hypothesis can be rewritten like  $\sigma_{tot,j}^2 = \sigma_{(t)j}^2 + \sigma_{t_0}^2 + \sigma_{(\ell)j}^2$ . Errors  $\sigma_{(\ell)j}$  on the determination of the distance travelled by photons are given by:

$$\sigma_{(\ell)1}^2 = \left( \frac{1}{cL_1} \right)^2 \left( (x_1^{(f)} - x^{(i)})^2 (\sigma_{x_1^{(f)}}^2 + \sigma_{x^{(i)}}^2) + (y_1^{(f)} - y^{(i)})^2 (\sigma_{y_1^{(f)}}^2 + \sigma_{y^{(i)}}^2) + (z_1^{(f)} - z^{(i)})^2 (\sigma_{z_1^{(f)}}^2 + \sigma_{z^{(i)}}^2) \right), \quad (5.24)$$

and

$$\sigma_{(\ell)2}^2 = \left( \frac{1}{cL_{12}} \right)^2 \left( (x_2^{(f)} - x_1^{(f)})^2 (\sigma_{x_2^{(f)}}^2 + \sigma_{x_1^{(f)}}^2) + (y_2^{(f)} - y_1^{(f)})^2 (\sigma_{y_2^{(f)}}^2 + \sigma_{y_1^{(f)}}^2) + (z_2^{(f)} - z_1^{(f)})^2 (\sigma_{z_2^{(f)}}^2 + \sigma_{z_1^{(f)}}^2) \right), \quad (5.25)$$

where, as in the previous cases,  $x^{(i)}, y^{(i)}, z^{(i)}$  are initial coordinates of the tracks, that means that of the common vertex of the two electrons and the first photon,  $x_j^{(f)}, y_j^{(f)}, z_j^{(f)}$  are coordinates of the track-ends, and  $\sigma_{x^{(i)}}, \sigma_{y^{(i)}}, \sigma_{z^{(i)}}, \sigma_{x_j^{(f)}}, \sigma_{y_j^{(f)}}, \sigma_{z_j^{(f)}}$  are the corresponding errors.

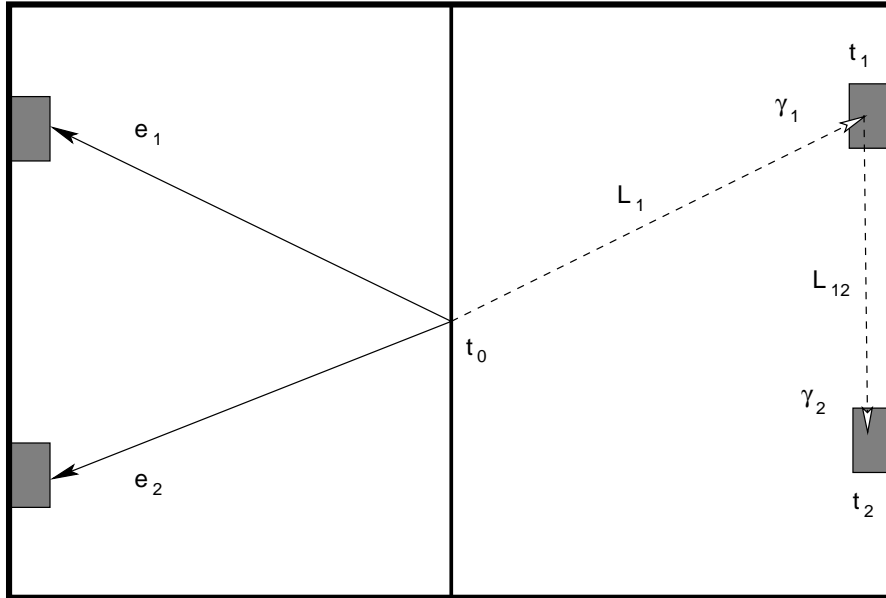


Figure 5.19: In this event only one of the two detected photons ( $\gamma_1$ ) comes from the vertex of the two electrons. The second photon,  $\gamma_2$ , is in reality generated by reflection or re-emission of the first one.

### Selection conditions for the $eeN\gamma$ events from the $2\nu\beta\beta$ g.s. $\rightarrow 0_1^+$ transition

The values of  $\chi_{\gamma ext}^2$  and of the corresponding probability  $Prob_{\gamma ext}$  are determined for each  $\gamma$ -cluster with deposited energy greater than 100 keV (see Sec. 5.8.3). If any of the  $\gamma$ -clusters

satisfies:

$$-\log(\text{Prob}_{\gamma ext}) < 2 , \quad (5.26)$$

then such photon is considered to be an external one and the event is rejected.

In the next stage, the internal hypothesis is tested. For each event,  $\gamma$ -clusters are scanned two by two and values of  $\chi_{\gamma\gamma int}^2$  are determined. The minimum value is however retained and used for the calculation of the probability  $\text{Prob}_{\gamma\gamma int}$  that the event contains two photons in time with the two electrons. Finally, the event is conserved if it satisfies the following condition:

$$-\log(\text{Prob}_{\gamma\gamma int}) < 2 . \quad (5.27)$$

The criteria of Eqs. 5.26 and 5.27 are based on Monte-Carlo simulations. Fig. 5.20 shows distributions of  $-\log(\text{Prob}_{\gamma ext})$  and  $-\log(\text{Prob}_{\gamma\gamma int})$  for the  $2\nu\beta\beta$  decay of  $^{100}\text{Mo}$  to the excited  $0_1^+$  state. Note that the sharp lines at the value of 19 are due only to the fact that  $-\log(\text{Prob}_{xxx})$  was reset to this value for events with  $\text{Prob}_{xxx}$  smaller than  $10^{-19}$ .

Although we could also test the alternative, reflection hypothesis (as it was done for electrons), Monte-Carlo simulations shows that the previous conditions (Eqs. 5.26 and 5.27) are powerful enough to significantly reduce external backgrounds and events from the  $2\nu\beta\beta$  decay to the ground state.

## 5.9 Final set of cuts for the eeN $\gamma$ channel

Thanks to the thorough studies of different conditions and cuts which were applied to the Monte-Carlo events for both the signal and all the significant backgrounds and which have just been detailed in this chapter, we can now give a complete list of the conditions and cuts appointed for the study of the  $2\nu\beta\beta$  decay of  $^{100}\text{Mo}$  to the excited  $0_1^+$  state in the NEMO3 experiment. The events to be retained as candidates for the  $2\nu\beta\beta$  decay to the  $0_1^+$  state have to satisfy all the following conditions:

- there are two tracks with negative curvature (see Sec. 5.6),
- the tracks have common vertex in foils delimited by  $\Delta z \leq 4$  cm and  $\Delta r \leq 4$  cm (see Sec. 5.6),
- the energy of each electron is greater than 200 keV (see Sec. 5.6), i.e.

$$E_{e_1} > 200 \text{ keV} \wedge E_{e_2} > 200 \text{ keV} ,$$

- there are no back-scattered electrons (see Sec. 5.6),
- both electrons have to satisfy the internal hypothesis (see Sec. 5.8.1), i.e.

$$-\log(\text{Prob}_{int}) < 2 \wedge -\log(\text{Prob}_{cross}) > 3 ,$$

- there are at least four fired scintillators: two fired by electrons and other two or more fired by photons,
- the energy sum of the two electrons satisfies  $E_{ee} < 1200$  keV (see Sec. 5.8.2),
- each  $\gamma$ -cluster satisfies  $E_\gamma < 600$  keV (see Sec. 5.8.2),

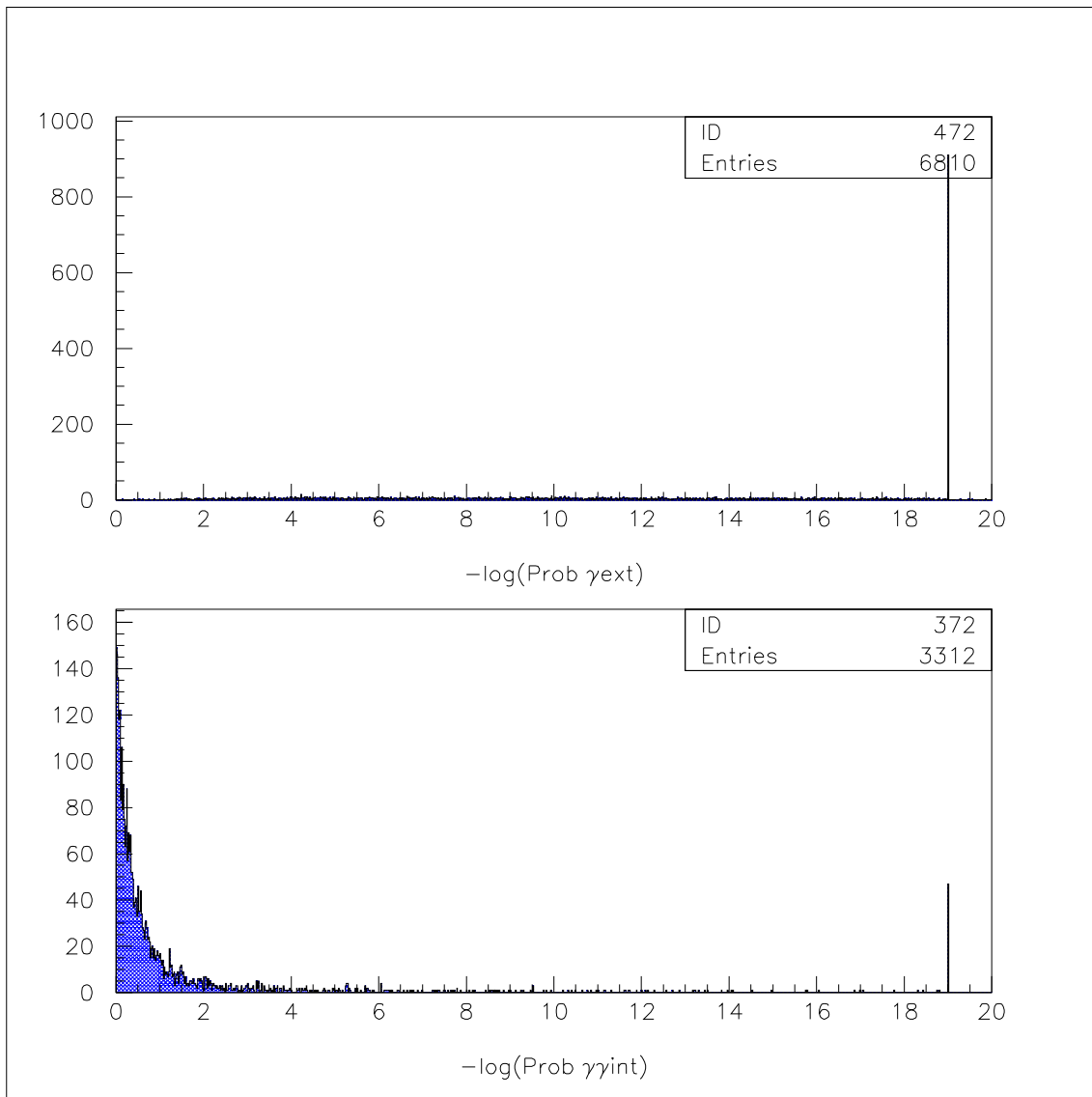


Figure 5.20: Distributions of probability for photons from the  $2\nu\beta\beta$  decay of  $^{100}\text{Mo}$  to the excited state in the cases of the external hypothesis (upper graph) and in the case of the internal hypothesis (lower graph). Note that events with  $-\log(\text{Prob}_{\gamma_{ext}}) > 19$  and  $-\log(\text{Prob}_{\gamma_{int}}) > 19$  respectively are accumulated at 19 forming then sharp lines at this value.

- the energy sum of all the  $\gamma$ -clusters is limited by  $200 \text{ keV} < E_{N\gamma} < 1200 \text{ keV}$  (see Sec. 5.8.2),
- there are at least two  $\gamma$ -clusters with  $\gamma$ -scintillators having deposited energy greater than 100 keV (see Sec. 5.8.3),
- there are no  $\gamma$ -clusters due to the interaction of external photons (see Sec. 5.8.4), i.e. they all fulfil

$$-\log(\text{Prob}_{\gamma ext}) > 2 ,$$

- there are two  $\gamma$ -clusters (photons) that are in time with the two electrons (see Sec. 5.8.4), i.e. the event satisfies

$$-\log(\text{Prob}_{\gamma\gamma int}) < 2 ,$$

- there are no delayed Geiger cells triggered by an  $\alpha$ -particle in the proximity of the reconstructed vertex (see Sec. 5.7).

In order to study the radon contribution to the  $eeN\gamma$  signal and also for the comparison between Monte-Carlo and experimental data, it is interesting to select  $eeN\gamma\alpha$  events too, i.e. events satisfying all the previous conditions with the only exception that we will ask for presence of delayed Geiger cells corresponding to real  $\alpha$ -particles (those with delay time greater than  $40 \mu\text{s}$ ).

## 5.10 Effect of the cuts for the $eeN\gamma$ channel

In this section, the effect of different stages of event selection for the  $eeN\gamma$  channel on internal, external, and radon backgrounds, as well as on the  $2\nu\beta\beta$  decay of  $^{100}\text{Mo}$  to both the ground and the excited  $0_1^+$  states are discussed. The following main stages of event selection are considered:

- 0) no cuts at all;
  - 1) selection of two  $e^-$  tracks having common vertex, each with an associated scintillator satisfying  $E_{e_j} > 200 \text{ keV}$ ;
  - 2) stage 1 plus internal hypothesis is satisfied by the electrons;
  - 3) stage 2 plus all the conditions on  $E_{ee}$ ,  $E_\gamma$ , and  $E_{N\gamma}$  are fulfilled by the event;
  - 4) stage 3 plus the time-of-flight conditions and absence of an  $\alpha$ -particle are satisfied;
- 4bis)** stage 3 plus the time-of-flight conditions and presence of an  $\alpha$ -particle are satisfied.

Each time the most discriminating conditions are mentioned and the numbers of selected events together with corresponding probabilities for different stages of selection are summarised in tables for each kind of studied process.

### 5.10.1 Internal background

As regards the internal background generated by isotopic impurities of  $^{208}\text{Tl}$  and  $^{214}\text{Bi}$  in source foils, there is relatively high probability, reaching about  $(3 - 5) \times 10^{-3}$ , to produce two-electron events through the Möller or Compton effects in the foils. These events are not eliminated by the time-of-flight test for electrons because they are of internal origin. The powerful conditions that remove a great part of these events are, first of all, that the number of fired scintillators has to be greater or equal to four, and then the energy cuts for  $E_{ee}$ ,  $E_{\gamma}$ , and  $E_{N\gamma}$ , especially their upper limits. In the next stage, the internal background contribution is further reduced when at least two  $\gamma$ -clusters with  $\gamma$ -scintillators of more than 100 keV are requested. In the end, there is a certain fraction of events with a probability of about  $(6 - 8) \times 10^{-5}$  which satisfy the complete set of conditions for the eeN $\gamma$  channel. The real background contribution, however, strongly depends on the level of  $^{208}\text{Tl}$  and  $^{214}\text{Bi}$  activities. Fortunately, this background was significantly reduced during the phase of the source foils purification<sup>4</sup> and, in consequence, does not represent any danger for the eeN $\gamma$  channel as it will be shown in Sec. 5.11.2. The effect of the different stages of the eeN $\gamma$  event selection in term of numbers of selected Monte-Carlo events and corresponding probabilities for both  $^{208}\text{Tl}$  and  $^{214}\text{Bi}$  are summarised in Tabs. 5.8 and 5.9.

Stage	Description of cuts	Selected	Probability
0	no cuts	229 570	0.459
1	two electrons	2 424	$4.85 \times 10^{-3}$
2	(1) & TOF(ee)	1 890	$3.78 \times 10^{-3}$
3	(2) & energy cuts	210	$4.20 \times 10^{-4}$
4	all the cuts	41	$8.2 \times 10^{-5}$

Table 5.8: Numbers of events and corresponding probabilities at different stages of event selection for internal background from  $^{208}\text{Tl}$ .

Stage	Description of cuts	Selected	Probability
0	no cuts	165 034	0.330
1	two electrons	1 653	$3.31 \times 10^{-3}$
2	(1) & TOF(ee)	1 396	$2.79 \times 10^{-3}$
3	(2) & energy cuts	166	$3.32 \times 10^{-4}$
4	all the cuts	33	$6.6 \times 10^{-5}$
4bis	all the cuts (with $\alpha$ )	3	$6.0 \times 10^{-6}$

Table 5.9: Numbers of events and corresponding probabilities at different stages of event selection for the internal background from  $^{214}\text{Bi}$ .

### 5.10.2 External background

We will discuss only the external background from  $^{208}\text{Tl}$  and  $^{214}\text{Bi}$  contained in the glass of the PMTs because, as it was previously stated in Sec. 4.8, it is the most significant contribution of

---

<sup>4</sup>For details, see Sec. 4.5.2 and Tab. 4.6.

the external background that has to be taken into account. From Tabs. 5.10 and 5.11 which give numbers of selected events and corresponding probabilities for both  $^{208}\text{Tl}$  and  $^{214}\text{Bi}$ , it can be seen that there is low probability on the order of  $10^{-6}$  to produce two-electron events. Most often, they are caused either by electrons crossing the detector from one scintillator, through the source foils, as far as to another scintillator; or by  $(e^+e^-)$  pair creation in the source foils. In both scenarios, the track curvature of one of the particles (incoming electron or positron) was probably rather straight and thus erroneously determined by the track reconstruction program to be the opposite curvature. If the time-of-flight test for electrons is applied, these events are then removed. Further reduction is achieved with the energy cuts for  $E_{ee}$ ,  $E_\gamma$ , and  $E_{N\gamma}$ , with the request of at least two  $\gamma$ -scintillators of two distinct  $\gamma$ -clusters with energy greater than 100 keV, and, at the end, with the time-of-flight tests for photons. So, the final contribution of this kind of background to the  $eeN\gamma$  channel is negligible.

Stage	Description of cuts	Selected	Probability
0	no cuts	167 148	$1.67 \times 10^{-3}$
1	two electrons	535	$5.35 \times 10^{-6}$
2	(1) & TOF(ee)	26	$2.6 \times 10^{-7}$
3	(2) & energy cuts	2	$2.0 \times 10^{-8}$
4	all the cuts	0	0

Table 5.10: Numbers of events and corresponding probabilities at different stages of event selection for external background from  $^{208}\text{Tl}$ .

Stage	Description of cuts	Selected	Probability
0	no cuts	150 903	$3.77 \times 10^{-4}$
1	two electrons	362	$9.05 \times 10^{-7}$
2	(1) & TOF(ee)	22	$5.5 \times 10^{-8}$
3	(2) & energy cuts	2	$5.0 \times 10^{-9}$
4	all the cuts	1	$2.5 \times 10^{-9}$

Table 5.11: Numbers of events and corresponding probabilities at different stages of event selection for external background from  $^{214}\text{Bi}$ .

### 5.10.3 $\beta\beta$ events from molybdenum

#### Excited state events

The probability that a decay from the  $2\nu\beta\beta$  decay of  $^{100}\text{Mo}$  to the excited  $0_1^+$  state produces a two-electron event is only 1 – 2% (compared to  $\sim 6\%$  for the  $2\nu\beta\beta$  decay to the ground state). The reason consists of the lower available kinetic energy for electrons which can together reach up to 1900 keV at maximum because a total energy of 1130 keV is always carried away by de-excitation photons. As regards the kinematic cuts, a certain reduction comes in particular from the requirement of at least four fired scintillators and from the  $E_{ee}$  and  $E_{N\gamma}$  cut-offs, mostly from their lower limits. At the next stage of the selection, further events are rejected because they do not contain at least two  $\gamma$ -clusters with enough deposited energy to be used

in the time-of flight tests for photons. Finally, the probability that an event from the  $2\nu\beta\beta$  decay to the excited  $0_1^+$  state satisfies the complete set of selection criteria is about  $3 \times 10^{-3}$  (see Tab. 5.12). Fig. 5.21 shows the distribution of these events in the two-dimensional  $E_{N\gamma}$  vs.  $E_{ee}$  plot. Although the value of the selection probability could seem relatively small, the selection criteria were optimised in order to conserve the maximum of unambiguously signed signal events and, at the same time, to significantly reduce all the possible backgrounds.

Stage	Description of cuts	Selected	Probability
0	no cuts	426 736	0.427
1	two electrons	16 854	$1.7 \times 10^{-2}$
2	(1) & TOF(ee)	11 352	$1.1 \times 10^{-2}$
3	(2) & energy cuts	6 802	$6.8 \times 10^{-3}$
4	all the cuts	2 728	$2.7 \times 10^{-3}$

Table 5.12: Numbers of events and corresponding probabilities at different stages of event selection for the  $2\nu\beta\beta$  decay of  $^{100}\text{Mo}$  to the excited  $0_1^+$  state.

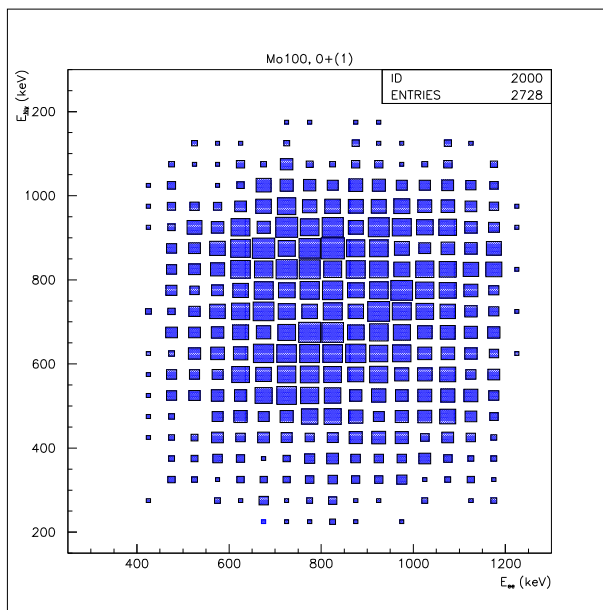


Figure 5.21: The distribution of finally selected  $eeN\gamma$  events for the  $2\nu\beta\beta$  decay of  $^{100}\text{Mo}$  to the excited  $0_1^+$  state in the  $E_{N\gamma}$  vs.  $E_{ee}$  plot.

### Ground state events

The probability to generate a two-electron event is for the  $2\nu\beta\beta$  decay to the ground state by far the highest from all the processes studied in the present work and it reaches about 6% (see Tab. 5.13). Nevertheless, the condition requesting at least four fired scintillators is very reducing and rejects almost all the two-electron events from the  $2\nu\beta\beta$  decay to the ground state because, as Fig. 5.22 and Tab. 5.14 show, less than 0.5% of decays are capable of producing more than one

photon. The remaining events are then further decreased in number by the rejection of events with back-scattered electrons and after the application of the kinematic cuts, in particular due to the upper limit of 1200 keV for the  $E_{ee}$  cut-off, as well as due to the lower limit of 200 keV imposed on  $E_{N\gamma}$ . After that, there is more rejection caused by the condition of asking for two  $\gamma$ -clusters with enough energy to apply the time-of-flight tests for photons. At the end, the probability to satisfy all the  $eeN\gamma$  selection conditions is about  $2 \times 10^{-6}$  which is more than 1000 times less than for the excited state events. Assuming, for example, the difference of two orders in the half-lives between the two transitions, there is still factor 10 – 15 in the number of expected events in favour of the  $2\nu\beta\beta$  decay to the excited  $0_1^+$  state.

Stage	Description of cuts	Selected	Probability
0	no cuts	429 077	0.248
1	two electrons	127 746	$6.38 \times 10^{-2}$
2	(1) & TOF(ee)	114 111	$5.70 \times 10^{-2}$
3	(2) & energy cuts	170	$8.5 \times 10^{-5}$
4	all the cuts	4	$2.0 \times 10^{-6}$

Table 5.13: Numbers of events and corresponding probabilities at different stages of event selection for the  $2\nu\beta\beta$  decay of  $^{100}\text{Mo}$  to the ground state.

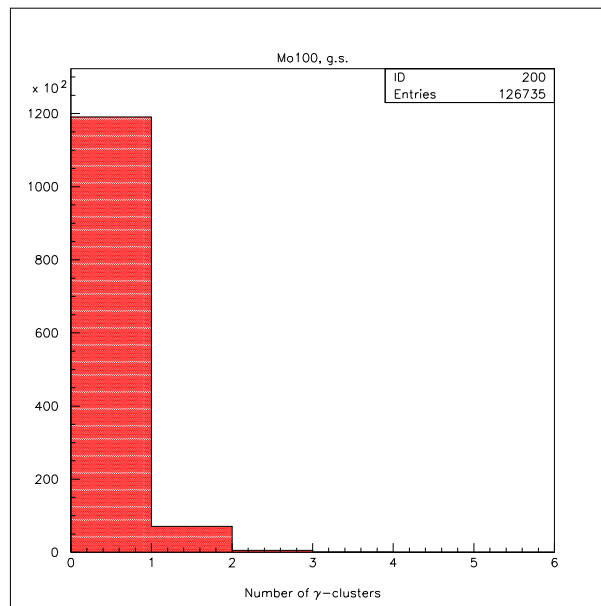


Figure 5.22: Distribution of the number of  $\gamma$ -clusters generated in the  $2\nu\beta\beta$  decay of  $^{100}\text{Mo}$  to the ground state.

#### 5.10.4 Radon contribution

As Tab. 5.15 shows, the probability that a  $^{214}\text{Bi} - ^{214}\text{Po}$  decay inside the detector produces a two-electron event is approximately 10 times lower than in the case of the internal background

# $\gamma$ -clusters	0	$\geq 1$	1	$\geq 2$
Proportion (%)	93.95	6.05	5.60	0.45

Table 5.14: Numbers of  $\gamma$ -clusters for the  $2\nu\beta\beta$  decay of  $^{100}\text{Mo}$  to the ground state.

from  $^{208}\text{Tl}$  and  $^{214}\text{Bi}$  contamination of the source foils. This probability is furthermore four times reduced when the time-of-flight test for electrons is applied. In fact, only those  $^{214}\text{Bi} - ^{214}\text{Po}$  decays giving two-electron events that occurred relatively close to the source foils were selected. The  $^{214}\text{Bi}$  atoms decay mainly through an  $e^- \gamma$  cascade (cf. Fig. 4.12) and can produce two electrons in the He gas of the wire chamber much less often than inside the source foils, which is the case of the  $^{214}\text{Bi}$  pollution of molybdenum, where the Möller and Compton effects intervene. Some typical  $^{214}\text{Bi}$  decays in the gas which will not be selected are illustrated in Figs. 5.9, 5.23, and 5.24.

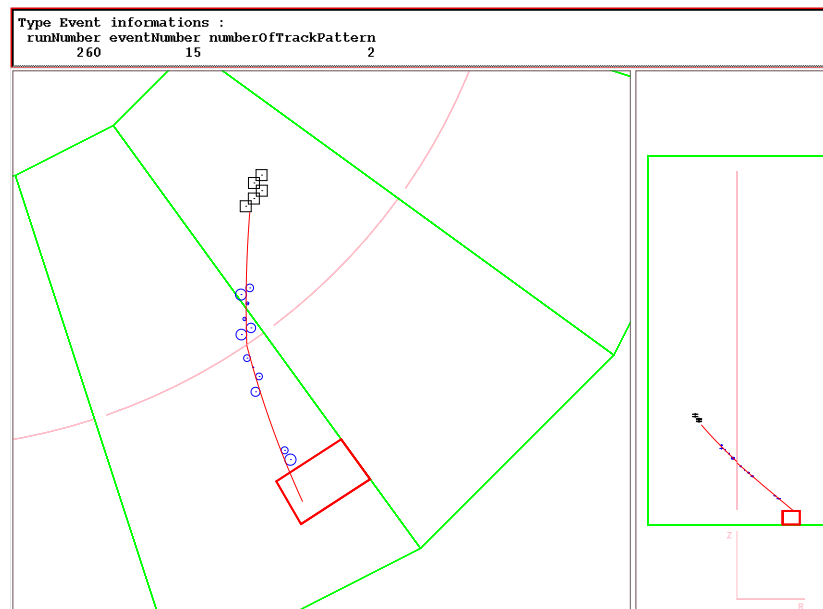


Figure 5.23: An example of a  $^{214}\text{Bi} - ^{214}\text{Po}$   $e\alpha$  event in the wire chamber gas. Although the electron crossing a source foil could be seen by the analysis program as a two-electron event with a common vertex in the foils, it will be rejected because one of the tracks have no associated scintillator.

If the energy cuts are applied, the selection probability decreases 10 times again to the level of about  $10^{-5}$ . The most discriminating criteria are the request for more than four fired scintillators and the upper limit of 1200 keV for the  $E_{ee}$  cut-off. At the next stage, the situation is similar to other kinds of background: a strongly reducing condition is again the demand of two  $\gamma$ -clusters containing each at least one scintillator with the deposited energy exceeding 100 keV. Finally, from the total of  $15 \times 10^6$  generated events, there are only 11 events that satisfied all the imposed cuts which is equivalent to a probability of about  $7 \times 10^{-7}$ . Although the probability is rather low, the level of danger of this background depends above all on the activity of radon inside the detector. If we process the same selection but with the demand of  $\alpha$ -particles in events, we

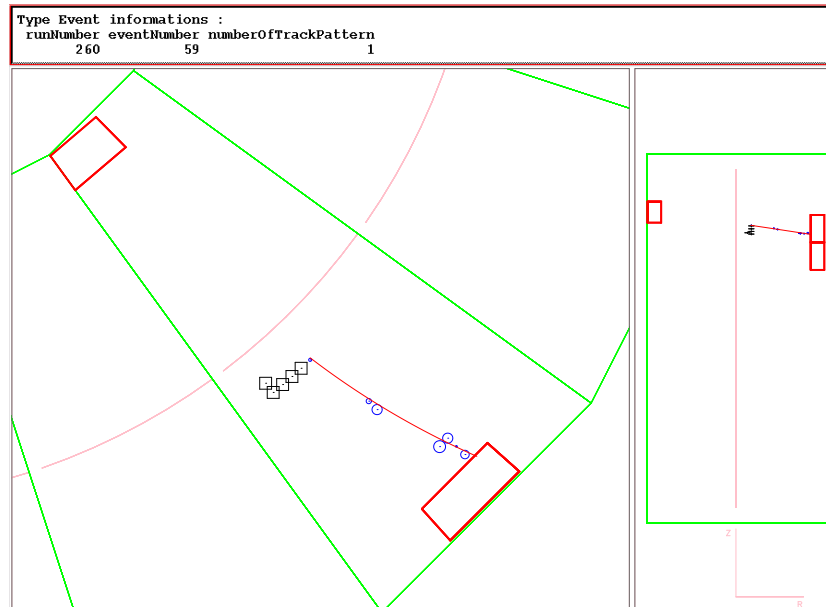


Figure 5.24: An example of a  $^{214}\text{Bi} - ^{214}\text{Po}$  e2 $\gamma$  $\alpha$  event generated in the wire chamber gas.

will also get 11 events. These results are summarised in Tab. 5.15 and three examples of eeN $\gamma$  $\alpha$  events after the stage 4bis of the event selection are shown in Figs. 5.26, 5.27, and 5.28. The distribution of the finally selected events of both types, i.e. with or without  $\alpha$ -particles, in the form of a two-dimensional  $E_{N\gamma}$  vs.  $E_{ee}$  plot, however with the upper limit of  $E_{ee}$  shifted up to 2000 keV, is presented in Fig. 5.25.

#	Description of cuts	Selected	Probability
0	no cuts	11 930 827	0.795
1	two electrons	4 917	$3.28 \times 10^{-4}$
2	(1) & TOF(ee)	1 852	$1.23 \times 10^{-4}$
3	(2) & energy cuts	171	$1.14 \times 10^{-5}$
4	all the cuts & no $\alpha$ 's	11	$7.3 \times 10^{-7}$
4bis	all the cuts & with $\alpha$ 's	11	$7.3 \times 10^{-7}$

Table 5.15: Numbers of events and corresponding probabilities at different stages of event selection for  $^{214}\text{Bi} - ^{214}\text{Po}$  events (background from radon).

The proportion between finally selected events with and without  $\alpha$ -particle is equal to 1. This ratio stays close to 1 even if we modify the upper limit imposed to  $E_{ee}$  from 1200 keV to 2000 keV as it can be seen from Tab. 5.16). This phenomenon is understandable because, in fact, only the decays close to the source foils can satisfy the complete set of cuts, and in particular the time-of-flight condition for electrons. About 50% of all these  $^{214}\text{Bi} - ^{214}\text{Po}$  decays occurring close to the source foils and producing two electrons will emit an  $\alpha$ -particle towards the foils where it will be stopped, while in the other 50% of decays the  $\alpha$ -particle will propagate in the opposite direction and will be then detected by the tracking wire chamber.

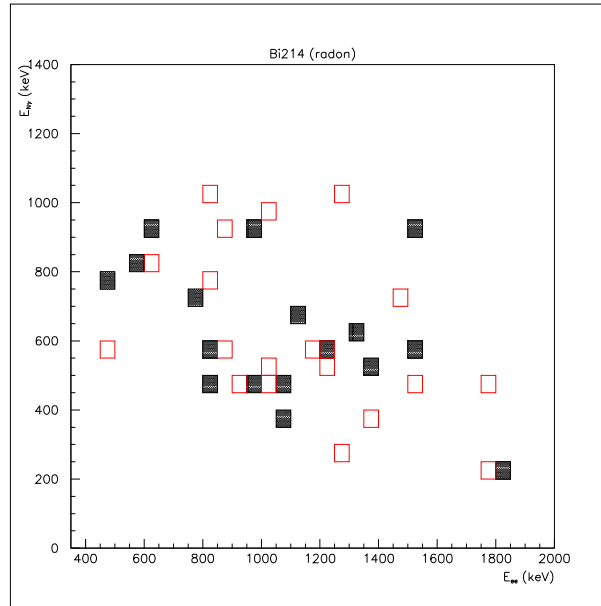


Figure 5.25: A two-dimensional  $E_{N\gamma}$  vs.  $E_{ee}$  plot for the finally selected events from  $^{214}\text{Bi}$  decay inside the wire chamber. The filled black boxes represent events without  $\alpha$ -particles, while the empty red one's correspond to events with  $\alpha$ -particles. Note that the upper limit of  $E_{ee}$  was pushed up to 2000 keV.

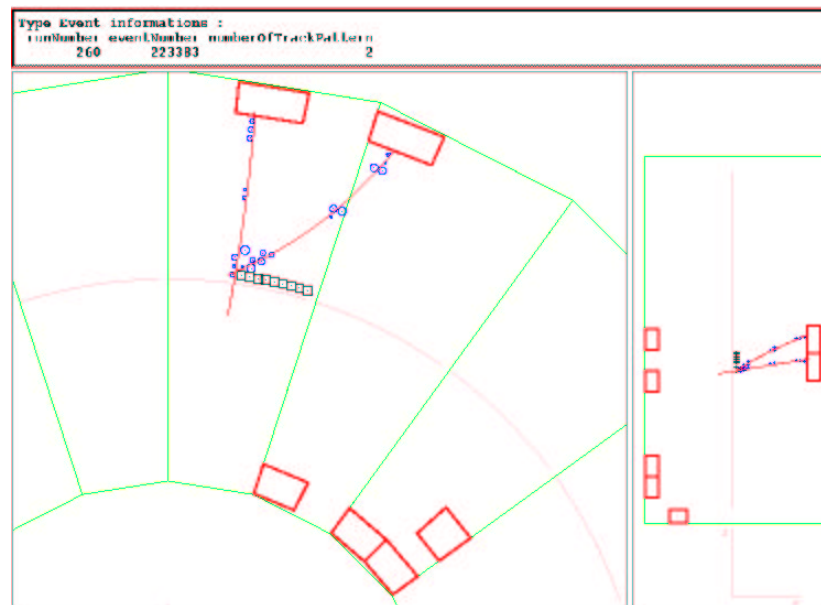


Figure 5.26: An example of a  $^{214}\text{Bi} - ^{214}\text{Po}$  decay generated in the wire chamber gas producing a two-electron event accompanied by an  $\alpha$ -particle which is represented here with squares corresponding to delayed Geiger cells.

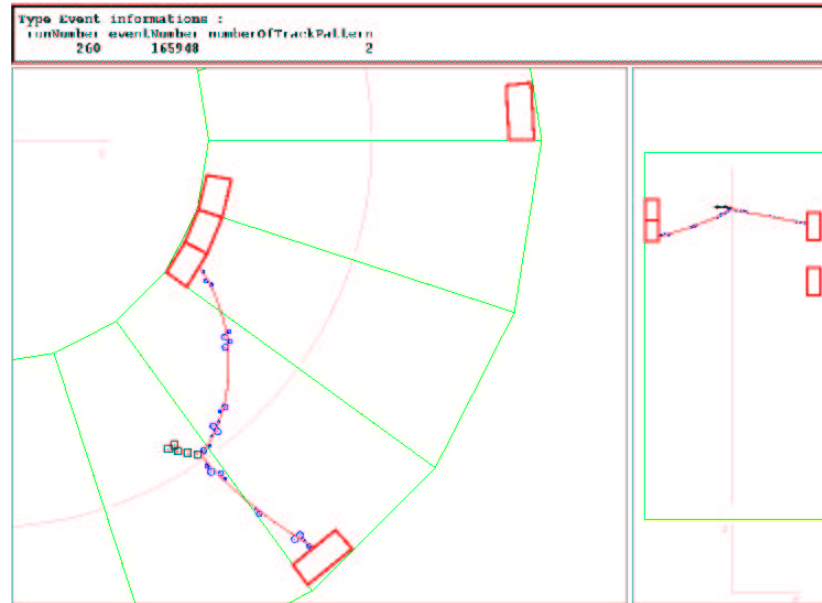


Figure 5.27: Another example of a simulated  $^{214}\text{Bi} - ^{214}\text{Po}$  decay in the gas of the wire chamber producing an  $ee2\gamma\alpha$  event.

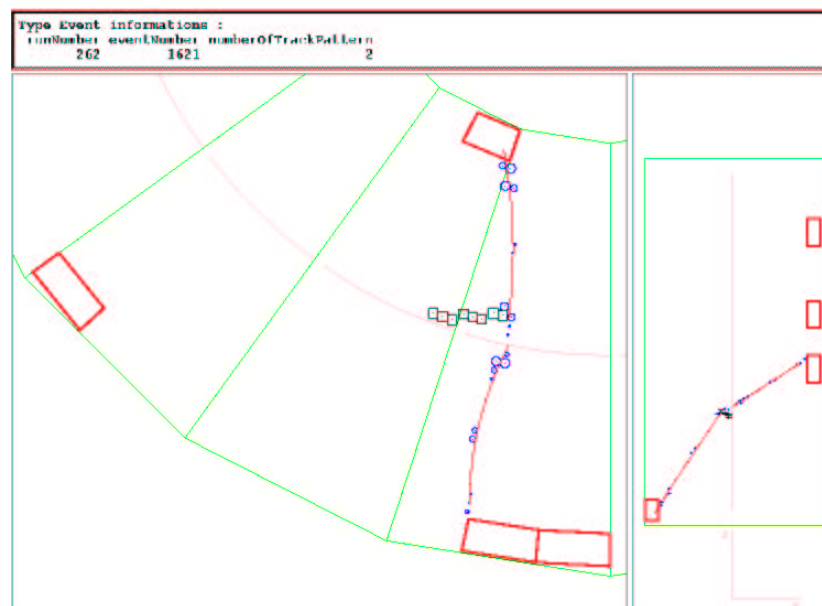


Figure 5.28: Top and transverse views of a  $^{214}\text{Bi} - ^{214}\text{Po}$  decay generated by Monte-Carlo in the gas of the wire chamber giving an  $ee2\gamma\alpha$  event. The  $\alpha$ -particle is represented by squares corresponding to delayed Geiger cells. The vertex of the decay is clearly inside the gas and one of the electrons had to cross through the source foils.

$E_{ee}$ cut-off applied in the eeN $\gamma$ selection	Number of events (Proportion)		
	all events	with $\alpha$	without $\alpha$
$E_{ee} < 2000$ keV	37 (100%)	22 (54%)	17 (46%)
$E_{ee} < 1200$ keV	22 (100%)	11 (50%)	11 (50%)

Table 5.16: Numbers of  $^{214}\text{Bi} - ^{214}\text{Po}$  events with and without detected  $\alpha$ -particle which satisfy all the cuts with two different  $E_{ee}$  cut-offs.

## 5.11 Number of expected events

### 5.11.1 Calculation of number of expected events

The number of expected events, derived from the radioactivity decay law and including the efficiency  $\eta$  of the considered channel can be expressed by the following formula:

$$N_{evt}(t) = \eta N_{at} \left( 1 - e^{-\ln 2(t/T_{1/2})} \right), \quad (5.28)$$

where  $N_{at}$  is the number of atoms in a sample ( $N_{at} = 4.2 \times 10^{25}$  for 7 kg of  $^{100}\text{Mo}$ ),  $t$  is the net data acquisition time, and  $T_{1/2}$  is the half-life of the studied decay mode. Because of the large value of  $T_{1/2}$  for  $\beta\beta$  decays compared to  $t$ , one can rewrite Eq. 5.28 in the following way:

$$N_{evt}(t) = \eta N_{at} \ln 2 \frac{t}{T_{1/2}}. \quad (5.29)$$

In the case of a radioactive source of known activity  $A$  (in Bq), the number of expected events after time  $t$  (in seconds) and with the detection efficiency  $\eta$  for a given channel is:

$$N_{evt}(t) = \eta A t. \quad (5.30)$$

### 5.11.2 Expected contributions to the eeN $\gamma$ channel

Knowing all the important parameters like the half-lives of the  $2\nu\beta\beta$  decay of  $^{100}\text{Mo}$  to the ground state and to the excited  $0_1^+$  state, as well as the activities of the considered backgrounds, we can deduce using Eqs. 5.29 and 5.30 numbers of events expected for a certain period  $t$ . Tab. 5.17 gives numbers of events expected for a perfect detector and for 12 sectors mounted with  $^{100}\text{Mo}$  foils with a total mass of 7 kg after respectively 1000 hr and 1 yr of data acquisition time. In the case of the  $2\nu\beta\beta$  (g.s.  $\rightarrow 0_1^+$ ) decay, two half-life values of  $6 \times 10^{20}$  yr and  $1 \times 10^{21}$  yr respectively are used because the experimentally obtained half-lives have been found inside this range (see Sec. 3.2). As regards the external background, the measured values of activities in  $^{208}\text{Tl}$  and in  $^{214}\text{Bi}$  of the PMT glass (the dominant contribution) are used. In the case of the internal contamination, the radiopurity upper limits<sup>5</sup> are applied here. Because of the variation with time of the level of  $^{222}\text{Rn}$  inside the wire chamber of NEMO3, especially during the autumn 2002 runs, the number of expected events for this kind of background is evaluated just with the average volumic activity of 30 mBq/m<sup>3</sup>.

Regarding Tab. 5.17, an important remark about the calculated values for the external background has to be made. They have been obtained with efficiencies given in Tabs. 5.10 and

---

<sup>5</sup>See Sec. 4.5.2 and Tab. 4.6.

Isotope	Process	$T_{1/2}$ or $A$	Number of events	
			1000 hr	1 yr
$^{100}\text{Mo}$	$2\nu\beta\beta \rightarrow 0_1^+$	$6 \times 10^{20}$ yr	<b>15.1</b>	<b>131.9</b>
		$1 \times 10^{21}$ yr	<b>9.0</b>	<b>79.1</b>
$^{100}\text{Mo}$	$2\nu\beta\beta \rightarrow \text{g.s.}$	$0.95 \times 10^{19}$ yr	0.7	6.1
$^{208}\text{Tl}$	internal bgd	$< 20 \mu\text{Bq/kg}$	$\approx 0$	$< 0.4$
$^{214}\text{Bi}$	internal bgd	$< 300 \mu\text{Bq/kg}$	$< 0.5$	$< 4.4$
$^{208}\text{Tl}$	external bgd	18 Bq	0	0
$^{214}\text{Bi}$	external bgd	300 Bq	2.7	23.7 <sup>a</sup>
<b><math>^{214}\text{Bi}</math></b>	<b>radon</b>	30 mBq/m <sup>3</sup>	<b>2.4</b>	<b>20.7</b>

<sup>a</sup>These two values have big uncertainties as it is discussed in the text. The limits  $N_{evt}(1000 \text{ hr}) \leq 0.36$  and  $N_{evt}(1 \text{ yr}) \leq 3.17$  which were determined experimentally by the means of special runs with a source of  $^{214}\text{Bi}$  have to be considered instead (see Sec. 6.4.3).

Table 5.17: Numbers of expected events issued from Monte-Carlo simulations for different studied processes after the application of the complete set of energy and TOF cuts for the eeN $\gamma$  channel. The ideal detector with 12 sectors mounted with 7 kg of  $^{100}\text{Mo}$  sources is considered here. The main contributions are in bold.

5.11. which could have, however, rather large errors resulting from limited statistics. In the case of  $^{208}\text{Tl}$  the number of  $1 \times 10^8$  decays generated by Monte-Carlo simulation program corresponds approximately to 1540 hr what could be sufficient at the present time for the comparison with currently available experimental data. In contrast, the number of  $4 \times 10^8$  generated decays of  $^{214}\text{Bi}$  is roughly equivalent to 370 hr of the real running time and is insufficient for comparison with the present experimental data. Thus the values of the expected contribution from external background due to  $^{214}\text{Bi}$  which are presented in Tab. 5.17 obviously have huge errors. For this reason the influence of the external background from these two isotopes had to be studied also experimentally. Special runs with sources containing  $^{208}\text{Tl}$  and  $^{214}\text{Bi}$  have been carried out as is explained further in Sec. 6.4.3. These runs confirmed the zero contribution from  $^{208}\text{Tl}$  and produced more reliable results for  $^{214}\text{Bi}$  which are the following:

$$N_{evt}(1000 \text{ hr}) \leq 0.36 \quad \text{and} \quad N_{evt}(1 \text{ yr}) \leq 3.17 \quad .$$

Nevertheless, the Monte-Carlo simulations of the external background were very useful for the definition of kinematic and temporal cuts, in particular during the period when no experimental data were yet available, i.e. during the construction of the NEMO3 detector and later during the phase of long and thorough tests of the experimental setup.

## 5.12 Conclusions

It can be concluded from the results presented in Tab. 5.17 that the contribution of the internal background to the eeN $\gamma$  channel is, as it was expected from the beginning, negligible. This is mainly due to the very good purity of the  $^{100}\text{Mo}$  source foils. According to the Monte-Carlo simulations, the contribution of the external background from  $^{208}\text{Tl}$  to the eeN $\gamma$  channel is also negligible. By contrast, the result obtained for the external background from  $^{214}\text{Bi}$  is controversial because of the great uncertainty resulting from the technical difficulty to generate enough of events of this kind with the simulation program. Finally, even the contribution from

the  $2\nu\beta\beta$  decay of  $^{100}\text{Mo}$  to the ground state is expected to be tiny; compared to the expected signal it would be 13 – 23 times smaller. At the present time, the most important background contribution comes from the  $^{214}\text{Bi} - ^{214}\text{Po}$  events in the gas of the wire chamber which are caused by the intrusion of radon inside the detector. The danger of this kind of background for the excited state signal is, of course, strongly dependant on the activity level of radon inside NEMO3. Although the ratio between the excited state events and the radon events is currently expected to be between 3.8 and 6.4 for the average radon activity of 30 mBq/kg and the half-life  $T_{1/2}^{2\nu\beta\beta}(^{100}\text{Mo}, 0_1^+)$  between  $6 \times 10^{20}$  yr and  $1 \times 10^{21}$  yr, it is preferable to achieve a significant reduction of the radon level inside the detector by a factor of ten in order to improve the signal/background ratio.

# Chapter 6

## Data analysis

At the beginning of this chapter, the software tools used for the data analysis and the triggers applied for data acquisition are described. The final selection criteria for the study of the  $2\nu\beta\beta$  decay of  $^{100}\text{Mo}$  to the excited  $0_1^+$  state are then recalled. Afterwards, a description of special runs with sources of  $^{208}\text{Tl}$  and  $^{214}\text{Bi}$ , with their results follow. The main part of this chapter is focused on the analysis of about 2900 hr of experimental data from the NEMO3 experiment which were available from May 2002 to May 2003. Finally, the result obtained from these data is given in the form of limits at 95% confidence level on the half-life value for the  $2\nu\beta\beta$  (g.s.  $\rightarrow 0_1^+$ ) decay of  $^{100}\text{Mo}$ .

### 6.1 Software tools for the data analysis

Experimental data from the NEMO3 detector are recorded in the form of n-tuples in **raw data format** which contain:

- general information about the current run: number and date of the run, number of recorded events, number and time of each event;
- data from the calorimeter: number of triggered scintillators, their location in the detector, and the contents of the ADC and TDC of the PMTs corresponding to these counters;
- data from the wire chamber: number of fired Geiger cells, their location, and the corresponding contents of the TDCs for the anodic and both top and bottom cathodic signals, as well as contents of slow TDCs<sup>1</sup>.

These raw data are then reformatted to so called **analysis format** which, compared to the raw data format, is enriched with new n-tuple fields that are useful for data analysis. The latter are, for instance:

- real energies and times with corresponding errors for fired scintillator counters recalculated from the TDC and ADC contents;
- reconstructed positions of charge particles' passage and corresponding errors for fired Geiger cells;

---

<sup>1</sup>For details, see Sec. 4.7.1.

- further track(s) information: number of reconstructed tracks, its(their) length(s), information about its(their) starting and ending point(s), position of reconstructed vertex(vertices), ID of scintillator(s) associated to the tracks(s) if any and the impact point(s) in scintillator(s), and information about its(their) curvature and fit parameters;
- $\alpha$ -track information whether an  $\alpha$ -track was reconstructed from delayed Geiger cells.

Files in the analysis format are produced with **anal.exe** program [155] developed in LAL Orsay. This program calls the NEMO3 database [156] containing all the time and energy calibrations, both laser and time-energy corrections, as well as the whole set of run parameters.

The proper data analysis, i.e. selection of interesting events, drawing of different spectra, distributions and so on, is individual and depends essentially on each user and on the analysed channel. Generally and partly also historically, the NEMO Collaboration uses mainly **FORTRAN** code and the **PAW** data analysis and display framework, nevertheless the structure of data allows the use of C(C++) and ROOT as well. For visualisation of events, we use a program called **Vis.exe** [155] which is a versatile, fully graphical tool developed in LAL Orsay for the NEMO3 experiment.

## 6.2 Definition of particles in real events

As the structures of the Monte-Carlo and real experimental data are exactly the same, definitions of particles for real data events will be identical to those given in Sec. 5.3. In a short review, the particles identified in the NEMO3 experimental data can be characterised in the following way:

- **electrons (positrons)** coming from the source foils are identified by a reconstructed track with negative (positive) curvature;
- **photons** are characterised by  $\gamma$ -clusters avoiding, however, back-scattered electrons capable of producing false photons;
- **$\alpha$ -particles** are revealed by delayed Geiger cell hits with delay time greater than 40  $\mu$ s in order not to confuse them with refired Geiger cells as detailed in Sec. 5.3.3.

## 6.3 Selection of events for the $eeN\gamma$ channel

Selection of the  $eeN\gamma$  events which may be considered as candidates of  $2\nu\beta\beta$  decay of  $^{100}\text{Mo}$  to the excited  $0_1^+$  state is based on studies of Monte-Carlo events presented in details in Chapter 5. Events can be selected according to the location of the reconstructed vertex and can be thus divided into the following two groups:

- events with the vertex located in molybdenum foils;
- events with the vertex located in the other, non-molybdenum foils.

In the case of the  $2\nu\beta\beta$  decay to the second excited state, the eight non-molybdenum sectors (sectors 06-07-08-09 and 17-18-19-00, cf. Fig. 4.7) are used for measurement of external and radon induced backgrounds. So, using the  $eeN\gamma$  channel, the background contribution to the signal can be, in addition to the estimation based on Monte-Carlo data, directly measured

with these non-molybdenum sectors. In the case of the  $eeN\gamma\alpha$  channel, the radon background contribution to the signal can be estimated from all the twenty sectors. The selection conditions and cuts for real data are the same as they were defined in Sec. 5.9 for the Monte-Carlo data and they are summarised in the following list:

### 1. Two-electron preselection

- there are two tracks with negative curvature (see Sec. 5.6),
- the tracks have a common vertex in the foils delimited by  $\Delta z \leq 4$  cm and  $\Delta r \leq 4$  cm (see Sec. 5.6),
- energy of each electron is greater than 200 keV (see Sec. 5.6), i.e.

$$E_{e_1} > 200 \text{ keV} \wedge E_{e_2} > 200 \text{ keV} ,$$

- there are no back-scattered electrons (see Sec. 5.6),
- both electrons have to satisfy the internal hypothesis (see Sec. 5.8.1), i.e.

$$-\log(\text{Prob}_{int}) < 2 \wedge -\log(\text{Prob}_{cross}) > 3 ,$$

### 2. Energy cuts

- there are at least four fired scintillators,
- the energy sum of the two electrons satisfies  $E_{ee} < 1200$  keV (see Sec. 5.8.2),
- each  $\gamma$ -cluster satisfy  $E_\gamma < 600$  keV (see Sec. 5.8.2),
- the energy sum of all the  $\gamma$ -clusters is limited by  $200 \text{ keV} < E_{N\gamma} < 1200$  keV (see Sec. 5.8.2),
- there are at least two  $\gamma$ -clusters with  $\gamma$ -scintillators having deposited energy greater than 100 keV (see Sec. 5.8.3),

### 3. Time-of-flight cuts for photons

- there are no  $\gamma$ -clusters due to the interaction of external photons (see Sec. 5.8.4), i.e. they all fulfil

$$-\log(\text{Prob}_{\gamma ext}) > 2 ,$$

- there are two  $\gamma$ -clusters (photons) that are in time with the two electrons (see Sec. 5.8.4), i.e. the event satisfies

$$-\log(\text{Prob}_{\gamma\gamma int}) < 2 ,$$

### 4. $\alpha$ -particles

- there are no delayed Geiger cells triggered by an  $\alpha$ -particle in the proximity of the reconstructed vertex (see Sec. 5.7).

## 6.4 Analysed runs

After thorough tests of the NEMO3 detector and its acquisition system, a great number of runs in the configuration for the double beta decay measurements have been carried out from May 2002 up to now (May 2003). These runs have been analysed in order to search for a signal of the double beta decay of  $^{100}\text{Mo}$  to the excited  $0_1^+$  state by the means of the selection criteria reviewed in Sec. 6.3 and built on both the physics constraints and Monte-Carlo simulations as explained in Chapter 5.

### 6.4.1 Trigger used for data acquisition

The data acquisition trigger<sup>2</sup> used in the runs for the study of double beta decay is defined in such a way that it allows us to record events with one or two electrons (or positrons) and with or without photons and  $\alpha$ -particles. It offers a wide choice of interesting data analysis channels like, for instance,  $e^-N\gamma$  ( $N = 1, 2, 3, \dots$ ),  $2e^-$ ,  $2e^-N\gamma$ ,  $e^-e^+$ ,  $e^-\gamma\alpha$ ,  $2e^-\gamma\alpha$  and so on for studies of different  $\beta\beta$  decay modes and the corresponding backgrounds.

The  $\beta\beta$  trigger uses information from both the calorimeter and the tracking wire chamber. Until the end of January 2003, we had been using a trigger, noted as Trigger 20, which was based on the following criteria:

1. at least one scintillator with deposited energy greater than 150 keV was fired,
2. there was at least one primitive track detected inside the detector.

A good primitive track is considered by this trigger to be either a primitive track made of at least of seven layers from nine containing fired Geiger cells in any half-sector of the detector, or two primitive half-tracks in two adjacent inner or outer half-sectors which allow the construction of a particle track connecting source foils and scintillator walls [154].

Then, since February 2003, a slightly modified trigger, Trigger 25, which conserves the main features from Trigger 20 but in addition allows us to save events with short tracks as well has been being used for the data acquisition. This trigger saves events which satisfy the following conditions:

1. at least one scintillator with deposited energy greater than 150 keV was fired,
2. there was at least a short track detected anywhere in the tracking volume of the detector.

The second condition means that the program providing the trigger tries to build a primitive track for each half-sector from at least three consecutive layers of fired Geiger cells, amongst which at least two would correspond either to the four layers close to the source foils, or to the three layers close to the scintillator walls [154].

### 6.4.2 Betabeta runs

The runs intended for the study of double beta decay in NEMO3 are called **betabeta runs**, they are alternatively denoted as  $\beta\beta$  runs. The real beginning of these runs is in May 2002, after the complete installation of the iron shielding (see Sec. 4.6.1) and a series of tests of the NEMO3 acquisition system. However, the runs have to be divided into two main groups according to two running periods which differ in operating conditions. The first period, called here **Period I**, corresponds to the  $\beta\beta$  runs taken from May to the end of December 2002 when the detector and the laser-based survey system were not yet perfectly tuned; some modifications to the detector were also done during this period. Additionally, the neutron shielding was still in different phases of its installation, and a relatively large number of PMTs (10 – 20%) were either unused for data acquisition because of various technical problems, or their energy and time calibrations were not yet available. Moreover, the wire chamber manifested some temporary instabilities seen as numerous self-discharging, noisy Geiger cells and by poor plasma propagation in the Geiger cells when the plasma prematurely stopped before reaching one or both of the anode wire ends. This behaviour, as well as the absence of some PMTs in the data, has consequences on the real

---

<sup>2</sup>See also Sec. 4.7.3

detection efficiency of the detector. The reduction of the efficiency for this period was estimated for the studied  $eeN\gamma$  channel using Monte-Carlo simulation and is presented further in Sec. 6.5.

Having completely installed the neutron shielding and after resolving the problems with instability of the wire chamber by addition of 1% of argon to enhance the quenching capability; together with the ultimate tuning and recalibration of the calorimeter, the experimental conditions are now much more stable and the data are more reliable. This period, called **Period II**, includes all the data from February 2003 to present (May 2003). Besides what has already been mentioned, the difference between Period I and Period II consist also in the trigger used for the data acquisition: we had been applying Trigger 20 during Period I and then, since February 2003, we have been using Trigger 25.

Tab. 6.1 summarises the monthly totals of net data acquisition time of analysed runs corresponding to Period I. All the runs were carried out with a magnetic field of 30 G and with complete iron shielding, nevertheless the neutron shielding was still under installation. The triggering rate for the  $\beta\beta$  runs was about 3 – 3.5 Hz at that time. Tab. 6.2 gives the monthly totals of the running time for the analysed runs from Period II. These runs have been carried out with a magnetic field of 25 G and with complete iron and neutron shielding. Due to the Trigger 25, the data acquisition rate of the  $\beta\beta$  runs was higher than for Period I and reached about 7 – 7.5 Hz.

Month	Running time (hh:mm)
May 2002	12:45
June 2002	146:04
July 2002	107:05
September 2002	227:07
October 2002	520:05
November 2002	437:10
December 2002	79:10
Total time	1529:26

Table 6.1: Monthly totals of net acquisition time of the  $\beta\beta$  runs of Period I used for data analysis.

Month	Running time (hh:mm)
February 2003	301:06
March 2003	351:51
April 2003	460:42
May 2003	276:34
Total time	1390:13

Table 6.2: Monthly totals of net acquisition time of the  $\beta\beta$  runs of Period II used for data analysis.

### 6.4.3 Runs with sources of $^{208}\text{Tl}$ and $^{214}\text{Bi}$

#### Description of runs

During the second half of January 2003, special runs with sources containing either  $^{208}\text{Tl}$  or  $^{214}\text{Bi}$  were carried out. Actually, we made use of sources of  $^{228}\text{Th}$  and  $^{226}\text{Ra}$  which were both in secular equilibrium with their daughters (see Fig. 4.15). The principal goal of this measurement was to study experimentally the influence of the external background coming from these two isotopes. The runs allowed us to reach a high number of recorded events in a couple of days which would not be possible with Monte-Carlo simulations owing to the rather low trigger efficiency for this kind of background (cf. Tab. 5.1) which implied a very long CPU time for the generation of a reasonable number of decays. Although these measurements cannot completely substitute Monte-Carlo simulations of the external background because they are not able to reproduce the exact geometric configuration, i.e. uniform distribution of  $^{208}\text{Tl}$  and  $^{214}\text{Bi}$  radioactivity in PMT glass, their principal advantage consists of very high statistics which, from the technical point of view, cannot be reached with Monte-Carlo simulations<sup>3</sup>. The comparison between experimental data from  $\beta\beta$  runs and theoretical predictions can now be performed with both Monte-Carlo simulations and these external background runs.

As the iron and neutron shielding have already been installed on NEMO3, the sources providing  $^{208}\text{Tl}$  and  $^{214}\text{Bi}$  activities could not be placed at the exterior of the detector. Despite this fact, the access to the central tower of the detector was still possible and thus runs were carried out in the most favourable geometry with the sources situated in the geometric centre of NEMO3, i.e. at the  $x = y = z = 0$  position. Other conditions of these runs, like the use of magnetic field, configuration of the acquisition system, type of trigger (Trigger 20 at that time) and so on, were the same as for standard  $\beta\beta$  runs. The parameters of these runs like the activities of sources respectively in  $^{208}\text{Tl}$  and  $^{214}\text{Bi}$  and the total run durations which were used for data analysis are summarised in Tab. 6.3.

Isotope	Activity		Running time (hh:mm)	Equivalent time (hr)
	source	PMTs		
$^{214}\text{Bi}$	20 kBq	300 Bq	38:06	2537
$^{208}\text{Tl}$	7 kBq	18 Bq	24:04	9360

Table 6.3: Activities of  $^{208}\text{Tl}$  and  $^{214}\text{Bi}$  sources, net running times, and corresponding equivalent times for acquisition without sources.

#### Results for the runs with sources of $^{208}\text{Tl}$ and $^{214}\text{Bi}$

After the application of all the selection conditions for the eeN $\gamma$  channel, which are listed in Sec. 6.3, there are no remaining events for the group of runs with the  $^{208}\text{Tl}$  source. This observation confirms results of Monte-Carlo studies of Sec. 5.11.2. As regards the runs with source of  $^{214}\text{Bi}$ , there is only one event, shown in Fig. 6.1, that fully satisfied all the selection criteria. Its parameters are listed in Tab. 6.4. The common vertex of the two  $e^-$  tracks is located in molybdenum foils of sector 03 and we cannot, however, exclude the hypothesis that the event originates from the  $2\nu\beta\beta$  decay of  $^{100}\text{Mo}$  to the excited state. Neither are we able to

---

<sup>3</sup>See also comments in Sec. 5.11.2

exclude the possibility that the event was produced by a  $^{214}\text{Bi} - ^{214}\text{Po}$  decay in the gas of the wire chamber. As these two decays follow the Poisson's probability distribution and given the fact that the running time was limited to a few dozens of hours it is preferable to just give a limit on the external background contribution from  $^{214}\text{Bi}$ . When Eq. 5.30 and the real detection efficiency (see Sec. 6.5) are used, we obtain the following limit on the  $^{214}\text{Bi}$  decay probability to contribute to the eeN $\gamma$  channel:

$$\eta \leq 3.35 \times 10^{-10}$$

and then the following numbers of expected events for 1000 hr and 1 yr of running time with a perfect detector:

$$\begin{aligned} N_{evt}(1000 \text{ hr}) &\leq 0.36 \\ N_{evt}(1 \text{ yr}) &\leq 3.17 \end{aligned}$$

Comparing this result with estimations done with Monte-Carlo data for the signal and for the different types of background (cf. Tab. 5.17), we may conclude that the contribution from the external background is negligible. Hence, the remaining and most bothering background is that from radon that penetrates the inside of the detector.

Run number	Event number	$E_{ee}$ (keV)	$E_{e_1}$ (keV)	$E_{e_2}$ (keV)	$E_{N\gamma}$ (keV)
1833	107471	982	480	502	710

Table 6.4: Parameters of the only event from runs with source of  $^{214}\text{Bi}$  that satisfied all the selection criteria for the eeN $\gamma$  channel.

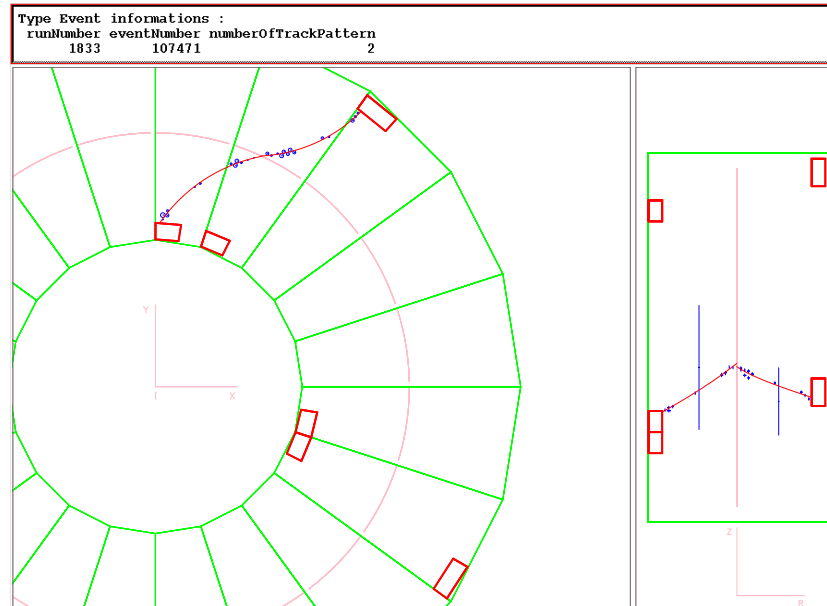


Figure 6.1: A view of the only event from runs with sources of  $^{208}\text{Tl}$  and  $^{214}\text{Bi}$  that satisfied all the selection criteria for the eeN $\gamma$  channel.

## 6.5 Estimation of the real detection efficiency

In order to compare experimental data with Monte-Carlo, it is necessary to reproduce the real working conditions of the detector in the Monte-Carlo simulations. Particularly during Period I of  $\beta\beta$  runs (see Sec. 6.4.2) when a relatively great number of PMTs (200 – 370) were either unused for the data acquisition or non-calibrated, the real detection efficiency of NEMO3 was significantly reduced. Even during Period II when the detector was well tuned, there are about 30 counters that are either not used for the data acquisition or without calibration. In addition to the reduction of the calorimeter’s performance, there was a certain inefficiency of the wire chamber encountered during Period I, caused by the temporary instability of some Geiger cells which were generating unstable zones of noisy, continuous self-discharge. This has to be taken into account as well. These cells are referred to as ‘hot’ Geiger cells.

### 6.5.1 Calorimeter efficiency estimation

In order to determine the real calorimeter efficiency  $\eta_{PMT}$  for a given period of runs, we will introduce the same bias into the Monte-Carlo in terms of missing or non-calibrated PMTs to simulate the real conditions of the runs. This means removing the counters that were physically missing in the real  $\beta\beta$  runs from the Monte-Carlo data and, as is done when processing the real experimental data, not using counters for which either energy or time calibration was not available. In addition to the division of runs into two groups, Period I and Period II, which are rather different in terms of running conditions, the former has also been split into two sub-periods: Period Ia and Period Ib. They differ in the number of PMTs missing for acquisition or without energy or time calibration (called here bad PMTs) and in the distribution of these counters inside the detector. Period Ia concerns runs carried out in May, June, July, and during the first part of September 2002 and it corresponds to 417 hr 16 min of the data taking. Period Ib stretches from the second part of September to the end of December 2002 and it covers 1112 hr 10 min of analysed data. The obtained calorimeter efficiencies for the studied  $eeN\gamma$  channel together with respective running times and numbers of bad PMTs for all the periods are given in Tab. 6.5. The average value for Period I evaluated from particular efficiencies and running times of Period Ia and Period Ib is given there too. Note the rather poor efficiencies related to Period I (Ia and Ib) when a great number of PMTs (377 and 202 respectively) could not be used in the data analysis. On the contrary, the calorimeter efficiency for Period II when only 43 PMTs have been unusable for the analysis is rather good and reaches 92%. This result is also true for the runs with sources of  $^{208}\text{Tl}$  and  $^{214}\text{Bi}$  since they were taken in the same working conditions.

Period of runs	Running time	Number of bad PMTs	$\eta_{PMT}$ (%)
Period Ia	417:16	377	56.4
Period Ib	1112:10	202	69.5
<b>Period I</b>	1529:26	—	<b>65.9</b>
<b>Period II</b>	1390:13	43	<b>91.7</b>

Table 6.5: Efficiency of the calorimeter,  $\eta_{PMT}$ , regarding the  $eeN\gamma$  channel for different running periods used for the current analysis.

### 6.5.2 Wire chamber efficiency estimation

A certain reduction to the global detection efficiency was also caused by temporary instabilities of the wire chamber during Period I. This was produced by either single noisy, continuously self-discharging Geiger cells (hot Geiger cells), or by zones in these hot cells. During the stage of reprocessing of the raw experimental data into the analysis format<sup>4</sup>, noisy Geiger cells are not used for the reconstruction of tracks. Consequently, zones made of such noisy hot cells produce dead regions from the point of view of the particle tracking. Another cause of the decrease of the wire chamber efficiency is bad plasma propagation of fired Geiger cells. This happens when the plasma propagation stops before reaching one or even both extremities of the anodic wire. In such a situation the determination of vertical position is affected which can result in incorrect track reconstruction. In the case that one or more of the four Geiger cell layers closest to each side of the source foils is hot, it can lead to an erroneous determination of the vertex position for this track.

In order to estimate the loss of efficiency to two-electron events detection caused by these effects by means of Monte-Carlo simulations, areas with these noisy Geiger cells were removed in Monte-Carlo data. The resulting average value obtained for the efficiency lost for the two-electron events during Period I is about 10% [157]. Thus the average efficiency of the wire chamber during this period for any two-electron channel is  $\eta_{GG} = 0.9$ . However, during Period II, the wire chamber efficiency  $\eta_{GG}$  was almost 100% thanks to a very good stability of the wire chamber and also thanks to a high rate of the complete plasma propagation which typically reached up to 90 – 95%.

### 6.5.3 Global efficiency of the detector

The global detector's efficiency  $\eta$  is then a product of the calorimeter and wire chamber efficiencies and can be written the following way:

$$\eta = \eta_{PMT} \cdot \eta_{GG} . \quad (6.1)$$

The calculated average values of  $\eta$  for both running periods are then  $\eta = 59.3\%$  for Period I and  $\eta = 91.7\%$  for Period II (see Tab. 6.6). In order to combine the results from both periods however, we will use efficient detection time  $T_{eff}$  defined as follows:

$$T_{eff} = \eta \cdot T_{acq} , \quad (6.2)$$

where  $T_{acq}$  is the net acquisition time for the considered period of  $\beta\beta$  runs. This time,  $T_{eff}$ , corresponds to the equivalent acquisition time for a perfect detector, i.e. with 100% efficiency, which would be necessary to achieve the same number of observed events as for the real detector with efficiency  $\eta$  and acquisition time  $T_{acq}$ .

## 6.6 Results for the $\beta\beta$ runs in the $eeN\gamma$ channel

### 6.6.1 Observation for Period I

Recall that an unfortunate feature of these  $\beta\beta$  runs is the reduced operating efficiency of the calorimeter due to a great number of PMTs either unavailable for acquisition or without energy or time calibration, and also by the partially decreased efficiency of the wire chamber. The

---

<sup>4</sup>See Sec. 6.1

Period of runs	$T_{acq}$	$\eta$	$T_{eff}$
Period I	1529:26	59.3%	906:57
Period II	1390:13	91.7%	1274:50

Table 6.6: The global detection efficiency ,  $\eta$ , for the  $eeN\gamma$  channel for two different periods of runs and the efficient time  $T_{eff}$  for these periods.

average efficiency of the detector for the  $eeN\gamma$  channel is estimated to reach 59.3% and thus the efficient detection time  $T_{eff}$ , which is equivalent to the necessary acquisition time with a perfect detector, is about 907 hr (see Tab. 6.6). It is important to also note that many PMTs missing in data were due to missing or switched-off high-voltage cards which sometimes caused the absence of entire internal or external scintillator walls from some sectors in the data. For this reason, the real proportion of number of sectors equipped with molybdenum to with the other sources is rather 10:8 during this period instead of normal rate of 12:8. This fact is important for the estimation of the background contribution in the  $eeN\gamma$  channel for sectors with molybdenum which is based on the number of events observed for this channel in non-molybdenum foils.

When the  $eeN\gamma$  selection criteria listed in Sec. 6.3 are applied to the set of  $\beta\beta$  runs from Period I, there are 17 events in molybdenum foils and another four events in non-molybdenum foils that satisfy all the conditions. Details about these events are given respectively in Tabs. 6.7 and 6.8. If analogous selection using the same criteria but accepting  $\alpha$ -particles is processed, then there are three events left in molybdenum foils and two in the other foils. Details about them are to be found in Tab. 6.9. Although the proportion of efficient sectors with molybdenum to other isotopes is 10:8, the proportion of numbers of observed events is 17:4 and is therefore much greater.

The level of background can be estimated using either only events without any  $\alpha$ -particles observed in the eight sectors with non-molybdenum sources (Method A), or by combining these events with events observed with  $\alpha$ -particles in both types of sectors (Method B). In the latter case, we consider that the only significant background in the  $eeN\gamma$  channel under the current set of selection conditions comes from radon and, in addition, that the proportion of events detected with an  $\alpha$ -particle to those without it is equal to one as has been proven by Monte-Carlo simulations in Sec. 5.10.4. In the first case, the estimated value of background is:

$$\overline{B} \pm \sigma_B = 5 \pm 2.5 \text{ (Method A)}$$

and it was found to be  $\overline{B} = 4 \cdot 10/8$  with  $\sigma_B = \sqrt{(10/8)^2 \cdot 4}$ . In the other case (Method B), it has to be calculated as a weighted average value according to the following formula:

$$\overline{B} \pm \sigma_B = \frac{\sum_i w_i b_i}{\sum_i w_i} \pm \left( \sum_i w_i \right)^{-1/2}, \quad (6.3)$$

where  $\overline{B}$  is the average value of background determined from background measurements  $b_i$ ,  $\sigma_B$  is the corresponding error, and  $w_i = 1/\sigma_i^2$ . The level of background calculated from Eq. 6.3 is then as follows:

$$\overline{B} \pm \sigma_B = 3.2 \pm 1.2 \text{ (Method B)} .$$

Afterwards, the values of the observed signal  $S$  and of the corresponding error  $\sigma_S$  for the two

methods of background measurement become the following:

$$\begin{aligned} S \pm \sigma_S &= 12.0 \pm 4.8 \quad \text{for Method A ,} \\ S \pm \sigma_S &= 13.8 \pm 4.3 \quad \text{for Method B .} \end{aligned}$$

The first result is at the level of 2.5 standard deviations, the other one is at the level of 3.2 standard deviations. Note that in order to claim a positive result, it is necessary to reach five or more standard deviations [158]. It is not yet the case, nevertheless we may give the upper and lower limits following the habitual procedure of the Particle Data Group [159]. The unified approach to the classical statistical analysis of small signals [160] is applied, particularly the method of confidence interval determination for Poisson processes with background. Then the following intervals at 95% confidence level (C.L.) for the number of signal events are obtained:

$$\begin{aligned} S &\in [4.84, 21.81] \quad \text{for Method A ,} \\ S &\in [6.26, 23.31] \quad \text{for Method B .} \end{aligned}$$

Using these values and the corresponding efficient time  $T_{eff}$ , we are able to determine from Eq. 5.29 the following half-life intervals at 95% C.L.:

$$\begin{aligned} T_{1/2} &\in [3.72 \times 10^{20}, 1.68 \times 10^{21}] \text{ yr} \quad \text{for Method A ,} \\ T_{1/2} &\in [3.48 \times 10^{20}, 1.30 \times 10^{21}] \text{ yr} \quad \text{for Method B .} \end{aligned}$$

As it has been proven previously in Secs. 5.11.2 and 6.4.3, the only significant background in the  $eeN\gamma$  channel that cannot be entirely suppressed comes from radon. It has been shown that in such cases the  $eeN\gamma$  events with the energy sum of the two electrons  $E_{ee}$  greater than 1200 keV cannot originate in the  $2\nu\beta\beta$  decay of  $^{100}\text{Mo}$  to the excited  $0_1^+$  state but in the  $^{214}\text{Bi} - ^{214}\text{Po}$  decay. Thus, it is also interesting to see what happens if the upper bound of the  $E_{ee}$  value is stretched as far as to 2000 keV. In the 1200 keV  $< E_{ee} < 2000$  keV energy window, there are two events without  $\alpha$ -particles in molybdenum foils and also two other events in the other foils, and one and three events respectively containing  $\alpha$ -particles (see Tab. 6.13). So, this observation of almost the same number of events for all the four cases is in a good agreement with our expectations to have inside this region a uniform background from radon.

The distribution of the  $eeN\gamma$  events with or without  $\alpha$ -particles selected either in the molybdenum or in the other source foils are presented in the following two-dimensional  $E_{N\gamma}$  vs.  $E_{ee}$  plots where the upper limit on the  $E_{ee}$  value is pushed up to 2000 keV:

- Fig. 6.2 – events without any  $\alpha$ -particle selected in Mo foils,
- Fig. 6.3 – events with  $\alpha$ -particle selected either in molybdenum or non-molybdenum foils,
- Fig. 6.4 – events with or without  $\alpha$ -particles detected in non-molybdenum foils,
- Fig. 6.5 – all the background events, i.e. events with  $\alpha$ -particles in both molybdenum and the other sources and events without  $\alpha$ -particles in non-molybdenum sectors.

### 6.6.2 Observation for Period II

Compared with Period I, runs from February 2003 to May 2003 (Period II) are characterised by good working conditions of both the tracking wire chamber and the calorimeter. With regard to the calorimeter, the PMTs were properly tuned and recalibrated. At present, only 34 of them,

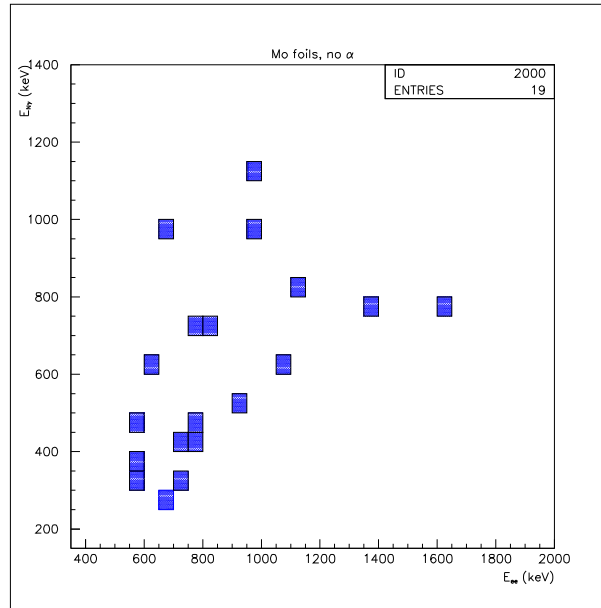


Figure 6.2:  $E_{N\gamma}$  vs.  $E_{ee}$  plot of events without any  $\alpha$ -particle which were selected in Mo foils and corresponding to the  $\beta\beta$  runs of Period I.

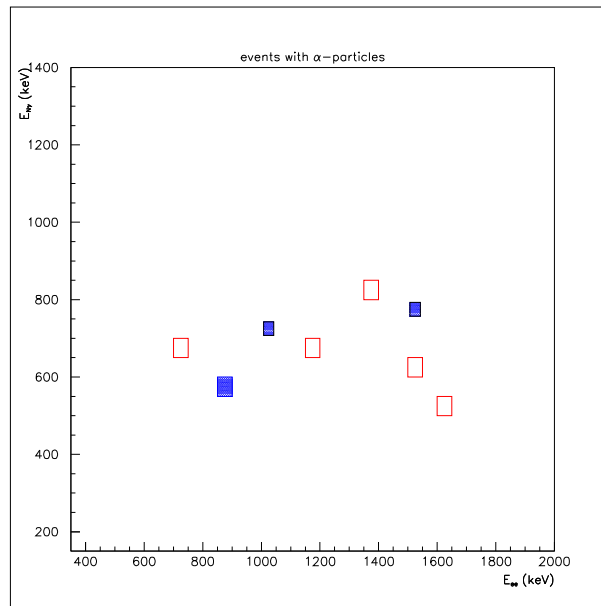


Figure 6.3:  $E_{N\gamma}$  vs.  $E_{ee}$  plot of events containing  $\alpha$ -particles selected either in molybdenum foils (plain blue boxes) or in non-molybdenum foils (empty red boxes) and corresponding to the  $\beta\beta$  runs of Period I.

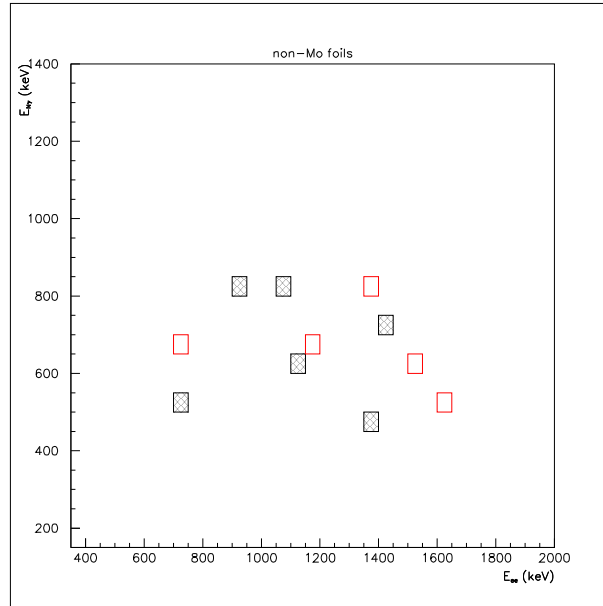


Figure 6.4:  $E_{N\gamma}$  vs.  $E_{ee}$  plot of events selected in non-molybdenum foils either without any  $\alpha$ -particle (patterned black boxes) or with detected  $\alpha$ -particle (empty red boxes) issued from the  $\beta\beta$  runs of Period I.

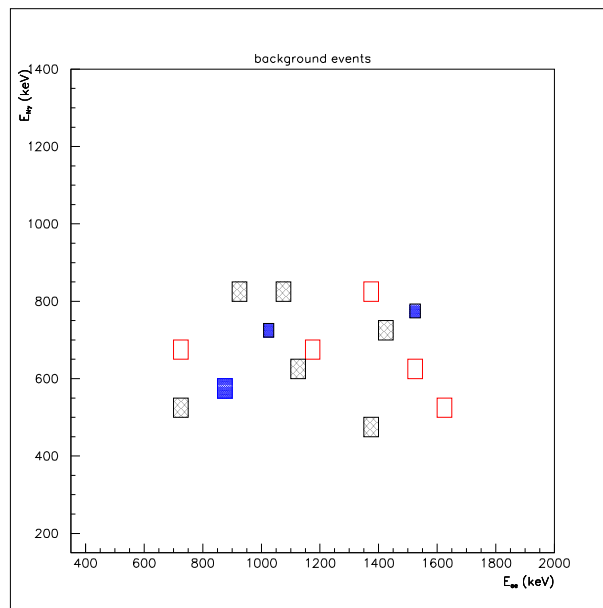


Figure 6.5:  $E_{N\gamma}$  vs.  $E_{ee}$  plot of all the selected background events corresponding to the  $\beta\beta$  runs of Period I: events with  $\alpha$ -particles in molybdenum (plain blue boxes) and non-molybdenum foils (empty red boxes), and events without any  $\alpha$ -particle in non-molybdenum foils (patterned black boxes).

Mo foils, events without $\alpha$ -particles					
Run number	Event number	$E_{ee}$ (keV)	$E_{e_1}$ (keV)	$E_{e_2}$ (keV)	$E_{N\gamma}$ (keV)
1540	120054	740	316	424	424
1542	78718	768	215	553	427
1548	15337	776	302	474	455
1557	24869	1097	626	471	601
1582	19834	674	339	335	277
1614	87803	811	551	260	735
1642	2693	753	238	515	745
1643	79727	931	364	567	518
1650	83179	668	298	370	952
1651	50281	1149	862	287	807
1655	42730	563	318	245	340
1655	78976	554	209	345	376
1660	23595	626	317	309	612
1667	101034	708	433	275	350
1681	51969	587	309	278	489
1696	36258	993	225	768	1107
1719	66240	953	348	605	965

Table 6.7: Parameters of events selected in Mo foils and without any  $\alpha$ -particle corresponding to  $\beta\beta$  runs of Period I that satisfied all the selection criteria for the eeN $\gamma$  channel.

which makes 1.75% of the total number of 1940 PMTs installed in NEMO3, cannot be currently used in the data acquisition. Consequently, the global detection efficiency for the eeN $\gamma$  channel is much better than for Period I and it reaches about 92% for the eeN $\gamma$  channel. So, the efficient detection time  $T_{eff}$  for this period is about 1275 hr of equivalent running time with a perfect detector.

After the application of selection criteria for the eeN $\gamma$  channel, which were summarised in Sec. 6.3, there are 12 events without any  $\alpha$ -particle that have been selected in the twelve sectors with  $^{100}\text{Mo}$  sources. Their list is given in Tab. 6.10. In addition, two other events have been selected in the eight sectors with non-molybdenum sources; their details are presented in Tab. 6.11. If we look for events satisfying the same set of conditions but containing an  $\alpha$ -particle close to the vertex of the two electrons, four events in molybdenum foils and two other events elsewhere are then observed; review of their principal parameters is given in Tab. 6.12.

The estimation of background level is realised the same way as it has been done for Period I<sup>5</sup> by two possible approaches: Method A and Method B. When the background estimation is produced on the basis of events selected in the non-molybdenum sectors (Method A), then the background level and its error are obtained as  $\overline{B} = 2 \cdot 12/8$  and  $\sigma_B = \sqrt{(12/8)^2 \cdot 2}$  which gives the following result:

$$\overline{B} \pm \sigma_B = 3.0 \pm 2.1 \text{ (Method A)} .$$

When the alternative method of background estimation, Method B, based on the weighted average value determined from three possible measurements of background is applied, then the

---

<sup>5</sup>See Sec. 6.6.1

non-Mo foils, events without $\alpha$ -particles					
Run number	Event number	$E_{ee}$ (keV)	$E_{e_1}$ (keV)	$E_{e_2}$ (keV)	$E_{N\gamma}$ (keV)
1568	103158	1101	863	238	646
1627	10577	936	619	317	811
1637	78057	1053	577	476	849
1661	20408	703	410	293	531

Table 6.8: Parameters of events selected in non-molybdenum foils and without any  $\alpha$ -particle corresponding to  $\beta\beta$  runs of Period I that satisfied all the selection criteria for the  $eeN\gamma$  channel.

Mo foils, events with $\alpha$ -particles					
Run number	Event number	$E_{ee}$ (keV)	$E_{e_1}$ (keV)	$E_{e_2}$ (keV)	$E_{N\gamma}$ (keV)
1376	15203	897	251	646	590
1717	126547	1044	714	330	734
1722	17037	867	242	625	565
non-Mo foils, events with $\alpha$ -particles					
Run number	Event number	$E_{ee}$ (keV)	$E_{e_1}$ (keV)	$E_{e_2}$ (keV)	$E_{N\gamma}$ (keV)
1637	131339	1178	535	643	681
1643	58744	745	320	425	686

Table 6.9: Parameters of events selected in the  $eeN\gamma$  channel in both molybdenum and non-molybdenum foils and containing  $\alpha$ -particles which correspond to  $\beta\beta$  runs of Period I.

following background level for twelve sectors with molybdenum sources is obtained:

$$\overline{B} \pm \sigma_B = 3.4 \pm 1.2 \text{ (Method B)} .$$

Regarding the observed signal  $S$  and the corresponding error  $\sigma_S$ , the values for each method are:

$$\begin{aligned} S \pm \sigma_S &= 9.0 \pm 3.7 \quad \text{for Method A} , \\ S \pm \sigma_S &= 8.6 \pm 3.7 \quad \text{for Method B} . \end{aligned}$$

The first result is at the level of 2.4 standard deviations, the second one is at the level of 2.3 standard deviations. After the application of the same statistical approach as has been used previously for events from Period I, the following intervals at 95% C.L. for number of signal events are determined:

$$\begin{aligned} S &\in [3.44, 17.34] \quad \text{for Method A} , \\ S &\in [3.06, 16.84] \quad \text{for Method B} . \end{aligned}$$

Using these values and applying Eq. 5.29, the following half-life limits at 95% C.L. are then calculated:

$$\begin{aligned} T_{1/2} &\in [6.57 \times 10^{20}, 3.31 \times 10^{21}] \text{ yr} \quad \text{for Method A} , \\ T_{1/2} &\in [6.77 \times 10^{20}, 3.72 \times 10^{21}] \text{ yr} \quad \text{for Method B} . \end{aligned}$$

The finally selected events with or without an  $\alpha$ -particle and observed either in molybdenum or in the other foils are represented in the form of the following two-dimensional  $E_{N\gamma}$  vs.  $E_{ee}$  graphs:

- Fig. 6.6 – events without any  $\alpha$ -particle selected in Mo foils,
- Fig. 6.7 – events with  $\alpha$ -particle selected either in molybdenum or non-molybdenum foils,
- Fig. 6.8 – events with or without  $\alpha$ -particles detected in non-molybdenum foils,
- Fig. 6.9 – all the background events, i.e. events with  $\alpha$ -particles in both molybdenum and the other sources and events without  $\alpha$ -particles in non-molybdenum sectors.

Note that the upper boundary imposed on the  $E_{ee}$  value was moved up to 2000 keV the same way as it has been done for Period I.

Mo foils, events without $\alpha$ -particles					
Run number	Event number	$E_{ee}$ (keV)	$E_{e_1}$ (keV)	$E_{e_2}$ (keV)	$E_{N\gamma}$ (keV)
1877	26933	1050	369	681	759
1882	228512	657	201	456	512
1886	90757	811	426	385	678
1943	362760	1091	669	422	692
1951	358079	1158	586	572	252
2048	17476	628	335	293	413
2050	246500	921	570	351	825
2054	105014	743	285	458	669
2123	81837	711	290	421	501
2182	128448	687	342	345	584
2205	268109	703	414	290	625
2235	62046	803	304	499	786

Table 6.10: Parameters of events selected in Mo foils and without any  $\alpha$ -particle corresponding to  $\beta\beta$  runs of Period II that satisfied all the selection criteria for the eeN $\gamma$  channel.

non-Mo foils, events without $\alpha$ -particles					
Run number	Event number	$E_{ee}$ (keV)	$E_{e_1}$ (keV)	$E_{e_2}$ (keV)	$E_{N\gamma}$ (keV)
1949	82186	423	222	201	998
2150	166394	994	767	227	957

Table 6.11: Parameters of events selected in non-molybdenum foils and without any  $\alpha$ -particle corresponding to  $\beta\beta$  runs of Period II that satisfied all the selection criteria for the eeN $\gamma$  channel.

### 6.6.3 Summary for both periods of runs

Although both of the considered periods of runs are rather different in terms of the working conditions of the detector, which is then reflected in the detector's efficiency for the eeN $\gamma$  channel,

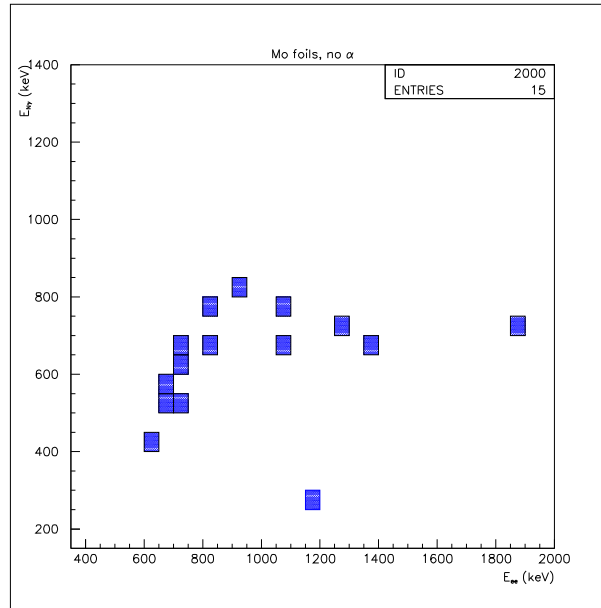


Figure 6.6:  $E_{N\gamma}$  vs.  $E_{ee}$  plot of events without any  $\alpha$ -particle which were selected in Mo foils and corresponding to the  $\beta\beta$  runs of Period II.

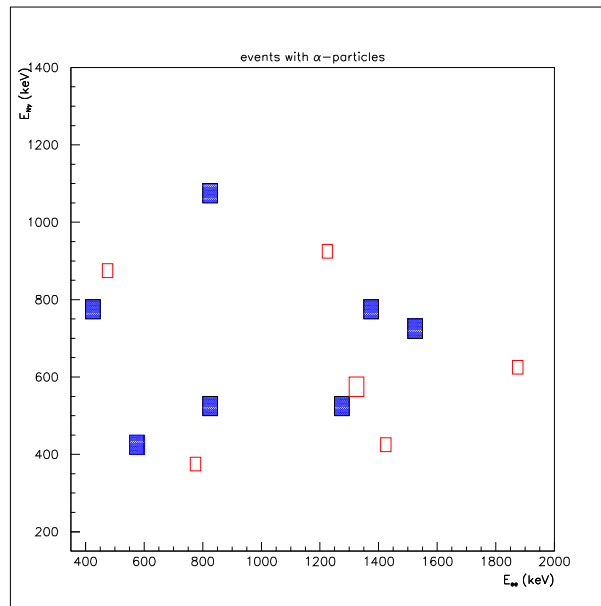


Figure 6.7:  $E_{N\gamma}$  vs.  $E_{ee}$  plot of events containing  $\alpha$ -particles selected either in molybdenum foils (plain blue boxes) or in non-molybdenum foils (empty red boxes) and corresponding to the  $\beta\beta$  runs of Period II.

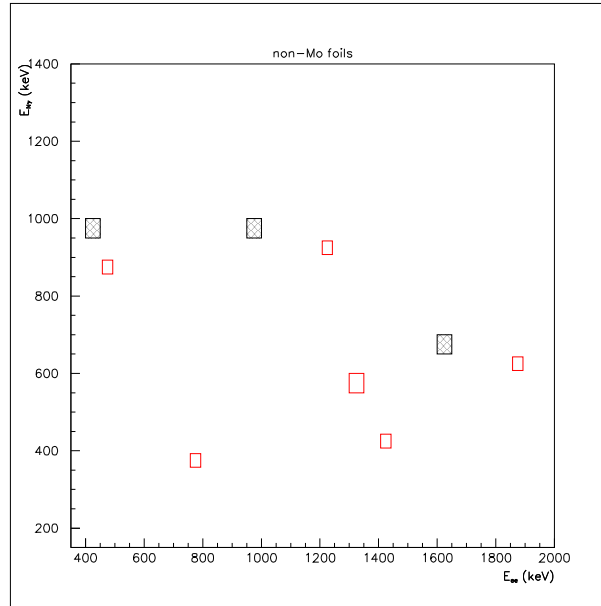


Figure 6.8:  $E_{N\gamma}$  vs.  $E_{ee}$  plot of events selected in non-molybdenum foils either without any  $\alpha$ -particle (patterned black boxes) or with detected  $\alpha$ -particle (empty red boxes) issued from the  $\beta\beta$  runs of Period II.

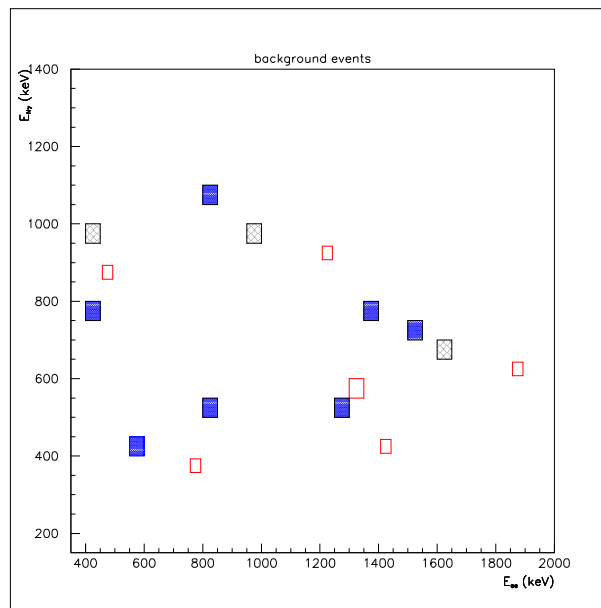


Figure 6.9:  $E_{N\gamma}$  vs.  $E_{ee}$  plot of all the selected background events corresponding to the  $\beta\beta$  runs of Period II: events with  $\alpha$ -particles in molybdenum (plain blue boxes) and non-molybdenum foils (empty red boxes), and events without any  $\alpha$ -particle in non-molybdenum foils (patterned black boxes).

Mo foils, events with $\alpha$ -particles					
Run number	Event number	$E_{ee}$ (keV)	$E_{e_1}$ (keV)	$E_{e_2}$ (keV)	$E_{N\gamma}$ (keV)
1887	1706	401	200	201	790
2032	101569	566	203	363	449
2053	171964	847	357	490	1062
2181	6082	823	503	320	505
non-Mo foils, events with $\alpha$ -particles					
Run number	Event number	$E_{ee}$ (keV)	$E_{e_1}$ (keV)	$E_{e_2}$ (keV)	$E_{N\gamma}$ (keV)
2056	406522	765	498	267	360
2137	350349	499	296	203	886

Table 6.12: Parameters of events selected in the  $eeN\gamma$  channel in both molybdenum and non-molybdenum foils and containing  $\alpha$ -particles which correspond to  $\beta\beta$  runs of Period II

it is possible to combine results of both periods by means of the efficient detection time,  $T_{eff}$ , defined previously by Eq. 6.2. In other words, the total running time for each considered period is, in fact, normalised by the corresponding efficiency for the  $eeN\gamma$  channel. Consequently, the total efficient time covering both Period I and Period II is simply a sum of partial efficient times and is then equal to 2181 hr 47 min. The addition of numbers of observed events can be done as well, nevertheless it is important to be careful when combining background contributions from both periods in order to estimate the background level in molybdenum foils. The reason consists of the different proportions between numbers of molybdenum and non-molybdenum sectors used for the acquisition and also on the estimation of background between the two periods.

Complete set of cuts with $E_{ee} < 1200$ keV				
Period of runs	Mo foils		other foils	
	without $\alpha$	with $\alpha$	without $\alpha$	with $\alpha$
Period I	17	3	4	2
Period II	12	4	2	2
Complete set of cuts with $1200 \text{ keV} < E_{ee} < 2000$ keV				
Period of runs	Mo foils		other foils	
	no $\alpha$	with $\alpha$	no $\alpha$	with $\alpha$
Period I	2	1	2	3
Period II	3	3	1	5

Table 6.13: A summary of numbers of finally selected events in the  $eeN\gamma$  channel for both considered periods of runs.

A summary for both periods, of numbers of observed events with or without  $\alpha$ -particles, in molybdenum and other foils, is given in Tab. 6.13. In total, 29 events have been observed in molybdenum foils. According to the method applied for background estimation, we obtain the

following values of background level in the sectors mounted with molybdenum:

$$\begin{aligned}\overline{B} \pm \sigma_B &= 8.0 \pm 3.3 \quad \text{for Method A ,} \\ \overline{B} \pm \sigma_B &= 6.5 \pm 1.6 \quad \text{for Method B .}\end{aligned}$$

Afterwards, the values of the signal  $S$  and of the corresponding error  $\sigma_S$  can be expressed as follows:

$$\begin{aligned}S \pm \sigma_S &= 21.0 \pm 6.3 \quad \text{for Method A ,} \\ S \pm \sigma_S &= 22.4 \pm 5.6 \quad \text{for Method B .}\end{aligned}$$

The result for Method A is at the level of 3.3 standard deviations and the signal/background ratio is equal to 2.6, while the result for Method B reaches 4.0 standard deviations and the signal/background ratio is 3.4. As none of these results does achieve or even exceed five standard deviations and thus according to habitual conventions for the presentation of experimental results, the conservative approach should be adopted. That means that the current results ought to be expressed in the form of intervals at a certain confidence level. In our case, the following intervals at 95% C.L. for number of signal events are determined:

$$\begin{aligned}S &\in [10.63, 31.37] \quad \text{for Method A ,} \\ S &\in [11.41, 33.47] \quad \text{for Method B .}\end{aligned}$$

As the Poisson distribution becomes symmetric and rather similar to the Normal (Gaussian) distribution for number of events greater than 20, it was possible to calculate the previous intervals using the Normal probability distribution instead of that of Poisson [161]. Finally, when the half-lives corresponding to these intervals are determined, the following limits at 95% C.L. on  $T_{1/2}$  of the  $2\nu\beta\beta$  decay of  $^{100}\text{Mo}$  to the excited  $0_1^+$  state in  $^{100}\text{Ru}$  are obtained:

$$\begin{aligned}T_{1/2} &\in [5.84 \times 10^{20}, 2.26 \times 10^{21}] \text{ yr} \quad \text{for Method A ,} \\ T_{1/2} &\in [5.83 \times 10^{20}, 1.71 \times 10^{21}] \text{ yr} \quad \text{for Method B .}\end{aligned} \tag{6.4}$$

These two intervals are in a good agreement with the previously published positive results of the  $T_{1/2}^{2\nu\beta\beta}$  for the g.s.  $\rightarrow 0_1^+$  transition which range from  $5.9 \times 10^{20}$  yr to  $9.3 \times 10^{20}$  yr and which are summarised in Tab. 3.2. In the near future, when more events will be accumulated in the studied eeN $\gamma$  channel, it will be possible to obtain a result at the level of five or more standard deviations and then it will be possible to officially publish the results of the NEMO3 experiment.

## 6.7 The origin of systematic errors

In this analysis, there are two different sources of systematic error. The first one is related to Monte-Carlo simulations, the second one is caused by uncertainties connected to the measurement of background for the eeN $\gamma$  channel.

The systematic error related to the performances of the Monte-Carlo simulation program have been previously studied by the NEMO Collaboration [164]. The study predicts a precision of 2% which is directly connected to the choice of parameters in the GEANT code for generation of events. For low energy electrons, errors arise mainly from scattering computations which depend on the step size used in the GEANT simulations. The real precision of the simulation program is, however, estimated to be about 5 – 6% if uncertainty on some cross-sections used by Monte-Carlo is also considered [165].

If the energy of fired scintillators is modified by 1% for Monte-Carlo data in order to simulate the effect of an energy shift which could be induced by a slight aberration in the energy calibration of the NEMO3 calorimeter, then the relative error of 1.3% is observed for the  $2\nu\beta\beta$  decay of  $^{100}\text{Mo}$  to the excited  $0_1^+$  state. For other studied processes, i.e. different kinds of backgrounds treated in Chapter 5, the effect is insignificant.

Another source of systematic error is actually the measurement of the background contribution for the  $eeN\gamma$  channel (see Sec. 6.6) which is based on direct measurement of background in non-molybdenum sectors. In the case of background from radon that penetrates into the detector, the study was focused only on  $^{214}\text{Bi} - ^{214}\text{Po}$  decays occurring in the gas of the wire chamber. However, it is also possible that  $^{214}\text{Bi}$  ions are deposited either on the wires, or on the source foils. In the latter case, a little difficulty arises from the fact that some of the NEMO3 sectors are mounted with metallic type source foils and some with composite ones (see Sec. 4.5). At present, it is not clear where the  $^{214}\text{Bi}$  ions are concentrated and which of the three possibilities is predominant. Even if all the three scenarios occur together, it is still difficult to estimate what are the real proportions of  $^{214}\text{Bi}$  ions that are in the wire chamber gas, on the wires, or on the surface of the foils. Studies in this direction are taking place within the NEMO Collaboration now [166].

Another problem related to the generation of  $^{214}\text{Bi} - ^{214}\text{Po}$  events is that in Monte-Carlo simulations an  $\alpha$ -particle has to cross through a Geiger cell to produce a delayed Geiger cell hit. In reality, due to its high ionization power, a Geiger cell can be triggered if an  $\alpha$ -particle simply passes close to it without the obligation of crossing through it; the Geiger cell will collect electrons produced by the ionization of the gas along the  $\alpha$ -track. This difference between Monte-Carlo simulations and real data appears in particular for  $\alpha$ -particles occurring in the intermediate gap where two consecutive Geiger cell layers are separated with scintillator blocks. This also happens if an  $\alpha$ -particle generated in the little gap between source foils and the first layer of Geiger cells goes straight to the foils, where it is stopped. The discrepancy between Monte-Carlo and real data only emerges when a single delayed Geiger cell would be triggered, which is rather rare. If there were more delayed Geiger cells fired by an  $\alpha$ -particle and one of them was not be seen in Monte-Carlo simulations, the  $\alpha$ -particle would be revealed anyway by the other delayed cells.

As the method of background estimation is based on the observation of the  $eeN\gamma$  or  $eeN\gamma\alpha$  events either in molybdenum foils or elsewhere, systematic error is slightly higher during Period I because of a certain inhomogeneity of the detector caused by a great number of uncalibrated PMTs or PMTs missing in data (switched off)<sup>6</sup>.

At the current stage, the question of the real systematic error does not yet have much importance for the study of the  $2\nu\beta\beta$  decay of  $^{100}\text{Mo}$  to the excited  $0_1^+$  state. Even if the systematic error reaches up to 10%, as was the case in NEMO2<sup>7</sup> [110], the statistic error is still much greater. For this reason, the subject of systematic error is not further developed in this work. In the future, when more events in the  $eeN\gamma$  channel have been accumulated and when the global error is dominated less by the statistic error, thorough study of the systematic error will be made.

---

<sup>6</sup>For details, see Secs. 6.4.2 and 6.5.1.

<sup>7</sup>Nevertheless, smaller systematic error than in NEMO2 attaining to 5 – 6% is expected for NEMO3

## 6.8 Conclusions

Despite the effort to open the energy cuts in order to collect maximum numbers of events from the  $2\nu\beta\beta$  decay of  $^{100}\text{Mo}$  to the excited  $0_1^+$  state, the number of events currently observed in the available data is still limited to a few dozen. Nevertheless, a result for the half-life of the  $2\nu\beta\beta$  decay of  $^{100}\text{Mo}$  to the excited  $0_1^+$  state of  $^{100}\text{Ru}$  at the level of five or more standard deviations can be expected from the NEMO3 experiment by the end of the current year 2003. In the future, when sufficient statistics have been accumulated, it will be also possible to produce the energy sum spectrum of the two electrons for the studied process. It would actually be the first time in the history that a double beta decay experiment would provide such spectrum for the  $2\nu\beta\beta$  decay to excited state.

The most bothering background in NEMO3 from the point of view of the  $eeN\gamma$  channel is the background coming from radon that penetrates into the tracking volume of NEMO3 either due to porosity or due to some tiny micro-holes. At the present time (May 2003), the level of radon activity inside the detector is still rather high from the point of view of the original requirements on background for the efficient measurement of neutrinoless double beta decay. To reach the desired sensitivity to  $0\nu\beta\beta$  decay, it is important to have less than one background event per year in the two-electron energy window of interest which extends from 2.8 to 3.2 MeV. Today, the background contribution from radon in this energy window is estimated to be about two events per year [162]. For this reason, a project to build an anti-radon tent surrounding the NEMO3 detector combined with an anti-radon setup and hence reducing the level of radon inside the detector by factor of 50 – 100 is currently being studied by the NEMO Collaboration [163]. The anti-radon device's fabrication and subsequent installation on the NEMO3 detector in the LSM laboratory is planned for the year 2004. In the case of the two-neutrino double beta decay to the excited  $0_1^+$  state, the situation is less dangerous than for the  $0\nu\beta\beta$  decay and, as it has been shown, it is possible to clearly identify the signal. At the present time, the signal/background ratio is about 3: 2.6 for Method A of the background level measurement and 3.4 for Method B. Before the installation of the anti-radon system, the current result given by Eq. 6.4 can be improved mostly by accumulation of more experimental data. Afterwards, once the anti-radon system is installed on the NEMO3 detector, the signal/background ratio would increase significantly. Then it would be even possible to release some of the cuts designed for the  $eeN\gamma$  channel and thereby increase number of observed events.

# Conclusion

Since May 2002, after five years of construction, the NEMO3 detector has been routinely taking data allowing fine measurements of different modes of the double beta decay of  $^{100}\text{Mo}$ ,  $^{82}\text{Se}$ ,  $^{116}\text{Cd}$ ,  $^{130}\text{Te}$ ,  $^{150}\text{Nd}$ ,  $^{96}\text{Zr}$ , and  $^{48}\text{Ca}$ . Up to now (May 2003), relevant  $2\nu\beta\beta$  decay signals have been observed for the principal isotopes present in higher quantity ( $^{100}\text{Mo}$ ,  $^{82}\text{Se}$ ,  $^{116}\text{Cd}$ , and  $^{130}\text{Te}$ ) in the detector. Moreover, the  $2\nu\beta\beta$  decay of  $^{100}\text{Mo}$  to the excited  $0_1^+$  state, which is the subject of the present Ph.D. thesis, has been also measured.

In this work, the detailed description of the double decay experiment NEMO3 is given. It describes the main parts of the detector (wire chamber, calorimeter, double beta decay sources, electronics, and techniques removing backgrounds) and all the possible backgrounds that have to be managed in the experiment. After that, this thesis fully explains the Monte-Carlo simulations of the studied processes ( $2\nu\beta\beta$  decay of  $^{100}\text{Mo}$  to the excited  $0_1^+$  state) and of all the relevant backgrounds (internal and external backgrounds from  $^{208}\text{Tl}$  and  $^{214}\text{Bi}$ ,  $2\nu\beta\beta$  decay of  $^{100}\text{Mo}$  to the ground state, radon in the gas of the wire chamber). Then, it deals with determination of optimal selection criteria for the measurement of the  $2\nu\beta\beta$  decay of  $^{100}\text{Mo}$  to the excited  $0_1^+$  state in the NEMO3 experiment. In the last part, the proper analysis of experimental data available from May 2002 to May 2003 is explained. Finally, the result obtained is presented in the form of the number of observed signal and background events which are subsequently interpreted in term of the half-life for the  $2\nu\beta\beta$  decay of  $^{100}\text{Mo}$  to the excited  $0_1^+$  state. As the level of five or more standard deviations is not yet reached, the conservative approach leads us to express the result in the form of the following interval at 95% confidence level:

$$\begin{aligned} T_{1/2}^{2\nu\beta\beta}(^{100}\text{Mo}, 0_1^+) &\in [5.84 \times 10^{20}, 2.26 \times 10^{21}] \text{ yr} \quad \text{for Method A ,} \\ T_{1/2}^{2\nu\beta\beta}(^{100}\text{Mo}, 0_1^+) &\in [5.83 \times 10^{20}, 1.71 \times 10^{21}] \text{ yr} \quad \text{for Method B .} \end{aligned}$$

These intervals of the  $T_{1/2}$  values are in a good agreement with previously published results from experiments that used HPGe  $\gamma$ -ray spectrometers.

As the NEMO3 detector continues to accumulate data, an improved result at five or more standard deviations, which would be officially published by the NEMO Collaboration, can be expected by the end of the year 2003. In the future, when a sufficiently high number of events from the  $2\nu\beta\beta$  decay of  $^{100}\text{Mo}$  to the excited  $0_1^+$  state have been collected, NEMO3 will be the first double beta decay experiment to produce the two-electron energy sum ( $E_{ee}$ ) and the single electron energy ( $E_e$ ) spectra for the  $2\nu\beta\beta$  (g.s.  $\rightarrow 0_1^+$ ) decay transition.

My personal contribution in the NEMO3 experiment during my Ph.D. study had several aspects. During the first period when the NEMO3 detector was still under construction, it consisted of thorough tests and then in tuning of both the wire chamber and the calorimeter as the individual sectors of NEMO3 were being installed in the LSM laboratory. The work on

the wire chamber and its electronics was carried out together with colleagues from LAL Orsay, while the work on the calorimeter was realised in close cooperation with collaborators from CENBG Bordeaux, IReS Strasbourg, and JINR Dubna. Besides the instrumental side, Monte-Carlo simulations of the  $2\nu\beta\beta$  decays to the excited and ground states and also various kinds of backgrounds were developed during this period, as well as programs for data analysis. Actually, both the simulations and the analysis program development continued when experimental data was already available because the real data brought new constraints like, for instance, the presence of radon inside the detector, instabilities of the wire chamber, zones of continuously self-discharging Geiger cells, and reduction of the global efficiency of the detector caused by a certain number of uncalibrated PMTs or PMTs physically missing in the data. These efforts achieved the definition of the eeN $\gamma$  analysis channel with a set of selection criteria optimised in order to reduce significantly backgrounds and to allow an efficient measurement of the  $2\nu\beta\beta$  decay of  $^{100}\text{Mo}$  to the excited  $0_1^+$  state of  $^{100}\text{Ru}$ .

During the second period when NEMO3 had already been collecting data, my contribution to the experiment consisted of the participation in data acquisition of  $\beta\beta$  runs in the LSM laboratory, as well as in carrying about special runs with neutron sources for the calibration of the experimental setup and later, runs with sources of  $^{208}\text{Tl}$  and  $^{214}\text{Bi}$  devoted for the experimental study of the external background contribution. Finally, my part in the NEMO3 experiment was also concerned with the analysis of experimental data. All the currently available data from  $\beta\beta$  runs, as well as from the special runs with sources of  $^{208}\text{Tl}$  and  $^{214}\text{Bi}$  have been analysed in order to search for a signal from the  $2\nu\beta\beta$  decay of  $^{100}\text{Mo}$  to the excited  $0_1^+$  state and in order to estimate the remaining background level. The analysis of the eeN $\gamma$  channel with the appropriate selection criteria presented in this work already gives a positive result, as mentioned above.

# Bibliography

- [1] W. Pauli, *On the earlier and more recent history of the neutrino* (1957) in: K. Winter (Ed.), *Neutrino Physics*, Cambridge University Press, 1991.
- [2] E. Fermi, *Z. Physik* **88** (1934) 161.
- [3] C.L. Cowan, F. Reines *et al.*, *Science* **124** (1956) 103.
- [4] F. Reines, *Rev. Mod. Phys.* **68** (1996) 317.
- [5] G. Danby *et al.*, *Phys. Rev. Lett.* **9** (1962) 36.
- [6] K. Kodama *et al.* (DONUT Collaboration), *Phys. Lett. B* **504** (2001) 218.
- [7] Y. Fukuda *et al.* (SuperKamiokande Collaboration), *Phys. Rev. Lett.* **81** (1998) 1562.
- [8] Q.R. Ahmad *et al.* (SNO Collaboration), *Phys. Rev. Lett.* **89** (2002) 011301; `nuc1-ex/0204008`.
- [9] Q.R. Ahmad *et al.* (SNO Collaboration), *Phys. Rev. Lett.* **89** (2002) 011302; `nuc1-ex/0204009`.
- [10] K. Eguchi *et al.* (KamLAND Collaboration), *Phys. Rev. Lett.* **90** (2003) 021802.
- [11] J.F. Beacom and P. Vogel, *Phys. Rev. Lett.* **83** (1999) 5222.
- [12] P. Vogel, *Čs. čas. fyz.* **50** (2000) 285.
- [13] Q. Ho-Kim and Ph.X. Yem, *Elementary Particles and Their Interactions – Concepts and Phenomena*, Springer, 1998.
- [14] G. Müller, *Gauge Theory of Weak Interactions*, Springer, 2000.
- [15] B.M. Pontecorvo, *J. Exptl. Theoret. Phys.* **34** (1957) 247.
- [16] D.O. Caldwell (Ed.), *Current Aspects of Neutrino Physics*, Springer, 2001.
- [17] L. Wolfenstein, *Phys. Rev. D* **17** (1978) 2369.
- [18] S.P. Mikheyev and A.Yu. Smirnov, *Sov. J. Nucl. Phys.* **42** (1985) 913.
- [19] K. Zuber, *Phys. Reports* **305** (1998) 295.
- [20] S.C. Curran, J. Angus, and A.L. Cockroft, *Nature* **162** (1948) 302.
- [21] S.C. Curran, J. Angus, and A.L. Cockroft, *Phys. Rev.* **76** (1949) 853.

- [22] A. Osipowicz *et al.* (KATRIN Collaboration), *Letter of Intent*, [hep-ex/0109033](http://ik1au1.fzk.de/~katrin/hep-ex/0109033);  
<http://ik1au1.fzk.de/~katrin/>
- [23] C. Weinheimer *et al.*, *Phys. Lett. B* **460** (1999) 219.
- [24] V.M. Lobashev *et al.*, *Phys. Lett. B* **460** (1999) 227.
- [25] E. Holzschuh, M. Fritschi, and W. Kuendig, *Phys. Lett. B* **287** (1992) 381.
- [26] R.G.H. Robertson *et al.*, *Phys. Rev. Lett.* **67** (1991) 957.
- [27] H. Kawakami *et al.*, *Phys. Lett. B* **256** (1991) 105.
- [28] S. Boris *et al.*, *Phys. Rev. Lett.* **58** (1987) 2019.
- [29] W.H. Barkas, W. Birnbaum, and F. Smith, *Phys. Rev.* **101** (1956) 778.
- [30] K. Assamagan *et al.*, *Phys. Rev. D* **53** (1996) 6065.
- [31] R. Barate *et al.*, *Eur. Phys. J. C* **2** (1998) 395.
- [32] T.J. Haines *et al.* (IMB Collaboration), *Phys. Rev. Lett.* **57** (1986) 1986.
- [33] K.S. Hirata *et al.*, *Phys. Lett. B* **205** (1988) 416.
- [34] Ch. Berger *et al.* (Fréjus Collaboration), *Phys. Lett. B* **269** (1991) 227.
- [35] R. Davis Jr., D.S. Harmer, and K.C. Hoffman, *Phys. Rev. Lett.* **20** (1968) 1205.
- [36] L. Oberauer, *Nucl. Phys. B* **77** (1999) 48.
- [37] T. Beau, PhD thesis, Université Paris VII, 2002.
- [38] J.N. Abdurashitov *et al.* (SAGE Collaboration), *Phys. Rev. Lett.* **77** (1996) 4708.
- [39] W. Hampel *et al.* (GALLEX Collaboration), *Phys. Lett. B* **388** (1996) 384.
- [40] H. Kwon *et al.*, *Phys. Rev. D* **24** (1981) 1097.
- [41] B. Achkar *et al.*, *Nucl. Phys. B* **434** (1995) 503.
- [42] F. Boehm *et al.*, *Phys. Rev. Lett.* **84** (2000) 3764.
- [43] M. Apollonio *et al.*, *Phys. Lett. B* **420** (1998) 397.
- [44] M. Apollonio *et al.*, *Phys. Lett. B* **466** (1999) 415; [hep-ex/9907037](http://www.hep-ex/9907037).
- [45] L. De Braeckelee, *Nuclear Physics B (Proc. Suppl.)* **87** (2000) 312.
- [46] Athanassopoulos *et al.* (LSND Collaboration), *Nucl. Instr. and Meth.* **A388**, (1997) 149;  
<http://www.neutrino.lanl.gov/LSND/>
- [47] G. Drexlin *et al.* (KARMEN Collaboration), *Nucl. Instr. and Meth.* **A289** (1990) 490;  
<http://www-ik.fzk.de/~karmen/>
- [48] Athanassopoulos *et al.* (LSND Collaboration), *Phys. Rev. Lett.* **81** (1998) 1774.

- [49] K. Eitel (KARMEN Collaboration), *Proceedings of the 23rd Intern. School of Nucl. Physics Neutrinos in Astro, Particle and Nuclear Physics*, Erice/Sicily, Sept. 18 – 26, 2001; Prog. Part. Nucl. Physics **48** (2002) 89, Ed. A. Faessler.
- [50] S.H. Ahn *et al.* (K2K Collaboration), Phys. Lett. B **511** (2001) 178.
- [51] S.G. Wojcicki, NuMI-L-224, 1996; <http://www-numi.fnal.gov/>
- [52] M.V. Diwan, NuMI-CONF-GEN-886, 2002; hep-ex/0211026.
- [53] M. Guler *et al.* (OPERA Collaboration), *Experiment Proposal*, CERN/SPSC 2000-028, SPSC/P318, LNGS P25/2000, 2000.
- [54] T. Tomoda, Rep. Prog. Phys. **54** (1991) 53.
- [55] A. Faessler and F. Šimkovic, J. Phys. G **24** (1998) 2139.
- [56] S.R. Elliott and P. Vogel, Annu. Rev. Nucl. Part. Sci. **52** (2002) 115; hep-ph/0202264.
- [57] M. Goeppert-Mayer, Phys. Rev. **48** (1935) 512.
- [58] M. Doi and T. Kotani, Prog. Theor. Phys. **87** (1992) 1207.
- [59] M. Doi and T. Kotani, Prog. Theor. Phys. **89** (1993) 139.
- [60] W.H. Furry, Phys. Rev. **56** (1939) 1184.
- [61] M. Doi, T. Kotani, and E. Takasugi, Phys. Rev. D **37** (1988) 2575.
- [62] E. Majorana, Nuovo Cimento **14** (1937) 171.
- [63] Ch.W. Kim and A. Pevsner, *Neutrinos in Physics and Astrophysics – Contemporary Concepts in Physics Volume 8*, Harwood Academic Publishers, 1993.
- [64] P. De Bievre and P.D.P. Taylor, Int. J. Mass Spectrom. Ion. Phys. **123** (1993) 149.
- [65] J. Suhonen and O. Civitarese, Phys. Reports **300** (1998) 123.
- [66] A. Griffiths and P. Vogel, Phys. Rev C **46** (1992) 181.
- [67] S. Stoica and I. Mihut, Nucl. Phys. A **602** (1996) 197.
- [68] M. Aunola and J. Suhonen, Nucl. Phys. A **602** (1996) 133.
- [69] J. Suhonen, Phys. Lett. B **477** (2000) 99.
- [70] J. Suhonen, Nucl. Phys. A **700** (2002) 649.
- [71] J. Suhonen, *Proceedings of the Workshop on Calculation of Double-Beta-Decay Matrix Elements MEDEX'01*, Czech. J. Phys. **52** (2002) 597.
- [72] H. Ejiri *et al.*, Nucl. Phys. A **611** (1996) 85.
- [73] T. Kirsten *et al.*, Phys. Rev. Lett. **20** (1968) 1300.
- [74] E.W. Hennecke, O.K. Manuel, and D.D. Sabu, Phys. Rev. C **11** (1975) 1378.

- [75] E.W. Hennecke, Phys. Rev. C **17** (1978) 1168.
- [76] B.T. Cleveland *et al.*, Phys. Rev. Lett. **35** (1975) 757.
- [77] K. Marti and S.V.S. Murty, Phys. Lett. B **163** (1985) 71.
- [78] C.E. Aalseth *et al.* (IGEX Collaboration), Phys. Rev. C **59** (1999) 2108.
- [79] C.E. Aalseth *et al.* (IGEX Collaboration), Phys. At. Nucl. **63** (2000) 1225.
- [80] L. Balysh *et al.* (Heidelberg–Moscow Collaboration), Phys. Lett. B **322** (1994) 176.
- [81] L. Baudis *et al.* (Heidelberg–Moscow Collaboration), Phys. Lett. B **407** (1997) 219.
- [82] M. Günther *et al.* (Heidelberg–Moscow Collaboration), Phys. Rev. D **55** (1997) 54.
- [83] H.V. Klapdor-Kleingrothaus, J. Hellmig, and M. Hirsh, J. Phys. G: Nucl. Part. Phys. **24** (1998) 483.
- [84] L. De Braeckeleer, *preprint submitted to World Scientific* (Aug. 10, 2000); C.E. Aalseth *et al.* (Majorana Collaboration), hep-ex/0201021.
- [85] C.E. Aalseth and H.S. Miley, Nuclear Physics B (Proc. Suppl.) **110** (2002) 392.
- [86] Ch. Briançon *et al.* (TGV Collaboration), Nucl. Instr. and Meth. in Phys. Res. A **372** (1996) 222.
- [87] V.B. Brudanin *et al.* (TGV Collaboration), Phys. Lett. B **495** (2000) 63.
- [88] I. Štekl *et al.* (TGV Collaboration), *Proceedings of the Workshop on Calculation of Double-Beta-Decay Matrix Elements MEDEX'01*, Czech. J. Phys. **52** (2002) 541.
- [89] I. Štekl *et al.* (TGV Collaboration), *Proceedings of the Workshop on Calculation of Double-Beta-Decay Matrix Elements MEDEX'99*, Czech. J. Phys. **50** (2000) 553.
- [90] E. Fiorini and T. Niinikoski, Nucl. Instr. and Meth. in Phys. Res. A **354** (1984) 83.
- [91] A. Alessandrello *et al.*, Phys. Lett. B **433** (1998) 156.
- [92] C. Brofferio *et al.*, *Proceedings of the Workshop on Calculation of Double-Beta-Decay Matrix Elements MEDEX'01*, Czech. J. Phys. **52** (2002) 531.
- [93] A. Alessandrello *et al.*, Phys. Lett. B **486** (2000) 13.
- [94] S. Pirro *et al.*, Nucl. Instr. and Meth. in Phys. Res. A **444** (2000) 71.
- [95] I.G. Irastorza, A. Morales, and S. Scopel, hep-ph/0108146.
- [96] M.K. Moe and D.D. Lowenthal, Phys. Rev. C **22** (1980) 2186.
- [97] S.R. Elliott, A.A. Hahn, and M.K. Moe, Phys. Rev. Lett. **59** (1987) 2020.
- [98] S.R. Elliott, M.K. Moe, M.A. Nelson, and M.A. Vient, J. Phys. G: Nucl. Part. Phys. **17** (1991) S145.
- [99] A. De Silva *et al.*, Phys. Rev. C **56** (1997) 2451.

- [100] V. Artemiev *et al.*, Phys. Lett. B **345** (1995) 564.
- [101] R. Luescher *et al.*, Phys. Lett. B **434** (1998) 407.
- [102] M. Danilov *et al.* (EXO Collaboration), Phys. Lett. B **480** (2000) 12.
- [103] H. Ejiri *et al.* (ELEGANTS V Collaboration), Nucl. Instr. and Meth. in Phys. Res. A **302** (1991) 304; H. Ejiri *et al.* (ELEGANTS V Collaboration), J. Phys. G: Nucl. Part. Phys. **17** (1991) S155.
- [104] K. Fushimi *et al.* (ELEGANTS V Collaboration), Phys. Lett. B **531** (2002) 190.
- [105] N. Ishihara, T. Ohama, and Y. Yamada, Nucl. Instr. and Meth. in Phys. Res. A **373** (1996) 325.
- [106] H. Ejiri, J. Engel, R. Hazama, P. Krastev, N. Kudomi, and R.G.H. Robertson, Phys. Rev. Lett. **85** (2000) 2917.
- [107] A. Barabash, *Proceedings of the Workshop on Calculation of Double-Beta-Decay Matrix Elements MEDEX'01*, Czech. J. Phys. **52** (2002) 567.
- [108] V.I. Tretyak and Yu.G. Zdesenko, At. Data and Nucl. Data Tables **80** (2002) 83.
- [109] M. Alston-Garnjost *et al.*, Phys. Rev. Lett. **71** (1993) 831.
- [110] D. Dassié *et al.* (NEMO Collaboration), Phys. Rev. **D51** (1995) 2090.
- [111] R. Arnold *et al.* (NEMO Collaboration), Nucl. Instr. and Meth. **A401** (1997) 144.
- [112] R. Arnold *et al.* (NEMO Collaboration), Nucl. Phys. **A636** (1998) 209.
- [113] R. Arnold *et al.* (NEMO Collaboration), Z. Phys. **C72** (1996) 239.
- [114] R. Arnold *et al.* (NEMO Collaboration), Nucl. Phys. **A658** (1999), 299.
- [115] D. González *et al.* (IGEX Collaboration), Nuclear Physics B (Proc. Suppl.) **87** (2000) 278.
- [116] A. Balysh *et al.* (Heidelberg–Moscow Collaboration), Phys. Lett. B **356** (1995) 450.
- [117] M. Doi, T. Kotani, and E. Takasugi, Prog. Theor. Phys. Suppl. **83** (1985) 1.
- [118] W.C. Haxton and G.J. Stephenson, Jr., Prog. Part. Nucl. Phys. **12** (1984) 409.
- [119] N. Kudomi *et al.* (ELEGANTS V Collaboration), Phys. Rev. C **46** (1992) R2132.
- [120] A.S. Barabash, A.V. Kopylov, and V.I. Cherenovsky, Phys. Lett. B **249** (1990) 186.
- [121] J.G. Hirsh, O. Castaños, P.O. Hess, and O. Civitarese, Phys. Rev. C **51** (1995) 2252.
- [122] S. Stoica, Phys. Lett. B **350** (1995) 152.
- [123] F. Šimkovic, P. Domin, and S.V. Semenov, J. Phys. G: Nucl. Part. Phys. **27** (2001) 2233.
- [124] A.S. Barabash *et al.*, Phys. Lett. B **345** (1995) 408.
- [125] D. Blum *et al.* (NEMO Collaboration), Phys. Lett. B **275** (1992) 506.

- [126] A.S. Barabash, R. Gurriarán, F. Hubert, Ph. Hubert, and V.I. Umatov, *Yadernaya fizika* **62** (1999) 2211 (*Phys. At. Nucl.* **62** (1999) 2039).
- [127] L. De Braeckelee, M. Hornish, A.S. Barabash, and V.I. Umatov, *Phys. At. Nucl.* **63** (2000) 1214.
- [128] L. De Braeckelee, M. Hornish, A.S. Barabash, and V.I. Umatov, *Phys. Rev. Lett.* **86** (2001) 3510.
- [129] D. Dassié *et al.* (NEMO Collaboration), *Nucl. Instr. and Meth.* **A309** (1991) 465.
- [130] R. Arnold *et al.* (NEMO Collaboration), *Nucl. Instr. and Meth.* **A354** (1995) 338.
- [131] Table of Isotopes, <http://ie.lbl.org/toi/>
- [132] Nuclear structure and decay data, <http://nucldata.nuclear.lu.se/database/masses/>
- [133] R. Arnold *et al.* (NEMO Collaboration), *Technical design and performances of the NEMO3 detector*, to be published in *Nucl. Instr. and Meth. in Phys. Res. A* in 2004.
- [134] C. Jollet, PhD thesis, Université Bordeaux I, 2002.
- [135] R. Arnold and V.I. Tretiak, *NEMO3 simulation program – User’s guide*, NEMO note IReS-1/2001, December 2001.
- [136] R. Arnold *et al.* (NEMO Collaboration), *Nucl. Instr. and Meth. in Phys. Res. A* **474** (2001) 93.
- [137] K. Errahmane, PhD thesis, Université Paris VII, 2001.
- [138] I. Štekl, contribution to the NEMO Collaboration Meeting, Chambéry, July 9 –11, 2002.
- [139] Ch. Marquet, PhD thesis, Université Bordeaux I, 1999.
- [140] Ch. Marquet *et al.* (NEMO Collaboration), *Nucl. Instr. and Meth. in Phys. Res. A* **457** (2001) 487.
- [141] F. Mauger, *The NEMO3 Trigger Documentation*, internal NEMO note, LPC Caen, July 2001.
- [142] Y. Perrin *et al.*, CASCADE: Toolkit for the construction of distributed real time data acquisition systems, *Conference Records of RT 93*, Vancouver, 1993.
- [143] L. Vála, *Proceedings of the Workshop on Calculation of Double-Beta-Decay Matrix Elements MEDEX’01*, *Czech. J. Phys.* **52** (2002) 557.
- [144] H. Ohsumi, R. Gurriarán, Ph. Hubert *et al.* (NEMO Collaboration), *Nucl. Instr. and Meth. in Phys. Res. A* **482** (2002), 832.
- [145] C. Berger *et al.*, *Nucl. Instr. and Meth.* **A262** (1987) 463.
- [146] G.T. Ewen, *Nucl. Instr. and Meth.* **A314** (1992) 373.
- [147] J. Busto, Y. Gonin, F. Hubert, Ph. Hubert, and J.-M. Vuilleumier, *Nucl. Instr. and Meth. in Phys. Res. A* **492** (2002) 35.

- [148] *CERNLIB*, CERN Program Library Short Write-ups, CERN, 1996.
- [149] *GEANT – Detector description and simulation tool*, CERN Program Library Long Write-up W5013, CERN, 1994.
- [150] R. Brun, O. Couet, C. Vandoni, and P. Zanmarini, *PAW – Physics Analysis Workstation*, CERN Program Library Long Write-up Q121, CERN, 1989.
- [151] H. Grote and M. Metcalf, *A simplified guide to the use of PATCHY*, CERN, 1980; J. Zoll, *PATCHY – Reference manual*, CERN, 1995.
- [152] A.I. Etienvre, PhD thesis, Université Paris XI, 2003.
- [153] R. Arnold, private communication.
- [154] F. Mauger, contribution to the NEMO Collaboration Meeting, Aussois, December 10 – 12, 2002.
- [155] Yu. Shitov, K. Errahmane, X. Sarazin, and L. Simard, *Description of the pre-analysis and visualisation programs developed at LAL*, internal NEMO note, LAL Orsay, May 2001.
- [156] Yu. Shitov and V. Tretyak, *NEMO database – User’s and programmer’s guide*, internal NEMO note, 2002.
- [157] V. Vasiliev, private communication.
- [158] A.G. Frodesen, O. Skjeggstad, and H. Tøfte, *Probability and Statistics in Particle Physics*, Universitetsforlaget, 1979.
- [159] Particle Data Group, *Eur. Phys. J. C* **Vol. 3** (1998) 1.
- [160] G.L. Feldman and R.D. Cousins, *Phys. Rev. D* **57** (1998) 3873.
- [161] D.C. Montgomery, *Design and analysis of experiments*, John Wiley & Sons, 1976.
- [162] L. Simard, contribution to the NEMO Collaboration Meeting, Aussois, December 10 – 12, 2002.
- [163] D. Lalanne, contribution to the NEMO Collaboration Meetings, Aussois, December 10 – 12, 2002; and Dubna, March 24 – 26, 2003.
- [164] V.I. Tretyak, contribution to the NEMO Collaboration Meeting, Prague, June 9 – 11, 1999.
- [165] R. Arnold, private communication.
- [166] L. Simard, contribution to the NEMO Collaboration Meeting, Gif-sur-Yvette, May 26 – 28, 2003.



**Abstract:** The NEMO3 detector was designed for the study of double beta decay and in particular to search for the neutrinoless double beta decay process ( $0\nu\beta\beta$ ). The intended sensitivity in terms of a half-life limit for the  $0\nu\beta\beta$  decay is of the order of  $10^{25}$  yr which corresponds to an effective neutrino mass  $\langle m_\nu \rangle$  on the level of  $(0.3 - 0.1)$  eV. The  $0\nu\beta\beta$  process is today the most promising test of the Majorana nature of the neutrino. The detector was constructed in the Modane Underground Laboratory (LSM) in France by an international collaboration including France, Russia, the Czech Republic, the USA, the UK, Finland, and Japan. The experiment has been taking data since May 2002.

The quantity of  $^{100}\text{Mo}$  in the detector (7 kg) allows an efficient measurement of the two-neutrino double beta decay ( $2\nu\beta\beta$ ) of  $^{100}\text{Mo}$  to the excited  $0_1^+$  state (eeN $\gamma$  channel). Monte-Carlo simulations of the effect and of all the relative sources of background have been produced in order to define a set of appropriate selection criteria. Both Monte-Carlo simulations and special runs with sources of  $^{208}\text{Tl}$  and  $^{214}\text{Bi}$  showed that the only significant background in the eeN $\gamma$  channel comes from radon that penetrated inside the wire chamber of NEMO3. The experimental data acquired from May 2002 to May 2003 have been analysed in order to determine the signal from the  $2\nu\beta\beta$  decay of  $^{100}\text{Mo}$  to the excited  $0_1^+$  state and the corresponding background level. The physical result, which was obtained at the level of four standard deviations, is given in the form of an interval of half-life values at 95% confidence level.

**Key-words:** neutrino, double beta decay, molybdenum,  $^{100}\text{Mo}$ , Monte-Carlo simulations, background.

---

**Résumé :** Le détecteur NEMO3 a été conçu pour l'étude de la double désintégration bêta et particulièrement pour la recherche de la double désintégration bêta sans émission de neutrino ( $0\nu\beta\beta$ ). La sensibilité attendue pour la désintégration  $0\nu\beta\beta$  est, en terme de la demi-vie de l'ordre de  $10^{25}$  ans, en terme de masse effective du neutrino cela correspond à une sensibilité  $(0,3 - 0,1)$  eV. Le processus  $0\nu\beta\beta$  représente aujourd'hui le test de la nature Majorana du neutrino le plus prometteur. Le détecteur a été construit au Laboratoire Souterrain de Modane (LSM) en France par la collaboration internationale (France, Russie, République Tchèque, États-Unis, Royaume-Uni, Finlande et Japon). La prise de donnée a commencé en mai 2002 et continue actuellement.

La masse de  $^{100}\text{Mo}$  dans le détecteur (7 kg) permet une mise en évidence de la double désintégration bêta avec émission de deux neutrinos ( $2\nu\beta\beta$ ) du  $^{100}\text{Mo}$  vers l'état excité  $0_1^+$  (canal eeN $\gamma$ ). Les simulations Monte-Carlo de l'effet et de tous les types de bruit de fond ont été effectuées pour définir un ensemble des critères de sélection appropriés. D'autre part des runs avec des sources du  $^{208}\text{Tl}$  et du  $^{214}\text{Bi}$  ainsi que des simulations Monte-Carlo de ces données ont montré que le seul bruit de fond significatif dans le canal eeN $\gamma$  vient du radon qui avait pénétré à l'intérieur de la chambre à fils de NEMO3. Les données expérimentales acquises de mai 2002 à mai 2003 ont été analysées pour déterminer le signal dû à la désintégration  $2\nu\beta\beta$  du  $^{100}\text{Mo}$  vers l'état excité  $0_1^+$  et le niveau de bruit de fond correspondant. Le résultat est donné sous la forme d'un intervalle de valeurs de la demi-vie au niveau de 95% de confiance. Cela correspond à une mise en évidence du processus au niveau de confiance de quatre écarts standards.

**Mots-clé :** neutrino, double désintégration bêta, molybdène,  $^{100}\text{Mo}$ , simulations Monte-Carlo, bruit de fond.

---

**Abstrakt:** Detektor NEMO3 byl navržen pro studium dvojitého rozpadu beta, především pro proces bezneutrinového rozpadu beta ( $0\nu\beta\beta$ ). Požadovaná citlivost je z hlediska poločasu rozpadu  $0\nu\beta\beta$  na úrovni  $10^{25}$  let, což odpovídá efektivní hmotnosti neutrina v rozmezí (0,3 – 0,1) eV. Proces  $0\nu\beta\beta$  je v dnešní době nejslibnějším testem Majoranovské povahy neutrina. Detektor byl zkonstruován v podzemní laboratoři LSM v Modane ve Francii v rámci mezinárodní spolupráce zahrnující Francii, Rusko, Českou republiku, USA, Velkou Británii, Finsko a Japonsko. Experiment začal se sběrem experimentálních dat pro  $\beta\beta$  proces v květnu 2002, přičemž tato měření pokračují i v současné době.

Množství isotopu  $^{100}\text{Mo}$  v detektoru (7 kg) umožňuje také efektivní měření dvouneutrinového dvojitého rozpadu beta ( $2\nu\beta\beta$ )  $^{100}\text{Mo}$  na vzbuzeu hladinu  $0_1^+$  (kanál  $eeN\gamma$ ). Simulace Monte-Carlo efektu a všech příslušných zdrojů pozadí byly uskutečněny za účelem stanovení souboru optimálních výběrových kritérií. Jak simulace Monte-Carlo, tak speciální měření se zdroji  $^{208}\text{Tl}$  a  $^{214}\text{Bi}$  ukázaly, že jediným významným zdrojem pozadí v kanále  $eeN\gamma$  je radon, který pronikl do drátové komory detektoru NEMO3. Experimentální data za období od května 2002 do května 2003 byla zpracována za účelem stanovení jak signálu pro  $2\nu\beta\beta$  rozpad  $^{100}\text{Mo}$  na vzbuzeu hladinu  $0_1^+$ , tak i příslušné úrovně pozadí. Fyzikální výsledek, který byl stanoven na úrovni čtyř standartních odchylek, je vyjádřen ve formě intervalu hodnot poločasu rozpadu a to na hladině významnosti 95%.

**Klíčová slova:** neutрино, dvojitý rozpad beta, molybden,  $^{100}\text{Mo}$ , simulace Monte-Carlo, pozadí.

---